Galaxy Evolution and Cosmology Studies using Luminous Red Galaxies

UNIVERSITY *of the*
WESTERN CAPE

Ando Ratsimbazafy
Department of Physics
University of the Western Cape

A thesis submitted for the degree of
Doctor of Philosophy

Supervisor : Prof. Catherine Cress
Co-Supervisor : Dr Steve Crawford

To my loving husband

Galaxy Evolution and Cosmology Studies using Luminous Red Galaxies

Ando Ratsimbazafy

Keywords:

- Cosmological parameters
- Early-type Galaxies
- Galaxy abundances
- Galaxy Evolution
- Galaxies
- Luminous Red Galaxies
- Observational cosmology
- Universe

Abstract

Name: Ando Ratsimbazafy

Title : Galaxy Evolution and Cosmology Studies using Luminous Red Galaxies

Date : 31^{st} of October 2014

There have been a number of attempts to measure the expansion rate of the Universe using age-dating of Luminous Red Galaxies (LRGs). Assuming that stars in LRGs form at the same time, age-dating of two populations of LRGs at different redshifts can provide an estimate of the time difference associated with the corresponding redshift interval (dz/dt). This gives a direct estimate of the Hubble parameter $H(z)$ at the average redshift of the two populations. In this thesis, we explore the validity of this method by using two different sets of data. Firstly, we select a homogeneous sample of passively evolving galaxies over $0.10 < z < 0.40$ from the Sloan Digital Sky Survey Data Release Seven (SDSS-DR7) catalogue by applying a refined criteria, which is based on absolute magnitude. Secondly, we carry out series of observations on the Southern African Large Telescope (SALT) to obtain spectra of LRGs at two narrow redshift ranges $z \simeq 0.40$ and $z \simeq 0.55$ in order to calculate the Hubble parameter $H(z)$ at $z \simeq 0.47$. We utilise two distinct methods of age-dating including the use of absorption Lick index lines and full spectral fitting on high signal-to-noise galaxy spectra from our sample.

By establishing the age-redshift relation of the quiescent, passively evolving galaxies from SDSS, we obtain three improved new observational $H(z)$ data points which are $H(z) = 76.8 \pm 5.3$ km s^{-1}Mpc^{-1} at $z \simeq 0.28$, $H(z) = 78.5 \pm 6.8$ km s^{-1}Mpc^{-1} at $z \simeq 0.30$ and $H(z) = 86.3 \pm 7.6$ km s^{-1}Mpc^{-1} at $z \simeq 0.32$ respectively. We also find another $H(z)$ value of 105 ± 39 km s^{-1}Mpc^{-1} at $z \simeq 0.47$ when age-dating LRGs observed with SALT. Combining all 4 data points with another 25 data points in the literature, we place better constraints on cosmological models and find the matter density parameter to be constrained by $\Omega_m = 0.32^{+0.05}_{-0.06}$ and the Hubble constant to be $H_0 = 68.5 \pm 2.4$. These results are very consistent with other studies. Through this work, we are able to demonstrate

that the cosmic chronometers approach can potentially be used to explore the evolution of the Universe.

DECLARATION

I declare that *Galaxy Evolution and Cosmology Studies using Luminous Red Galaxies* is my own work as well as the outcome of scientific collaborations stated below, that it has not been submitted before for any degree or examination in any other University. The content of this thesis includes work presented in the cited research papers and conference proceedings; and that sources I have used or quoted have been indicated and acknowledged as complete references.

Ando Ratsimbazafy

October 2014

Signed : .....

List of publications

Refereed Papers:

- **"Luminous Red Galaxies in Simulations: Cosmic Chronometers?"**
  Crawford S., **Ratsimbazafy A.**, Cress C., Olivier E., Blyth S., van der Heyden K.
  2010, Monthly Notices of the Royal Astronomical Society, 406, 2569

- **"Age-dating Luminous Red Galaxies observed with the SALT"**
  Ratsimbazafy A., Cress C., Crawford M., SCALPEL group
  2014, Monthly Notices of the Royal Astronomical Society, to be submitted

- **"SDSS-LRG spectra: Full spectral fitting vs Lick indices"**
  Ratsimbazafy A., Cress C., Crawford S., et al.
  2014, Monthly Notices of the Royal Astronomical Society, in preparation

Conference Proceedings:

- **"Studying Luminous Red Galaxies to probe H(z) at high redshift"**
  Ratsimbazafy A., Cress C., Crawford S., 2013, IAUS, 295, 185

- **"Age-dating Stellar Populations of Luminous Red Galaxies"**
  Ratsimbazafy A., Cress C., Crawford S., Maraston C., Nichol R., Thomas D., 2012, IAUS, 284, 265

- **"Using Luminous Red Galaxies as Cosmic Chronometers"**
  Crawford S., Blyth S., Cress C., Olivier E., **Ratsimbazafy A.**, van der Heyden K., 2011, AAS, 43, 214.06

- **"Stellar populations in Luminous Red Galaxies: cosmic chronometers?" Ratsimbazafy A.**, Cress C., Blyth S., Crawford S., Olivier E., van der Heyden K., 2010, IAUS, 262, 414

Acknowledgements

I would like to acknowledge here those who have helped to bring this work to fruition. Foremost, a very special thanks to Prof **Catherine Cress** for her unlimited enthusiasm by advising me during this project, for her patient and encouraging manner of her supervision. I would also like to express my gratitude to Dr **Steve Crawford** for his willingness to be my co-supervisor, for his invaluable guidance and enthusiasm during this project.

More generally, many thanks to the SCALPEL Group and staff members at SAAO, especially **Petri Vaisanen** and **David Gilbank** for their invaluable inputs, suggestions and helps while obtaining observations with SALT in Sutherland and reducing optical data. And also many thanks to all UWC postdocs and colleagues at UWC and SAAO for helping me when I was stuck on some problems. A big special thanks to **Mathew Smith** for all fruitful discussions and his invaluable and endless helps along this project. Not forgetting, **Elodie Giovannoli**, **Russell Johnston**, and **Patrice Okouma**.

Thanks to **Mina Koleva** for her help on ULySS during the wonderful time attending the workshop on "Multiwavelength Studies of Populations in Clusters and Groups " in Parys - Free State

This work used observations obtained with the Southern African Large Telescope (SALT) under program 2011-3-RSA_OTH-026 and 2012-1-RSA_OTH-013 (PI: Ando Ratsimbazafy).

I am grateful to the Centre of High Performance Computing (CHPC) team for allowing me to use their facility and giving me the access to their clusters when I run COSMOMC.

Part of this work also uses data from the Sloan Digital Sky survey (SDSS) data archive. Funding for the SDSS and SDSS-II has been provided by the Alfred P. Sloan Foundation, the Participating Institutions, the National Science Foundation, the U.S. Department of Energy, the National Aeronautics and Space Administration, the Japanese Monbukagakusho, the Max Planck Society, and the Higher Education Funding Council for England. The SDSS Web Site is **http://www.sdss.org/**.

The SDSS is managed by the Astrophysical Research Consortium for the Participating Institutions. The Participating Institutions are the American Museum of Natural History, Astrophysical Institute Potsdam, University of Basel, University of Cambridge, Case Western Reserve University, University of Chicago, Drexel University, Fermilab, the Institute for Advanced Study, the Japan Participation Group, Johns Hopkins University, the Joint Institute for Nuclear Astrophysics, the Kavli Institute for Particle Astrophysics and Cosmology, the Korean Scientist Group, the Chinese Academy of Sciences (LAMOST), Los Alamos National Laboratory, the Max-Planck-Institute for Astronomy (MPIA), the Max-Planck-Institute for Astrophysics (MPA), New Mexico State University, Ohio State University, University of Pittsburgh, University of Portsmouth, Princeton University, the United States Naval Observatory, and the University of Washington.

I acknowledge funding from the National Research Funding/ Square Kilometer Array (NRF/SKA), from the Centre of High Performance Computing (CHPC), and from the Royal Society Bilateral to allow me visiting the Institute of Cosmology and Gravitation (ICG) in Portsmouth - UK.

I would like to extend special thanks to my friends and family for their support, encouragement and basement. Finally, I dedicate this thesis to my husband **Andry Rajoelimanana**, in memory of all happiness and sadness that we both have gone through during this thesis.

List of Figures

List of Tables

Contents

Chapter 1

Introduction

1.1 The theoretical background

Cosmology is the study of the Universe as a whole particularly its contents, formation, evolution, and eventual fate. In the last three decades scientists have developed a simple model which describes the Universe. It is named the Lambda Cold Dark Matter (ΛCDM) model and is frequently referred to as the "standard model". This model is the simplest and the best model that is able to provide a reasonable explanation of all properties of the cosmos (e.g. the Cosmic Microwave Background (CMB), the large scale structure, the chemical abundances, the expansion and acceleration of the Universe, etc.). The ΛCDM (Λ Cold Dark Matter) model assumes that General Relativity (GR) is the correct theory of gravity. Despite the rapid improvement in observational technology and computational simulations, there are still some big challenges awaiting an attempt to match the theoretical to the observational cosmology.

This chapter deals with the introduction of the modern cosmology model, the general concept of galaxy formation and evolution, and the extragalactic objects used for this study.

1.1.1 Galaxy formation and evolution in a ΛCDM Universe

1.1.1.1 Short overview of theoretical cosmology

All modern cosmological models are based on Einstein's general theory of relativity (1915). The spacetime of the Universe can be described by solving Einstein's general relativistic field equation defined as

$$G_{\mu\nu} = \frac{8\pi G}{c^4} T_{\mu\nu} \tag{1.1}$$

where $G_{\mu\nu}$ the left-hand side of the equation 1.1 describes the geometry of the space time, and it is presented in a form of the metric of the space-time $g_{\mu\nu}$. The right-hand side of the equation 1.1 expresses the matter content of the Universe, specified by $T_{\mu\nu}$ which is

the sum of the stress-energy tensors for the various components of energy, baryons, radiation, neutrinos, dark matter and possibly others.

Since on the largest scales (>100 Mpc) the universe appears homogeneous and there are no observations that seem to pick out preferred directions, we can model the Universe as homogeneous (constant density) and expanding isotropically (the same in all directions). This is called the Cosmological Principle. Under these assumptions and with the Universe filled with one or more perfect fluids, the geometry of the Universe is greatly simplified and described by the Friedmann-Robertson-Walker metric (FRW):

$$\mathrm{ds}^2 = (\mathrm{cdt})^2 - \mathrm{R}^2(\mathrm{t}) \left[\frac{\mathrm{dr}^2}{1 - \mathrm{kr}^2} + (\mathrm{rd}\theta)^2 + (\mathrm{rsin}\theta \mathrm{d}\phi)^2 \right] \tag{1.2}$$

where k describes the curvature of the space which can be *closed* ($k > 0$), *flat* ($k = 0$) or *open* ($k < 0$); $R(t)$ is the dimensionless scale factor in function of the cosmic time; and the coordinates $(\mathrm{r}, \theta, \phi)$ are comoving coordinates.

The above equation can be written in tensor notation as

$$\mathrm{ds}^2 = \mathrm{g}_{\mu\nu} \mathrm{dx}^\mu \mathrm{dx}^\nu \tag{1.3}$$

where the non-vanishing components are

$$\mathrm{g}_{00} = 1, \quad \mathrm{g}_{11} = -\frac{\mathrm{R}^2}{1 - \mathrm{kr}^2}, \quad \mathrm{g}_{22} = -\mathrm{R}^2\mathrm{r}^2, \quad \mathrm{g}_{33} = -\mathrm{R}^2\mathrm{r}^2\mathrm{sin}^2\theta \tag{1.4}$$

Values of $g_{\mu\nu}$ and their derivatives give the 16 components of $G_{\mu\nu}$ on the left hand side of Einstein's field equations. We obtain:

$$\mathrm{G}_{00} = 3(\mathrm{cR})^{-2}(\dot{\mathrm{R}} + \mathrm{kc}^2), \quad \mathrm{G}_{11} = -\mathrm{c}^{-2}(2\mathrm{R}\ddot{\mathrm{R}} + \dot{\mathrm{R}}^2 + \mathrm{kc}^2)(1 - \mathrm{kr}^2)^{-1} \tag{1.5}$$

On the right hand side of Einstein's field equations, the stress-energy tensor is given by

$$\mathrm{T}_{\mu\nu} = (\mathrm{p} + \rho\mathrm{c}^2)\frac{\mathrm{v}_\mu \, \mathrm{v}_\nu}{\mathrm{c}^2} - \mathrm{pg}_{\mu\nu} \tag{1.6}$$

We note that ρc^2 is the energy density. After substituting equations 1.5 and 1.6 into Einstein's equations 1.1, we obtain Friedmann's equations:

$$\frac{\dot{\mathrm{R}}^2 + \mathrm{kc}^2}{\mathrm{R}^2} = \frac{8\pi\mathrm{G}}{3}\rho, \tag{1.7}$$

$$2\frac{\ddot{\mathrm{R}}}{\mathrm{R}} + \frac{\dot{\mathrm{R}}^2 + \mathrm{kc}^2}{\mathrm{R}^2} = -\frac{8\pi\mathrm{G}}{\mathrm{c}^2}\mathrm{p} \tag{1.8}$$

The first equation (equation 1.7) describes a direct connection between the mass densities in the Universe and the expansion rate; the second equation (equation 1.8) shows that it may

accelerate. From equations 1.7 and 1.8, we obtain:

$$2\frac{\dot{\mathrm{R}}}{\mathrm{R}} = -\frac{8\pi \mathrm{G}}{3\mathrm{c}^2}(\rho \mathrm{c}^2 + 3\mathrm{p}) \tag{1.9}$$

which demonstrates that the acceleration decreases with increasing pressure and energy density. ρ is the mass density of all components present in the Universe (dust, radiation etc.) and p the total pressure. In that equation, G represents Newton's gravitational constant and c the speed of light. Since the Universe is approximated to be an ideal perfect fluid, the equation of state is given by:

$$\mathrm{p} = \omega \rho \mathrm{c}^2 \tag{1.10}$$

where the parameter ω is called the equation of state parameter. Given the equation of state 1.10, the total mass density of all components in the Universe is given by

$$\rho = \sum_{\mathrm{i}} \rho_{\mathrm{i}}^0 (\mathrm{R}/\mathrm{R}_0)^{-3(1+\omega_{\mathrm{i}})} \tag{1.11}$$

where ρ_{i}^0 is the mass density of each component at the current time, ω_{i} its equation of state and R_0 is the scale factor at the current time. The value of the ω_i will depend upon the component of the Universe. There are three main cases:

- $\omega_{\mathrm{m}} = 0 \rightarrow \mathrm{p} = 0$ dust Universe, *matter* dominated
- $\omega_{\mathrm{r}} = \frac{1}{3} \rightarrow \mathrm{p} = \frac{1}{3}\rho \mathrm{c}^2$ radiative Universe, *radiation* dominated
- $\omega = -1 \rightarrow \mathrm{p} = -\rho \mathrm{c}^2$ De Sitter Universe, *vacuum* dominated behaving like cosmological constant

For $\omega = -1$, the equation 1.11 becomes

$$\rho = \sum_{\mathrm{i}} \rho_{\mathrm{i}}^0 \tag{1.12}$$

We note that the Hubble parameter is defined as $\mathrm{H} \equiv \dot{\mathrm{R}}/\mathrm{R}$. It shows how fast the Universe is expanding. H_0 is its current value and it is called Hubble constant and often parametrized in terms of the dimensionless number h, where:

$$\mathrm{h} = \frac{\mathrm{H}}{100 \text{ km s}^{-1}\mathrm{Mpc}^{-1}} \tag{1.13}$$

Equation 1.2 gives the cosmological redshift when we plug $\mathrm{ds}^2 = 0$ (null geodesic for a light ray)

$$\mathrm{z} = \frac{\mathrm{R}_0}{\mathrm{R}} - 1 \tag{1.14}$$

From equation 1.7, it can be shown that if

$$\rho = \rho_{\rm cri} \equiv \frac{3{\rm H}^2}{8\pi{\rm G}} \tag{1.15}$$

the curvature is zero ($k = 0$). This time-dependent energy density that makes the Universe spatially flat is known as the critical density. Current energy densities of matter components are often expressed in terms of dimensionless density parameter, $\Omega_{\rm i}^0 \equiv \rho_{\rm i}^0/\rho_{\rm cri}^0$.

The simplest solutions to the Einstein equations (from equation 1.7) which are known as Friedmann cosmology models, are now explicitly expressed as

$$\mathrm{H} = \mathrm{H}_0\sqrt{\Omega_{\rm r}(\mathrm{R}/\mathrm{R}_0)^{-4} + \Omega_{\rm m}(\mathrm{R}/\mathrm{R}_0)^{-3} + \Omega_\Lambda - \Omega_{\rm k}(\mathrm{R}/\mathrm{R}_0)^{-2}} \tag{1.16}$$

where the different types of Ω: Ω_r, Ω_m, Ω_Λ, and Ω_k are respectively the density parameters of radiation, non-relativistic matter, cosmological constant, and curvature. The equation 1.16 is one of the most important equations in cosmology since it provides the relation between comoving distance to redshift in terms of the key cosmological parameters such as the Hubble constant and the current energy density of the constituents of the Universe.

1.1.1.2 Concordance Cosmology

In 1922, Alexander Friedmann found the solution of the Einstein's field equations that suggests the expanding Universe. At almost the same time, Georges Lemaître proposed the first model that later known as the "Big Bang model" and the distance-redshift relation that could explain the expansion of the cosmos. Both studies along with the metric given by Howard P. Robertson and Arthur G. Walker yield to the well-known Friedmann-Lemaître-Robertson-Walker (FLRW) solution of the gravity equations, and which fits better the observable Universe. It is then in 1929, that the observational confirmation of the expanding Universe was discovered by E. Hubble by showing the linear relation between the recession velocity of galaxies and their distance (Hubble's law[1]). He applied the technique of redshift introduced by Vesto Slipher one decade before, using galaxies spectra. Then a more advance measurement of the expansion was made in 1998 when the Hubble Space Telescope (HST) observed distant supernovae type Ia (SN Ia). The type Ia supernovae are all consistent in term of their absolute luminosity profiles allowing their use as standard candles across cosmological distances. The goal of the SN Ia surveys was therefore to establish the Hubble relationship by determining their distances and redshifts. In the early 1990's, it was believed that the expansion rate would decrease as time went on. However, recent observations of high redshift SN Ia showed that the expansion of the Universe was actually accelerating and it has not been slowing (Perlmutter *et al.*, 1999; Riess *et al.*, 1998; Schmidt *et al.*, 1998).

[1]The Hubble's law is given by $\vec{v} = H_0\vec{r}$, where H_0 is the constant of proportionality and is known as the Hubble constant. This relation is valid to a distance up to some 100 of Mpc but it has to be corrected at larger scales

The observed supernovae were about 25% fainter than expected, suggesting that they were further away than they should be.

So from the expanding Universe, everything appears moving away from each other which leads to the conclusion that in the past everything comes together. This is a strong support of the initial explosion known as the Big Bang scenario and the model proposed by Lemaître. Therefore, the concordance model is based on the fact that the Universe has expanded from a primordial hot and dense initial condition in the past and continues to expand to the present time. After the Big Bang, as the Universe was growing, the plasma and the radiation within became cooler (matter-radiation decoupling), and the CMB radiation was emitted at that time. The CMB was first discovered by Penzias & Wilson (1965). It is the most powerful pieces of evidence for supporting the Big Bang theory as it shows the radiation left over from that early stage.

Current observational data strongly indicate that the Universe is highly isotropic and homogeneous at sufficiently large scale, implying that no specific center or special directions exists in the Universe. Yet there was no evidence which can validate the cosmological principle at the time when Friedmann and Lemaître investigated the simplest possible matter distribution while finding solutions to Einstein's field equations. The observational evidences of isotropy in the Universe came from the distribution of radio sources (Blake & Wall, 2002), the Cosmic X-ray background (Fabian & Barcons, 1992), and the CMB. However, the study of the large scale matter distribution by Hogg *et al.* (2005), which was used to test the homogeneity of the Universe, favours the idea that the Universe is homogeneous.

The most acceptable model which provides the best descriptions of the Universe is the ΛCDM model since it is able to reasonably explain the observable Universe. The Greek letter Λ means the cosmological constant, which is the dark energy. The most important cosmological observations that this model could fit are: the existence and structure of the CMB, the accelerating expansion of the Universe using distant galaxies and SN Ia, the large scale structure and the abundance of light elements in the early Universe. In the ΛCDM model, the Universe is spatially flat and dominated by a cosmological constant Λ associated with dark energy with $\Omega_\Lambda \sim 0.7$, a non-relativistic cold dark matter with $\Omega_m \sim 0.25$ and a non-relativistic baryonic matter with $\Omega_b \sim 0.05$. The determination of the exact values of these components which constitute the total energy density of the Universe predicts its past and future behaviour. The cosmological constant has a value of ω_Λ = -1. There are other important parameters such as the Hubble constant H_0, the amplitude of the linear power spectrum on the scale of $8h^{-1}$Mpc, σ_8 and many more (some of them are listed in table 1.1), which all describe the ΛCDM cosmology.

Although the cosmological observations support the Hot Big Bang model, this model suffers from some problems such as

- the horizon problem which deals with questions about the causal connection between far away sides of the Universe,

- the spatial geometry of the Universe (flatness problem). The Big Bang model does not seem to predict a flat Universe however the strongest constraint on the flatness comes from fluctuations in the CMB. The Cosmic inflation model Guth (1981) seemed to resolve these problems, when it is combined with the Hot Big Bang model to form the accepted theory which used to adequately describe the observable Universe.

Besides the problems cited above, there are other observations which appear to disagree with the predictions of the ΛCDM model, at about 2σ confidence level, few examples are given below:

- High redshift SNe Ia appear brighter than what we would expect in the ΛCDM model (Kowalski *et al.*, 2008). The persistence of the discrepancy using even more data would lead to the conclusion that the Universe in the past was decelerating faster than the ΛCDM model predicts it to be.

- The amplitude of the large-scale velocity flows (400 km s^{-1}) may be larger than what is expected in the ΛCDM (Abate & Erdoğdu, 2009; Watkins *et al.*, 2009). The possible explanations for that are the statistical fluctuation, or serious physical reasons such as presence of the non-inflationary perturbations, a time-dependant Newton's constant, or a presence of a giant void at a distance of few Gpc.

- There are missing dwarf galaxies in the observed local group. Based on the prediction from the ΛCDM, one would expect to observe on average more dwarf galaxies (Peebles, 2007). This could be due to astrophysical effects where, for example, a detectable star population has not formed in some small dark matter haloes or incorrect prediction of the model.

Nonetheless, the ΛCDM model is still the best fit to the observational data despite the discrepancies between the observations and predictions.

Dark energy: The existence of an exotic component called *"dark energy"*, besides ordinary matter and radiation, is the most popular way to explain the accelerating Universe. The nature of the "*dark energy*" component remains unclear, but it is known to be very homogeneous, not very dense and it is not known to interact through any of the fundamental forces other than gravity. Many suggestions of its nature have been proposed. It could be the same property as the energy density of the vacuum (cosmological constant Λ) with $\omega = -1$ (Carroll *et al.*, 1992), or a new type of dynamical energy fluid "quintessence" with $-1 < \omega < -1/3$ (González-Díaz, 2000), or a phantom energy with $\omega < -1$ (Dvali *et al.*, 2000). Current surveys like the Dark Energy Survey (DES, The Dark Energy Survey Collaboration, 2005) are also aiming to uncover the nature of the dark energy, by measuring the brightness of about 3000 supernovae including distant ones.

In a standard Λ model (where a constant is added to the right hand side of the equation 1.1), it is unclustered on all scales and is constant with time (although this is not the case in other models of dark energy). Independent of its precise nature, dark energy would need a strong negative pressure in order to explain the actual acceleration in the expansion rate of the Universe. It can be demonstrated in the FRW metric, described in previous section, that the cosmic factor $\ddot{\mathrm{R}}$ is positive if the equation state of the Universe is $\omega < -1/3$.

Some observational evidence of the presence of the dark energy comes from:

- the accelerating expansion provided by the absolute magnitude–redshift of SNe Ia or the Hubble diagram (Perlmutter *et al.*, 1999; Riess *et al.*, 1998).

- the positions and amplitudes of acoustic peaks in the CMB anisotropy, which show that the Universe is very close to spatially flat if the mass/energy density of the Universe equals to the critical density. More precisely, the position of the first peak of the angular power spectrum constrains the spatial curvature of the Universe to be $\Omega_k = 0.015^{+0.020}_{-0.016}$ (Spergel *et al.*, 2003) and that the baryon contribution exactly agrees with that predicted from the Big Bang Nucleosynthesis (BBN). Combining the CMB anisotropy results from the Wilkinson Microwave Anisotropy Probe (WMAP) satellite with an independent measurement of the Hubble constant provides some indication that non-relativistic matter makes up only a quarter of the critical density, however the energy density of radiation is negligible. This leads to the conclusion that the energy which constitutes the Universe is dominated (by three quarters) by an extra component above the ordinary or dark matter and radiation. It should be uniform on cosmological scales in order not to conflict with the formation of the large-scale structure and the BBN.

- the cross-correlation between CMB anisotropies and low redshift matter distribution such as galaxies and radio-sources through the detection of the integrated Sachs-Wolf effect [1] (ISW Afshordi *et al.*, 2004; Boughn & Crittenden, 2005; Fosalba *et al.*, 2003). This means that the presence of the dark energy affects CMB anisotropies directly through the ISW effect. In a Universe dominated by dark energy, gravitational wells decay on large distance scales. This affects the large-angle CMB spectrum since photons that travel through the large gravitational well gain energy. A positive correlation at $z < 1$ has been detected by several groups.

- the large-scale structure. The recent large-scale galaxy survey like WiggleZ Dark Energy survey (Glazebrook *et al.*, 2007) which aimed to analyse the galaxy distribution in order to check further evidence of dark energy. Through this analysis, the survey was able to

[1] The Integrated Sachs-Wolfe effect is caused by gravitational red/blueshifts affecting CMB photons propagating from the last scattering surface and encountering gravitational potentials (i.e. large matter concentrations)

measure the cosmic distance using the Baryon Acoustic Oscillations (BAO) [1] standard ruler technique and the growth of the structure using the redshift-space distortions. Results from this survey are consistent with the prediction of the ΛCDM model in term of the growth rate of the structure (Blake *et al.*, 2011a) and confirm a cosmic acceleration ($\omega < -1/3$) independent from the supernovae surveys (Blake *et al.*, 2011b).

- observational $H(z)$ data. Details on $H(z)$ measurement method are given in section 1.2. It has been widely used to examine the accelerated cosmic expansion and constrain properties of dark energy.

Dark matter: The remaining components of the energy density are dominated by hypothetical matter (Zwicky, 1933) in non-relativistic form of an unknown nature, called "*dark matter*". It is invisible but can still be detected through its gravitational effects. In the current scenario of structure formation, it is believed to consist of particles which interact only through the force of gravity. Observations of light elements in the Universe and the theory of BBN dictate that it is not composed of baryons. It may be composed of particles that interact through weak interaction. The particle candidates that have been considered include neutralinos (the lightest supersymmetric particle), exotic neutrinos, axions, jupiters and black holes of mass $< 100\ M_{\odot}$. These coincide with the common definition of "cold dark matter" (Peebles, 1980). At early times these particles are non-relativistic, with mean velocities that are small relative to the mean expansion of the Universe (neutrinos with masses <30 eV are excluded). For both the dark matter ($\Omega_{\rm DM} \simeq 0.23$) and the baryons ($\Omega_{\rm B} \simeq 0.04$), the equation of state is $\omega = 0$, and the density is diluted like $\rho \propto a^{-3} \propto (1+z)^3$. Dark matter plays an important role in structure formation because of its gravitational interaction. The gravitational Jeans instability which allows compact structures to form, is not balanced by any force such as radiation pressure. As a result, dark matter begins to collapse into a complex network of dark matter haloes well before ordinary matter, which is impeded by pressure forces. Without dark matter, the epoch of galaxy formation would occur substantially later in the Universe than is observed.

Evidence that dark matter exists comes from:

- observations of the dynamics of galaxies (galaxy rotation curves). It was found that velocities of stars towards the edge of a spiral galaxy remain nearly constant with increasing distance from the galactic center, not as expected them to be (Rubin *et al.*, 1985). If there is a visible matter dominated, these velocities would increase with the radial distance from the core of the galaxy. This implies that the galaxy must contain dark matter in the form of a halo and about five to ten times the mass of the visible matter.

[1] Technically, BAO is some sort of periodic fluctuations in the matter power spectrum or equivalently a characteristic scale in the galaxy distribution. The scale of the acoustic oscillations provides a standard ruler which can be used to determine distances to galaxies and constrain the nature of dark energy

- observations of the dynamics of clusters. Galaxy clusters are an ensemble of galaxies held together by their mutual gravitational attraction. However, their velocities are found to be too large for galaxies to remain gravitationally bound by their mutual attractions, implying the existence of other matter than the visible one. Zwicky, with his pioneering study of the Coma cluster, showed that if the entire attractive gravitational force came only from the luminous, visible matter, the cluster would disperse.

- the temperature distribution of hot gas in galaxies and clusters of galaxies (Markevitch *et al.*, 2004). From the X-ray studies, galaxy clusters exhibit very hot intergalactic gas. The total mass of this gas is two times greater than that of the galaxies. This mass is still not enough to keep the galaxies in the cluster, implying the presence of different mass.

- gravitational lensing. This technique can be used to predict the amount of material in the cluster in order to create its gravitational field. From this measurement, the total mass of the cluster is much larger than the ordinary matter of the stars and the gas combined, which typically consists of 5% from the visible matter, 10% from the hot gas and the rest from the dark matter.

Constraints on cosmological parameters have been established so far using data from different type of observations. The latest basic set of cosmology parameters are from the *PLANCK* (Planck Collaboration *et al.*, 2013) and WMAP 9-year release data (Hinshaw *et al.*, 2013) listed in table 1.1. The different columns of table 1.1 list the best fit-parameters obtained by using different joints measurements: WMAP means WMAP9 data alone. The PLANCK column gives results of the *PLANCK* temperature power spectrum data alone. The WMAP9+BAO+H_0 column gives measurements when combining WMAP9, BAO and applying priors on H_0. PLANCK+WMAP is the combinatiion of PLANCK with the additional inclusion of WMAP polarization at low multipoles. The cosmological model defined by the current set of cosmological parameters is defined as standard model. It aims mainly to provide a more accurate description of the actual and high-redshift Universe, as indicated by various observational data.

1.2 Cosmic Chronometers

In recent times, there have been numerous observations and several methods used to place tighter constraints on cosmological parameters. As discussed above, these include the CMB, BAO (Eisenstein *et al.*, 2005; Percival *et al.*, 2010), Supernovae type Ia (Riess *et al.*, 1998), as well as probes of the growth of structure via weak (Refregier, 2003) and strong lensing (Cao *et al.*, 2012) and cluster of galaxies abundance (Haiman *et al.*, 2001) plus several others. All of these constrain the expansion history using geometric measurements: e.g. the BAO

Table 1.1: The cosmological parameters deduced from different type of data where a flat cosmological model $\Omega_m + \Omega_\Lambda = 1$ is assumed. All ΛCDM model parameters are given with 68% confidence intervals.

Parameter	WMAP	WMAP+BAO+H_0	PLANCK	PLANCK+WMAP
$\Omega_b h^2$	0.02264±0.00050	0.0226±0.00043	0.02207±0.00033	0.02205±0.00028
$\Omega_c h^2$	0.1138±0.0045	0.1157±0.0023	0.1196±0.0031	0.1199±0.0027
Ω_Λ	0.721±0.025	0.712±0.010	0.686±0.020	$0.685^{+0.018}_{-0.016}$
n_s	0.972 ±0.013	0.971±0.010	0.9616±0.0094	0.9603±0.0073
τ	0.089 ±0.014	0.088±0.013	0.097±0.038	$0.089^{+0.012}_{-0.014}$
$10^9\Delta^2_{\mathcal{R}}$ or $\ln(10^10A_s)$	2.41±0.10	$2.427^{+0.078}_{-0.079}$	3.103±0.072	$3.089^{+0.024}_{-0.027}$
t_0	13.74±0.11	13.750±0.085	13.813±0.058	13.817±0.048
H_0	70.0±2.2	69.33±0.88	67.4±1.4	67.3±1.2
σ_8	0.821±0.023	0.830±0.018	0.834±0.027	0.829±0.012
z_{reion}	10.6 ± 1.1	10.5 ± 1.1	$11.4^{+4.0}_{-2.8}$	11.1±1.1

Notes:
$\Omega_b h^2$: Physical baryon density
$\Omega_c h^2$: Physical cold dark matter density
Ω_Λ : Dark energy density (ω = -1)
n_s : Scalar spectral index
τ : Reionization optical depth
$10^9\Delta^2_{\mathcal{R}}$: Curvature perturbations at $k_0 = 0.002$ Mpc^{-1}, $\ln(10^{10}A_s)$: Log power of the curvature perturbations at $k_0 = 0.005$ Mpc^{-1},which is the notation used by PLANCK
t_0 : Age of the Universe (Gyr)
H_0 : Hubble expansion factor, H_0 = 100 h km s^{-1} Mpc $^{-1}$
σ_8 : Density fluctuations on 8 h^{-1}Mpc scales
z_{reion} : Redshift of reionization

use standard rulers and SNe are used as standard candles. Each one of these methods presents its own pros and cons, for instance a dependence on integrated quantities such as the luminosity distance. A complementary technique known as *Cosmic Chronometers* (CC), originally proposed by Jimenez & Loeb (2002), consists of directly tracking the expansion history of the Universe by using massive and passively evolving early-type galaxies.

The basic idea of this method is measurement of the differential age evolution between two ensembles of LRGs as a function of their redshifts, which provides a direct estimate of the Hubble parameter and hence the expansion rate over cosmic time $H(z)$ (Jimenez & Loeb, 2002):

$$\mathrm{H(z)} = -\frac{1}{(1+\mathrm{z})}\frac{\mathrm{dz}}{\mathrm{dt}} \tag{1.17}$$

The most important part of this equation is the derivative quantity dz/dt that can be approximated as a differential quantity $\Delta z/\Delta t$, potentially reducing systematics from absolute age determination. With this method, only the galaxy evolution that takes place between the redshifts where the difference is taken, is the most important. All the advantages of this method have been discussed in Crawford *et al.* (2010a); Jimenez & Loeb (2002); Jimenez *et al.* (2003); Liu *et al.* (2012); Moresco *et al.* (2011, 2012a); Simon *et al.* (2005); Stern *et al.*

(2010a); Zhang *et al.* (2012). The overall approach is valid when assuming that most stars in these galaxies formed near the beginning of the universe at a similar time (as supported by observations cited in Jimenez & Loeb (2002)), then measuring the age difference between ensembles of LRGs at two different redshifts provides the differential quantity $\Delta z/\Delta t$ required to estimate $H(z)$. The accurately estimated ages can then be taken as a cosmic chronometer. Some systematic errors in the absolute age measurements have been a subject of discussion, but such errors could be cancelled by using the relative age of these galaxies at different redshifts. Our focus is then to determine the relative ages of galaxies.

There are a number of potential extragalactic objects that can be used to determine the age of the Universe, such as the metal-poor globular clusters (Carretta *et al.*, 2000; Chaboyer *et al.*, 1996), white dwarfs (Hansen *et al.*, 2004), the radioactive decay of nuclear elements in meteorites (Fowler, 1987) and in the spectra of the metal poor stars (Dauphas, 2005). All of these are capable of estimating the age of the Universe at the present day, but not the age at different redshifts. In the case of meteorites, it is impossible to obtain a sample from high redshift, while globular clusters are too faint at high redshifts to be used effectively.

1.2.1 Previous work on CC

The CC method has been used in some ways to measure the observed Hubble parameter up to redshift $z \sim 1.8$, to set constraints on the nature of dark energy, and to recover the local Hubble constant (Capozziello *et al.*, 2004; Dantas *et al.*, 2007; Ferreras *et al.*, 2001, 2003; Jimenez & Loeb, 2002; Jimenez *et al.*, 2003; Liu *et al.*, 2012; Moresco *et al.*, 2012a; Samushia *et al.*, 2010; Simon *et al.*, 2005; Stern *et al.*, 2010a; Verkhodanov *et al.*, 2005; Zhang *et al.*, 2012, etc.). In each measurement, the authors assumed that LRGs are massive, passively-evolving elliptical galaxies and homogeneous populations which form their stars at high redshift, and fit a single burst equivalent age to galaxies. A number of scientists (Carson & Nichol, 2010; Crawford *et al.*, 2010a; Simon *et al.*, 2005; Stern *et al.*, 2010a) have attempted to improve this method by pointing out the need for better stellar population models fitting, better selection targets, larger samples and better quality data to precisely determine H(z).

The original idea was suggested by Jimenez and collaborators (Jimenez & Loeb, 2002). They improved their $H(z)$ measurement from year to year. In 2003, their first test used the upper envelope of the age-redshift relation of the ages of SDSS-LRGs (Jimenez *et al.*, 2003) in order to constrain the equation of the state of dark energy. In 2005, they used another data set from the SDSS-LRGs in the range of $0.1 < z < 1.8$ to obtain 8 $H(z)$ values (Simon *et al.*, 2005). They improved their $H(z)$ measurements by combining samples of rich galaxy clusters observed with Keck/LRIS instruments with other samples from SDSS-LRGs, SPICES and VVDS (Stern *et al.*, 2010a). When they applied the same approach using low redshift spectroscopic data of passively ETGs, they obtained a Hubble constant of H_0=72.6±2.9(stat) ±2.3 (syst) km Mpc^{-1} s^{-1} which is consistent with other results (Moresco *et al.*, 2011). They

then applied the CC method to a larger spectroscopic sample of ETGs (MGS, SDSS-LRGs, zCOSMOS, K20 etc.) in the redshift range of $0.15 < z < 1.4$ and obtained an independent $H(z)$ measurements at 5-12% accuracy, providing the proof of the accelerating expansion of the Universe (Moresco *et al.*, 2012a). In Moresco *et al.* (2012b) the cosmological applications from the $H(z)$ measurements including the properties of the neutrinos were reported.

In a different way, Melia & Maier (2013) have explored the feasibility and reliability of the CC method in the $R_h = ct$ Universe. This model was recently proposed by Melia & Shevchuk (2012), where the Hubble scale $R_h = c/H$ is at all time equal to the distance ct that light has travelled since the Big Bang. In this model, the scale factor is proportional to cosmic time and there is neither acceleration nor deceleration of the expansion of the Universe. Basically, they compared the available $H(z)$ measurements with the ΛCDM and the $R_h = ct$ models. According to them, the fitting of the observational $H(z)$ data with both models revealed that the $R_h = ct$ Universe is more likely than ΛCDM to account for the observed $H(z)$ profile.

1.3 LRGs in the literature

Luminous Red Galaxies (LRGs) are intrinsically luminous ($L > 3L^*$, where L^* refers to the "knee" in the galaxy luminosity function and corresponds approximately to the luminosity of the Milky Way) early-type galaxies (Eisenstein *et al.*, 2005; Wake *et al.*, 2006). They can be selected via their red colours (Eisenstein *et al.*, 2001). They have photometric properties consistent with an old, passively evolving stellar population (Bernardi *et al.*, 2006; Faber, 1973; Visvanathan & Sandage, 1977). They are shown to have relatively homogeneous spectral properties (Eisenstein *et al.*, 2003; Faber, 1973), and are identified with little recent star formation activity (Roseboom *et al.*, 2006). All of these characteristics make them ideal tracers of large scale structure at intermediate redshifts ($0.3 < z < 1$).

Some characteristics of LRGs found in the literature include:

- LRGs are found in and around the cores of clusters. One can say that these objects are very similar to brightest cluster galaxies (BCG), implying that they are good candidates to detect and study clusters at optical wavelengths. They are the most massive and bright galaxies which provide us with high signal-to-noise ratio spectra. In the semi-analytical models of galaxy evolution, the stellar mass of LRGs can be tracked and they predict that seventy-five per cent of the stellar mass of these galaxies are already in place by $z \sim 1$ (e.g. Bauer *et al.*, 2005; De Lucia & Blaizot, 2007; Wake *et al.*, 2006). They dominate the stellar mass density of the Universe (Fukugita *et al.*, 1996; Hogg *et al.*, 2002). The uniformly red and old stellar populations of LRGs have traditionally been interpreted as evidence for a formation scenario in which these galaxies form in a single intense burst of star formation at high redshift and are passively evolving to the present day (Barber *et al.*, 2007; De Lucia *et al.*, 2006; Gallazzi *et al.*, 2005). This

indicates that the more massive a galaxy is, the earlier most of its stars were formed. The passive evolution is defined here as the fact that stars in LRGs formed exclusively at very early epochs and at the same time, then these galaxies evolved passively since their initial burst of star formation, which represents the general assumption of this study.

- They are strongly biased objects, having a value of b $\sim$ 2 where b is the linear bias and relates in the linear regime, the underlying mass density distribution being to that of the luminous tracers via $\delta_{\rm g} = {\rm b}\delta_{\rm m}$ (Padmanabhan *et al.*, 2007). Using the 2SLAQ LRG survey, Ross *et al.* (2008) have obtained the clustering amplitude of the LRGs. This has been exploited to constrain cosmological parameters (e.g Cabré & Gaztañaga, 2009; Eisenstein *et al.*, 2005; Gaztañaga *et al.*, 2009a; Sánchez-Blázquez *et al.*, 2009) on different scales, to constrain the mass of the dark matter haloes which host these galaxies and to probe their merger history (Masjedi *et al.*, 2006; Ross *et al.*, 2007; Zehavi *et al.*, 2005).

- Demonstrated by previous observational studies, LRGs found in high-density environments have older stellar populations than in low-density (e.g. Bower *et al.*, 1990; Trager *et al.*, 2008) as predicted by the hierarchical galaxy formation models. And ages of the stellar populations in the larger galaxies are older than those in smaller galaxies located in both environments, this is known as "downsizing". In hierarchical growth of structure, larger structures like rich clusters have been assembled with collapses and mergers of smaller structures.

- Barber *et al.* (2007) have used the population synthesis models to estimate the mass, metallicities and star formation histories of LRGs by fitting measured spectral indices using a large library of high resolution spectra. They found that majority of stars in LRGs formed at redshift around $z \simeq$ 1.1-1.9 with 80% of their stellar masses have already been assembled around $z \simeq$ 0.7-1.1.

- Conroy *et al.* (2007) used N-body simulation to study the merger histories of the dark matter haloes which they assumed hosted LRGs. They also suggested that LRGs are tidally disrupted.

- Numerous amount of LRGs are radio quiet Active Galactic Nuclei (AGN). They are far away below the detection limit of different radio surveys like Faint Image of the Radio Survey at Twenty-cm (FIRST). Therefore, the median-stacking technique is needed to achieve the required sensitivity. Hodge *et al.* (2009) have detected and studied properties of faint radio AGNs in LRG populations. They found that the lower the luminosity of LRGs the stronger the evolution of their radio power over the redshift range of $z = 0.45$ and $z = 0.75$, which possibly is a signature of AGN downsizing. They

also showed strong cosmic evolution of AGN activity over the redshift range of $z = 0.2$ and $z = 0.7$ for overall LRGs dominated by low-luminosity AGNs. This implies that the total AGN heating in these massive galaxies would considerably increase with redshift.

- The semi-analytical model of De Lucia *et al.* (2006) has also successfully matched the luminosity, colour and morphology of local elliptical galaxies, where the more massive ones would be LRGs. Almeida *et al.* (2008) have studied properties of LRGs in hierarchical cosmology using two different models from Durham : the Bower and Baugh models. They have shown that the luminosity function and the clustering of LRGs are closely matched to the observed properties of LRGs, as well as many observables which are well produced. Note that these two models have different mechanisms to suppress the formation of massive galaxies: the Bower *et al.* (2006) model uses the AGN-feedback to prevent gas from cooling in massive haloes; while the Baugh (2006) model involves superwinds to eject gas before it is turned into stars.

1.4 Thesis outline

1.4.1 The goal of this thesis

Measuring the Hubble parameter today, H_0, continues to be a major goal of observational cosmology. This parameter plays an important role, not only for studying different astronomical events in a wide range of the cosmic scales, from the large scale structure to the local galaxies, but it is also a key parameter for various cosmological calculations such as the physical distance to objects, their ages, their sizes and the matter-energy contents of the Universe. There are many observational techniques to probe this parameter. One of those techniques comes from the use of expansion rate over cosmic time $H(z)$, obtained from the differential ages or CC which has been discussed in section 1.2.

The principal aim of this project is to measure the expansion rate of the Universe $H(z)$ over the redshift range of $0.1 < z < 1.0$, by age-dating LRGs, thereby providing an interesting constraint on the nature of dark energy. In this work, we will investigate the CC approach by using a large sample of homogeneous passively evolving galaxies from the archival data SDSS-DR7 over a redshift range of $0.10 < z < 0.40$. In addition, some massive selected LRGs observed with the SALT telescope in two narrow redshift ranges centred on $z \simeq 0.40$ and $z \simeq 0.55$ will be used to measure $H(z)$ at $z \simeq 0.47$. Finally, the $H(z)$ measurements from both samples (SDSS-LRGs and SALT-LRGs) will be combined with recent and available $H(z)$ in the literature to investigate their constraints on the determination of cosmological parameters.

1.4.2 Contents

The structure of this thesis has been organised to follow the three aims of this project, with an additional chapter about the stellar population synthesis.

Chapter 2 highlights the important key ingredients of the stellar populations synthesis models. Some basic introduction to a simple stellar population model is given as well as the stellar population of early type galaxies.

Chapter 3 outlines the technique of age-dating and the selection criteria used for retrieving galaxies from SDSS archive data. The galaxies ages are used to reconstruct the age-redshift relation $t(z)$, and to measure the Hubble parameter $H(z)$.

Chapter 4 focuses mainly on the measurement of the Hubble parameter $H(z)$ at $z \simeq 0.47$ using LRGs observed with SALT. Prior to the measurement, the process of reducing long-slit spectra from SALT and the method adopted to estimate the ages of these galaxies are explained. Furthermore, we discuss some issues about the estimated errors. Finally, the Hubble parameter $H(z = 0.47)$ measurement is provided.

Chapter 5 presents the method used to constrain the cosmological parameters when combining our $H(z)$ measurements with external datasets.

Chapter 6 summarizes and discusses our results. The outlook to the future work in this research is also given.

Chapter 2

Stellar populations synthesis models

2.1 Introduction

In this chapter, the basics of the Stellar Populations Synthesis (SPS) models are introduced, including the necessary ingredients, and problems each model faces as each SPS model has its own particularities. Stellar population studies are necessary to constrain the galaxy formation and evolution, because different formation/event scenarios can possibly leave certain imprints in the stellar content of galaxies. SPS models are important tools in the interpretation of the integrated light contents of a stellar population of galaxies, for instance their mean age, colours, line indices, chemical composition, stellar formation histories, mass-to-light ratios, stellar mass, stellar kinematics and their overall evolutionary history. In addition, the formation of a galaxy can be explained as different pieces of stellar type/systems put together in different ways, yielding a different parameter space of ages and chemical compositions of its overall stellar populations. The derivation of these stellar population parameters can be accomplished by using either photometry or spectroscopy data fitting. Each method of fitting has its pros and cons. The great advantage of the spectral fitting (full, absorption line indices) is high accuracy on the derived parameters and the possibility of studying chemical abundance. This is not possible through photometric fitting where results usually suffer from the age-metallicity degeneracy, although obtaining photometry data does not require the long observational integration times required for spectroscopy.

Apart from the widely used model of stellar evolutionary population synthesis of Worthey *et al.* (1994), it is not yet sure which model is the most accepted model despite important progress in the last two decades, with regard to the best way of handling the Thermally Pulsating-Asymptotic Giant Branch (TP-AGB), Blue straggler, differential effect of stellar rotation and evolution (binary stars), coverage of the parameter space in the stellar libraries, resolution of the population models etc. The modelling of the stellar evolution becomes more

and more precise especially in the red Giant Branch and AGB phases (e.g. Lançon *et al.*, 2007). However, the creation of SPS models is still limited by certain physical issues. One of those issues is the evolution of binary stars. No popular SPS model includes the effects of binary star evolution. The collision and mass exchange between the binary stars affect the integrated spectrum of the stellar populations leading to younger ages for Galactic globular clusters and galaxies. This means that a big effort has to be made in order to match correctly stellar population theory with observations.

The basic idea of this project is the consideration of the fact that LRGs have formed their stars in one single burst at the same time in the past. Thus we particularly focus on so-called single-age and single metallicity models known as the Simple Stellar population (SSP) models. In reality, a galaxy should not be considered known as a SSP because of the existence of different stellar metallicity, age and system, not like star clusters which are usually considered as a SSP. A composite stellar population which is a combination of different SSPs can, however, be a solution for a complex population. Therefore, understanding SSPs is crucial while studying any type of stellar population of galaxies.

2.2 Stellar population model parameters

Prior to the analysis of the stellar populations, it is necessary to introduce all the basic parameters produced by the models. The following three parameters represent the stellar population characteristics of a galaxy.

Age depends on the star formation activity in the galaxy. Young age means recent star formation activity whereas old age indicates no sign of ongoing star formation.

The metallicity is defined as:

$$\text{metallicity, Z} = \frac{\text{mass of heavy elements}}{\text{mass of (H + He)}} \tag{2.1}$$

where mass of heavy elements refers to the overall content of all elements other than hydrogen or helium, and mass of (H+He) refers to the mass of the hydrogen and helium. Note that the metallicity is also known as the metallicity of the gas from which the stars were born and does not reflect further mixing. However, when we observe stars, we observe the composition at this moment at the photosphere. Therefore there can be some consistency. The metallicity is often converted to [Fe/H] which tracks the metallicity relative to solar:

$$[\text{Fe/H}] = \log_{10}\left(\frac{\text{Z}}{\text{Z}_{\odot}}\right) \log_{10}\left((1 - \text{Y} - \text{Z}) \,/\, (1 - \text{Y}_{\odot} - \text{Z}\odot)\right) \tag{2.2}$$

and given in units of *decimal exponent* or dex ($\text{dex(x)} = 10^{\text{x}}$). $Z_{\odot}$ is the solar ratio equal to 0.02 dex. The use of this nomination decreases the discrepancies in models due to stellar

lifetime differences in the sets of isochrones (Worthey *et al.*, 1994). Some models often use the notation [Z/H] which is the total metallicity instead of [Fe/H]. These two notations are related and can be written as (Tantalo *et al.*, 1998; Thomas *et al.*, 2003; Trager *et al.*, 2000):

$$[\mathrm{Z/H}] = [\mathrm{Fe/H}] + \mathrm{A}[\alpha/\mathrm{H}] \tag{2.3}$$

where A is the ratio between enhanced and suppressed elements in the spectrum of the galaxy $\mathrm{A} = -\dfrac{\Delta[\mathrm{Fe/H}]}{\Delta[\alpha/\mathrm{Fe}]}$. Its value is not universal, it depends on the mixture in the models. For example, Thomas *et al.* (2003) found a value of 0.94.

Element abundances provide the direct evidence of the nucleosynthetic processes which took place along the evolutionary path of a star: from main-sequence all the way to supernovae (SN). For example, different elements such as Mg, C, O are formed in the explosion of type-II SN[1], and Fe-peak elements are formed in the explosion of type-Ia SN[2] . The chemical abundances are referred to by their fractional abundances by weight and can be specified as just (X,Y,Z), depending on the type of models, where:

X = fractional abundance by weight of hydrogen

Y = fractional abundance by weight of helium

Z = fractional abundance by weight of everything else.

and X+Y+Z = 1. Table 2.1 shows the solar fractional abundance.

The $\alpha-$element abundance ratio $[\alpha/\mathrm{Fe}]$ is found to decrease with increasing duration of star formation activity (Thomas *et al.*, 2005), therefore it commonly reveals the enrichment efficiency and the star formation efficiency. This comes from the fact that the first stars to explode in type-Ia SN take about a Gyr (Tolstoy *et al.*, 2009).

$$[\alpha/\mathrm{Fe}] \approx \frac{1}{5} - \frac{1}{6}\log\ \mathrm{t} \tag{2.4}$$

Table 2.1: Solar fractional element abundance. Credit from Moore (2001).

Element		Fractional abundance by weight	References
hydrogen	$X_\odot$	0.709	
helium	$Y_\odot$	0.274	Anders & Grevesse (1989)
everything else	$Z_\odot$	0.0169	Vandenberg (1985)

[1]The type II supernovae are results of a rapid (a few Myr after a star birth) explosion of a massive star ($8\mathrm{M}_\odot < \mathrm{M}_{\mathrm{star}} < 40\mathrm{M}_\odot$)

[2]The type Ia supernovae 's explosion occurs at least 1Gyr behind the SN II

2.3 The simple stellar population

In these models, all stars are formed at the same time (with age t), with a distribution in mass given by a chosen initial mass function (IMF), and with identical chemical composition. All models are not limited by these three important points, some advanced models have implemented the evolutionary processes such as enrichment of the interstellar medium, differential loss of various elements by galactic winds, time-dependent IMF, etc. At the moment, these processes are not fully understood and no agreement has yet been reached about these problems.

The SPS models provide the expected Spectral Energy Distribution (SED) of a stellar population as function of the key parameters which will be discussed below. In general, all models rely on:

- the theoretical stellar isochrones
- the stellar spectral libraries
- and the IMF.

The above components can be combined in another way as follows:

$$f_{SSP}(t, Z) = \int_{m_{low}}^{m_{high}(t)} f_{star}[T_{eff}(M), \log\, g(M)|t, Z]\ \Phi(M)dM \tag{2.5}$$

where M is the initial stellar mass (when stars are at zero age and still on the main sequence phase), $\Phi(M)$ is the IMF, f_{star} is a stellar spectrum, and f_{SSP} is the SSP spectrum which depends on the metallicity Z and time t. m_{low} represents the lower mass limit generally taken as the hydrogen burning limit i.e. $0.1M_{\odot}$ or $0.08M_{\odot}$, while m_{high} is higher mass limit and is prescribed by the stellar evolution. From the isochrones, one can determine the relation between the effective temperature T_{eff}, log g (g is the stellar surface gravity) and M as a function of t and Z. Equation 2.5 can be explicitly explained as the following: an empirical or theoretical library of individual stellar spectra is used to assign spectra of stars in various stage of the isochrones, after which the spectral energy distribution of SSP model is the integration of spectra of individual stars along the isochrone according to a chosen stellar IMF. This typical determination of SSP models is not universal, each model builder has his/her own ingredients on top of the common approach. For example, the inclusion of the treatment of TP-AGB stars (e.g. Le Borgne *et al.*, 2004; Maraston, 2005). Normally, all SPS models are found to be working as a *black-box*, since users do not fully understand how the SPSs are built up. Here we will go through the details of the most important ingredients.

An example of the spectral evolution of a fixed metallicity (solar) SSP model computed from BC03 (Bruzual & Charlot, 2003) synthesis code is shown in figure 2.1. The spectra of young age and hot stars are dominated by the blue light, however those of older populations peak in the red part of the spectrum.

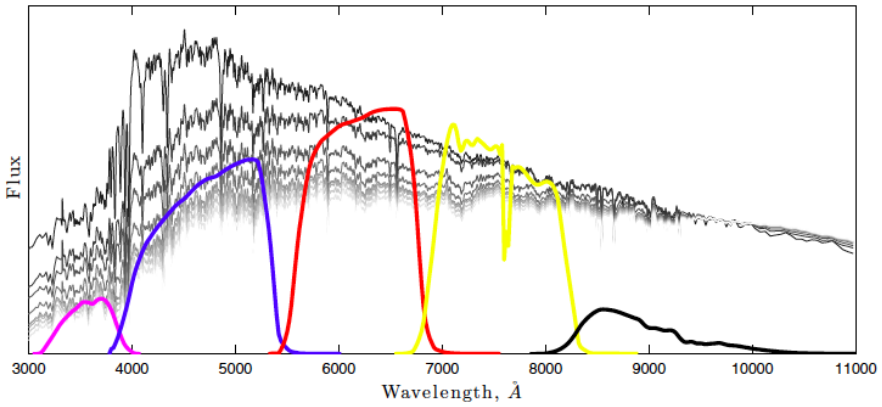

Figure 2.1: The evolution of spectra of a Simple Stellar Population of solar metallicity computed from the BC03 population synthesis code. From top to the bottom is young star spectrum to old star spectrum (from 1 to 15Gyr). The colour lines are the SDSS filter bandpasses: $u-$band in mangeta, $g-$band in blue, $r-$band in red, $i-$band in yellow and $z-$band in black. This illustrates the dominance of the blue light in the spectra of young stars. Credit from Paudel (2011).

2.3.1 The Initial Mass Function

The stellar IMF is defined as the initial distribution of stellar masses along the main sequence. This fundamental parameter along with the efficiency of the star formation quantifies the conversion of the gas into stars. Despite its fundamental role, a question is still remained whether it is "universal" or environment-dependent. The universality means that the ratio of low-mass stars to high-mass stars in a newborn stellar population is the same throughout the Universe. Originally, Salpeter (1955) showed that the IMF has a power-law form with an index $x = 2.35$ for $0.4 < \mathrm{M} < 10\ \mathrm{M}_{\odot}$. Kroupa (2002) claimed that the IMF is universal where only at $\mathrm{M} < 1\mathrm{M}_{\odot}$, x deviates from the Salpeter IMF. This becomes a challenge to the evolutionary theory of stars, because without this deviation the amount of mass in a stellar population model can become very large, implying some confusion with dynamical measurements of mass in galaxies since those should be at least as large as the mass in stars and stellar remnants. According to the review of Bastian *et al.* (2010), there is no clear evidence for variation of the IMF with the initial conditions and/or environment after the first generations of stars.

From the galaxy formation and evolution studies point of view, the stellar IMF is assumed to be an universal function, which is supported by various direct measurements (counting the individual stars (Kroupa, 2002)). Such measurements are somehow limited to the Milky Way and its satellites, and cover a limited range in properties such as total and specific star formation rate, density/pressure, and galaxy environment. However, studies of several samples of galaxies suggest that there is a possible variation of the stellar IMF depending on the properties of a galaxy, even after accounting for variations in star formation history,

extinction and metallicity. These studies are based on the integrated light from galaxies and providing only an indirect technique of measurement.

The IMF is the first ingredient that modellers tune to reproduce the observable parameters of a galaxy. The choice of the IMF has a direct impact on all the calculated models and hence influences the observational properties of the stellar populations in galaxies. The majority of all the SSP models are computed with an IMF as a power-law of Salpeter index above a few solar masses (Salpeter, 1955) and a log-normal (Chabrier, 2003) or shallower power-law (Kroupa, 2001) for masses $< 1M_{\odot}$. In addition, an IMF that evolves with time cannot be excluded and a stepper (i.e increasingly bottom-heavy) IMF should be used while studying massive elliptical galaxies (Spiniello *et al.*, 2011; van Dokkum & Conroy, 2010, 2011). Furthermore, recent studies also have suggested that the stellar IMF becomes stepper in low luminosity (Hoversten & Glazebrook, 2008) and low surface brightness (Meurer *et al.*, 2009), and may evolve with the cosmic time becoming top-heavy (i.e. flatter) in high redshift galaxies (Wilkins *et al.*, 2008).

In a recent review, Conroy (2013) discusses the important roles of the IMF in SPS modelling:

- it determines the overall normalization of the stellar mass-to-light ratio, a shift (up to a factor 2) in the mass-to-light ratio found in some bands is due to the uncertainty in the IMF, yielding a possible change in the colour evolution of a galaxy by 0.1 mag in V-K at intermediate ages (Conroy *et al.*, 2009).

- it determines the rate of luminosity evolution for a passively evolving population (e.g. Conroy *et al.*, 2009; Tinsley, 1980; van Dokkum, 2008)

- it affects the SED of composite stellar populations, since composite populations have a range of turnoff masses that contribute to the integrated light (e.g. Pforr *et al.*, 2012)

- it has a small affect on the shape of the SED of single stellar populations, since the integrated light of these populations is largely dominated by stars at approximately the same mass i.e., the turnoff mass.

2.3.2 The isochrone

The isochrones are time dependent evolutionary tracks of stars in the theoretical H-R diagram with same initial composition and various initial masses. The construction of isochrones is done by the stellar evolution calculations for stars from the hydrogen burning limit (≈ 0.1 $M_{\odot}$) to the maximum stellar mass (≈ 100 $M_{\odot}$). It is usually based on different approach of modelling and by choosing various initial chemical compositions, time, mass. Apart from age and chemical composition, opacities and convection need to be specified during the calculation of an isochrone. Nevertheless, there are some processes that need to be considered properly in constructing the isochrones, such as mass loss, rotation effects, close binary interactions,

and TP-AGB or AGB evolutions etc. On the one hand, there is a poor understanding of the supergiant and AGB phases. Stars in these phases are bright and have a short time-scale, they make a major contribution to the light in the infrared, but their numbers in the H-R diagram are not very large. On the other hand, the mass loss is very difficult to model, although it is important for calculating the evolutionary tracks of these stars. All of these issues lead to important and major uncertainties in the isochrones that closely affect the predictions resulting from the SPS calculations (e.g. Charlot *et al.*, 1996; Conroy *et al.*, 2009; Lee *et al.*, 2007; Yi, 2003).

Table 2.2 summarises the possible and most popular existing isochrone tables which cover a wide range in ages, chemical compositions, and variety of evolutionary phases. SPS modellers often use the Padova models for the different ranges of age and metallicity, but with the combination of Geneva models at young ages.

Table 2.2: List of popular and widely used isochrones in the literature

Name of models	Comments	References
Padova	including TP-AGB	Bertelli *et al.* (1994); Girardi *et al.* (2000)
BaSTI	including TP-AGB	Cordier *et al.* (2007); Pietrinferni *et al.* (2004)
Geneva	including Wolf-Rayet phase, no low mass stars	Meynet & Maeder (2000); Schaller *et al.* (1992)
Y^2	including RGB, HB evolutions	Yi *et al.* (2001); Yi (2003)
Darthmouth	including RGB, HB evolutions	Dotter *et al.* (2008)
Victoria Regina	including RGB, HB evolutions	Vandenberg (1985); VandenBerg *et al.* (2006)
Lyon	including very low mass stars, brown dwarfs	Baraffe *et al.* (1998); Chabrier & Baraffe (1997)
	including post-AGB	Schoenberner (1983); Vassiliadis & Wood (1994)

2.3.3 Stellar libraries

The stellar libraries are one of the most important ingredients used in constructing SPS models. That is because stellar spectral libraries, in combination with theoretical isochrones, are used to convert the outputs of stellar evolutionary calculations (T_{eff}, g) as a function of metallicity Z into observational parameters and SEDs (equation 2.5). The set of stellar spectra must cover a homogeneous range of effective temperature T_{eff}, gravity g and metallicity for either theoretical or empirical libraries. During the last decade, the spectral range, spectral resolution and homogeneity in the parameter ranges of the stellar libraries have been improved significantly (see Tables 2.3 and 2.4). Changing stellar libraries has an impact on the determination of the age and chemical composition of the models (Cid Fernandes & González Delgado, 2010). In addition, there are also significant observational obstacles while

constructing the SSP integrated spectra and parameters with empirical libraries, such as lack of stellar spectra covering a wide range of parameter space, limited wavelength coverage and spectral resolution, flux calibration and correction for atmospheric absorption. However, with theoretical libraries, problems with lines lists, treatment of convection etc. can arise. Theoretical stellar libraries are usually computed with solar-scaled abundance ratios, whereas empirical stellar libraries are composed of stars in the solar neighbourhood, which are basically stars with low metallicity and $\alpha-$enhanced ($[\alpha/Fe] \sim 0.3$). This has an impact when fitting observable galaxy spectra (e.g. massive elliptical galaxies, Worthey *et al.* (1992)). It is necessary to take into consideration the non-solar abundance ratios when creating the evolutionary synthesis models.

The SSP models used in this study were computed using different libraries. Some highlights of these stellar libraries are given below. The SSP model description itself is given later in chapter 3 section 3.7.7.

MILES The MILES library [1] (Sánchez-Blázquez *et al.*, 2006) contains 985 stars providing one of the most complete libraries. Spectra were obtained at the Isaac Newton Telescope in La Palma. They cover a wavelength range from 3500 to 7500 Å with a spectral resolution of 2.3 Å FWHM. The individual spectrum is well flux calibrated. This library represents a significant improvement in term of stellar parameters coverage compared to the other libraries especially the Lick/IDS library. Nevertheless, this library has a small number of hot stars (over 15000 K). Originally all atmospheric parameter values are taken from the literature, meaning they are not homogeneous. Cenarro *et al.* (2007) have made them as homogeneous as possible to span a large range in atmospheric parameters ($2748 < T_{eff} < 36000$ K, $0.0 < \log g < 5.50$ dex, $-2.93 < [Fe/H] < +1.65$ dex). Milone *et al.* (2011) measured [Mg/Fe] abundance ratio of the $\sim$ 76% of stars in the MILES library which makes the creation of new SSP models with empirical α-enhancements possible (for example: PEGASE.HR models with MILES (Prugniel *et al.*, 2011)).

ELODIE 3.1 This new version of the library [2] (Prugniel & Soubiran, 2001; Prugniel *et al.*, 2007) contains 1388 high resolution stellar spectra with a sampling of 0.55 Å FWHM (or $R = \Delta\lambda/\lambda$=10 000 at λ = 5500 Å) covering the wavelength range 3900 - 6800 Å. The spectra were obtained with the echelle spectrograph ELODIE at the 193 cm telescope at the Observatoire de Haute-Provence. It covers a wide range of atmospheric parameters. The library is flux calibrated with a broad-band photometric precision of 2.5% and narrow band precision of 0.5%. Details on the spectra as well as the determination of the atmospheric parameters are found in Prugniel & Soubiran (2001). The number of template spectra in its current version is 1962 and was obtained from 1388 stars. Its coverage in terms of stellar

[1] http://www.iac.es/proyecto/miles/pages/stellar-libraries/miles-library.php
[2] http : //www.obs.u − bordeaux1.fr/m2a/soubiran/elodie$_{l}$ibrary.html

parameters is one of the best among the currently available libraries. However, the number of cooler stars and lower metallicity are still lacking. The high resolution and the extensive coverage (for an empirical library) of the parameter space of this version makes this library suitable for stellar population studies.

STELIB STELIB libary [1] (Le Borgne *et al.*, 2003) contains 249 spectra with a resolution of $\approx$ 3 Å FWHM in the wavelength range of 3200 - 9500 Å. Spectra were obtained with the 1m Jacobus Kaptein Telescope in La Palma. This library includes stars in different spectral types and luminosity classes covering a wide range of metallicity. Its coverage in the parameters space, however is very limited compared to the other libraries, for instance, the lack of stars with [Fe/H] < -1.0. Many of the stars do not complete the full spectroscopic observation along the wavelength range cited above, and mostly all spectra suffer from telluric contamination. A large range of atmospheric parameters in this library was taken from the literature, including parameters of some stars which are part of the ELODIE library (Prugniel & Soubiran, 2001).

Martins & Coelho (2007) carried out a comparative study of these three libraries, and concluded that hot stars are missing in most of them. All three libraries tend to have the majority of their stars having temperatures between 5000 and 7000 K and miss a certain amount of stars in lower temperatures ($<$ 4000 K). MILES has the best coverage for lower temperatures, while ELODIE has it at higher temperatures. STELIB has only an O star and only one dwarf below 4000 K. Linking the study done by Cenarro *et al.* (2007) about the attempt to homogenize the MILES library, stars whose temperatures are outside the above range (near the system reference temperature i.e. 4000 - 6300 K) might not be as homogeneous as they wanted it to be (Maraston & Strömbäck, 2011).

Table 2.3: List of the most up-to-date empirical stellar libraries

Name	FWHM (Å)	Spectral range (Å)	No stars	Comments	References
PICKLES		1150 - 25000	131	flux calibrated	Pickles (1998)
ELODIE	0.55	4100 - 8800	1388	echelle	Prugniel *et al.* (2007)
STELIB	3.0	3200 - 9500	249	flux calibrated	Le Borgne *et al.* (2003)
INDO-US	1.0	3480 - 9464	1273	poor flux calibrated	Valdes *et al.* (2004)
MILES	2.3	3500 - 7500	985	flux calibrated	Sánchez-Blázquez *et al.* (2006)
NGSL		1700 - 10200	$\sim$100	flux calibrated	Heap & Lindler (2011)
IRTF		8000 - 25000	210	flux calibrated	Rayner *et al.* (2009)
XSL		3200 - 24800	240	flux calibrated	Chen *et al.* (2011)
UVES-POP		3070 - 10300	300		Bagnulo *et al.* (2003)
LW2000		5000 - 25000	100		Lançon & Wood (2000)

[1] http://webast.ast.obs-mip.fr/stelib

Table 2.4: List of some theoretical stellar libraries.

Name	Resolution	Spectral range (Å)	T_{eff} (K)	log(g)	metallicity
Rodríguez-Merino *et al.* (2005)	50000	850 - 4700	3000 - 50000	0 -5	-2.0< [M/H] <0.5
Munari *et al.* (2005)	20000 2000	2500 - 10500	3500 - 47500	0 -5	-2.0< [M/H] <0.5 [α/Fe] = 0.0,0.4
Coelho *et al.* (2005)	high	3000 - 18000	3500 - 7000	0 -5	-2.0< [M/H] <0.5 [α/Fe] = 0.0,0.4
Martins *et al.* (2005) (Granada)	0.3 Å	3000 - 7000	3000 - 55000	-0.5 - 5	0.04 < Z < 0.001

Note: [M/H] is another notation of metallicity, often described as metallicity ratio or total metal abundance, where M refers to as the metal or elements heavier than Helium.

2.4 Age-metallicity degeneracy

Spectra of early type galaxies suffer form the age-metallicity degeneracy issues. Both parameters vary with the spectra and colours of the elliptical galaxies in a similar way. Therefore it is difficult to determine age and metallicity independently for those galaxies. In particular, increasing either metallicties or ages will make the galaxy appear redder. Precisely, an age change about +30% on the isochrones has the same effect on the spectra as a +20% change on the metallicity. This was introduced by Worthey (1999) and is widely known as the "3/2 rule" (see figure 2.2). He also realized that individual spectral indices (Lick indices, see chapter 3) are more sensitive to age (Balmer lines) as well as to metallicity (e.g. Fe4668 and Fe5270). He suggested that it is possible to break the degeneracy on condition that such spectral indices are properly calibrated and carefully chosen. The most common and successful combinations of spectral indices are joining Hydrogen Balmer lines as an indicator of age and metallic features which are sensitive to the different elements such as Fe lines or Mg. In addition, these spectral line indices are known to be almost insensitive to the reddening of the continuum due to dust absorption.

It seems that the degeneracy gets worse when using spectral indices at low S/N and in the presence of dust in the galaxy. The latter problem will cause reddening, which acts in the same way as increasing metallicity or age. However, a distinct separation of age and metallicity can be obtained by using spectral indices at very high S/N ($\gtrsim$ 100 Carson & Nichol, 2010; Kuntschner, 2000; Trager *et al.*, 2000). In addition, full spectral fitting at moderate to high S/N is also a robust way to disentangle the degeneracy since more spectral information is available on the overall spectrum than those obtained with few spectral indices (Koleva *et al.*, 2009; Sánchez-Blázquez *et al.*, 2011).

2.5 Stellar population in ETGs and LRGs

2.5.1 Early-type galaxies

Studying the evolution of luminous red galaxies will also improve the understanding of the evolution of ETGs, since LRGs are a subset of the overall ETGs with extreme luminosities and

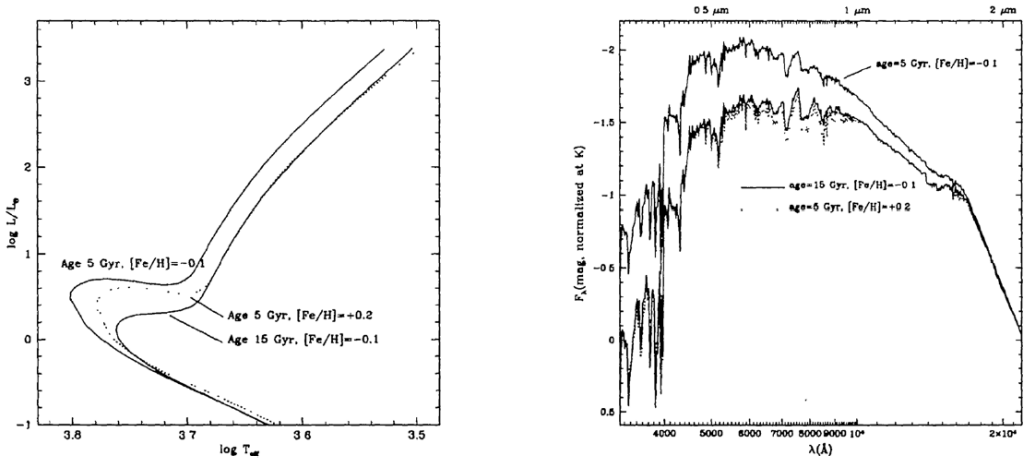

Figure 2.2: The age-metallicity degeneracy. The isochrones of 3 times the age or twice the metallicity have nearly the same spectra. Credit from Worthey (1999)

colours. Galaxies are found to occupy two distinct regions in colour-magnitude space known as the red sequence and the blue cloud (Blanton *et al.*, 2003; Strateva *et al.*, 2001). There is also an underpopulated space known as the green valley between the two distributions, which is made up with red late type galaxies. The blue cloud is made up mostly of star-forming late type galaxies, and is a broad distribution with large scatter in colour at all magnitudes. The red sequence is made up mostly of early type galaxies with little continuing star formation. From the results of the relation between mass and metallicity, ETGs lie along a tight colour-magnitude relation (Bower *et al.*, 1992; Gallazzi *et al.*, 2006) in the sense that the most massive are the most metal rich and consequently redder. From these observations, one can consequently deduce that all the stars in ETGs are formed at one epoch when the Universe was less than half of its current age and their ages are asymptotic to the age of the Universe at the present epoch (Renzini, 2006). In the ΛCDM model, ETGs should be assembling over a range of epochs, not only at one epoch in the past, but when smaller galaxies containing little gas merge, very little star formation occurs, hence large systems can be built up via "dry mergers". The amount of stellar mass contained in the red galaxies population has approximately doubled since $z = 1$ (Faber *et al.*, 2007). This increasing mass is mostly due to stellar mergers.

The denser environment of galaxies like galaxy clusters, where interactions and merging are very common in the past, offer a valuable laboratory for studying and understanding the evolution of ETGs. However, only observations at high redshift can help with the understanding of their formation. Some efforts have been made in that direction by building more sensitive and powerful telescopes.

The structural/dynamical parameters of ETGs, such as the luminosity L, effective radius R_e, effective surface brightness μ_e, colour, line-strength indices, and central velocity dispersion

σ_c, are all known to follow certain scaling relations which is very important in understanding their formation and evolution. Therefore, theoretical studies of ETGs (simulations) must reproduce these relations in order to understand the origin and evolution of these galaxies.

2.5.1.1 The fundamental plane

From observations, ETGs were found to cluster close to a plane known as *Fundamental Plane* (FP). This is a plane in the three dimensional space relating the central velocity dispersion σ_c, effective radius R_e and $< I_e >$ the average effective surface brightness within R_e, precisely expressed as:

$$R_e \propto \sigma^{\alpha} < I_e >^{\beta} \tag{2.6}$$

where the exponents α and β vary according to the specific band used for measuring the luminosity (Djorgovski & Davis, 1987; Dressler *et al.*, 1987). The projection of the FP over the (R_e,I_e) coordinate plane provides the Kormendy relation (Kormendy, 1977), a projection over the (σ,$L = 2\pi R_e^2 I_e$) plane however generates the Faber-Jackson relation (Faber & Jackson, 1976). The FP is poorly affected by the problem of the age-metallicity degeneracy, since it is tightly dependent on the mass-to-light ratio (M/L) which in its turn sensitive to the age (interpreted as differences in stellar populations or the dark matter content). Therefore, the FP is an important tool in understanding the ETGs evolution over cosmic time by converting it into a mass–M/L relation.

2.5.1.2 Colour-magnitude, colour-σ and other relations

Baum (1959) was the first to discover that there is a tight relation between colour and magnitude (CM) of ETGs, following the work by Visvanathan & Sandage (1977). From the relation, ETGs are found to have uniform stellar populations, and evolved passively since at least ∼1 Gyr ago. ETGs also follow a tight colour $-\sigma$ relation where σ is the central velocity dispersion. Its small intrinsic scatter in colour was interpreted as an age dispersion by Bower *et al.* (1992) and was used to set tight age constraints on the corresponding age formations of galaxies. Several studies also obtained the age $-\sigma$ relation (e.g. Caldwell *et al.*, 2003; Nelan *et al.*, 2005; Thomas *et al.*, 2005). The slopes from the CM and the colour-σ can be used to study the amount of the merging process that constituted the observed galaxies today. The merging process is interpreted as being responsible for increasing the luminosity and the central velocity dispersion while keeping the colour the same, hence the observed relations stay flat and wide. Another relation found when studying ETGs is between the absorption index Mg_2 and the central velocity dispersion. This relation however depends on the different ranges of the galaxy mass. Therefore, the $Mg_2 - \sigma$ relation implies that more massive ETGs have more heavy elements (steeper slope) for galaxies with masses below $\sim 10^{11} M_{\odot}$. Whereas the opposite behaviour (flatter slope and the scatter increases) is observed for more massive

galaxies (Spolaor *et al.*, 2010). The remaining question, however is what drives those relations the age or metallicity?

2.6 Different SSP models used

Since two different age-dating techniques were used in this analysis, namely full spectral fitting and Lick indices analysis, two types of SSPs were then employed. The details of the population models are described in chapter 3 in section 3.7.7 but lists of them are provided here.

- **Lick index fitting** the updated stellar population models of Lick absorption-line indices with variable element abundance ratios of Thomas *et al.* (2011, hereafter TMJ) were used. These models are based on the evolutionary stellar population synthesis code of Maraston (1998, 2005)
- **Full spectral fitting** four SSP models were used: Pegase-HR SSPs computed with the ELODIE 3.1 library (Le Borgne *et al.*, 2004), VAZDEKIS models computed with the MILES library (Vazdekis *et al.*, 2010), GALAXEV models computed with STELIB library (Bruzual & Charlot, 2003), and the new high spectral resolution stellar population models of Maraston & Strömbäck (2011) computed with MILES library.

Chapter 3

H(z) measurement with SDSS-LRGs

3.1 Introduction

The age-dating of galaxies is an important topic in galaxy evolution and an active area of research. During the last few decades it has been widely exploited by the creation of synthetic stellar population tools. There are a number of stellar population synthesis codes available (e.g. Bruzual & Charlot, 2003; Conroy *et al.*, 2009; Maraston, 2005; Vazdekis *et al.*, 2010) which can be used to generate synthetic spectra. These synthetic spectra are used to estimate different parameters such as age, metallicity, chemical abundance and star formation history of a galaxy. Basic details on the synthetic spectra models have been discussed in chapter 2. There are different ways to determine the galaxy age, such as the SED fitting, the Lick indices fitting and the full spectral fitting. In this work, we estimate the age of LRGs using both full spectral and Lick indices fitting. The full spectral fitting method takes into account all the information of the spectrum, it can include the continuum, all lines and specific spectral features. The advantage of this method over the Lick indices fitting is that the full spectral fitting is less sensitive to extinction, quality of the flux calibration, or elements ratio effects. The full spectral fitting gives more precise result (Koleva *et al.*, 2008) because it uses relatively higher total (integrated over all pixels) S/N. Moreover, this method is also not limited by the physical broadening of lines, since the internal kinematics is determined simultaneously with the population parameters (Koleva *et al.*, 2008). It is more sensitive to changes in the spectral resolution. However, the Lick indices fitting focuses on the importance of using the strength or equivalent width of lines and specific spectral features. The line-strength study also helps us to measure more straightforwardly the relative change in the individual element abundances. It requires a high signal-to-noise (S/N) spectrum and very reasonable spectral resolution (Thomas *et al.*, 2005, 2011). The accuracy of the age determination depends on the fact that all lines are well defined and well resolved, not forgetting also the different

calibration applied during the measurement.

In order to overcome this problem, Carson & Nichol (2010) performed a stacking method in order to increase the S/N of LRG spectra. They co-added spectra with similar properties in each redshift bin before estimating the mean ages of the galaxies by using the standard Lick absorption line indices. They reported the age-redshift relation but did not go further to address the $H(z)$ measurement and constrain on cosmological parameters. Liu *et al.* (2012) also applied the stacking method and used the full spectral fitting method on the combined spectra in order to derive the age-redshift relation from which they measured the local Hubble constant H_0.

In this chapter, we discuss the selection criteria applied in order to form a homogeneous, quiescent and passively evolving galaxy sample. We also compare the performance of the different fitting techniques and models while providing an estimation of the systematics errors. This includes comparing the full spectra fitting and the use of the standard Lick absorption indices. The derived parameters from each method as well as the detailed procedure to estimate $H(z)$ will be discussed. We then compare our $H(z)$ with all available $H(z)$ measurements in the literature.

3.2 The Sloan Digital Sky Survey

The Sloan Digital Sky Survey (Abazajian *et al.*, 2003, 2004, 2005, 2009; Adelman-McCarthy *et al.*, 2006, 2007, 2008; Ahn *et al.*, 2012, 2014; Aihara *et al.*, 2011; Stoughton *et al.*, 2002; York *et al.*, 2000) includes both photometric and spectroscopic surveys mapping Π steradians of the extragalactic sky (Figure 3.1 and 3.2). All observations are carried out using a 2.5 m telescope (Gunn *et al.*, 2006) at Apache Point Observatory, which equipped with the large format mosaic CCD camera to produce near-simultaneous photometry and with two double fiber-fed spectrographs to obtain extragalactic spectra. The survey has imaged more than 200 million objects using five optical bands *u, g, r, i, z* (Fukugita *et al.*, 1996) and has taken spectra of 40 - 60% of them, including 560 000 galaxies. The imaging data is reduced by an automatic pipeline called PHOTO (Lupton *et al.*, 2001). They all are processed and calibrated (Hogg *et al.*, 2001), allowing selection of galaxies, quasars and stars for follow-up spectroscopy observations with the same telescope. Not all photometric objects are simultaneously observed spectroscopically (see the difference between the two coverages in figures 3.1 and 3.2). Nevertheless, there is notably a big improvement in terms of the number of spectroscopic observed objects compared to the previous data release. Galaxies classified as the *main galaxy sample* are galaxies with Petrosian r-band magnitude $14.5 < \mathrm{m_{r,Petro}} < 17.7$ and a mean surface brightness limit $\mu < 24.5$ mag arcsec^{-2} (Strauss *et al.*, 2002). The SDSS LRG selection is based on their colour and magnitude yielding a sample of intrinsically red galaxies different from the main galaxy sample in terms of their faintness and distance (Eisenstein *et al.*, 2001). Richards *et al.* (2002) defined the selection criteria for Quasar candidates

and is technically based on the stellar locus outlier (established by 2-3 photometric colours) and matching unresolved sources to the FIRST radio catalogues.

Each spectroscopic plate, which has a circular field of view with a radius of 1°, can collect 592 objects plus 48 spectrophotometric standards and night sky with the aid of fibers. Each fiber must be separated from its center at least 55" apart because of its finite size (Blanton *et al.*, 2003). The tiling algorithm is used to perform the fiber allocation by maximizing the number of objects that can be observed. Not all the spectra are necessary for the general survey. Some specific studies require special observations outside the normal program and they are executed using *special plates*. After completing its two phases of operation (SDSS-I, 2000-2005; SDSS-II, 2005-2008), the SDSS survey is now (2008 -2014) continuing through the third Sloan Digital Sky Survey phase (SDSS-III). SDSS-III consists of four surveys executed simultaneously using different sets of spectrographs, including the Baryon Oscillation Spectroscopic survey (BOSS) which maps the Universe on large scale and measures the scale of the BAO in the clustering of the matter.

This study is based on the seventh data release (DR7) of SDSS (Abazajian *et al.*, 2009) which covers 11,663 square degrees images in the five band filters and 9,380 square degrees of spectroscopic area providing spectra of 929,555 galaxies, 121,373 quasars and 464,261 stars. The total SDSS LRG sample in that release covers about 19% of the sky.

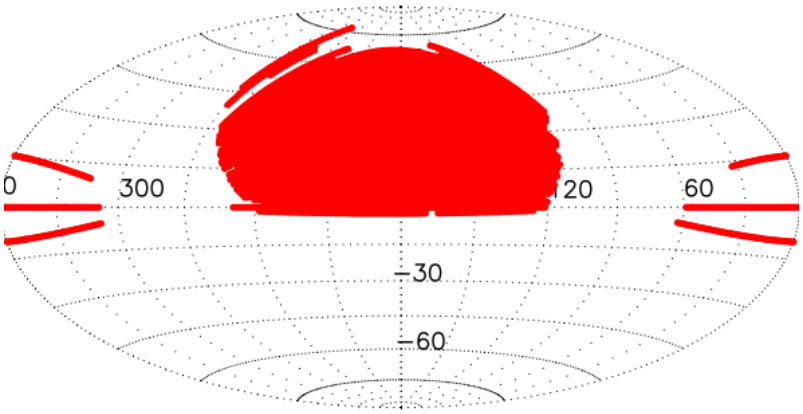

Figure 3.1: The photometric sky coverage of the SDSS DR7 data. The coverage area is the red shaded region on the celestial sphere as a projection of equatorial coordinates.

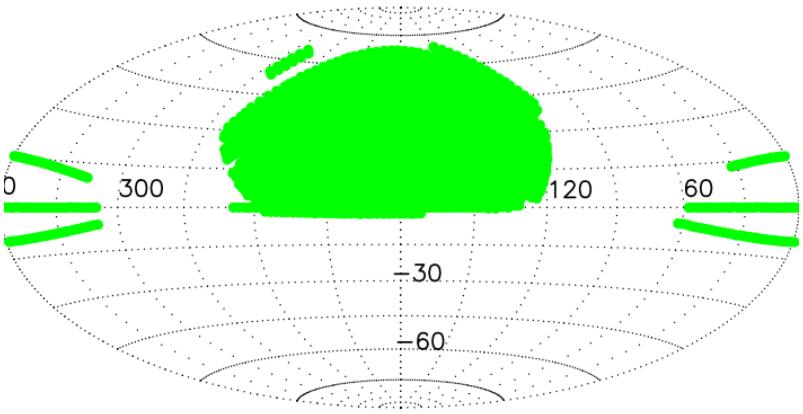

Figure 3.2: The spectroscopic sky coverage of the SDSS DR7 data. The coverage area is the green shaded region on the celestial sphere as a projection of equatorial coordinates.

3.3 SDSS spectroscopic data

The SDSS spectra were used as well as the photometric catalogue from Catalogue Archive Server (CAS[1]). The detailed information on the SDSS photometric data will be described in the next section. The different processing steps applied to the spectroscopic data and details on their format are described here as in Stoughton *et al.* (2002). As mentioned above, all SDSS spectra are obtained using the two fiber-fed spectrographs covering the rest-frame wavelength range of $3800 - 9200$ Å at a resolution of $\lambda/\Delta\lambda \simeq 2000$ Å (FWHM ~ 2.4 Å at 5000 Å) using 3" diameter fibers. Each spectrograph has two cameras (red and blue), hence four CCD detectors in total, and produces 320 spectra. The circular plate must be drilled in order to hold the fibers in the focal plane of the telescope. The nominal exposure time for each plate is typically 45 minutes followed by an additional calibration time for arcs, flat fields, spectrophotometric standards. The target coordinates have been already generated based on their photometric properties.

The two-dimensional pipeline `spectro2d` also called `idlspec2d` (IDL code) is used to reduce the raw data, calibrate images, extract the one-dimensional spectra from the two-dimensional exposures, stack multiple exposures into combined spectra, and produce corresponding masks and noise estimates. The output format of this pipeline is `spPlate` which contains the final reduced spectra for all 640 fibers on a given plate in one single FITS file. The `spPlate` spectra are then analysed by the one-dimensional pipeline `spectro1d` (also an IDL code) in order to measure absorption and emission lines, determine redshifts and classify spectra by object type. Details on all of these processes can be found in Stoughton *et al.* (2002) and SubbaRao *et al.* (2002).The format `spSpec` is generated by this process

[1]http://cas.sdss.org/dr7/en/

which is also a FITS image with six binary extensions. The primary HDU image contains the flux calibrated spectrum, the spectrum with continuum subtracted , the estimate of the one sigma error per pixel, and the mask array. The output wavelengths are in Angstroms but in vacuum wavelengths while all spectra are expressed in 10^{-17}ergs cm^{-2}s^{-1}Å^{-1}. The HDU 1 and 2 contain the list of the measured properties of the individual emission and absorption lines in the spectrum. The HDU 3 contains the redshift determinations based on set of emission lines. The redshift determinations from cross-correlations are listed in the HDU 4, however the list of calculated Lick indices are stored in HDU 5. Finally, the HDU 6 has an additional mask information and the spectral resolution as a function of wavelength. Additional and important informations are stored in the primary header such as velocity dispersion, final redshift value, S/N etc. The typical S/N of a galaxy near the main sample flux limit is 10 per pixel. The accuracy of the spectrophotometric calibration is about 4% rms for point sources (Adelman-McCarthy *et al.*, 2008), while for the wavelength calibration is about 2 km s^{-1}. Note that the telluric NaD feature is left out and not corrected by the sky-subtraction/telluric procedure in the SDSS reduction pipeline.

3.4 SDSS photometric parameters

The catalogue archive server contains the measured parameters of all objects observed photometrically and spectroscopically. However the data archive server (DAS[1]) gives the detailed data of the object from the CAS such as corrected frames, binned images, mask images, atlas images, colour images, spectra, spectral plots etc. Both formats `spPlate` and `spSpec` are obtained from the DAS server. The SDSS/ Skyserver is known as the CAS server too. All the data processed by the SDSS pipeline are stored and arranged in different tables in the database, so everyone can retrieve it easily by applying a SQL[2] query. The explanation of each table and each available parameter are provided by the SDSS Schema Browser[3]. Thus it is necessary to consult this before querying something from the database and check in which table is stored the needed parameter and under which name. The catalogue data includes object IDs, positions, magnitudes, and many other measured quantities along with their units. For the work carried out here, the `PhotoObjAll`, `SpecObjall` and `sppParams` tables as well as the function `fGetUrlFitsSpectrum` have been used, these are described in table 3.1. The function is like a predefined sequence of commands used to extract spectrum of each object. In total, there are 95 tables and 224 functions listed in the Schema Browser. Some tables are linked by a specific parameter, for example the photometric database `PhotoObjAll` and the spectroscopic database `SpecObjall` are linked by the parameter `ObjID` or `bestObjID`.

[1] http://das.sdss.org/www/html/
[2] Structured Query Language
[3] http://cas.sdss.org/astrodr7/en/help/browser/browser.asp

Table 3.1: Description of each table queried from the SDSS sky server.

Name of table	Description
`PhotoObjAll`	contains the measured parameters of each photometric target
`Photoz`	contains photometric redshifts as well as the absolute magnitudes and k-corrections for all objects in the `PhotoObjAll` table
`SpecObjall`	contains the measured spectral parameters for each spectroscopic target
`sppParams`	contains outputs from the `Spectro` Parameter Pipeline (spp)
Name of function	Description
`fGetUrlFitsSpectrum`	produces the URL link (with the help from DAS) to the spectrum (in FITS file) of an object spectrum given its spectroscopy ID

The parameters needed from the photometric database are concerning the r -band de Vaucouleurs radii (deVRad_r), the r -band de Vaucouleurs profile axis ratio (deVAB_r). These two parameters are used to perform the aperture correction on the measured Lick absorption indices. Details about the aperture correction is discussed in section 3.7.3.5

3.4.1 SDSS redshift and velocity dispersion

The velocity dispersion, magnitudes and redshifts can be obtained from the `sppParams` database (See table 3.1 for its description). The spectroscopic pipeline `spectro1d` determines the redshift and radial velocity of the SDSS spectra with their associated uncertainties. These parameters are determined from cross correlation of stellar, emission line galaxy and quasar template spectra obtained during the SDSS commissioning (Stoughton *et al.*, 2002). The redshift is derived from absorption features only by masking emission lines during the cross-correlation procedure with the stellar templates (Tonry & Davis, 1979). The corresponding redshift errors are given by the widths of the cross-correlation function peaks. It has been found that the cross-correlation technique tends to increase the statistical error and contribute a systematic error depending on the spectral type. Abazajian *et al.* (2004) determined a systematic error of order 10 km s^{-1} for A to K stars at SNR > 10. The typical redshift errors determined from repeat observations are about 30 km s^{-1} (Stoughton *et al.*, 2002). However Yanny *et al.* (2004) found an error of 20 km s^{-1} from repeating observations of F stars and 25 km s^{-1} for A stars. For verification and validation of the redshift results, the SDSS pipeline has also used another method of redshift measurement called *emission-line redshift* in which the redshift is determined by matching detected emission lines to a list of common galaxy and quasar emission lines. At the end, the pipeline assigns a *final* redshift value to each object spectrum by choosing either the emission line redshift or cross-correlation redshift with the highest confidence level (`zConf`).

To check the accuracy and the quality of the redshift determination, the SDSS pipeline produces different number of flags assigned to the measured redshift. For instance the parameter `zConf` reports the redshift confidence, it has to have a value of 1.0 to insure a high confidence in the redshift. `zStatus` gives the redshift status which helps to determine if

the cross-correlation and emission line redshifts are consistent. The best quality spectra are expected to have `zStatus` = 3 which means both redshifts are consistent, or `zStatus` = 4 which means a high confidence in the cross-correlation redshift. `zWarning` shows the redshift warning flags, the ideal is to have a value of `zWarning` = 0 which indicates that no warning flags have been set.

The SDSS velocity dispersion pipeline is made to estimate the velocity dispersion only for specific objects (not objects with strong emission lines, but objects whose spectra are dominated by the light of red giant stars). It selects objects which satisfy the spectroscopic parameters shown in table 3.2 (Bernardi *et al.*, 2003). This pipeline also requires that the average SNR in the restframe wavelength range 4200 Å $< \lambda <$ 5800 Å is greater than 10 per pixel. Bernardi (2007) investigated the accuracy of the SDSS velocity dispersions and found an overestimated value about $\sigma < 150$ km s^{-1} for using DR5 spectra. Due to this bias, they have changed the method of Fourrier fitting to the direct fitting and have made some improvements. The velocity dispersion measurements smaller than about $\sigma < 70$ km s^{-1} (instrumental resolution of the SDSS spectra) and greater than $\sigma < 420$ km s^{-1} (maximum velocity dispersion in the template spectra) should not be used. Actually, the SDSS velocity dispersion is not used in this analysis unless for comparison with our own measurement. Details on the step used for our velocity measurement are given in section 3.5.2.

Table 3.2: SDSS velocity dispersion pipeline parameters

Parameter	Value	Description
`specClass`	= 2	spectra classified as galaxy
`zStat`	= 4	redshift with high confidence from the cross-correlation
`zWarning`	= 0	no warnings flags from the spectroscopic pipeline
`eClass`	< 0	PCA classification, typical of early-type galaxy spectra
`redshift`	< 0.4	redshift less than 0.4

3.5 Emission lines measurements

3.5.1 The MPA-JHU and SDSS DR7 Emission lines

The SDSS spectroscopic pipeline produces measurements that are not fully completed because of its simplicity. The emission and absorption line-strength measurements are included. The pipeline is not set to perform a correction for the nebular emission line contamination on the absorption features. The emission contamination implies an underestimation of the true values of the absorption line-strengths. Therefore this correction is very important for some objects with strong emission lines (AGN or star-bursting systems). In addition, when measuring the emission lines the SDSS pipeline does not take into account the inclusion of the

reddening by dust and the consideration of the prior on the relative strength of recombination lines (Oh *et al.*, 2011). The MPA-JHU group have tried to solve those problems. They have reprocessed the SDSS galaxy spectra by creating a code of fitting stellar population models of Bruzual & Charlot (2003) (BC03) and the updated of BC03 to a continuum to prioritise the need of more treatment of the stellar continuum and emission lines. They made the measured emission lines available to the public[1]. There is some complexity found when extracting measurements from these catalogues and the quality of the measurements has not been addressed properly. There is also an improved value-added catalogue available in the SDSS database only for the DR9. This new catalogue was produced by the Portsmouth Stellar Kinematics and Emission Line Fluxes group (Thomas *et al.*, 2013), by using the adapted version of the software Gas AND Absorption Line Fitting (GANDALF), an IDL code developed by Sarzi *et al.* (2006). Our own emission line measurement will thus be performed with the same software GANDALF. The emission line correction is needed for further analysis.

3.5.2 Correction for Emission lines with GANDALF

To measure the strength of the nebular emission observed in the SDSS spectra, a combination of the penalized Pixel Fitting (pPXF) (Cappellari & Emsellem, 2004) and GANDALF (Sarzi *et al.*, 2006) routines was used. Not only the strength of the nebular emission lines were measured, but the velocity dispersions of each galaxy were also obtained. This will enable us to obtain the missing value of velocity dispersion for object filtered by the SDSS pipeline as described in section 3.4.1 paragraph 3. For the stellar population study, this process is very necessary before measuring stellar line-strength indices separately as it can correct for any nebular emission contribution. The pPXF code fits the stellar kinematics (velocity and dispersion) using a maximuum penalized likelihood approach, and parametrizes the line-of-sight velocity distribution (LOSVD). GANDALF fits the best combination of stellar spectral templates and Gaussian emission line templates to a given galaxy spectrum simultaneously to separate stellar continuum and absorption lines from the ionised gas. GANDALF makes use of multiplicative polynomials to adjust the shape of the continuum and correct uncertainties from dust extinction and flux calibration. The stellar population models of Bruzual & Charlot (2003) used in Tremonti *et al.* (2004), which consist of 38 different sets of spectra, were adopted as stellar templates. Although there are other libraries which can cover larger parameter such as the MILES library (985 stellar templates), we decided to use the BC03 models which have only 38 different sets of the spectra. We chose the smaller number of stellar templates to speed up the fitting procedure since the original sample is too big. In addition to the cleaned emission line spectrum along with the best fit stellar population template, this code also outputs the kinematics of the gas, the emission line fluxes and equivalent

[1]The data and catalogues are available from http://www.mpa-garching.mpg.de/SDSS/

widths on the resulting Gaussian emission line template.

Table 3.3: Emission lines measured with GANDALF

Index (1)	Name (2)	Wavelength (Å) (3)	Relative strength to (line) (4)	free/tied (5)
0	HeII	3203.15		tied to 25
1	[NeV]	3345.81		tied to 25
2	[NeV]	3425.81		tied to 25
3	[OII]	3726.03		tied to 25
4	[OII]	3728.73		tied to 25
5	[NeIII]	3868.69		tied to 25
6	[NeIII]	3967.40		tied to 25
7	H5	3889.05	0.037 (H_α)	tied to 24
8	Hϵ	3970.07	0.056 (H_α)	tied to 24
9	Hδ	4101.73	0.091 (H_α)	tied to 24
10	Hγ	4340.46	0.164 (H_α)	tied to 24
11	[OIII]	4363.15		tied to 25
12	HeII	4685.74		tied to 25
13	[ArIV]	4711.30		tied to 25
14	[ArIV]	4740.10		tied to 25
15	Hβ	4861.32	0.350 (H_α)	tied to 24
16	[OIII]	4958.83	0.350 ([OIII]λ5007)	tied to 25
17	[OIII]	5006.77		tied to 25
18	[NI]	5197.90		tied to 25
19	[NI]	5200.39		tied to 25
20	HeI	5875.60		tied to 25
21	[OI]	6300.20		tied to 25
22	[OI]	6363.67	0.333 ([OI]λ6300)	tied to 25
23	[NII]	6547.96	0.340 ([NII]λ6584)	tied to 25
24	Hα	6562.80		free
25	[NII]	6583.34		free
26	[SII]	6716.31		tied to 25
27	[SII]	6730.68		tied to 25
28	[ArIII]	7135.67		tied to 25

GANDALF allows users to set the range of wavelength of the fit, and the way they want the fit in terms of the emission line constraints. Following the general setting (Sarzi *et al.*, 2006; Tremonti *et al.*, 2004), we imposed the kinematics of [NII]λ6583 on all forbidden lines, whereas all recombination lines were tied to Hα (See table 3.3). This strategy was set in order to recover very weak nebular features (Tremonti *et al.*, 2004). In addition, the long wavelength range of SDSS spectra allows one to obtain a decrement on the strength of the Balmer lines by recombination theory (see the relative strength of the Balmer lines to Hα in column 4 of table 3.3). However, if either [NII]λ6584 or Hα lines are weak or undetectable,

the kinematics of all lines were tied to [OIII]λ5007. This line is easy to detect in that case. The skylines and NaD were masked during the procedure. Table 3.3 summarizes the list of the emission lines fitted and their relative strengths.

In general, the requirement for a line to be detected is A/N $\geqslant 3$ (the amplitude-to-noise ratio) according to Sarzi *et al.* (2006), where A is the amplitude of the Gaussian fit to the line and N is the median spectrum noise within the narrow wavelength region centred on the line. We applied this line detection criterion for our galaxies with further constraints on EW values of Hβ, Hα and [OIII]λ5007 to be nearly zero (See next section 3.6.2). Figure 3.3 and 3.4 give examples of fits with GANDALF showing spectra with and without emission lines respectively.

In order to see the performance of the software, a comparison of the measured velocity dispersion and the nebular emission line values with those in MPA-JHU is given in appendix A. From the subsample that we used for the comparison, the estimated central velocity dispersions agree with the MPA-JHU measurements as expected since the same stellar template (Tremonti *et al.*, 2004) and the procedure are considerably the same.

3.6 Selection

3.6.1 Sample Selection

To estimate the Hubble parameter $H(z)$ by using the age-redshift relation, it is necessary to pay attention to the selection criteria in order to create a homogeneous and large sample of oldest populations. In Crawford *et al.* (2010b), we established a new criteria based on the rest-frame luminosity of galaxies. We found that using rest-frame colour-cut of $B - V > 0.81$ and an absolute magnitude cut by $M_V < -23$ yields a far more homogeneous sample than using the apparent magnitude cuts by Eisenstein *et al.* (2001). As a test, we have applied this criteria to the Millennium Simulation database, and obtained an improved homogeneous sample of objects with similar star formation histories and formation redshifts. We applied this new criteria to select a sample of galaxies from SDSS DR7 catalogue (Abazajian *et al.*, 2009). Our sample contains galaxies restricted to a redshift range of $0.10 < z < 0.40$.

The SDSS spectra of the selected galaxies are mostly at the wavelength range of $3800 < \lambda < 9200$ Å with a median resolution of $\lambda/\Delta\lambda \sim 2000$ Å (approximately 2.4 Å) which is quite similar to the resolution of the SEDs models. For the analysis presented here, we do not use the Lick indices measurements from the standard SDSS pipeline, as they were not calibrated onto the Lick/IDS system (see section 3.7.2). Instead we measure our own line-strengths after matching the instrumental resolution. However, we do use the other derived parameters such as redshift, velocity dispersion, magnitudes, the r -band de Vaucouleurs radii (deVRad_r), the r -band de Vaucouleurs profile axis ratio (deVAB_r) which are available through the CAS.

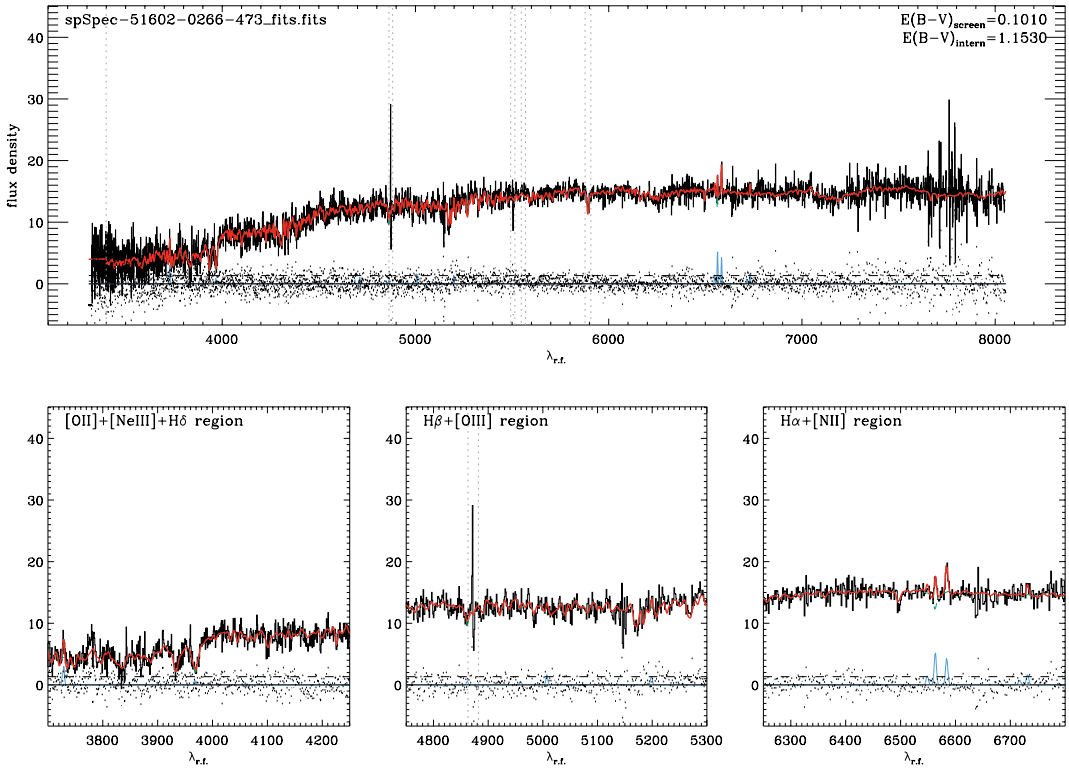

Figure 3.3: Example of the GANDALF fitting procedure showing a spectrum at rest-frame with detected emission lines ([OII], [NII] and Hα). The observed spectra are showing in black lines. The best fit spectra (in red) are composed of the stellar population and emission lines templates. Residuals from the fit are also shown. The three bottom panels are zoomed regions showing the different emission lines. Doted vertical lines are masked from the fits (Skylines and NaD)

3.6.2 Quiescent selection

LRGs sometimes show a little evidence of recent or ongoing star formation which manifests in their spectra as emission lines, and some fraction of LRGs exhibit AGN activity (Roseboom *et al.*, 2006). These emission lines are associated with HII regions which are produced by strong UV light from O and B stars ionizing the surrounding HI. Our study involves some galaxies at low redshift, where the contamination from the bulges in late type galaxies is important. The presence of the emission lines also affects the absorption lines analysis. For example, the absorption indices Hβ, Hγ, Hδ are often affected by emission lines, their line-strengths then become weak which lead to older ages. Fe5015 is affected by [OIII]λ5007 emission. Mg_b is affected by [NI]λ5199 emission.

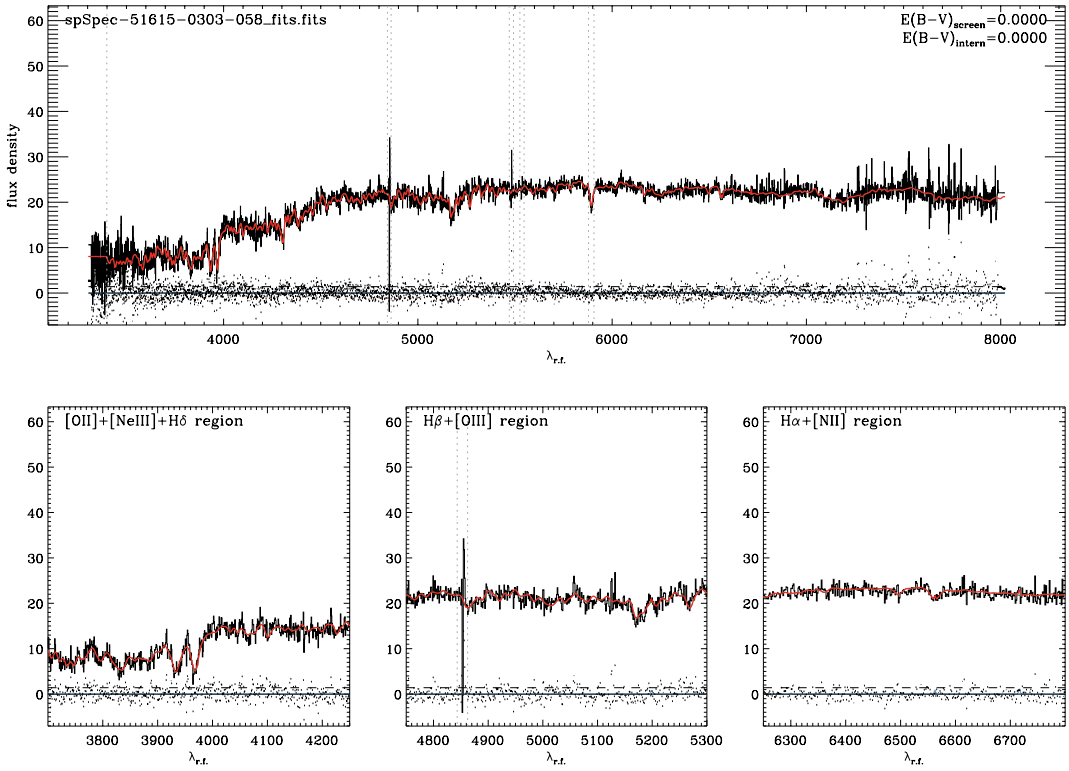

Figure 3.4: Example of the GANDALF fitting procedure showing a spectrum at rest-frame without detected emission lines. Legends are the same as in figure 3.3

Furthermore, emission lines are popularly used as indicators for the ionization of the interstellar gas in galaxies, and can be used to classify galaxies into either star forming galaxies (emission line ratios like HII region) or AGN-ionized galaxies. This classification was proposed by Baldwin, Phillips and Terlevich (Baldwin *et al.*, 1981) known widely as BPT diagram, which is commonly based on [NII]λ6584/Hα vs [OIII]λ5007/Hβ ratios. Hα and Hβ are typically the two strongest optical emission lines in star forming galaxies and the luminosity of [OIII]λ5007 emission line is the tracer of the strength of activity in AGN galaxies (Kauffmann *et al.*, 2003).

To overcome these problems, we further selected galaxies without star formation and AGN activities, meaning that the sample selection is based on the objects consistent with nearly zero emission lines in Hβ, Hα and [OIII]λ5007 (Carson & Nichol, 2010; Roseboom *et al.*, 2006). We also used the stellar kinematics form GANDALF to make further selection based on the velocity dispersion. We only used a massive sample with a velocity dispersion cut 200 $< \sigma <$ 400 km s^{-1}. The output nebular emission line models from GANDALF have also been

subtracted from the galaxy spectra in order to get an emission-free spectra which we used for the rest of the analysis. The emission-free spectra were used to get rid of the possible remaining emission lines (for example [OII], [SII], [NII]). We performed the age-dating on both emission-free spectra and original spectra, and found that the final results were not affected by the choice.

Figure 3.5 illustrates the cuts applied to the original sample. The quiescent galaxies in Hβ, and [OIII]λ5007 equivalent widths (EWs) distributions are those that lie near the peak of the distribution around zero emission line in Hβ, Hα and [OIII]λ5007.

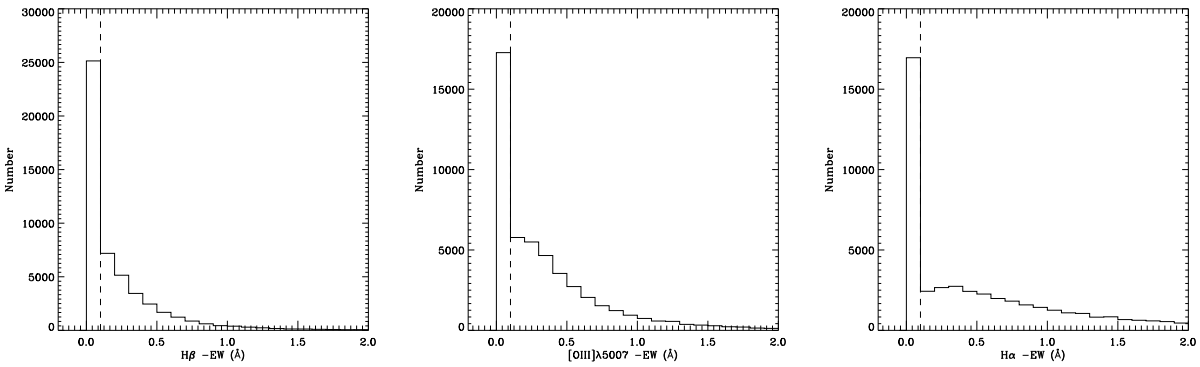

Figure 3.5: Distributions of the EWs of the emission lines of all galaxies in the initial sample. From left to right: distributions of the EWs of Hβ, [OIII] and Hα. The dashed lines show the cut applied to the original sample in order to create a quiescent galaxy sample.

After applying all of these criteria, our final sample contains 4 428 galaxies. Figure 3.6 represents its redshift distribution and shows clearly that there are few objects at $z < 0.2$. The numbers of galaxies selected initially are very large compared to the final numbers ($\sim 10\%$ of the initial sample, see table 3.4). This implies that the rest-frame based selection criteria gives less quiescent and non-quiescent luminous and very red galaxies than the original selection by Eisenstein *et al.* (2001). We note that the original selection gives 71 971 LRGs (in DR7) and 23 883 quiescent LRGs (Liu *et al.*, 2012) at $0.0 < z < 0.40$. Carson & Nichol (2010); Liu *et al.* (2012) usually relaxed the definition of the quiescent galaxies while our criteria are stricter.

3.6.3 High signal-to-noise spectra

Another way to estimate the SSP parameters of a sample based on the line-strength distribution is to combine the individual spectra into a high S/N average spectrum. By co-adding spectra in the same different redshift bin, the effect of the sky subtraction residual on the line-strength measurement will be greatly reduced. This gives more accurate result in terms of the line-strength fitting than the low S/N individual spectra, which gives large errors on

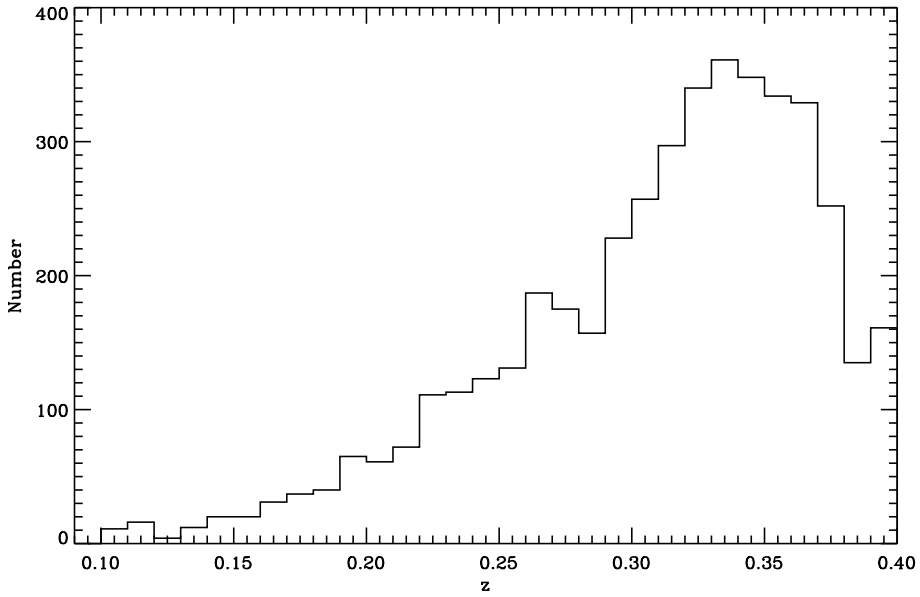

Figure 3.6: The redshift distribution of our final sample. At z $<$ 0.20, the number of galaxies is less than 100.

Table 3.4: List of objects before and after selection.

Redshift	Initial number	Final number
0.10 $<$ z $<$ 0.12	853	27
0.12 $<$ z $<$ 0.14	1025	16
0.14 $<$ z $<$ 0.16	1243	40
0.16 $<$ z $<$ 0.18	1646	68
0.18 $<$ z $<$ 0.20	2061	105
0.20 $<$ z $<$ 0.22	2377	133
0.22 $<$ z $<$ 0.24	2830	224
0.24 $<$ z $<$ 0.26	2990	255
0.26 $<$ z $<$ 0.28	3449	361
0.28 $<$ z $<$ 0.30	4156	385
0.30 $<$ z $<$ 0.32	5470	554
0.32 $<$ z $<$ 0.34	7102	701
0.34 $<$ z $<$ 0.36	6897	682
0.36 $<$ z $<$ 0.38	6145	581
0.38 $<$ z $<$ 0.40	2399	296
Total	50 425	4 428

the Lick index EWs. The stacking method also helps for the full spectral fitting to accurately derive the SSP parameters, especially when the sample contains a low number of objects.

We followed more or less the technique of stacking in Carson & Nichol (2010). We divided galaxies into redshift bins and chose a redshift bin of $\delta z = 0.02$. For each bin, we co-added the

spectra of the individual galaxies within the bin to obtain a very high S/N stacked spectrum. The individual spectra are normalized by the average flux in the 4000-5500 Å wavelength region. After de-redshifting all spectra (using redshift in pixel given by $\Delta\log\lambda/0.0001$ where 0.0001 is the dispersion per pixel in $\log_{10}$ wavelength), they were cropped to a common wavelength range. The individual spectra were then combined on a pixel-by-pixel basis using a weighted mean, where the weights are determined from the errors associated with the flux in each pixel and bad pixels have their weights set to zero. The uncertainty of the weighted mean flux was calculated using the weighted standard deviation technique. The total S/N varies according to the number of galaxies that contribute to each bin; it increases as $\approx \sqrt{N}$ where N is the number of galaxies within a bin. The weights were also used to produce the instrumental response function (IRF) for the co-added spectra using individual IRF for each galaxy. The IRF for the stacked spectra is used to match the SDSS instrumental resolution to the Lick/IDS resolution.

While de-redshifting individual spectrum, the uncertainty is insignificantly small since the redshift in pixel was used and it yields an error of < 0.5 pixels which corresponds to 1Å over the wavelength range 4000-5000 Å for objects in the redshift range $0.10 < z < 0.4$. This uncertainty was added in quadrature to the error on the redshift of the object produced by the SDSS pipeline. The final error on the redshift was then used for the Lick index measurements in order to determine the impact of the radial velocity on the errors of the measured line-strengths (see section 3.7.3.2).

The spectroscopic parameters estimated by SDSS pipeline such as velocity dispersion and redshift did not follow the same procedure as the spectra, however the parameter mean of the sample within a bin was taken with its error estimated from the standard propagation technique. The error on the redshift (as well as the velocity dispersion) decreases as N increases, hence it can become negligible for large N. The mean of the sample was also used for the photometric parameters such as deVRad_r and deVAB_r. These two parameters will be used later for making aperture corrections. The error on these parameters also become negligible when the number of galaxies is very large.

From here on, we continue our analysis with the stacked spectra at each redshift bin. However for comparison, individual spectra are eventually used. Figure 3.7 illustrates the evolution of the stacked spectra from $z = 0.11$ (the top spectrum) to $z = 0.35$ (the bottom spectrum). The difference in the age of the Universe for ΛCDM cosmology model between the two redshifts is around 2.43 Gyr. Clearly, the difference between the strength of the absorption lines are noticeable between each spectrum, hence with such variation the difference in age between redshift is obtained. With redshift step of $\delta z = 0.02$ we obtained 15 combined spectra in the range of $0.10 < z < 0.40$.

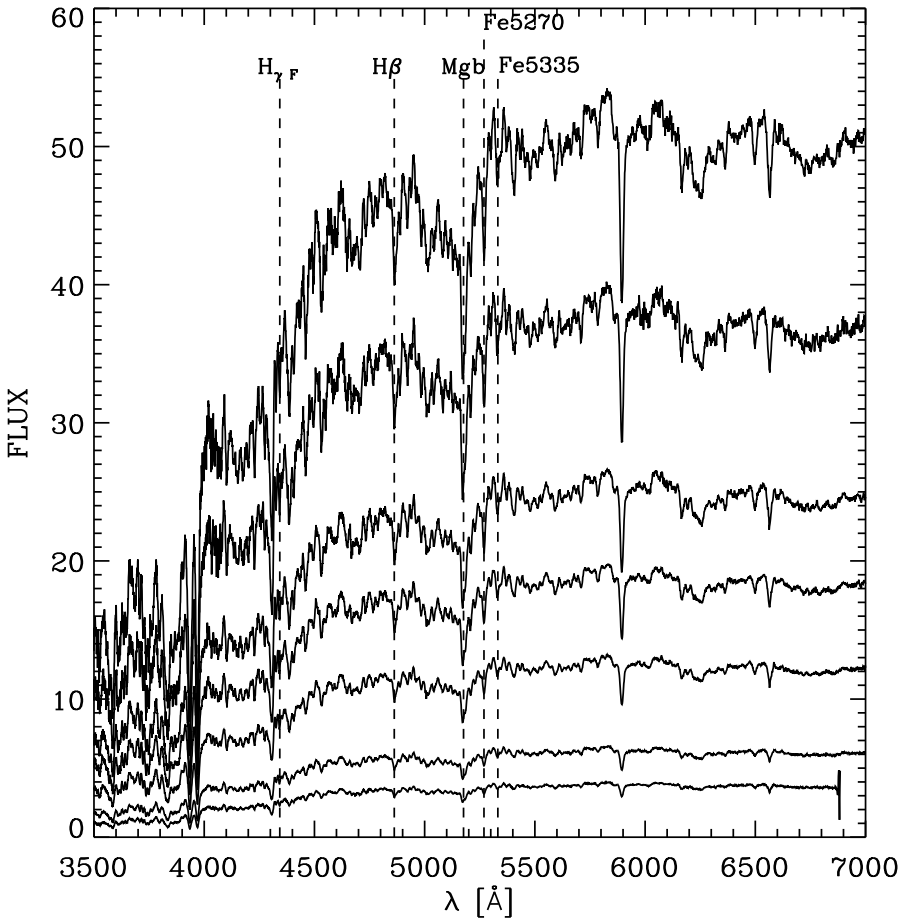

Figure 3.7: Evolution of the stacked spectra with the centered redshift at the rest-frame wavelength 3500 - 7000 Å. This evolution is from $z = 0.11$ (top) to $z = 0.35$ (bottom) with an interval of $\delta = 0.04$. The Lick indices used for the age-dating are also shown in this plot. The vertical scale is magnified by a factor of 10.

3.7 Spectral fitting techniques

3.7.1 Lick indices analysis

As an outcome of the long time project, Faber *et al.* (1985), Worthey *et al.* (1994) and Worthey & Ottaviani (1997) have created a library of stellar spectra and defined ranges of the spectral index system known as the Lick indices system. They used the Imaging Dissecting Scanner (IDS) on the Shane 3m telescope at the Lick Observatory to observe and analyse these stars. The system is used to derive stellar population characteristics through the evolutionary synthesis of the integrated spectra. It can be applied to any type of galaxies and star clusters. Twenty five absorption Lick indices have been defined in the wavelength range $4000 < \lambda < 6000$ Å at ~ 9 Å resolution. These different indices include atomic absorption lines (narrow

features) and six molecular bands (broad features). The line-strength of the atomic features are conventionally expressed in Å whereas the molecular indices have their line-strength given in magnitudes. The wings of an absorption feature might vary depending on different factors, such as the instrumental resolution, element abundances or velocity dispersion of the stellar population, even though the definitions of the bandpasses are fixed. Thus the value of the equivalent width (EW) is not a true EW. Following the standard definitions (Cardiel *et al.*, 1998; González, 1993), the atomic (I_a) and molecular (I_m) indices are defined as follows

$$\mathrm{I_a} = \int_{\lambda_1}^{\lambda_2} \left(1 - \frac{\mathrm{F_{I\lambda}}}{\mathrm{F_{C\lambda}}}\right) \mathrm{d}\lambda \quad \mathrm{I_m} = -2.5\log_{10}\left[\left(\frac{1}{\lambda_2 - \lambda_1}\right)\int_{\lambda_1}^{\lambda_2} \frac{\mathrm{F_{I\lambda}}}{\mathrm{F_{C\lambda}}}\mathrm{d}\lambda\right] \tag{3.1}$$

where $F_{I\lambda}$ and $F_{C\lambda}$ are the fluxes per unit wavelength in the index passband and continuum respectively. The wavelengths λ_1 and λ_2 are the wavelengths definitions of the central passband. Table 3.5 shows the wavelength definitions of the different Lick indices system which consist of a central index band, and blue and red continuum bands. Figure 3.8 illustrates one example of the index measurement by showing the definition of each passband. The index is defined by the central feature passband which is shown in green, while the two adjacent pseudocontinuum passbands are given in blue and red.

The flux in the pseudocontinuum could usually be obtained by interpolating the flux of the observed spectrum between two adjacent spectral regions and is determined as follows:

$$\mathrm{F_{C\lambda}} \equiv \mathrm{F_b}\frac{\lambda_\mathrm{r} - \lambda}{\lambda_\mathrm{r} - \lambda_\mathrm{b}} + \mathrm{F_r}\frac{\lambda - \lambda_\mathrm{b}}{\lambda_\mathrm{r} - \lambda_\mathrm{b}} \tag{3.2}$$

where

$$\mathrm{F_b} \equiv \int_{\lambda_{\mathrm{b1}}}^{\lambda_{\mathrm{b2}}} \frac{\mathrm{F_\lambda}}{\lambda_{\mathrm{b2}} - \lambda_{\mathrm{b1}}}\mathrm{d}\lambda, \quad \mathrm{F_r} = \int_{\lambda_{\mathrm{r1}}}^{\lambda_{\mathrm{r2}}} \frac{\mathrm{F_\lambda}}{\lambda_{\mathrm{r2}} - \lambda_{\mathrm{r1}}}\mathrm{d}\lambda \tag{3.3}$$

and

$$\lambda_\mathrm{b} = \frac{\lambda_{\mathrm{b2}} + \lambda_{\mathrm{b1}}}{2}, \quad \lambda_\mathrm{b} = \frac{\lambda_{\mathrm{r2}} + \lambda_{\mathrm{r1}}}{2} \tag{3.4}$$

and λ_{b2}, λ_{b1}, λ_{r2} and λ_{r1} are the wavelength definitions of the blue and red bandpasses.

Worthey *et al.* (1994) used polynomial fitting functions to model the behaviour of the 20 metallic absorption features along with one Balmer line Hβ, whilst there were originally 11 of them proposed (Faber *et al.*, 1985). The four indices of the two Balmer lines Hδ_A, Hδ_F, Hγ_A and Hγ_F were later introduced by Worthey & Ottaviani (1997). All 25 indices are very sensitive to the effective temperature ($\mathrm{T_{eff}}$), surface gravity (g) and metallicity (Z[Fe/H]) of a star. Worthey and his collaborators built the stellar population models (single age, single metallicity) of Lick indices out of the polynomial fits which were used to predict index values for stars along the evolutionary isochrones. An additional extension was later included to the models and that is the effect of variable $\alpha-$element enhancements on the predicted line-strengths (e.g. Thomas *et al.* (2003)). Meanwhile, González (1993) (among others) came up

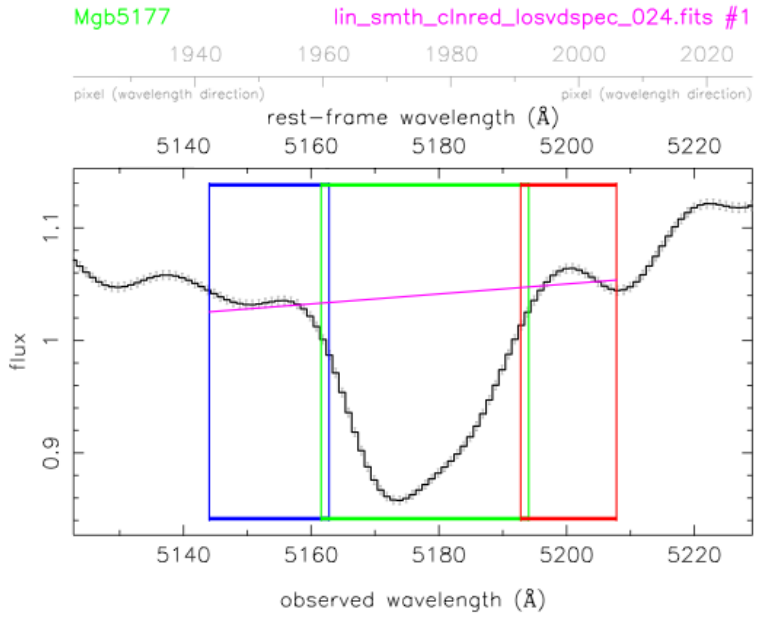

Figure 3.8: Example of the line-strength of the atomic index Mgb which is used for age-dating LRGs. The different passbands employed during the measurement are shown: the central passband which represents the index passband is shown in green, the two adjacent pseudocontinuum passbands are given in blue and red. This example was run with the program `indexf` using the stacked spectra of all galaxies within redshift bin $0.24 < z < 0.26$.

with the idea of combining indices in order to define a good mean metallicity indicator. The mean metallicity <Fe> replaces the two iron indices Fe5270 and Fe5335 and is given by the equation 3.5. The [MgFe] index is introduced as the geometric mean of $\mathrm{Mg_b}$ and <Fe>, given by equation 3.6

$$< \mathrm{Fe} >= \frac{\mathrm{Fe5270} + \mathrm{Fe5335}}{2} \tag{3.5}$$

$$[\mathrm{MgFe}] = \sqrt{\mathrm{Mg_b} \times < \mathrm{Fe} >} \tag{3.6}$$

By adopting the fixed wavelength definitions, the use of the Lick indices faces other problems such as nebular emission lines, dust and telluric features. Gas emission lines are the most important since they will contaminate the absorption line spectra. For example the line-strength of the Hα index is directly affected by Balmer emission from ionised gas. However, some of the indices are indirectly affected by nebular emission line contamination. Section 3.5.2 discusses the possible correction to overcome the emission line contamination.

Table 3.5: Lick/IDS index definitions. Line-strengths of the atomic indices are expressed in Å, while line-strengths of the molecular indices are in magnitudes.

name	index bandpass		blue bandpass		red bandpass		unit
$H\delta_A$	4083.500	4122.250	4041.600	4079.750	4128.500	4161.000	Å
$H\delta_F$	4091.000	4112.250	4057.250	4088.500	4114.750	4137.250	Å
CN_1	4142.125	4177.125	4080.125	4117.625	4244.125	4284.125	mag
CN_2	4142.125	4177.125	4083.875	4096.375	4244.125	4284.125	mag
Ca4227	4222.250	4234.750	4211.000	4219.750	4241.000	4251.000	Å
G4300	4281.375	4316.375	4266.375	4282.625	4318.875	4335.125	Å
$H\gamma_A$	4319.750	4363.500	4283.500	4319.750	4367.250	4419.750	Å
$H\gamma_F$	4331.250	4352.250	4283.500	4319.750	4354.750	4384.750	Å
Fe4383	4369.125	4420.375	4359.125	4370.375	4442.875	4455.375	Å
Ca4455	4452.125	4474.625	4445.875	4454.625	4477.125	4492.125	Å
Fe4531	4514.250	4559.250	4504.250	4514.250	4560.500	4579.250	Å
Fe4668	4634.000	4720.250	4611.500	4630.250	4742.750	4756.500	Å
$H\beta$	4847.875	4876.625	4827.875	4847.875	4876.625	4891.625	Å
Fe5015	4977.750	5054.000	4946.500	4977.750	5054.000	5065.250	Å
Mg_1	5069.125	5134.125	4895.125	4957.625	5301.125	5366.125	mag
Mg_2	5154.125	5196.625	4895.125	4957.625	5301.125	5366.125	mag
Mg_b	5160.125	5192.625	5142.625	5161.375	5191.375	5206.375	Å
Fe5270	5245.650	5285.650	5233.150	5248.150	5285.650	5318.150	Å
Fe5335	5312.125	5352.125	5304.625	5315.875	5353.375	5363.375	Å
Fe5406	5387.500	5415.000	5376.250	5387.500	5415.000	5425.000	Å
Fe5709	5696.625	5720.375	5672.875	5696.625	5722.875	5736.625	Å
Fe5782	5776.625	5796.625	5765.375	5775.375	5797.875	5811.625	Å
NaD	5876.875	5909.375	5860.625	5875.625	5922.125	5948.125	Å
TiO_1	5936.625	5994.125	5816.625	5849.125	6038.625	6103.625	mag
TiO_2	6189.625	6272.125	6066.625	6141.625	6372.625	6415.125	mag

3.7.2 SDSS Lick indices

The SDSS pipeline underestimates the Lick indices as no calibration to the Lick system has been applied to them. In addition, the absorption line-strength values are not corrected for the impact of nebular emission leading, to an underestimation of the true strength of the absorption line features. The MPA-JHU group (e.g. Tremonti *et al.* (2004)) has also attempted to re-process the SDSS galaxy data in order to calculate new absorption line-strengths. According to Oh *et al.* (2011), it is not yet clear what systematic problem may have affected the extraction of the physical parameters listed in the MPA-JHU catalogues, and it is not possible to verify the quality of their measurements. For all of these reasons, we measured our own absorption line-strength after calibrating to the Lick/IDS system.

3.7.3 Transforming Spectra to Lick/IDS system

In order to compare the measured indices to those of the SSP models, it is necessary to transform the measured line-strengths onto the Lick/IDS system. It is important to note that the spectra obtained by Lick group which are used to define the Lick indices were not flux calibrated, therefore the shape of the continuum of Lick/IDS spectra are different from any calibrated spectra. The usual and necessary steps to transform a spectrum not observed with the IDS instrument are as follows:

- Matching the spectral resolution of the observed spectrum to that of the Lick/IDS system.
- Measuring the line-strengths using the Lick index definitions displayed in table 3.8 following steps in section 3.7.3.2
- Correcting line-strengths for the effect of LOSVD.
- Applying the Lick offsets which requires observation of a number of Lick library standard stars.
- Applying the aperture corrections.

Details of these steps are given in the next sections.

3.7.3.1 Matching spectral resolution

Transforming SDSS spectra to the Lick system means degrading the high resolution of SDSS spectra to adapt to the lower resolution of the IDS spectrograph. The reason for this is that the Lick/IDS calibrated SSP models predict the measured line index strengths for a stellar population in the rest frame at the resolution of the Lick/IDS system, meaning all observed absorption features must be at the same instrumental resolution as the Lick/IDS system and at the rest frame before comparing them with a SSP model of line-strengths. IDS spectrograph has an instrumental resolution which varies with wavelength between $\sim 8.4 - 11$Å FWHM. However, SDSS spectra have slightly different wavelength dependent instrumental resolution. To match the instrument resolution, we strictly followed the approach of Worthey & Ottaviani (1997) by convolving the SDSS spectra with a wavelength dependent Gaussian Kernel with the width:

$$\sigma_{\rm smooth}(\lambda) = \sqrt{\frac{\mathrm{FWHM}(\lambda)^2_{\rm Lick} - \mathrm{FWHM}(\lambda)^2_{\rm SDSS}}{8\ln 2}} \tag{3.7}$$

3.7.3.2 Measuring Lick indices with `indexf`

The broadened and emission line cleaned spectra were then analysed with `indexf`[1] (Cardiel, 2010). It is a program written in C++ in order to measure the line-strength indices represented in table 3.5 according to equation 3.1. Cardiel (2010) computed the line-strength errors by adopting the same methodology as in Cardiel *et al.* (1998) resulting from the propagation of random errors (e.g. photon statistics, read-out noise). In general, the expected errors in the atomic (I_a) and molecular (I_m) indices are expressed as a function of the mean S/N per Å and can be written as follows:

$$\sigma(I_a) \simeq \frac{c_1 - c_2\ I_a}{S/N(Å)} \tag{3.8}$$

$$\sigma(I_m) \simeq \frac{c_3}{S/N(Å)} \tag{3.9}$$

where I_a is the line-strength of the atomic index and c_1, c_2 and c_3 are the coefficients for typical line-strength features. These coefficients are calculated by the program using the formulae below and already given in table 1 in Cardiel *et al.* (1998).

$$c_1 \equiv \Delta\lambda_c c_2 \tag{3.10}$$

$$c_2 \equiv \sqrt{\frac{1}{\Delta\lambda_c} + \left(\frac{\lambda_r - \lambda_c}{\lambda_r - \lambda_b}\right)^2 \frac{1}{\Delta\lambda_b} + \left(\frac{\lambda_c - \lambda_b}{\lambda_r - \lambda_b}\right)^2 \frac{1}{\Delta\lambda_r}} \tag{3.11}$$

$$c_3 \equiv 2.5\ c_2\ \log_{10}e \tag{3.12}$$

where $\Delta\lambda_b$, $\Delta\lambda_c$ and $\Delta\lambda_r$ are the passband widths in blue, central and red respectively.

This program also estimates the effects of errors on radial velocity by performing a Monte Carlo simulation on the measured index using the error on the galaxies radial velocity. We take into consideration the contribution of this uncertainty (σ_{rad}) in the line-strength index due to the radial velocity error as in Carson & Nichol (2010). This is added in quadrature to the random error in the line-strength index associated with the photon statistics and read-out noise $\sigma_{photon+ccd}$ (expressed as $\sigma(I_a)$ and $\sigma(I_m)$ in equations 3.8 and 3.9 respectively) in order to obtain the error on the measured line-strength.

$$\sigma_I^2 = \sigma_{photon+ccd}^2 + \sigma_{rad}^2 \tag{3.13}$$

[1] **http://pendientedemigracion.ucm.es/info/Astrof/software/indexf/indexf.html**

3.7.3.3 Correcting line-strengths for the effect of LOSVD

In general, the absorption features observed in the galaxy spectra symbolize a convolution of the luminosity weighted integrated spectrum of the stellar population present in the instrumental broadening and the LOSVD of the stellar populations. The measured line-strengths thus depend on the LOSVD of the spectrum, specifically on the velocity dispersion of the stellar population which is a victim of the effect of smearing the absorption feature out of the Lick/IDS index band and into the side bands, hence depressing the measured index.

In order to compare the indices to stellar population models, which are obviously based on stellar spectra, a correction for the broadening induced by the velocity dispersions of the galaxies must be done to the measured indices. To achieve this, we followed the technique in Oh *et al.* (2011). GANDALF fit provides as outputs the optimal combination of the stellar templates and the best stellar model files. The latter is the optimal template convolved by the LOSVD obtained during the GANDALF/pPXF fit procedure and adjusted for dust reddening. We analysed the difference between the values of the indices measured on both of them. If the LS is the index measurement on the broadened and emission cleaned spectra, $\mathrm{LS}_{\mathrm{optimal}}$ is the index measurement on the optimal spectra, and $\mathrm{LS}_{\mathrm{model}}$ is the index measurement on the best stellar model spectra. The corresponding index value corrected for the effect of LOSVD can be determined as follows:

$$\mathrm{LS}_{\mathrm{corr}} = \mathrm{LS} \times \frac{\mathrm{LS}_{\mathrm{optimal}}}{\mathrm{LS}_{\mathrm{model}}} \tag{3.14}$$

3.7.3.4 Lick offsets

The next step in transforming observations onto the Lick/IDS system is to correct for systematic offsets between the measured line-strengths and the objects already on the Lick/IDS system. These variations are mainly due to the imperfection of the Lick /IDS spectra regarding the non-flux calibration, hence different spectral shapes. It is then necessary to observe a number of Lick library standard stars which were already observed by the Lick/IDS system with the same instrumental set-up as the actual observed galaxy in order to correct for offsets. In addition, these offsets help to remove the final systematic differences introduced by the different instrumentations used. Carson & Nichol (2010) have already extracted and analysed 13 Lick stellar library from the SDSS archive. After matching the SDSS resolution to the Lick/IDS system, they determined the offsets from the true Lick system for each index. Not only the mean offset of each index is negligible ($\leq 2\sigma$) but the stellar population models of Lick indices used in this study (models by Thomas *et al.*, 2011) are also not tied to the non-flux-calibrated Lick/IDS system anymore. Therefore, we did not apply any offsets to the measured line-strengths. It is important to note that Lick index offsets are crucial when using stellar population models based on non-flux-calibrated stellar libraries as Lick/IDS library (e.g. Thomas *et al.*, 2003; Worthey & Ottaviani, 1997).

3.7.3.5 Aperture correction

The size and shape of the spectrograph aperture and the distance to the galaxy are other factors which affect the measured velocity dispersion and the absorption line-strengths in a galaxy. Moreover, elliptical galaxies are found to display radial gradients in their velocity dispersions and in their absorption line indices (Mehlert *et al.*, 2003). It is crucial to correct for these gradients when comparing the measured indices to other results in the literature. The current correction also is necessary when comparing data over a large redshift range in redshift since the fixed spectrograph aperture will collect different physical scales of objects depending on their distances.

Jorgensen *et al.* (1995) established a method of converting the rectangular apertures into the equivalent circular apertures of a diameter $2r_{ap}$. With this method, values of the velocity dispersion observed through both apertures should be similar to within 4%. The conversion is approximately given by:

$$2\mathrm{r_{ap}} \approx 1.025 \times 2(\mathrm{xy}/\pi)^{1/2} \tag{3.15}$$

where x and y are the width and length of the rectangular aperture. They also demonstrated that the measured velocity dispersion, on the circular aperture, relies upon the aperture radius. It has been normalized and measured through an aperture with a radius of $\mathrm{r_e}/8$, where $\mathrm{r_e}$ is the effective radius. The velocity dispersion profile normalized to σ_{e8}, which is the velocity dispersion measured through an aperture of $\mathrm{r_e}/8$, is presented by a power law in the form:

$$\frac{\sigma_{\mathrm{ap}}}{\sigma_{\mathrm{e8}}} = \left(\frac{\mathrm{r_{ap}}}{\mathrm{r_e}/8}\right)^{\alpha} \tag{3.16}$$

where α is the velocity dispersion gradient.

One can name the velocity dispersion corrected as σ_{corr} which is equivalent to the σ_{e8}, and it can be measured through an aperture with a radius $\mathrm{r_{e/8}}$. The effective radius can be determined from $\mathrm{r_e} \equiv (\mathrm{b/a})^{1/2}\mathrm{r_{deV}}$, where $\mathrm{r_{deV}}$ is the deVaucouleurs radius, b and a are respectively the semi-minor and semi-major axis of the galaxy. Values of (b/a) are the inverse values of the SDSS r-band photometry parameter deVAB_r, whereas $\mathrm{r_{deV}}$ is the parameter deVRad_r which is the deVaucouleurs fit scale radius. For the stacked spectra in each redshift bin, those two parameter values were the mean values of the sample.

The aperture correction for the measured line-strengths can also be deducted from equation 3.16 and given by:

$$\log(\mathrm{I_{corr}}) = \log(\mathrm{I_{rap}}) - \alpha_{\mathrm{I}}\log\left(\frac{\mathrm{r_{ap}}}{\mathrm{r_{e/8}}}\right) \tag{3.17}$$

for atomic indices, and

$$\mathrm{I_{corr}} = \mathrm{I_{rap}} - \alpha_{\mathrm{I}}\log\left(\frac{\mathrm{r_{ap}}}{\mathrm{r_{e/8}}}\right) \tag{3.18}$$

for molecular indices, where I_{rap} is the measured index for the circular aperture, and α_I is the radial gradient for the given index. We adopted the velocity and index gradients measured by Mehlert *et al.* (2003). Note that the uncertainties on the measured logarithmic index gradients were not taking into account since they are not provided and might contribute more on the uncertainty of the final calibrated indices.

3.7.4 TMJ model description

In this work, we make use of the flux calibrated stellar population models of Lick absorption line indices and variable element abundance ratios of Thomas *et al.* (2011). These models are the extension versions of the Thomas *et al.* (2003) models and are based on the flux calibrated Medium-resolution Isaac Newton Telescope library of empirical spectra MILES (Sánchez-Blázquez *et al.*, 2006). Thomas *et al.* (2003) created their stellar population models of Lick indices and elements abundance ratios based on the evolutionary stellar population synthesis code of Maraston (1998, 2005) with inputs: the stellar evolutionary track from Cassisi *et al.* (1997) and Bono *et al.* (1997) and a Salpeter stellar initial mass function. The models cover ages from 1 to 15 Gyr, metallicities from 1/200 to 3.5× solar abundance and $\alpha-$abundance [α/Fe] from 0.0 to 0.5 dex, where α constitutes the sum of the following different elements: O, Ne, Mg, Si, S, Ar, Ca, Ti, Na and N. Some improvements were made in Thomas *et al.* (2004) by including higher Balmer absorption-line indices. They also found that these Balmer indices are very sensitive to the changes in the [α/Fe] ratio for supersolar metallicities. In Thomas *et al.* (2011), they updated their models by creating flux calibrated models, hence models are no longer tied to the non-flux-calibrated Lick/IDS system. In addition, the models used the MILES library which has a resolution comparable to the SDSS resolution (Beifiori *et al.*, 2011), therefore we do not need to correct for instrumental spectral resolution. The new models cover the same ages as the previous ones (0.1 to 15 Gyr), but metallicities from -2.25 to 0.67 dex and [α/Fe] from -0.3 to 0.5 dex. The key novelty of the new model predictions is also the inclusion of errors estimates which were found to be very small and well below the errors from the observational indices around solar metallicity, but rising toward the highest and lowest metallicities. They provided two different models for the public, one based on the stellar evolutionary tracks in Cassisi *et al.* (1997) as used for the previous models, and the other one based on Padova (Girardi *et al.*, 2000) evolutionary tracks.

3.7.5 Method of fitting

After applying all appropriate corrections, we used the χ^2-minimization method to fit the measured Lick absorption line indices with the TMJ models. It has been proved that using this method is more reliable for extracting stellar population parameters than using the two line index diagram method (Caldwell *et al.*, 2009). Thomas *et al.* (2011) provide only 25 ages,

6 [Fe/H] and 4 [α/Fe] values. For statistical study, it is necessary to broaden the original grid of the model predictions by interpolating the initial values of parameters to a higher resolution. The cubic spline interpolation was performed using equal step lengths to obtain 150 age values from 0.1 to 15 Gyr, 31 [Fe/H] values from -1.25 to 0.67 dex and 51 [α/Fe] values from -0.3 to 0.5 dex. The computed χ^2 between model predictions and our observed index values over n indices considered is:

$$\chi^2 = \sum_{\mathrm{i}=1}^{\mathrm{n}} \left(\frac{\mathrm{I_i^{obs}} - \mathrm{I_i^{model}}}{\sigma_\mathrm{i}} \right)^2 \tag{3.19}$$

where $\mathrm{I_i^{model}}$ is the $\mathrm{i^{th}}$ Lick line index of the model predictions for a given age, metallicity and $\alpha-$abundance ratio, and $\mathrm{I_i^{obs}}$ is the observed Lick line index measured from the stacked spectra. We did not consider using the error estimates associated with the models. Errors on the best-fit parameters are computed using 500 Monte-Carlo simulations by perturbing the uncertainty of the observed indices with some random numbers.

Choosing index Using many diagnostic lines yields more reliable and accurate results. Furthermore, using multiple index fitting allows all available indices to be fitted as each one of them contains important information about the individual derived parameters. However, the use of all indices is still a subject of debate since the model predictions have problems reproducing some of the measured indices of Galactic Globular Clusters and elliptical galaxies (Thomas *et al.*, 2003). In addition, the derived SSP parameters depend on the type of indices used (Carson & Nichol, 2010; Sánchez-Blázquez *et al.*, 2006). Using a certain number of indices gives more scatter on the derived SSP ages than using only four usual indices: Hβ, Mg$_b$, Fe5270, Fe5335 (Loubser *et al.*, 2009). Some indices are also affected by interstellar absorption lines, like NaD index. The inclusion of the non solar $\alpha-$element abundance ratios seems to partially solve the problem but the overall problem still remains unsolved. Thomas *et al.* (2011) and Johansson *et al.* (2012) developed a χ^2 fitting technique using most of the indices but split them into different set of indices in each step of the fitting. This procedure helps to overcome the problem that certain indices are sensitive to certain elements and chemical species.

The Balmer line Hβ is mostly used as an age indicator, and Mg$_b$, Fe5270, Fe5335 are good tracers of metallicity. We therefore chose these four indices. We also used the Hγ_F to test the age-redshift relation as it was found to generate a well defined age-redshift relation (Carson & Nichol, 2010). All the calibrated line-strength indices and the measured S/N per resolution element in Hβ are listed in table 3.6. Figure 3.9 illustrates the evolution of each index over the redshift range of $0.10 < z < 0.40$. It is clear that these evolutions are consistent with that of a passively evolving galaxy where Hβ and Hγ_F indices increase with redshift, and the metallicity indices Mg$_b$ and <Fe> decrease with redshift. The Mg$_b$ index shows more scatter and variability than the other indices. The line-strength indices at high redshift might

be contaminated by telluric emission/absorption lines which could affect the Mg_b, Fe5270, Fe5335 indices. The full spectrum fitting will highlight the contamination. However, the iron lines do not seem to be significantly affected, as well as $H\gamma_F$ or $H\beta$ index . The latter will not be affected until $z \sim 0.48$ where it is redshifted into the telluric line. Therefore, the age estimate would be safe in this work as most information comes from $H\gamma_F$ or $H\beta$ index. Large error bars at low redshift are from the low S/N spectra. The errors associated with the calibrated line-strength indices are only the random error in the line-strength index associated with the photon statistics and read-out noise, since the errors in the line-strength indices due to the radial velocity errors were very tiny and did not contribute much to the final errors.

Table 3.6: Calibrated line-strength indices of the stacked spectra.

Redshift	$H\gamma_F$	$H\beta$	Mg_b	Fe5270	Fe5335	SNR[a]
$0.10 < z < 0.12$	-1.707 ±0.045	1.760 ± 0.044	4.736 ± 0.051	2.815 ± 0.058	2.471 ± 0.059	155
$0.12 < z < 0.14$	-1.729 ±0.080	1.675 ± 0.078	4.590 ± 0.093	2.866 ± 0.084	2.621 ± 0.088	88
$0.14 < z < 0.16$	-1.515 ± 0.050	1.722 ± 0.054	4.586 ± 0.055	2.775 ± 0.053	2.468 ± 0.060	127
$0.16 < z < 0.18$	-1.577 ± 0.045	1.837 ± 0.048	4.425 ± 0.043	2.845 ± 0.046	2.536 ± 0.052	143
$0.18 < z < 0.20$	-1.435 ± 0.039	1.770 ± 0.046	4.520 ± 0.037	2.787 ± 0.040	2.491 ± 0.043	150
$0.20 < z < 0.22$	-1.397 ± 0.039	1.851 ± 0.049	4.619 ± 0.039	2.748 ± 0.038	2.589 ± 0.041	141
$0.22 < z < 0.24$	-1.472 ± 0.033	1.751 ± 0.033	4.252 ± 0.030	2.785 ± 0.030	2.449 ± 0.035	205
$0.24 < z < 0.26$	-1.302 ± 0.033	1.777 ± 0.031	4.434 ± 0.028	2.732 ± 0.031	2.536 ± 0.033	218
$0.26 < z < 0.28$	-1.406 ± 0.032	1.815 ± 0.029	4.447 ± 0.026	2.770 ± 0.026	2.468 ± 0.029	235
$0.28 < z < 0.30$	-1.218 ± 0.035	1.801 ± 0.029	4.293 ± 0.025	2.747 ± 0.027	2.496 ± 0.034	235
$0.30 < z < 0.32$	-1.125 ± 0.034	1.846 ± 0.024	4.389 ± 0.023	2.848 ± 0.028	2.468 ± 0.030	278
$0.32 < z < 0.34$	-1.097 ± 0.034	1.837 ± 0.022	4.402 ± 0.025	2.703 ± 0.025	2.467 ± 0.027	314
$0.34 < z < 0.36$	-1.070 ± 0.040	1.872 ± 0.024	4.109 ± 0.026	2.696 ± 0.026	2.434 ± 0.032	281
$0.36 < z < 0.38$	-1.035 ± 0.040	1.932 ± 0.025	4.265 ± 0.028	2.810 ± 0.032	2.441 ± 0.045	277
$0.38 < z < 0.40$	-0.929 ± 0.050	1.984 ± 0.035	4.217 ± 0.044	2.588 ± 0.061	2.348 ± 0.060	195

(a): S/N per $Å^{-1}$ in $H\beta$

3.7.6 SSP parameter results

Table 3.7 lists the fitting results of the line-strength indices extracted from the stacked spectra with the TMJ models. Two different sets of indices were used: a combination of $H\beta$, Mg_b, Fe5270, Fe5335 indices and a combination of $H\gamma_F$, Mg_b , Fe5270, Fe5335 indices. All derived parameter results are also displayed in figure 3.10 and 3.11. From both plots - panels (a), the derived ages decrease with redshifts. It is more apparent when using the combination of $H\gamma_F$, Mg_b, Fe5270, Fe5335 indices. Galaxy ages tend to be older and less scattered when using the combination of $H\beta$, Mg_b, Fe5270, Fe5335 indices than using the combination of metallicity lines with $H\gamma_F$, approximately 2 Gyr difference in average. This confirms what Carson & Nichol (2010) found in their analysis. The variability of the ages depends on the variability of the both indices: $H\beta$ and $H\gamma_F$. The trend of the age-redshift relation when using $H\gamma_F$ is

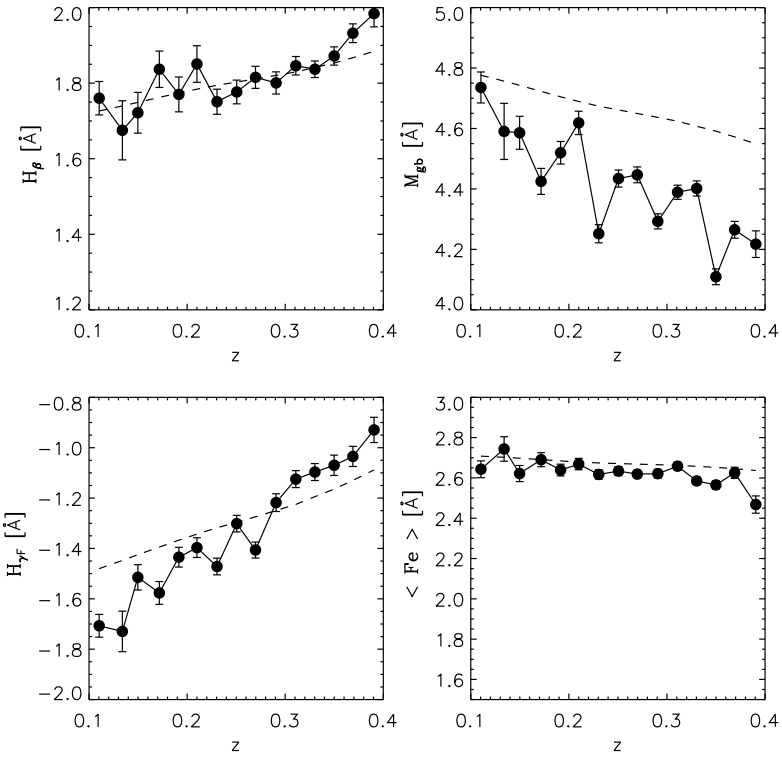

Figure 3.9: Plots of the line-strengths Hβ, Hγ_F, Mg$_b$, <Fe> as a function of redshift. The dash lines represent the expected variation in the line-strengths for an object with [Z/H] = 0.37 and [α/Fe] = 0.27 with an age formation of 4.5 Gyr in the ΛCDM cosmology. All the line-strength indices show a clear evolution with the redshift which are consistent with the evolution of a passively evolving galaxy.

much steeper than that using Hβ. In addition, it does not follow the expectations of the age evolution in the ΛCDM Universe.

The overall [Z/H] and [α/Fe] should be flat for a passively evolving galaxy sample. However, using Hβ index provides less variability in metallicity and α-element than that of using Hγ_F index. The [Z/H] also increases by a value >0.02 dex when using Hγ_F index, while [α/Fe] increases by 0.05 dex. This leads to the remark that even though the evolution of Hβ and Hγ_F tend to follow the evolution of the passively evolving objects, they provide inconsistent parameter estimates.

The index-index plots are also given in order to check the robustness of the SSP results and the reliability of the fits. Figure 3.12 shows the [MgFe]-Hβ (panel (a)), [MgFe]-Hγ_F (panel (b)) space grids and the calibrated indices. The composite index [MgFe] was used as a metallicity indicator and calculated using the definition introduced by Thomas *et al.* (2003), different from equation 3.6:

$$[\mathrm{MgFe}] \equiv \sqrt{\mathrm{Mgb}(0.72.\mathrm{Fe5270} + 0.28.\mathrm{Fe5335})} \tag{3.20}$$

This definition is much better than the definition given by González (1993) (equation 3.6) in order to eliminate the residual of [α/Fe] dependence of the index [MgFe]. The dotted and solid lines in the plots are the TMJ models with [α/Fe] = 0.3 and [α/Fe] = 0 respectively. The metallicity and age are efficiently separated. It has been proved by this plot that the derived metallicities are in the range of 0 <[Z/H]< 0.35 with an [α/Fe] of approximately 0.3 by using either Hβ or Hγ_F, exactly as listed in table 3.7. The derived ages show clearer evolution, meaning more scatter, when using Hγ_F than using Hβ. However, the age-metallicity degeneracy is considerably worse when Hγ_F is used with [MgFe] than when Hβ is used. The Hγ_F line becomes weaker while [MgFe] line becomes stronger as the age and metallicity of these populations increase. Subsequently, this degeneracy affects the interpretation of the age and chemical evolutions of these galaxies over our redshift range studied herein.

Table 3.7: SSP parameter results using line-strength of Hβ, Mg$_b$, Fe5270, Fe5335 indices, and using line-strength of Hγ_F, Mg$_b$, Fe5270, Fe5335 indices

	using Hβ, Mg$_b$, Fe5270, Fe5335			**using Hγ_F, Mg$_b$, Fe5270, Fe5335**		
Redshift	**Age (Gyr)**	**[Z/H] (dex)**	**[α/Fe] (dex)**	**Age (Gyr)**	**[Z/H] (dex)**	**[α/Fe] (dex)**
$0.10 < z < 0.12$	10.103 ± 1.356	0.237 ± 0.061	0.355 ± 0.018	11.282 ± 0.515	0.189 ± 0.025	0.345 ± 0.012
$0.12 < z < 0.14$	11.294 ± 1.046	0.197 ± 0.040	0.278 ± 0.021	10.246 ± 1.197	0.228 ± 0.059	0.291 ± 0.018
$0.14 < z < 0.16$	11.005 ± 1.088	0.166 ± 0.044	0.326 ± 0.017	9.564 ± 1.016	0.208 ± 0.049	0.347 ± 0.013
$0.16 < z < 0.18$	9.352 ± 1.183	0.204 ± 0.045	0.292 ± 0.018	9.809 ± 0.315	0.185 ± 0.012	0.288 ± 0.009
$0.18 < z < 0.20$	10.234 ± 0.155	0.183 ± 0.001	0.313 ± 0.008	8.246 ± 1.281	0.246 ± 0.061	0.343 ± 0.012
$0.20 < z < 0.22$	10.628 ± 0.389	0.185 ± 0.013	0.316 ± 0.010	7.321 ± 0.165	0.305 ± 0.001	0.363 ± 0.010
$0.22 < z < 0.24$	11.242 ± 0.652	0.067 ± 0.026	0.261 ± 0.007	8.706 ± 0.793	0.171 ± 0.037	0.287 ± 0.005
$0.24 < z < 0.26$	10.537 ± 1.329	0.145 ± 0.057	0.298 ± 0.014	6.834 ± 1.078	0.272 ± 0.054	0.340 ± 0.009
$0.26 < z < 0.28$	9.465 ± 0.150	0.183 ± 0.001	0.314 ± 0.005	9.010 ± 0.184	0.184 ± 0.005	0.329 ± 0.013
$0.28 < z < 0.30$	10.202 ± 1.418	0.111 ± 0.060	0.284 ± 0.018	7.402 ± 0.873	0.203 ± 0.045	0.321 ± 0.012
$0.30 < z < 0.32$	9.209 ± 0.551	0.187 ± 0.020	0.297 ± 0.014	5.750 ± 0.198	0.306 ± 0.012	0.344 ± 0.009
$0.32 < z < 0.34$	8.875 ± 0.200	0.183 ± 0.001	0.321 ± 0.012	5.415 ± 0.077	0.305 ± 0.001	0.367 ± 0.002
$0.34 < z < 0.36$	8.899 ± 1.423	0.101 ± 0.057	0.276 ± 0.019	6.190 ± 0.138	0.184 ± 0.009	0.313 ± 0.003
$0.36 < z < 0.38$	6.706 ± 1.220	0.240 ± 0.061	0.324 ± 0.014	5.020 ± 0.087	0.305 ± 0.001	0.352 ± 0.013
$0.38 < z < 0.40$	6.144 ± 0.796	0.219 ± 0.055	0.354 ± 0.015	4.628 ± 0.111	0.305 ± 0.005	0.373 ± 0.012

3.7.7 Full spectral fitting with ULySS

It has been proved that the full spectral fitting gives good and efficient precision on the fitting results since it uses relatively high S/N ratio (Koleva *et al.*, 2008). The full spectrum fitting treats the shape of the flux in the pixel-pixel basis and does not account the continuum, unlike the SED fitting procedures which use only the observed spectra as a mix of stellar populations at different ages and metallicities. Nevertheless the latter gives general information about the star formation history of the observed galaxies. In the last decades, many codes of full spectrum fitting have been made available to the public, such as STARLIGHT (Cid Fernandes *et al.*, 2005), STECKMAP (Ocvirk *et al.*, 2006a,b), MOPED (Heavens *et al.*, 2000), ULySS (Koleva *et al.*, 2009), VESPA (Tojeiro *et al.*, 2007), NBURSTS (Chilingarian *et al.*, 2007)

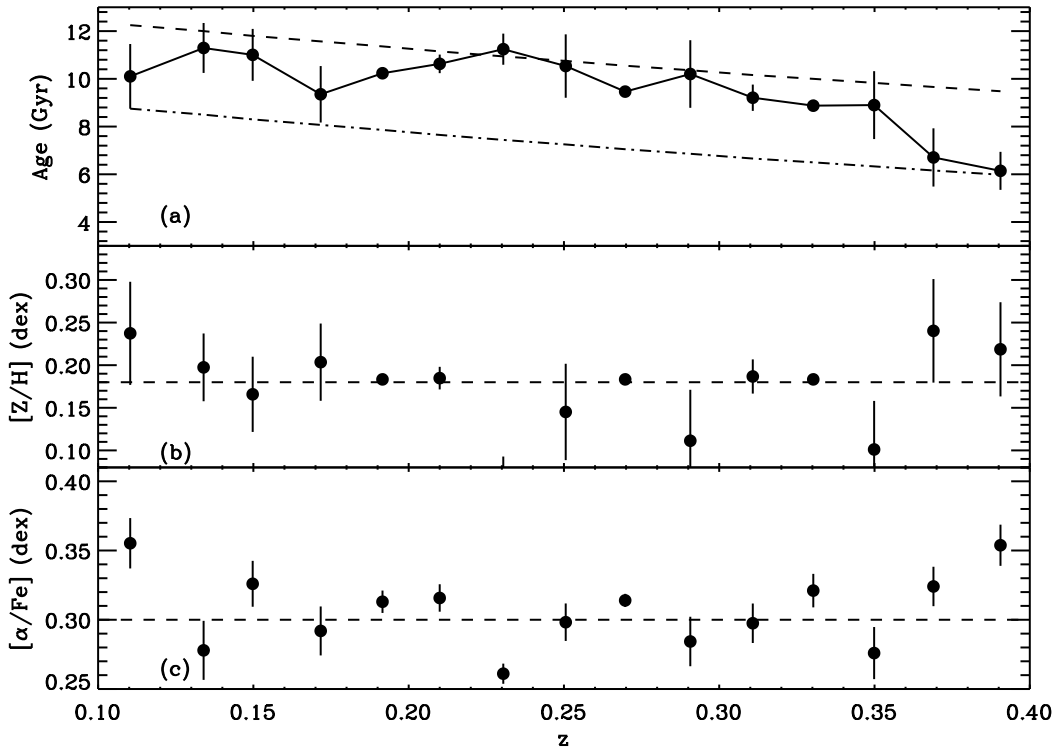

Figure 3.10: The evolution of the derived parameters with redshift when using Hβ, Mg$_b$, Fe5270, Fe5335 of the stacked spectra. Panel (a) shows the age evolution with redshift, low redshift objects are older than the high redshift objects, the dashed line represents the age of the Universe for a flat ΛCDM cosmology, the dot dashed line shows a t_U(z) - 3.5 Gyr showing the age scatter. Panel (b) and (c): show the evolution of metallicity [Z/H] and [α/Fe] with redshift, the straight dashed line shows if these objects follow no chemical evolution since we have selected quiescent objects. However few objects lie on this line due to the significant scatter on the line-strength of Mg$_b$.

etc. Their improvements are basically due to the recently arrival of large and complete stellar libraries. Different codes can give very comparable results (e.g Dias *et al.*, 2010; Koleva *et al.*, 2008; Liu *et al.*, 2013).

3.7.7.1 ULySS

The University of Lyon Spectroscopic analysis Software (ULySS) is a package of full spectral fitting for the study of the stellar populations of galaxies and star clusters. It is written in IDL. The basic idea is to compare an observed spectrum with sets of model spectra in order to derive the characteristics of the stellar population (age, star formation and chemical history) and the internal kinematics of galaxies and star clusters; and to estimate stellar atmospheric

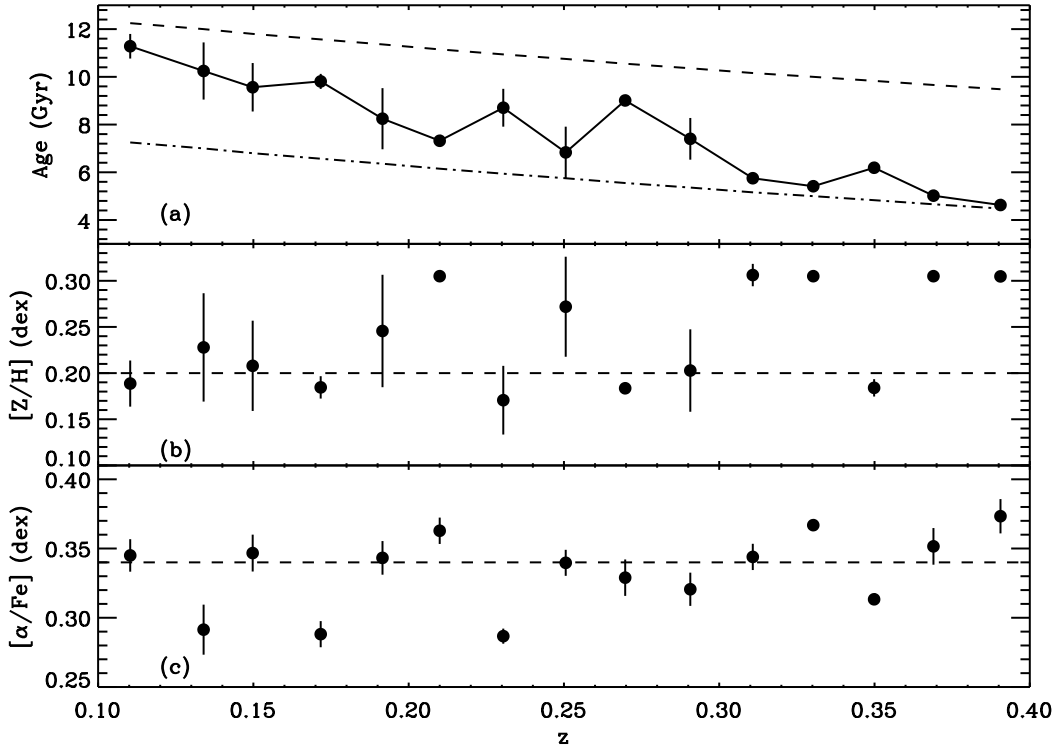

Figure 3.11: The evolution of the derived parameters with redshift when using $H\gamma_F$, Mg_b, Fe5270, Fe5335 of the stacked spectra. Panel (a) shows the age evolution with redshift, low redshift objects are older than the high redshift objects, the dashed line represents the age of the Universe for a flat ΛCDM cosmology, the dot dashed line shows a $t_U(z)$ - 5 Gyr showing the age scatter. Panel (b) and (c): show the evolution of metallicity [Z/H] and [α/Fe] with redshift, the straight dashed line shows if these objects follow no chemical evolution since we have selected quiescent objects. However few objects lie on this line due to the significant scatter on the line-strength of Mg_b.

parameters (effective temperature, surface gravity, metallicity and radial velocity) of stars. It fits not only the strongest absorption features but also all the individual line in the spectrum. ULySS minimizes the χ^2 between the observations and a combination of SSP models, to fit the characteristics of the population and the LOSVD at the same time. Precisely, an observed spectrum is fitted with a model expressed as a linear combination of non linear components convolved with a LOSVD and multiplied by a polynomial at the same time. A component is a non linear function of, for example, age, [Fe/H] and wavelength.

In the case of SSP fit, we represent the observable spectrum as:

$$\mathrm{Obs}(\lambda) = \mathrm{P_n}(\lambda) \times \mathrm{LOSVD}(\mathrm{v_{sys}}, \sigma) \otimes \sum_{\mathrm{i=0}}^{\mathrm{i=m}} \mathrm{W_i SSP_i}(\mathrm{Age}, [\mathrm{Fe/H}], \lambda) \tag{3.21}$$

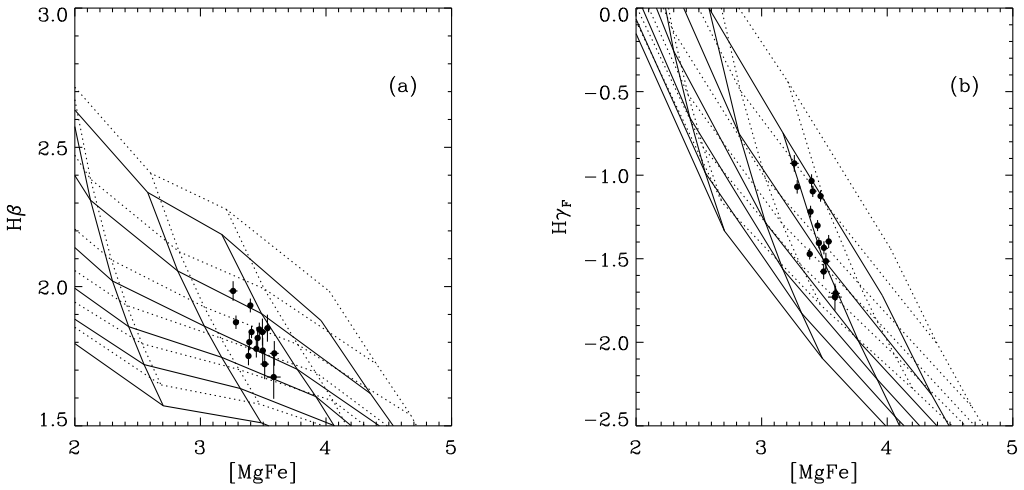

Figure 3.12: Index-index plots. Panel (a) [MgFe]-Hβ index plot, panel (b) [MgFe]-Hγ_F index plot. The grid correspond to the TMJ models with [α/Fe] = 0 (solid lines), and [α/Fe] = 0.3 (dotted lines). From the bottom age lines are 15, 12, 10, 8, 5, 3 Gyr. From right to left, [Z/H]=0.67, 0.35, 0.00, -0.33, -1.35, -2.25. The composite index [MgFe] was calculated as defined in Thomas *et al.* (2003) and the associated errors were calculated using the propagation of error technique. The galaxy indices are plotted in black points. All index measurements are given in Å. All galaxies lie between 0 <[Z/H] < 0.35 space with an [α/Fe] = 0.3, ages show clear evolution (∼5 Gyr) when using Hγ_F index, as confirmed by the χ^2 fitting results.

where W_i are the weights of each of the SSPs. The LOSVD is parametrized by the systemic velocity v_{sys} and the velocity dispersion, σ. The use of multiplicative polynomial P_n of order n makes this method insensitive to the effects of the flux calibration uncertainties and the galactic extinction. From the previous equation, one can see that the multiplicative polynomial is trying to match the SSP models to the observed spectrum. If the spectra are flux calibrated, the shape of the polynomial allows us to evaluate the accuracy of the calibration and also reveals the systematic reddening caused by dust in galaxy, if present. The order of the polynomial was carefully chosen. It does not need to be very low or high to avoid an unsuitable match between the investigated observed spectra and model spectra. The stability of the SSP fitting results as a function of the multiplicative polynomial order was investigated, see section 3.7.7.3. More details of this technique of fitting are found in Koleva *et al.* (2009).

Besides the simple SSP fit, ULySS provides the possibility of exploring and visualizing the parameter space with χ^2 maps, convergence maps and Monte-Carlo simulations. These options help us to study the complex problem of the SSP fitting which is the degeneracy between parameters and the multiple minima in the parameter space. The process of the Monte-Carlo simulations consists of repeating the fit several times by adding a random Gaussian noise to the spectrum defined by the users estimated noise either by the S/N or by an

error spectrum.

χ^2 maps allow to visualize the location of eventual local minima and provide a view of the topology of the parameters space. Maps are generated by choosing a 2D projection of the parameters space (e.g. age and metallicity) and performing an optimization over all the other parameters for each node of these parameters. Any local minimum and degeneracy can be identified on such map.

Convergence maps provide another tool used to explore the parameter space, i.e. to evaluate the convergence region where the solution (the absolute minimum of the χ^2) lies in a grid of guesses. Ideally, the convergence paths should lead to only one point, meaning the solution is stable and independent of the guesses but this is not necessarily the case because of the local minima and degeneracies.

Apart from the above, ULySS has many advantages compared to other full spectral fitting packages. For instance, it uses all the good pixels which are weighted, and minimizes all the parameters at the same time, providing the most significant and almost accurate parameter outputs despite the degeneracies between parameters. Koleva *et al.* (2008) compared the routine STECKMAP (STEllar Content and Kinematics via Maximum a Posteriori) (Ocvirk *et al.*, 2006a,b) with ULySS. STECKAMP is optimized to deliver star-formation history reconstruction and it performs slightly worse when analyzing SSPs. ULySS, on the other side, uses a simple parametrisation method with which it is easy to visualize and understand the parameter space topography. Liu *et al.* (2013) compared fit results from using ULySS and the STARLIGHT codes (Cid Fernandes *et al.*, 2005). The later uses the Simulated Annealing Algorithm and the Metropolis Algorithm of the MCMC method which search for the optimized parametric results in the whole space to minimize the χ^2 value. Despite the fact that both codes can give consistent results, ULySS provides older ages and richer metallicities for LRGs. In addition, stellar population studies of Galactic clusters using ULySS gave similar results to those obtained from the color-magnitude diagrams (Koleva *et al.*, 2008). Analysis of Lick/IDS index system along with full spectral fitting led by Michielsen *et al.* (2007) proved the reliability of this technique as well.

3.7.7.2 Spectral synthesis models used

The ULySS package has incorporated a number of models with different libraries. Additional models are also available on the official website. It is also possible to bring other models with the appropriate format of ULySS. Koleva *et al.* (2008) conducted a study using various models included in the package and found that the Pegase.HR/Elodie 3.1 (PE) and Vazdekis/MILES (VM) models are the most reliable and trustworthy of all models. By fitting the observed galaxies with different SSP models, the goals are to see whether the results are model dependent, and to study the uncertainties on the derived parameters, particularly on ages, and also, if those uncertainties will able us to obtain errors on H(z) within <3 % precision.

A brief description of each SSP models used in this study is described here and summarised in table 3.8.

Pegase/Elodie 3.1 - PE The Pegase-HR code[1] is developed by Le Borgne *et al.* (2004). They compute the synthetic spectral models using the high resolution stellar library ELODIE v3.1 (Prugniel *et al.*, 2007), which has a spectral resolution of 0.55Å (FWHM) and a wavelength coverage of 3900 - 6800Å. The evolutionary tracks of the isochrones are taken from the Padova group *Padova 1994* (Bertelli *et al.*, 1994). They computed SSP models with Salpeter IMF (Salpeter, 1955) with mass from 0.1 to 120 $M_{\odot}$ and a slope of -1.35. The PE models cover age from 0.01 to 20 Gyr and [Fe/H] from -2.30 to 0.70 dex, consisting of 68 number of ages and 7 metallicities which is 476 SSPs in total. These models include a treatment of TP-AGB stars different from the Maraston (2005). They were generated entirely in a different fashion that Maraston's models. In particular, a global interpolator was used to generate spectra at the gaps of the parameter space. Note that the stellar library used in PEGASE models is a product of an echelle spectrograph, meaning that the connections of the different multiplicative polynomial orders can never be perfect .

Vazdekis/Miles - VM Vazdekis models are based on the models developed by Vazdekis *et al.* (2010) (advanced version of the previous models from Vazdekis (1999) and Vazdekis *et al.* (2003)) and the MILES library Sánchez-Blázquez *et al.* (2006), which has a resolution of 2.3Å (FWHM) and 3525 - 7500 *Å* wavelength range. The stellar library is believed to be the best existing flux calibrated library up-to-date. These models use the Padova 2000 isochrones (Girardi *et al.*, 2000) which has hotter red giant branch stars. The SSP models are computed with Salpeter IMF (Salpeter, 1955) with mass from 0.1 to 100 $M_{\odot}$ and a slope of -1.35. VM models cover age from 0.1 to 17.7 Gyr and [Fe/H] from -2.32 to 0.22 dex, consisting of 343 SSPs in total (49 number of ages and 7 metallicities). These models take into account the TP-AGB coverage and envelope ejection, but no corrections have been made on the latest phases of the stellar evolution.

Galaxev/STELIB - BC03 These synthesis population models are the most widely used models. The Galaxev models (Bruzual & Charlot, 2003) are built using the STELIB library (Le Borgne *et al.*, 2003), which has a resolution about 3Å FWHM across the whole spectral range 3200 - 9500 Å, and *Padova 1994* isochrones. Actually, three sets of isochrones have been used to recover all phases between zero age main sequence and the beginning of the TP-AGB: Padova 1994, Padova 2000 and Geneva (Charbonnel *et al.*, 1996, 1999; Schaller *et al.*, 1992) evolutionary tracks. This is because the Padova 1994 recovers well the low metallicities from 0.0001 to 0.10 while the Padova 2000 library represents the low and intermediate mass stars and the third library is only for computing the solar metallicity. The overshooting was

[1] http://www2.iap.fr/pegase/pegasehr/

taken into account to better predict the observations of galactic stars, RGB and the HB of globular clusters. However, the post-AGB and the TP-AGB phases for low and intermediate mass stars were replaced with those by Vassiliadis & Wood (1994). The authors of the models found that the Padova 2000 would overpredict old ages for elliptical galaxies, due to the fact that red giant branch is 50-200 K warmer in Padova 2000, hence they officially chose the Padova 1994 as their standard model of isochrones.

The STELIB library contains 249 stellar spectra, but only 187 of them have associated measured metallicity and only these can be used to compute the predicted SSPs. The SSP models are computed with Chabrier IMF (Chabrier, 2003) with a mass of 0.1 to 100 $M_{\odot}$ and have a slope of -1.35. BC03 models cover age from 0.1 to 20 Gyr and [Fe/H] from -2.3 to 0.4 dex, consisting of 696 SSPs (116 number of ages and 6 metallicities).

Maraston & Strömbäck/MILES - M11 Maraston & Strömbäck (2011) have recently updated their stellar population models into higher spectral resolution ones. They computed models based on four different stellar libraries: Pickles, ELODIE, STELIB and MILES. Apart from the resolution, these new models are pretty much the same as the previous version (Maraston, 2005). They kept the same ingredients as the stellar energetics, the atmospheric parameters and the treatment of the TP-AGB and the horizontal branch morphology.

On the one hand, it would be good to compare SSP estimate results from both techniques of age-dating even though Maraston & Strömbäck (2011) have compared the Lick indices calculated on their MILES based integrated model SEDs and those from Thomas *et al.* (2011). On the other hand, TMJ models of Thomas *et al.* (2011) are based on the majority of the ingredients of the M11 models, in particular the use of the stellar evolutionary tracks from Cassisi *et al.* (1997). We also chose the SSP models based on MILES library and computed using Salpeter isochrone for comparison. In these models, they added few high-resolution of cool stars from MARCS library (Gustafsson *et al.*, 2008) for completeness. Note that this library contains theoretical stars with a wide range of cool stars (2500 - 8000 K) at very high resolution (R = 20 000) over a wavelength range 1300 - 200 000Å. In addition, the chemical composition of these spectra follow the general trend of the Milky way stars as any empirical libraries (i.e. having the α-elements [α/Fe] = 0.1-0.3 and metallicity $-0.25 < [\mathrm{Fe/H}] < -1.0$). Moreover, optical colours of stars in MARCS library also match those based on empirical stars. According to Maraston & Strömbäck (2011), the inclusion of these cool stars did not affect the shape of the empirical spectral more precisely around the V band. They also mentioned that there is fairly poor sampling of stellar parameter space at the lowest metallicity. Therefore, we were forced to further reduce the range of parameters to conform with ULySS format. The flux units were changed to be 10^{-7} $L_{\odot}/M_{\odot}/$Å (where $L_{\odot} = 3.82610^{33}$erg/s and $M_{\odot} = 1.98910^{33}$g). At the subsolar metallicity, the intermediate-red was chosen to be the horizontal branch morphology. The final template grids have a wavelength range of 3525 - 7500 Å with a resolution of 2.5Å (FWHM). The M11 models

cover age from only 2 to 15 Gyr and [Fe/H] from -1.30 to 0.30 dex (14 number of ages and 4 metallicities).

In order to test the new grids of M11 models, the SSP parameters of the open cluster M67 were derived and compared with results from the other models in the package. The M67 long slit spectrum (Schiavon *et al.*, 2004) is already included in the package. This spectrum is assembled from spectra of individual stars in the clusters. Schiavon *et al.* (2004) obtained a spectroscopic age of 3.5±0.5 Gyr (at solar metallicity [Fe/H] = 0.00 dex) for this cluster using spectrophotometric indices, which is consistent with the age derived from fitting isochrones to the colour-magnitude diagram of the cluster. However, Leaman (2012) derived the intrinsic metallicity spreads of this cluster, which is about [Fe/H] = -0.19.

After matching the instrumental resolution of the observed spectrum and the model, we obtain the SSP equivalent characteristics: age and metallicity from each model fit of M67 which are listed in table 3.9. Age and metallicity values estimated by each model, including M11, are fairly consistent with the age and metallicity predicted by Schiavon *et al.* (2004) and Leaman (2012) respectively. However, BC03 models overestimate the age by almost a factor of 2 although it is still in the range of ages found in the literature for M67. This implies that our new SSP grids built from the SSP spectra of Maraston & Strömbäck (2011) can be used to age-date our LRG sample.

Table 3.8: List of models used with UlySS

Models	Library	FWHM (Å)	Wavelength (Å	Age (Gyr)	[Fe/H] (dex)	IMF	Isochrones
PE	Elodie	0.55	3900 - 6800	0.01 - 20	-2.30 - 0.70	Salpeter	Padova 1994
VM	Miles	2.3	3525 - 7500	0.1 - 17.7	-2.32 - 0.22	Salpeter	Padova 2000
BC03	Stelib	3	3200 - 9500	0.1 - 20	-2.30 - 0.40	Chabrier	Padova 1994
M11	Miles	2.5	3525 - 7500	2 - 15	-1.30 - 0.30	Salpeter	Cassisi

Note that all models used in this analysis have not included the α-enhancements into the algorithm used to build them. In case [α/Fe] was taken into account, and in return it is estimated together with all parameters (age and [Fe/H]), [α/Fe] would not dramatically affect the outputs values of age and metallicity too much. Prugniel and collaborators (2011) have released few stellar population models with variable chemical composition. They measured [α/Fe] of the spectra in the library and compared to the theoretical grid. The library was then corrected to some given values of [α/Fe] using differential effects computed in the theoretical library. After creating interpolators for these corrected libraries which are in the form of functions generating a spectrum for a given T_{eff}, log g and [Fe/H], model predictions at the chosen [α/Fe] were then built. These new models will be necessary later on, for the purpose of comparing SSP results derived from using Lick absorption indices with those from using

full spectrum fitting .

Table 3.9: SSP parameters of M67

Models	Age (Gyr)	Metallicity (dex)	χ^2
PE	3.90±0.06	-0.108±0.004	0.97
VM	3.20±0.03	-0.063±0.005	0.65
BC03	5.57±0.09	-0.232±0.005	2.39
M11	4.13±0.07	-0.105±0.003	0.71

3.7.7.3 Methods of fitting

As mentioned in section 3.5.2, the co-added spectra are made from the clean absorption line spectra free from emission line contamination. The cleaned spectra were obtained during the process of subtraction of emission line spectra from the observed ones with GANDALF routine. The latter can also perform foreground galactic extinction correction which is very important before the fitting. It simply requires the Schlegel *et al.* (1998) E(B − V) reddening value. For each galaxy, E(B − V) parameter is calculated as in chapter 4 section 4.4.4 in order to perform the correction.

Briefly, the following corrections were applied to the individual galaxy spectrum within each redshift bin prior to the stacking process:

- de-reddening for Galactic extinction following the model of Calzetti *et al.* (2000) and using the E(B − V) reddening value of Schlegel *et al.* (1998)
- emission line correction
- all spectra were brought to the rest-frame wavelength and to a common wavelength range.

The co-added spectra were then fitted by ULySS using the different models listed above. For comparison between the physical properties derived from fitting the co-added spectra and from fitting all spectra of the galaxies, we also performed individual fitting of all galaxies within the redshift bin. After the appropriate corrections were applied, individual galaxy spectrum was fitted with the four models.

LSF matching The first step on the fitting procedure is to match the resolutions between the observed spectra and models. The spectral resolution is characterized by the instrumental broadening or the Line Spread Function (LSF). The LSF for spectra is equivalent to the Point Spread Function (PSF) for images. The LSF varies with wavelength (Koleva *et al.*, 2009),

depending on the spectrograph, on the slit and on the position in the field for 2 or 3D spectra. In addition, the LSF is not necessary a gaussian. Most importantly, the models which are used to analyse the observed spectra have a finite resolution, i.e. frequently have a specific LSF finer than the one of the observation. Therefore to analyse an observed spectrum we have to take into account the relative LSF of the observation with respect to the models. The LSF is very important and necessary when studying the internal kinematics or precisely the physical broadening of the lines. Matching spectral resolution by ULySS consists of determining the relative LSF between the model and the observation and then injecting this relative LSF into the model. It could be determined using calibration observations such as arc lamp, standard star, twilight spectrum and a spectrum of a star of known atmospheric parameters. In case it is unknown these parameters can firstly be determined with ULySS. Alternatively, if no stellar spectrum is available, a galaxy spectrum can be used to analyse the LSF, therefore the internal kinematics of all objects in the sample can be determined relative to this reference.

As in Koleva *et al.* (2009), we used the SDSS template stars from M67 which is already part of the package. It was determined using wavelength intervals of 600 Å spaced by 300 Å by fitting it with each model, then injected to each one of them to generate the resolution-matched models by a certain convolution function. From now on, the resolution-matched models were always used for SSP fitting.

Fitting conditions The fitting was performed in the whole wavelength coverage of the co-added and individual spectra for VM, BC03 and M11 models, whereas it was restricted to be in the range of 4000 - 5500 Å for PE models since it is the only model whose wavelength range are less than SDSS wavelength range. Many prominent absorption features are still included in the chosen wavelength range. Even though some important spectral features are missing to accurately determine the age and [Fe/H], they are still useful to constrain the best fit parameters. The choice of this wavelength range was determined by investigating the quality of the fit of the observed spectra with models while changing the limit of the wavelength. It is important to note the problem with the flux calibration of the ELODIE library used by the PE models at the blue end of the spectra. Therefore, the extreme blue end was also not used during the spectral fitting. When we used that blue end of the spectra, including H & K lines, the quality of the fit decreased and the results were biased by $\sim$4 Gyr toward older ages. In addition, both models and observations (especially when the number of spectra to be stacked is small, it is also valid for the individual spectra) have low S/N in this region of the spectrum. Moreover, the exclusion of the H & K lines is also due to the general lack of cold dwarf stars in the models as it has been excluded by a number of studies (e.g Koleva *et al.*, 2008). When the blue end was fixed and the red end varied, the same bias was found until the wavelength limit of 5500 Å was set where the parameter values became stable. Furthermore, the region bluewards of 6800 Å is the region where a lot of telluric lines

are found in both of the observed and model spectra.

We set some priors on the allowed ages and metallicities of the model spectra. The upper age limit was set to be the age of the Universe at each redshift. However we relaxed the lower limit to be at 1 Gyr for PE, VM, and BC03 models, and 2 Gyr for M11 models because of the lack of model grids beyond this value for these specific models. The initial guess was set to be 8 Gyr since LRGs are expected to be old. Regarding the metallicity, the initial guess was set to be 0.1 dex consistent with the metallicity of LRGs found in many literatures (e.g. Liu *et al.*, 2012, 2013; Zhang *et al.*, 2012). The metallicity of LRGs were found to be similar, meaning no evolution with redshift, and its values are found between 0.1 dex and 0.2 dex (Carson & Nichol, 2010; Jimenez *et al.*, 2003; Liu *et al.*, 2012; Zhang *et al.*, 2012). We also set a limit on the allowed metallicity from 0.0 dex to 0.2 dex. These priors and initial guesses on ages and metallicities were set to be the same for either co-added spectra fitting or individual fitting.

The order of the multiplicative polynomial P_n which is used to adjust the shape of the continuum, can be set freely by the user of ULySS. In order to achieve reasonable and stable output parameter values, we carried out a study of the variation of the fit results, literally looking closely at the χ^2 variation with increasing the order n. A very high S/N spectrum was chosen from the sample of galaxies in the redshift bin of $0.24 < z < 0.26$ and fitted with all the models. Figure 3.13 represents the variation of the χ^2 values resulting from each fit while increasing the order of the multiplicative polynomial. The χ^2 values are normalized to the χ^2 value for n = 30 for each model. The plot shows that the χ^2 values do not really increase for n greater than ∼12 and almost stay flat after this value. Therefore, there is no need to go greater than the order 12 and lesser than the default order of ULySS package which is 10. An order around ∼12 was chosen for all galaxy fits in this analysis.

The outliers, telluric lines and possible spikes or undesirables features (e.g. residuals from the sky lines removal) in the galaxy spectrum were rejected from the fit by specifying the cleaning algorithm.

3.7.7.4 Comparing the different fits

Figure 3.14 illustrates the PE, VM, BC03 and M11 fits of the stacked spectrum at $0.24 < z < 0.26$. This is only an example of the fits, but all fits using the four models are presented in appendix B. A detailed comparison is shown in figure 3.15. Again the metallicity range of the comparisons was at the solar metallicity to super-solar metallicity i.e $0.0 < [Fe/H] < 0.20$, while the age range for comparison was restricted to ages between 2 Gyr and the age of the Universe depending on the redshift. The regions of the strong telluric lines, the CN band, NaD band, any possible spikes and the outliers were masked. The main wavelength range and the residuals are plotted together.

Looking only at the general fits, one can notice some inconsistencies between observed spectra and models although both the fit is fairly good. The rms residuals in the whole

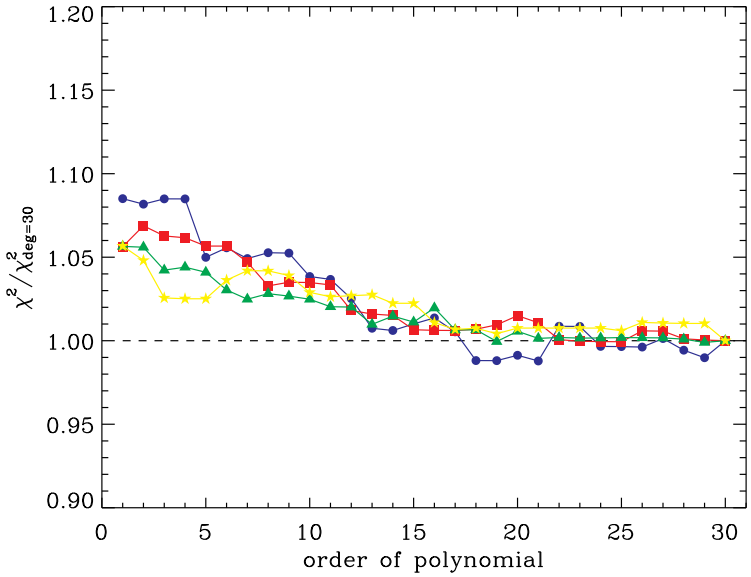

Figure 3.13: The χ^2 value as a function of the order of the multiplicative polynomial used for adjusting the shape of the spectra. The χ^2 values are normalized to the χ^2 value using an order 30. The χ^2 values are from fitting a high S/N spectrum at $0.24 < z < 0.26$ with PE models (red squares), VM models (green triangles), BC models (blue circles), and M11 models (yellow stars). The normalized χ^2 values become stable at an order of polynomial around ~ 12.

wavelength range are between 0.02 - 0.04. PE models give the lowest rms residuals. The wavelength restriction of the fitting with such models might explain this situation.

At first glance, all models, with exception of PE models, fail to fit perfectly the regions around 6300 - 7000 Å and around the sky absorption line 5100 Å which is the region of Mg triplet (but BC03 is the worst in that region), at CN band near 4160 Å and at 6900Å. The Mg triplet are found to be deeper in the observations than in the best-fit models for high metallicity objects (the case of the LRGs). The different α- enhancement of the ellipticals with respect to the abundance pattern of the library provides an explanation for that. At high metallicity, almost all stellar libraries are scaled-solar. It seems that using a semi-empirical library can improve the fit and determine the enhancement as shown in Prugniel *et al.* (2007), but with M11 models which used a semi-empirical library, the mismatch is still visible. This is not surprising, since they added low metallicity theoretical library on their library. Furthermore, the flux of the MILES library is also found to drop around ∼6000 Å (Maraston & Strömbäck, 2011). In all the fits, the listed regions were masked automatically from the fits and considered as some outliers.

More examination of the residuals leads to the mismatch around the Fe4668 band, using all models. The origin of this is either in the models or in the observations. A possible explanation could be from the process of stacking or from the model ingredients such as

evolutionary tracks, IMF etc.

Comparing BC03 with PE and VM models, Koleva *et al.* (2008) found systematics biases between BC03 and the other two models. The reasons for the above discrepancies might also be due to the poor metallicity coverage of the stellar library STELIB used by the models. They overestimate the metallicity of their models for [Fe/H] > 0 dex and underestimate the metallicity of their models for -1 $<$ [Fe/H] < 0. The stellar library is strongly concentrated at solar metallicity, therefore they are not reliable for galaxies whose metallicities are outside the solar metallicity. For the purpose of this study, however, we believe they are adequate. In addition, some systematics were also found in the wavelength calibration of STELIB library with respect to ELODIE and MILES libraries (Koleva *et al.*, 2008). However, PE and VM were found to have consistent results since ELODIE and MILES libraries which are respectively used by the models, have comparable coverage in the parameter spaces. The MILES library is also used by M11 models, providing no large inconsistencies compared to the other models in the fitting. In the next section, we compare in detail the derived SSP parameters from each model.

3.7.7.5 SSP parameter results

In this section, we present the SSP parameter results from the spectral fitting of the stacked spectra using PE, VM, BC03 and M11 models. Furthermore, the average parameters from the individual fits are also given.

The results of the combined and individual fits are presented in table 3.10, 3.11, 3.22 and 3.13 from using PE, VM, BC03 and M11 models respectively. The average parameters from the individual fits were calculated using the weighted mean; and the weights were calculated from the errors on the parameters. The corresponding errors are the uncertainties of the weighted mean. Parameters with zero errors had their weights set to zero. In general, parameter values from both fits are reasonably consistent (some details on that are discussed later in the next paragraph) without considering the strength of the error bars. When it is taken into account, these error bars on the averaged parameters indicate a large spread in the derived parameters from individual spectra. This is not surprising since the final sample includes galaxies with velocity dispersions ranging from 200 km s^{-1} to 400 km s^{-1} in the same redshift bin. Even though they are in the same redshift bin, the line measurements and the derived parameters (ages and metallicities) should be different as seen in different figures of section 3.8.3.

The error on each parameter from the stacked spectra fitting is supposed to be the 1-σ errors computed from the covariance matrix in the MPFIT[1] function used by ULySS. These errors are very tiny since many galaxy spectra were combined to produce the stacked spectra and the errors on the spectra became smaller. Therefore the "perror" (parameter

[1] http://cow.physics.wisc.edu/ craigm/idl/idl.html

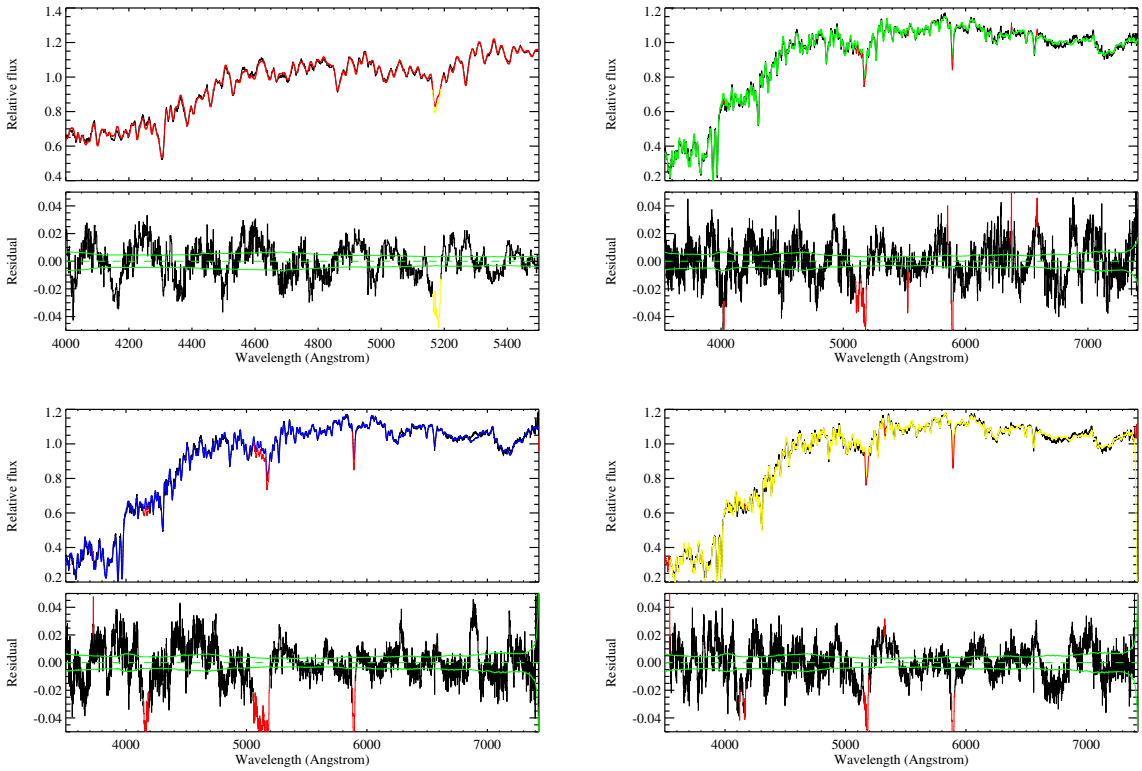

Figure 3.14: Fitting stacked spectra with PE (red), VM (green), BC03 (blue) and M11 (yellow) models. All upper panels of each subfigure display the stacked spectra at $0.24 < z < 0.26$ (black lines) and the best fit models (coloured spectra). All bottom panels show the residual from the fits, the solid green lines are the 1σ deviation and the dashed green lines represent zero residuals. Red and yellow (in the first plot) regions were rejected from the fits. They were masked due to the telluric lines, the interstellar absorption line (NaD), and automatic rejection of outliers.

errors returned by MPFIT) were no longer presented as the true parameter errors. Instead of "perror" , the "pcerror" was rather used in order to increase the uncertainties on each parameter. The "pcerror" was calculated as the product of the χ^2 value to the "perror", i.e the estimated parameter uncertainties were computed by scaling "perror" by the measured χ^2 value. We assumed that all fits were good quality assuming large χ^2 values (> 1), meaning small spectral errors, and that gives validity to this approach.

Figure 3.13 presents the χ^2 values of the stacked spectra fitting at each redshift. The χ^2 values depend on the number of combined galaxies. At low redshift $z < 0.20$ the number is small and the χ^2 values from each fit using the four models are fairly similar, while at high redshift $z > 0.20$ the number of galaxies is increasing, meaning small spectral error. The χ^2 values are dramatically increasing with the number of spectra at each redshift bin. Basically the χ^2 should be normalized to the error in the spectra, thus it should be constant independent of the number of spectra. But the more spectra we combine the smaller the

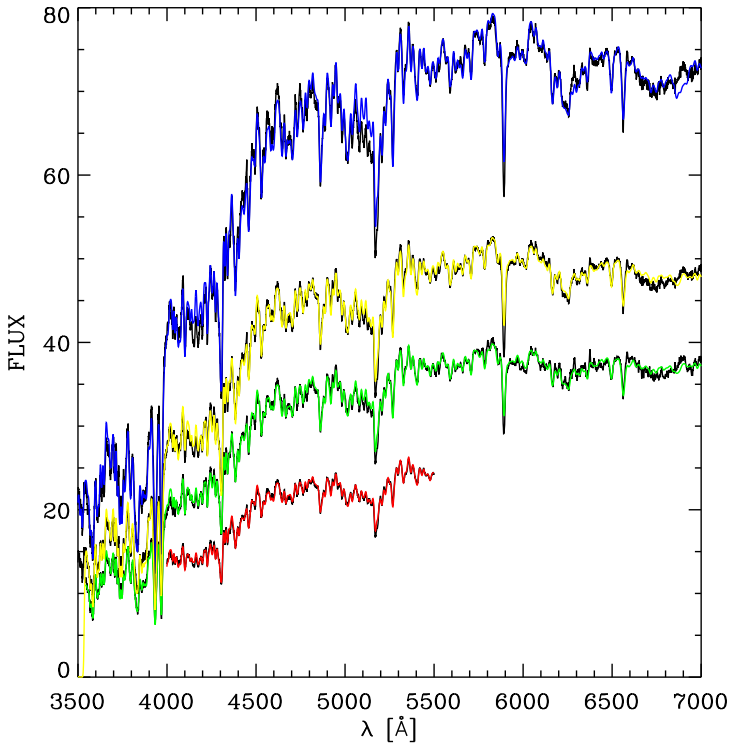

Figure 3.15: Comparison of the each fitting of a stacked spectrum at $0.24 < z < 0.26$ using PE models (Red), VM models (green), BC03 models (blue) and M11 models (yellow). The vertical scale is magnified by a factor of 20.

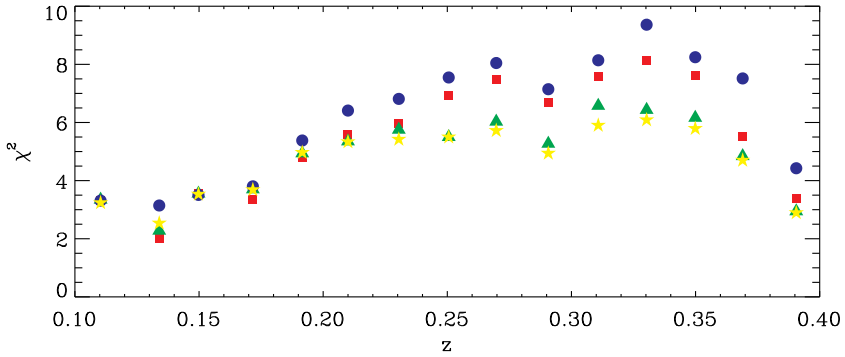

Figure 3.16: The χ^2 value of each stacked spectra fitting at each redshift. The fits were performed using PE models (red squares), VM models (green triangles), BC03 models (blue circles) and M11 models (yellow stars).

error becomes, therefore it varies with the level of spectral error.

BC03 models were always found here to give large χ^2 values compared to the other models, but not so large that the difference is not reflected on the distribution of the χ^2 values (figure

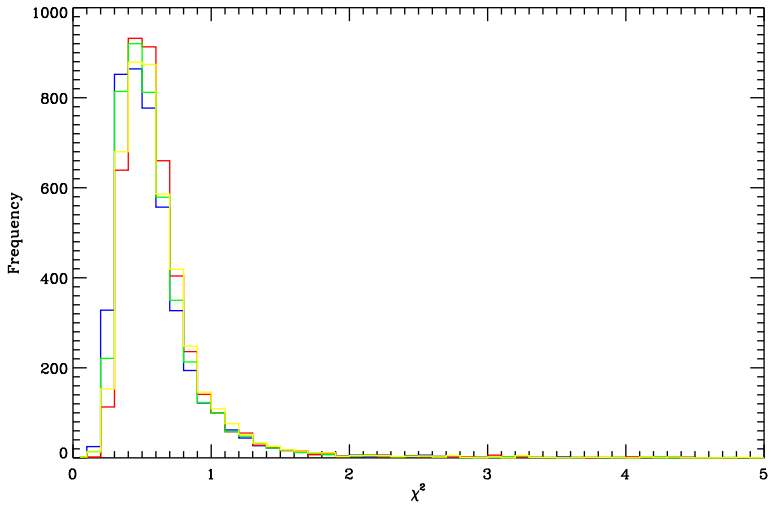

Figure 3.17: The χ^2 histogram from the individual fits. The fits were performed using PE models (red), VM models (green), BC03 models (blue) and M11 models (yellow).

3.17). This is also proved while fitting the cluster M67, see results in table 3.9. It is then difficult to identify which model fits better the sample. Normally, the models that can give the minimum χ^2 value should be the ideal. However, in our situation, each model has its pros and cons. M11 and VM models give us the lowest values of χ^2, meaning that models which used MILES library fit better the passively evolving galaxy. One would say the M11 models represent the best models since they provide the lowest χ^2 values of both models. However not only are SSP equivalent ages from these models reasonably flat with redshift, but they also do not fit properly the whole sample: a small fraction was fitted compared to the other models. Our main concern in this analysis is to find models which can give us a good age-redshift relation in order to calculate $H(z)$ accurately. Therefore, the χ^2 values from the fits are not the only consideration.

When performing individual fitting, almost all χ^2 values from each fit are found to be less than 1, as shown in figure 3.17. The tail found in the χ^2 histogram represents the χ^2 values of the galaxies whose ages hit the upper limits (age of the Universe as a function of their redshift). Their age values can be seen in the age-redshift plots in figure 3.28, 3.29, 3.30 and 3.31. Several reasons cause this situation: for instance low S/N, spectral resolution, quality of the observed spectra and the models, and the accuracy of the models etc.

When looking at each SSP parameter closely, the age and metallicity values extracted from the stacked spectra and the mean values from the individual fitting are quite similar in general. The metallicity values are found to spread between $0.08 < [\mathrm{Fe/H}] < 0.20$ dex and have an overall average of 0.13 dex. This justifies that LRGs are found to have similar metallicity and their values are found to be above solar as in many studies (Jimenez *et al.*, 2003; Liu *et al.*, 2012; Zhang *et al.*, 2012). They do not show any chemical evolution with

Table 3.10: SSP parameter results using stacked spectra and mean parameters using individual fitting. Spectral fitting using PE models

	Stacked spectra			Individual spectra		
Redshift	**Age** (**Gyr**)	[**Fe/H**] (**dex**)	σ (**km s^{-1}**)	$<$ **Age** $>$ (**Gyr**)	$<$ [**Fe/H**] $>$ (**dex**)	$<\sigma>$ (**km s^{-1}**)
$0.10 < z < 0.12$	6.34 ± 0.10	0.12 ± 0.01	291.95 ± 2.93	6.27 ± 0.46	0.12 ± 0.06	289.29 ± 37.44
$0.12 < z < 0.14$	6.56 ± 0.12	0.10 ± 0.00	279.15 ± 3.29	6.23 ± 0.75	0.13 ± 0.06	272.10 ± 38.41
$0.14 < z < 0.16$	5.99 ± 0.11	0.10 ± 0.00	275.00 ± 2.80	5.70 ± 1.43	0.09 ± 0.06	266.66 ± 28.20
$0.16 < z < 0.18$	6.18 ± 0.09	0.10 ± 0.00	279.86 ± 2.52	6.43 ± 1.34	0.09 ± 0.05	272.31 ± 27.73
$0.18 < z < 0.20$	5.93 ± 0.12	0.10 ± 0.00	282.14 ± 2.61	5.54 ± 1.69	0.09 ± 0.06	269.92 ± 31.66
$0.20 < z < 0.22$	5.74 ± 0.22	0.06 ± 0.01	279.03 ± 3.00	5.75 ± 1.53	0.09 ± 0.06	270.16 ± 36.00
$0.22 < z < 0.24$	5.93 ± 0.11	0.10 ± 0.00	287.53 ± 2.41	6.19 ± 1.70	0.08 ± 0.05	272.65 ± 31.72
$0.24 < z < 0.26$	5.17 ± 0.19	0.10 ± 0.00	291.40 ± 2.68	5.85 ± 1.50	0.08 ± 0.06	279.27 ± 34.70
$0.26 < z < 0.28$	5.51 ± 0.17	0.10 ± 0.00	290.24 ± 2.50	4.68 ± 2.06	0.08 ± 0.06	275.32 ± 33.73
$0.28 < z < 0.30$	4.97 ± 0.14	0.10 ± 0.00	285.22 ± 2.52	5.50 ± 1.62	0.08 ± 0.06	272.38 ± 32.67
$0.30 < z < 0.32$	4.92 ± 0.16	0.10 ± 0.00	287.49 ± 2.48	4.75 ± 1.68	0.09 ± 0.06	273.29 ± 36.37
$0.32 < z < 0.34$	4.71 ± 0.14	0.10 ± 0.00	292.45 ± 2.46	4.20 ± 1.63	0.10 ± 0.06	275.97 ± 39.38
$0.34 < z < 0.36$	4.84 ± 0.14	0.10 ± 0.00	291.56 ± 2.60	3.94 ± 1.57	0.09 ± 0.06	271.13 ± 40.92
$0.36 < z < 0.38$	4.69 ± 0.14	0.10 ± 0.00	291.73 ± 2.56	3.70 ± 1.42	0.09 ± 0.06	271.63 ± 40.63
$0.38 < z < 0.40$	4.28 ± 0.21	0.10 ± 0.00	294.22 ± 2.89	3.45 ± 1.20	0.11 ± 0.06	275.97 ± 44.04

Table 3.11: SSP parameter results using stacked spectra and mean parameters using individual fitting. Spectral fitting using VM models

	Stacked spectra			Individual spectra		
Redshift	**Age** (**Gyr**)	[**Fe/H**] (**dex**)	σ (**km s^{-1}**)	$<$ **Age** $>$ (**Gyr**)	$<$ [**Fe/H**] $>$ (**dex**)	$<\sigma>$ (**km s^{-1}**)
$0.10 < z < 0.12$	7.05 ± 0.24	0.15 ± 0.01	301.36 ± 2.49	7.66 ± 1.97	0.17 ± 0.03	293.86 ± 38.77
$0.12 < z < 0.14$	6.89 ± 0.29	0.14 ± 0.01	284.62 ± 3.08	7.19 ± 2.08	0.18 ± 0.04	275.65 ± 42.61
$0.14 < z < 0.16$	6.02 ± 0.15	0.15 ± 0.01	280.34 ± 2.43	6.33 ± 2.75	0.15 ± 0.05	268.92 ± 30.23
$0.16 < z < 0.18$	6.78 ± 0.43	0.10 ± 0.01	282.78 ± 2.21	8.09 ± 2.09	0.15 ± 0.05	276.79 ± 29.08
$0.18 < z < 0.20$	6.29 ± 0.36	0.10 ± 0.01	289.36 ± 2.28	7.28 ± 1.88	0.16 ± 0.05	276.88 ± 31.59
$0.20 < z < 0.22$	5.77 ± 0.13	0.15 ± 0.01	283.74 ± 2.33	5.06 ± 2.42	0.16 ± 0.04	276.28 ± 33.66
$0.22 < z < 0.24$	5.91 ± 0.13	0.14 ± 0.01	287.44 ± 2.08	6.21 ± 1.98	0.15 ± 0.05	278.96 ± 32.24
$0.24 < z < 0.26$	5.77 ± 0.12	0.14 ± 0.01	288.18 ± 2.02	5.70 ± 1.68	0.16 ± 0.05	284.27 ± 35.54
$0.26 < z < 0.28$	5.59 ± 0.10	0.15 ± 0.01	289.54 ± 2.01	4.83 ± 2.01	0.16 ± 0.04	281.26 ± 35.59
$0.28 < z < 0.30$	5.45 ± 0.09	0.14 ± 0.01	286.29 ± 1.95	5.20 ± 1.56	0.15 ± 0.05	276.23 ± 32.91
$0.30 < z < 0.32$	5.19 ± 0.11	0.18 ± 0.01	293.58 ± 2.01	4.65 ± 1.52	0.15 ± 0.05	277.89 ± 37.05
$0.32 < z < 0.34$	4.99 ± 0.18	0.18 ± 0.01	293.18 ± 1.92	4.39 ± 1.59	0.15 ± 0.06	280.66 ± 39.70
$0.34 < z < 0.36$	4.02 ± 0.09	0.19 ± 0.01	296.99 ± 2.07	4.15 ± 1.48	0.13 ± 0.06	274.22 ± 42.02
$0.36 < z < 0.38$	3.91 ± 0.09	0.18 ± 0.01	304.42 ± 2.18	3.80 ± 1.31	0.14 ± 0.06	276.20 ± 39.18
$0.38 < z < 0.40$	3.79 ± 0.10	0.19 ± 0.01	305.52 ± 2.47	3.69 ± 1.24	0.15 ± 0.06	279.81 ± 41.96

redshift, and are very flat in mostly all the models used in this analysis, unless few objects are used for the stacking or for fitting in the given redshift bin. The SSP equivalent ages from both fittings clearly show the age evolution with redshift or age-redshift relationship. Low redshift objects are older than high redshift objects.

The mean velocity dispersions from the individual fits are less than velocity dispersions from the stacked spectra, and are valid for all models. The possible systematic differences between the two values are from the different methods used for their derivation. Apparently, it is fairly noticeable, especially using the stacked fitting, that only VM and M11 models

Table 3.12: SSP parameter results using stacked spectra and mean parameters using individual fitting. Spectral fitting using BC03 models

	Stacked spectra			Individual spectra		
Redshift	**Age (Gyr)**	**[Fe/H] (dex)**	σ **(km s^{-1})**	**< Age > (Gyr)**	**< [Fe/H] > (dex)**	**< σ > (km s^{-1})**
0.10 < z < 0.12	6.12 ± 0.20	0.17 ± 0.00	284.46 ± 2.53	8.23 ± 1.65	0.15 ± 0.03	281.66 ± 37.17
0.12 < z < 0.14	6.75 ± 0.28	0.15 ± 0.01	269.99 ± 3.68	6.57 ± 1.68	0.11 ± 0.03	260.88 ± 42.12
0.14 < z < 0.16	5.68 ± 0.14	0.15 ± 0.00	262.65 ± 2.53	6.14 ± 2.30	0.15 ± 0.04	254.32 ± 29.78
0.16 < z < 0.18	6.70 ± 0.19	0.15 ± 0.01	264.07 ± 2.40	6.49 ± 2.37	0.17 ± 0.03	262.80 ± 29.70
0.18 < z < 0.20	7.22 ± 0.25	0.14 ± 0.01	271.51 ± 2.48	6.73 ± 1.96	0.16 ± 0.03	264.57 ± 31.75
0.20 < z < 0.22	5.25 ± 0.14	0.15 ± 0.01	262.39 ± 2.71	4.81 ± 2.65	0.18 ± 0.03	260.94 ± 32.41
0.22 < z < 0.24	5.30 ± 0.12	0.15 ± 0.01	268.37 ± 2.40	5.64 ± 1.93	0.17 ± 0.03	265.16 ± 32.52
0.24 < z < 0.26	4.94 ± 0.10	0.16 ± 0.01	272.19 ± 2.42	5.56 ± 1.79	0.17 ± 0.03	270.78 ± 35.25
0.26 < z < 0.28	4.92 ± 0.09	0.16 ± 0.01	269.52 ± 2.37	5.10 ± 2.20	0.18 ± 0.03	266.73 ± 35.03
0.28 < z < 0.30	4.84 ± 0.08	0.14 ± 0.01	263.88 ± 2.36	5.03 ± 1.72	0.18 ± 0.04	262.77 ± 32.61
0.30 < z < 0.32	4.47 ± 0.08	0.16 ± 0.01	271.23 ± 2.33	4.35 ± 1.82	0.17 ± 0.04	265.05 ± 36.53
0.32 < z < 0.34	4.38 ± 0.07	0.16 ± 0.01	272.04 ± 2.41	4.39 ± 1.59	0.17 ± 0.04	266.58 ± 38.92
0.34 < z < 0.36	4.09 ± 0.08	0.18 ± 0.01	268.23 ± 2.47	3.97 ± 1.34	0.17 ± 0.04	260.35 ± 40.53
0.36 < z < 0.38	3.87 ± 0.14	0.18 ± 0.01	274.51 ± 2.70	3.56 ± 1.25	0.17 ± 0.05	260.20 ± 38.67
0.38 < z < 0.40	3.73 ± 0.07	0.20 ± 0.00	277.87 ± 3.07	3.58 ± 1.14	0.16 ± 0.06	263.37 ± 42.27

Table 3.13: SSP parameter results using stacked spectra and mean parameters using individual fitting. Spectral fitting using M11 models

	Stacked spectra			Individual spectra		
Redshift	**Age (Gyr)**	**[Fe/H] (dex)**	σ **(km s^{-1})**	**< Age > (Gyr)**	**< [Fe/H] > (dex)**	**< σ > (km s^{-1})**
0.10 < z < 0.12	5.08 ± 0.06	0.21 ± 0.00	295.27 ± 2.45	5.84 ± 1.75	0.15 ± 0.05	291.89 ± 37.24
0.12 < z < 0.14	5.06 ± 0.10	0.21 ± 0.00	282.98 ± 3.20	5.56 ± 1.63	0.17 ± 0.02	272.68 ± 42.28
0.14 < z < 0.16	4.89 ± 0.07	0.21 ± 0.00	280.86 ± 2.44	5.53 ± 1.59	0.19 ± 0.03	266.77 ± 31.88
0.16 < z < 0.18	5.04 ± 0.07	0.21 ± 0.00	280.35 ± 2.30	6.00 ± 2.34	0.17 ± 0.03	272.65 ± 27.98
0.18 < z < 0.20	5.07 ± 0.07	0.21 ± 0.00	288.66 ± 2.34	6.26 ± 2.21	0.16 ± 0.08	273.50 ± 30.92
0.20 < z < 0.22	4.73 ± 0.07	0.21 ± 0.00	283.36 ± 2.37	5.54 ± 2.24	0.13 ± 0.07	273.90 ± 31.10
0.22 < z < 0.24	4.71 ± 0.06	0.21 ± 0.00	285.12 ± 2.03	5.79 ± 2.22	0.12 ± 0.07	275.55 ± 33.48
0.24 < z < 0.26	4.65 ± 0.06	0.21 ± 0.00	288.13 ± 2.00	5.35 ± 1.51	0.12 ± 0.07	283.07 ± 36.00
0.26 < z < 0.28	4.57 ± 0.05	0.21 ± 0.00	289.86 ± 1.98	4.95 ± 1.44	0.14 ± 0.07	281.57 ± 35.49
0.28 < z < 0.30	4.47 ± 0.15	0.21 ± 0.01	282.56 ± 1.89	5.05 ± 1.26	0.12 ± 0.07	277.19 ± 33.54
0.30 < z < 0.32	4.46 ± 0.05	0.21 ± 0.00	298.70 ± 1.93	4.68 ± 1.45	0.11 ± 0.07	280.62 ± 37.35
0.32 < z < 0.34	4.34 ± 0.05	0.21 ± 0.00	296.08 ± 1.89	4.74 ± 1.53	0.12 ± 0.08	284.88 ± 41.50
0.34 < z < 0.36	4.18 ± 0.05	0.21 ± 0.00	299.70 ± 2.03	4.66 ± 1.50	0.10 ± 0.07	280.18 ± 44.27
0.36 < z < 0.38	4.11 ± 0.05	0.21 ± 0.00	307.65 ± 2.18	4.59 ± 1.44	0.10 ± 0.07	282.80 ± 41.35
0.38 < z < 0.40	4.00 ± 0.19	0.21 ± 0.02	305.50 ± 2.48	4.37 ± 1.30	0.09 ± 0.07	287.90 ± 47.42

provide very consistent velocity dispersions, which are due to the same stellar library (MILES) used by both models. In addition, the age $-\ \sigma_{\rm v}$ of ETGs were found to follow a power-law relationship with a slope which varies from 0.4 to 1.2 (e.g Caldwell *et al.*, 2003; Liu *et al.*, 2012; Nelan *et al.*, 2005; Smith *et al.*, 2009; Thomas *et al.*, 2005). The difference in the age $-\ \sigma_{\rm v}$ scaling relation (slope) might be due to the differences in the sample selection and the numerous calibrations before determining luminosity weighted ages (Nelan *et al.*, 2005). When performing a power-law fitting for each redshift bin, the mean values of the slope for all redshift bins are found to fall in that range values. However the errors on the slope values

which are the standard deviations are found to be higher since there are significant scatter in the slope values. Each mean slope value from each model is given below.

The comparison between both ages using four models are shown in all panels (a) of figures 3.18, 3.11, 3.20 and 3.13. In the same plots but panels (b), the comparison between metallicities is presented, whereas the comparison of both velocity dispersions is shown in panels (c). Those comparisons are with the error bars, not very noticeable for the results of stacked spectra. The typical errors bars on the mean parameter values are 20 times bigger than the typical error bars on the parameter values extracted from the stacked spectra fitting.

In the case of PE models, both ages agree with an rms difference of 1 Gyr. The obvious discrepancies between the two age results are at $z > 0.32$. However, the metallicity values from the stacked spectra fitting are almost stagnated at the value of 0.10 dex. Since the metallicity is held fixed in the range of $0 <$ [Fe/H] < 0.2 dex and the initial guess at 0.10 dex, the error on this parameter is reported by the mpfit function as zero. The latter is also available for the individual fits whose parameters hit the boundary limits. The fact of limiting both parameters (age, metallicity) and the wavelength range probably explain the constant value of metallicity. However, almost similar values with a little offset of $\sim$0.02 dex are found with the individual fits but with errors. The rms difference between two values of σ_v is 1.5 km s^{-1} in log value. The mean slope of the power-law relationship between age $- \sigma$ value for all redshift bins is 0.51 ± 0.34.

The SSP-equivalent ages extracted from the stacked spectra using VM models agree with those from the individual fits with an rms difference of $\sim$0.08 Gyr without considering the mean age at $z = 0.17$ where only few objects were fitted. The metallicities from the stacked fits lie around 0.15 dex for almost 50 % of all values which agree with the estimated mean values from the individual fits. The rms difference between two values of σ_v is roughly 1.5 km s^{-1} in log value, and the mean slope of the age $- \sigma$ relationship is found to be 0.66 ± 0.57.

In the case of M11 models, there is a significant difference between all parameter values from both fits. The age-redshift relation from the stacked spectra fitting is almost flat with only 1 Gyr difference between age at $z \simeq 0.11$ and age at $z \simeq 0.39$. It is supposed to be 2.6 Gyr difference if the models follow the ΛCDM cosmology. These models are found to underestimate the metallicity and age values. The limits of the grid in metallicity has been reached therefore the fit fails and the returned error is zero. However, the case is different on the mean ages and metallicities from the individual fitting apart from the low redshift ones where few objects were fitted. The calculated rms difference between both ages is 1.5 Gyr. The estimated metallicities from the stacked spectra fitting are found to have the same problem as those using PE models even though no wavelength range limits were set. The poor sampling and coverage of stellar parameter space may explain this situation. The rms difference between two values of σ_v is roughly 1.5 km s^{-1} in log value, and the mean slope of the age $- \sigma$ relationship is found to be 0.44 ± 0.30.

Out of the four models used in this analysis, only BC03 models give reasonable agreement in all parameters: ages, metallicities and velocity dispersions. Estimated parameters from the stacked spectra agree with the mean parameters from the individual fitting, with an rms difference of ∼0.7 Gyr in age (without considering ages at $z = 0.10$ where almost 2 Gyr of difference was found, and few objects were co-added to form the stacked spectrum and to be fitted individually) and 0.05 dex in metallicity and 1.2 km s^{-1} in $\log\sigma_v$. Figure 3.22 shows the comparison between estimated parameters from both fittings using BC03 models. The mean slope value of the age-σ_v relationship is 0.80 ± 0.49 which is comparable to the value found in Liu *et al.* (2012) while using the same models on LRG sample. They found a value of 0.77 ± 0.25. Note that stellar templates from the BC03 models assembled by Tremonti *et al.* (2004) were used to measure the original velocity dispersions of the sample used in this analysis, which was performed by pPXF in GANDALF. These velocity dispersions were used to select the final sample (see section 3.6.2). They are plotted in panel (b) of figure 3.22 in blue diamonds as a reference. This explains the consistency between the three values of velocity dispersions. All results also yield to the remark that ELODIE and MILES libraries provide higher velocity dispersions than STELIB library used in BC03 models.

3.7.7.6 Comparison between models

From the previous section, only BC03 models are able to give fairly consistent values in all parameters using combined and individual spectra. But how are they compared to the parameter values using the other models? The velocity dispersion values have been compared in the previous section, therefore SSP-equivalent age and metallicity are used for comparison in this section. Some metallicities stay constant for some models when using the stacked spectra fitting. Thus the model comparison focuses on SSP mean results from the individual fitting.

Figure 3.23 shows the comparison between the mean SSP-equivalent ages extracted from the individual fitting using PE, VM, BC03 and M11 models. Figure 3.24 represents the comparison between the mean metallicities results from fitting individual galaxy with VM, BC03 and M11. Out of the four models, PE models give the lowest metallicities (see table 3.10). Therefore, it is not worth comparing these metallicities with the other results. In all plots, the upper panels represent either age or metallicity comparison between two models, whereas all residuals are plotted in lower panels.

The PE-VM comparison between ages (panel (a)) reveals a consistency more specifically at high redshift $z \gtrsim 0.20$ with an rms less than 0.5 Gyr. When performing a comparison between these two models, Koleva *et al.* (2008) also found a relative consistency between both results in high metallicity. The differences in values at low redshift $z \lesssim 0.20$, which are valid in all models, come from the fact of using a smaller number of galaxies within redshift bins and from the models themselves. Each model was generated using its own ingredient (please refer to the section 3.7.7.2 for more details). PE-BC03 comparison between ages

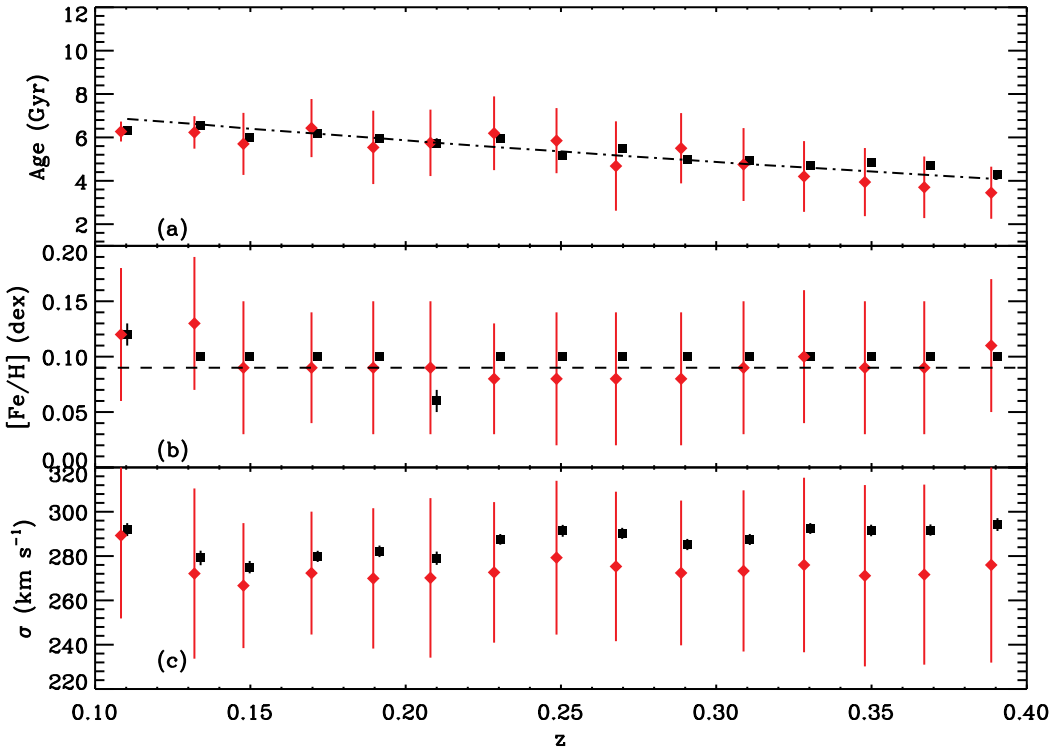

Figure 3.18: Comparison of the SSP properties extracted from the stacked spectra (black squares) and the average parameters of the individual fitting (red diamonds) by using PE models. Panel (a), (b) and (c) shows the SSP equivalent ages, metallicities and velocity dispersions in each redshift bin from both fitting. For the reconstruction of the age-redshift relation, the dot-dashed line indicates age of the Universe $t_U(z)$ - 5.4 Gyr in the ΛCDM cosmology and it is only for reference. Panel (b) illustrates the chemical evolution of the population. Both fittings show flat metallicities, meaning there is no evolution. A little offset of 0.002 was applied to the redshift for clarity.

(panel (b)) shows an rms of 1 Gyr over all redshift. It shows a reasonable consistency as claimed by Koleva *et al.* (2008) and confirmed here, whereas PE-M11 (panel (c)) comparison shows a 1 Gyr difference in age at high redshift. All comparisons with PE models yield to the conclusion that restricting the wavelength of the fits with these models do not provide any significant biases.

The comparisons of all models with M11 (panels (c), (e), (f) of figure 3.23 and panels (b), (c) of figure 3.24) remarkably show a significant rms about 2 Gyr in age and 0.07 dex in metallicity. However, a precise agreement is found between BC03 and VM models in almost all ages (rms $<$ 0.5 Gyr) at the same metallicities (rms $<$ 0.05 dex). These two models give the best consistency between age and metallicity in overall comparisons. Despite the inaccuracy of the wavelength calibration and poor metallicity coverage of BC03, our results

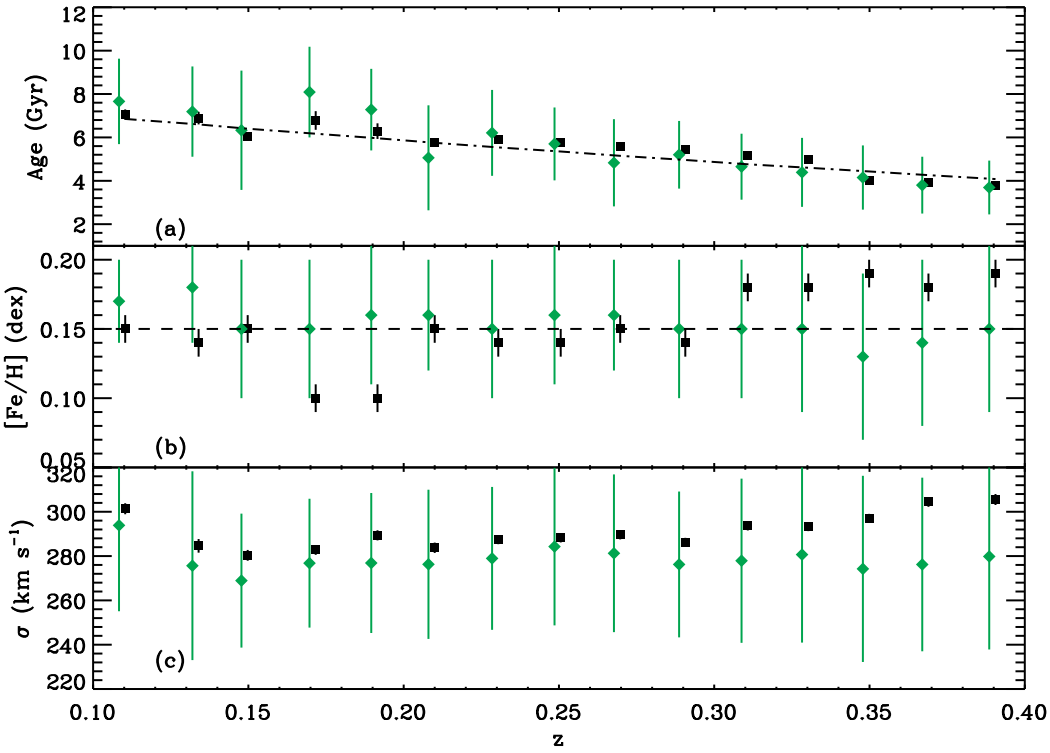

Figure 3.19: Comparison of the SSP properties extracted from the stacked spectra (black squares) and the average parameters of the individual fitting (green diamonds) by using VM models. Panel (a), (b) and (c) shows the SSP equivalent ages, metallicities and velocity dispersions in each redshift bin from both fitting. For the reconstruction of the age-redshift relation, the dot-dashed line indicates age of the Universe $t_U(z)$ - 5.4 Gyr in the ΛCDM cosmology and it is only for reference. Panel (b) illustrates the chemical evolution of the population. Both fittings show flat metallicities, meaning there is no evolution. A little offset of 0.002 was applied to the redshift for clarity.

indicate that BC03 and VM models can better fit older galaxies with high metallicity such as LRGs, followed by the PE models and lastly the M11 models. The failure of M11 models is most probably due to the lack of the parameter coverage and sampling. Dias *et al.* (2010) performed extensive comparisons between different models using full spectral fitting with ULySS and STARLIGHT packages on star clusters. Models used are PE, BC03 and VM. They found that the choice of codes has more impact on the results than the choice of the models. Nonetheless, PE vs BC03 comparison showed the best agreement between age and metallicity using both packages. Both models can better fit intermediate age objects with subsolar metallicity.

Since the model of Lick absorption indices of TMJ uses the same evolutionary population code as M11, it is more reasonable to compare SSP results from both models with same

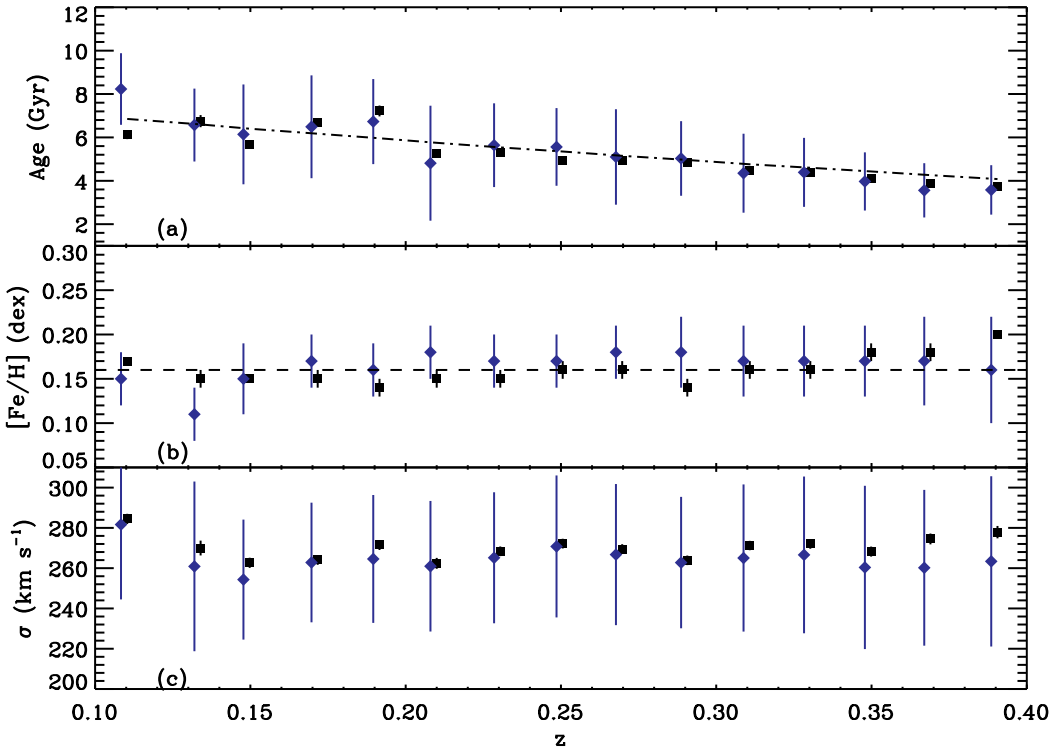

Figure 3.20: Comparison of the SSP properties extracted from the stacked spectra (black squares) and the average parameters of the individual fitting (blue diamonds) by using BC03 models. Panel (a), (b) and (c) shows the SSP equivalent ages, metallicities and velocity dispersions in each redshift bin from both fitting. For the reconstruction of the age-redshift relation, the dot-dashed line indicates age of the Universe $t_U(z)$ - 5.4 Gyr in the ΛCDM cosmology and it is only for reference. Panel (b) illustrates the chemical evolution of the population. Both fittings show flat metallicities, meaning there is no evolution. A little offset of 0.002 was applied to the redshift for clarity.

ingredients than those from other models like PE, or BC03 or VM. As seen in section 3.7.6, age estimates using the Lick index fitting are very old. Compared with the M11 models, there are more than 4 Gyr difference between both SSP-equivalent ages. However, the metallicity from both models seems to agree with an rms difference of about 0.07 dex. Note that the metallicity expressed as [Z/H] in the Lick index models was transformed into [Fe/H] notation by using the definition in equation 2.3 in chapter 2 for consistency. The reason for this significant difference in ages comes from the lack of sampling of M11, or the use of only few indices with TMJ compared with all informations (features) used in full spectrum fitting.

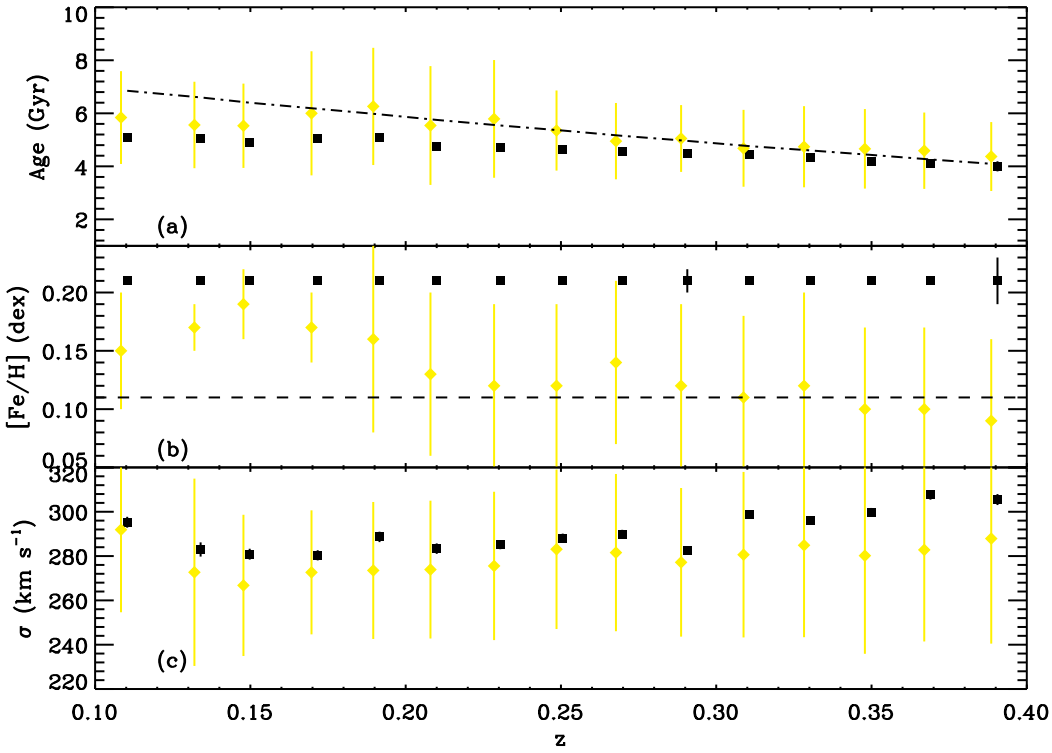

Figure 3.21: Comparison of the SSP properties extracted from the stacked spectra (black squares) and the average parameters of the individual fitting (yellow diamonds) by using M11 models. Panel (a), (b) and (c) shows the SSP equivalent ages, metallicities and velocity dispersions in each redshift bin from both fitting. For the reconstruction of the age-redshift relation, the dot-dashed line indicates age of the Universe $t_U(z)$ - 5.4 Gyr in the ΛCDM cosmology and it is only for reference. Panel (b) illustrates the chemical evolution of the population. Both fittings show flat metallicities, meaning there is no evolution. A little offset of 0.002 was applied to the redshift for clarity.

3.7.7.7 Reliability of the fits on the combined spectra

Since SSP fitting always involves the problem of degeneracy between parameters and multiple local minima in the parameter spaces, it is important to check the reliability of the fitting and validate all SSP results. Firstly, it has been shown in the previous section that using different models gives consistent results despite the numerous differences in the model ingredients. Moreover, ULySS provides some good ways to validate the results of the fitting, such as the Monte Carlo simulations, χ^2 maps and convergence maps. In addition, a comparison with previous works is also another technique to test the results.

Monte Carlo (MC) simulations and convergence maps were performed to visualise the degeneracies and multiple minima in order to validate the SSP results. A series of 500 MC

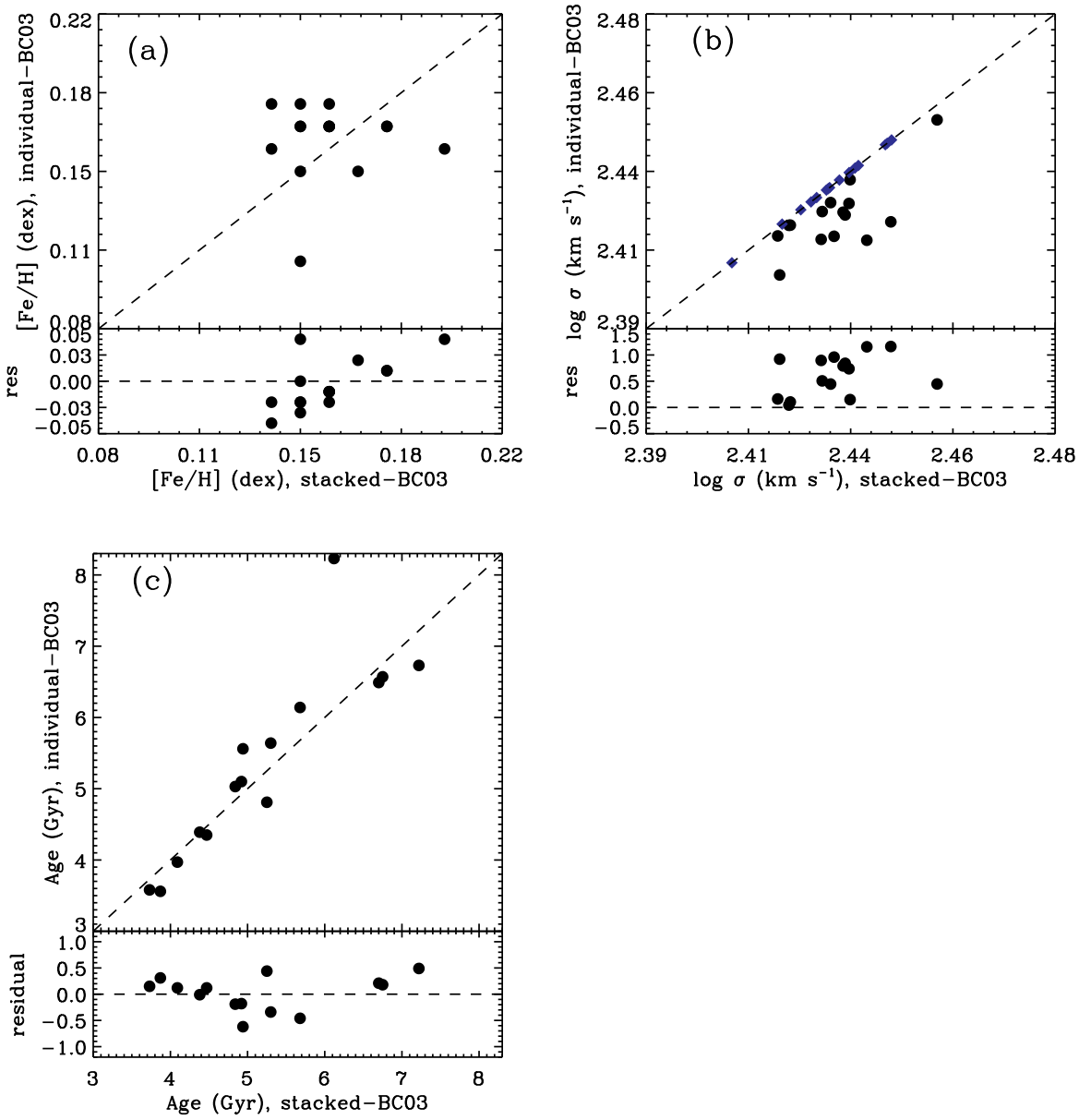

Figure 3.22: Comparison between the SSP properties extracted from the stacked spectra and the average parameters of the individual fitting (black circles) by using BC03 models. The dashed lines represent the one-to-one relations. All lower panels illustrate the residuals between the two values. The blue diamonds represent the original values of velocity dispersions calculated through pPXF/GANDALF routines, which used to select the final sample.

simulations were performed. In each step, MC simulations repeat a fit by adding a random Gaussian noise to the spectrum. The amplitude of the added noise was based on the estimated noise associated with the observed spectrum. The same S/N determined for the Lick index measurement on the co-added spectra was applied. The same setting as in section 3.7.7.3

was applied to the fits: same wavelength ranges, same prior on metallicity and age. The SSP estimated values were then the mean values of the distributions of the simulations, while the corresponding errors were calculated from the standard deviation of the distributions.

Table 3.14: Monte Carlo simulation results on the stacked spectra. "Age-fit" is the age from the best fit, while"Age-mc" is the age from the simulations. Errors on the age-fit are the 1-σ computed from the covariance matrix by mpfit function.

	PE models		VM models		BC03 models		M11 models	
Redshift	**Age − fit (Gyr)**	**Age − mc (Gyr)**	**Age − fit (Gyr)**	**Age − mc (Gyr)**	**Age − fit (Gyr)**	**Age − mc (Gyr)**	**Age − fit (Gyr)**	**Age − mc (Gyr)**
$0.10 < z < 0.12$	6.34 ± 0.05	6.21 ± 0.06	7.05 ± 0.13	7.70 ± 0.99	6.11 ± 0.11	7.76 ± 0.13	5.08 ± 0.03	5.29 ± 0.51
$0.12 < z < 0.14$	6.55 ± 0.08	6.48 ± 0.09	6.88 ± 0.19	5.63 ± 0.76	6.74 ± 0.15	6.43 ± 0.28	5.05 ± 0.06	5.19 ± 1.12
$0.14 < z < 0.16$	5.99 ± 0.06	6.11 ± 0.08	6.02 ± 0.08	6.03 ± 0.09	5.68 ± 0.07	6.61 ± 0.49	4.88 ± 0.03	5.47 ± 1.57
$0.16 < z < 0.18$	6.17 ± 0.05	6.31 ± 0.07	6.77 ± 0.22	6.77 ± 0.42	6.70 ± 0.09	6.92 ± 0.39	5.03 ± 0.03	5.50 ± 1.39
$0.18 < z < 0.20$	5.93 ± 0.05	6.04 ± 0.08	6.28 ± 0.16	6.28 ± 0.35	7.21 ± 0.10	6.91 ± 0.24	5.06 ± 0.03	6.18 ± 2.29
$0.20 < z < 0.22$	5.74 ± 0.09	5.73 ± 0.14	5.76 ± 0.05	5.72 ± 0.28	5.25 ± 0.05	5.52 ± 0.11	4.73 ± 0.03	5.43 ± 1.54
$0.22 < z < 0.24$	5.92 ± 0.04	6.10 ± 0.07	5.90 ± 0.05	5.85 ± 0.05	5.29 ± 0.04	5.66 ± 0.19	4.70 ± 0.02	9.37 ± 2.70
$0.24 < z < 0.26$	5.16 ± 0.07	5.73 ± 0.12	5.76 ± 0.05	4.13 ± 0.02	4.94 ± 0.03	5.36 ± 0.04	4.64 ± 0.02	7.70 ± 3.03
$0.26 < z < 0.28$	5.51 ± 0.06	5.67 ± 0.17	5.59 ± 0.04	4.66 ± 0.74	4.91 ± 0.03	5.36 ± 0.05	4.57 ± 0.02	4.62 ± 0.01
$0.28 < z < 0.30$	4.96 ± 0.05	5.48 ± 0.10	5.45 ± 0.03	5.50 ± 0.02	4.83 ± 0.03	5.33 ± 0.04	4.47 ± 0.06	4.47 ± 0.01
$0.30 < z < 0.32$	4.92 ± 0.06	5.16 ± 0.15	5.18 ± 0.04	4.74 ± 0.32	4.46 ± 0.02	4.45 ± 0.01	4.46 ± 0.02	4.37 ± 0.01
$0.32 < z < 0.34$	4.71 ± 0.04	4.86 ± 0.11	4.98 ± 0.06	4.10 ± 0.33	4.38 ± 0.02	4.41 ± 0.02	4.33 ± 0.01	4.29 ± 0.01
$0.34 < z < 0.36$	4.83 ± 0.05	4.67 ± 0.17	4.02 ± 0.03	4.03 ± 0.29	4.08 ± 0.02	3.89 ± 0.03	4.18 ± 0.02	4.15 ± 0.02
$0.36 < z < 0.38$	4.69 ± 0.05	4.46 ± 0.23	3.91 ± 0.04	3.76 ± 0.03	3.87 ± 0.05	3.75 ± 0.02	4.11 ± 0.02	4.01 ± 0.01
$0.38 < z < 0.40$	4.28 ± 0.11	4.20 ± 0.19	3.79 ± 0.05	3.70 ± 0.05	3.72 ± 0.03	3.67 ± 0.05	3.99 ± 0.10	4.01 ± 0.02

Convergence maps were performed to visualise the local minima in the parameter space. These show the convergence paths from a grid of guesses to the individual SSP results. The results are supposed to be independent regardless of the number of initial guesses. In all cases, the adopted convergence maps led to the original best fit solutions, meaning consistent results. All of these indicate the robustness of the full spectral fitting with ULySS package.

Table 3.14 presents the age results of the MC simulations applied to the combined spectra. Both techniques give consistent results even though some deviations are found in some redshift which may be caused by the limitation on the parameters and the effect of the estimated noise. In addition, uncertainties from the MC simulations are larger because these simulations take into account the age-metallicity degeneracy while uncertainties estimated from the normal fit do not. The effect of the limits on metallicity is also apparent when using both techniques, precisely when performing fits with PE and M11 models. Although, there is a large difference between both derived ages for the BC03 models in the lowest redshift bin. This is might due to the estimated noise because when the convergence and χ^2 maps were performed, both results converge to the best fit results.

3.8 Age-redshift relationship

The important part of measuring the $H(z)$ is through the age-redshift relationship of passive elliptical galaxies. The accuracy of the $H(z)$ measurement comes from well constructed evolution of the mean luminosity weighted age. Different age-redshift relationships from each

fitting are presented in this section.

3.8.1 Stacked spectra - Lick indices fitting

As mentioned in section 3.7.6, the use of the Hβ index as an age indicator with the combination of metallicty indices Mg$_b$, <Fe> does not provide a very accurate age-redshift relation. Apparently, the Hγ_F index instead of the Hβ does not provide one either, but gives a steeper slope on the age-redshift relation. Further fitting analysis was made to constrain the age-redshift relation. We set some priors on [Z/H] and [α/Fe]. The limit of [Z/H] was set to be in the range of $0.20 < [Z/H] < 0.30$ dex, while the [α/Fe] limits were $0.20 < [Z/H] < 0.4$ dex as the metallicity and the α-element of LRGs are found to be in those ranges. This time, however, the combination of Hγ_F, Mg$_b$, and <Fe> was used.

The reconstruction of the age-redshift relation is plotted in figure 3.25, showing the impact of putting some priors on [Z/H] and [α/Fe] parameters. There is a little change especially with a slope of the age-redshift relation, following ΛCDM with exception at high redshift. However the SSP equivalent ages stay older as in figure 3.11 panel (a). The evolution in [α/Fe] with redshift is somewhat the same as in 3.11 panel (c). [Z/H] are mostly constant, unlike those in figure 3.11 panel (b). However the uncertainty on each parameter decreases . The scatter of the age estimates over the redshift range is about 5 Gyr as expected from the ΛCDM model and consistent with previous work by Carson & Nichol (2010).

3.8.2 Stacked spectra - full spectrum fitting

Figure 3.26 presents the age-redshift relationship from the full spectral fitting of the combined spectra using PE, VM, BC03 and M11 models. The overall SSP equivalent ages are fairly consistent with each other, with the exception of the M11 models. Details on the comparison is found in section 3.7.7.6. Each model is able to estimate a well defined and expected age evolution with redshift: galaxies become younger with redshift , and follow the ΛCDM cosmology, apart from the M11 models where it is almost flat (1 Gyr difference). This leads to the confirmation that these objects were approximately formed at the same time, a age formation around 5.4 Gyr. When using BC03 models, the age-redshift result found in this analysis is quite similar to the age-redshift relation found in Liu *et al.* (2012). It is important to note that all derived ages as well as the results found in Liu *et al.* (2012) are relative ages.

As stated before, the error bars on the ages were obtained by scaling the parameter errors by the measured χ^2 values. Large error bars are noticeable at low redshift $z < 0.20$, where few objects (see figure 3.6) were stacked to form the combined spectra, and where ages are evolving differently: they exhibit more scatter. At high redshift $z > 0.20$, the evolution of age is more stable. For the number of objects at low redshift, only ages above the redshift 0.20 were considered for the $H(z)$ measurements.

3.8.3 Individual spectra - full spectrum fitting

It is necessary to know if the physical properties of galaxies extracted from the combined spectra in each redshift bin represent the mean properties of all galaxies. As described in section 3.7.7.5 the mean ages and metallicities, with the exception of the velocity dispersions obtained from individual fitting are still consistent with that obtained from the combined spectra fitting, when appropriate calculation of the mean was used. In this section, we also present the difference in the output results when using mean, median and weighted mean.

Figure 3.27 shows the weighted mean of the ages which have already been presented in section 3.7.7.5. Here they are plotted with their associated errors which are obtained from the weighted standard deviation. For clarity only, estimate ages from the same redshift bin with different SSP models are plotted with small offsets. The reason for this is to clearly distinguish each age. As when using combined spectra, the evolution in age with redshift shows the expected behaviour, following a ΛCDM cosmology models, although, the significant scatter is still present at low redshift $z < 0.20$. The estimate ages in that redshift are also not used for $H(z)$ measurements.

To overcome the problem at low redshift, the median, and the mean of ages were also calculated. Figures 3.28, 3.29, 3.30 and 3.29 illustrate the comparison between the three values of ages with different models. The open squares on each plot are weighted mean ages with associated errors obtained from the weighted standard deviation. All filled squares are mean ages and filled diamonds are median ages. Mean and median ages are plotted without associated error bars. The mean ages would be associated with the standard deviation of the sample. However the median ages would be associated with the error on the mean. The scatter in age values at low redshift is still present either using median or normal mean, whereas they are very stable and follow the same trend as the weighted mean ages at high redshift. The normal mean age values are greater than the weighted mean and the median values. The median and normal mean values depend on the distribution of the individual age of galaxy.

The individual fits (grey points in all plots) are different from model to model. In each individual fitting with models, few ages touch the boundary limitation, which is the age of the Universe. These ages have contributed less in the measured weighted mean ages since their errors were automatically returned as zero by the MPFIT function, hence high confidence in the weighted mean age values. These are due to the reasons as stated before (low S/N, spectral quality of models and the observed, etc.). The number of galaxies that fall into this situation changes with models. With M11 models, the number is very high. The estimate ages are almost scattered around young ages (4 - 5 Gyr) over the entire redshift. However, with the other models, the spread of the estimated ages are mostly from 4 Gyr to 9 Gyr without considering the ages near the edge.

3.9 H(z) estimates

By using the age-redshift relation at $z > 0.20$, the Hubble parameter $H(z)$ can now be determined. The point is to use all available ages in that redshift. We therefore adopted the linear fitting procedure to fit ages in a specific redshift bin. If the straight line is given by t = Az + B and the error on ages are σ_{ti}, the best fit parameters were returned by the mpfit function. The advantage of the MPFIT function is that by giving the name of the function it iterates multiple times toward the best solution and returns the 1-σ errors on the parameters. Recalling the definition of $H(z)$ in chapter 1 equation 1.17, the slope A of the fit will be the value of dt/dz. Hence, the Hubble parameter at the effective redshift is given by the following equation:

$$\mathrm{H(z_{eff})} = -\frac{1}{(1+\mathrm{z_{eff}})}\left(\frac{\mathrm{dt}}{\mathrm{dz}}\right)^{-1} \tag{3.22}$$

where $\mathrm{z_{eff}} = (\mathrm{z_{max}} + \mathrm{z_{min}})/2$. The difference Δz in $\mathrm{z_{min}}$ and $\mathrm{z_{max}}$ should not be great and not be small. After testing different Δz (from lowest 0.8 to highest 0.16), the optimized Δz was 0.14 with which all ages have been used and the number of ages were the same. This implies 8 age datapoints were used in each subsample, leading to 3 values of $H(z)$ at $z \simeq 0.32$, $z \simeq 0.30$ and $z \simeq 0.28$. The corresponding error on the $H(z)$ was obtained by using the error propagation technique, and it is given by:

$$\sigma_{\mathrm{H}} = \frac{1}{(1+\mathrm{z_{eff}})}\frac{\sigma_{\mathrm{slope}}}{\mathrm{slope}^2} \tag{3.23}$$

where the σ_{slope} is the error on the slope A and which is the 1-σ error returned by the MPFIT function. Table 3.15 lists the results of the parameter fits and the estimated $H(z)$ using PE, VM, BC03, M11 and TMJ models. We also present $H(z)$ values when fitting all ages (10 datapoints) over the redshift range $0.20 < z < 0.40$. Columns named **(1)** lists $H(z)$ estimates calculated over $0.24 < z < 0.40$, columns named **(2)** over $0.22 < z < 0.38$, columns named **(3)** over $0.20 < z < 0.36$, whereas columns named **(all)** lists $H(z)$ estimates over the entire redshift $0.20 < z < 0.40$. All parameter fits expressed with the footnote " a" are results from ages extracted from the stacked spectra fitting, whereas the footnote "b" represents all parameter fits when using mean ages from individual fits.

Figure 3.33, 3.34, 3.35 and 3.36 show the estimates $H(z)$ using the different models using age-redshift relations at $z > 0.20$. The ages extracted from the stacked spectra, and mean ages (weighted mean) were used to determine three different $H(z)$ values. Again, the errors associated with the ages from the stacked spectra fitting are the scaling errors; while the errors associated with the mean ages from the individual fits are the weighted standard deviation.

Looking at each measurement, BC03 models are the only models which can give reasonable values in both fittings. The $H(z)$ results match the ΛCDM cosmology. The use of the mean ages does provide significant uncertainties on the $H(z)$ estimates. We will consider the $H(z)$

measurements by using the ages extracted from the full spectral fitting of the stacked spectra for further analysis. The use of the BC03 models to age-date passively evolving ellipticals allows us to measure the $H(z)$ using the cosmic chronometers method. These models are very efficient in constructing accurate age-redshift relationship, hence reliable $H(z)$ measurement. This study confirms the use of BC03 models by many scientists who have worked on the cosmic chronometers technique (e.g. Jimenez *et al.*, 2003; Liu *et al.*, 2012; Simon *et al.*, 2005; Stern *et al.*, 2010a; Zhang *et al.*, 2012). It does not mean that the other models do not fit the passively evolving ellipticals. They fit but the sensitivity of the models leads to the inaccuracy of the age-redshift relationship hence failure of the $H(z)$ measurement.

Table 3.15: Results of the linear fitting using ages extracted from the stacked spectra (a) and using the mean ages from the individual fitting (b). Columns named (1), (2), (3) show results from fitting the three subsamples of ages, where $H(z)$ measurements are at $z \simeq 0.32$, $z \simeq 0.30$ and $z \simeq 0.28$ respectively. Columns named "all" show results from fitting all the ages in $0.20 < z < 0.40$, where all $H(z)$ measurements are at $z \simeq 0.30$. $H(z)$ is in units of km s^{-1}Mpc^{-1}.

	PE models				**VM models**				**BC03 models**			
	1	**2**	**3**	**all**	**1**	**2**	**3**	**all**	**1**	**2**	**3**	**all**
$slope^a$	-6.10	-8.60	-9.26	-8.47	-16.5	-16.17	-13.1	-13.97	-9.64	-9.58	-8.85	-9.33
σ^a_{slope}	1.3	1.04	1.16	0.88	0.78	0.82	0.88	0.60	0.66	0.82	0.78	0.54
H^a	121.3	87.5	82.5	88.7	44.8	46.5	58.3	53.8	76.7	78.4	86.2	80.5
σ^a_H	26.8	10.6	10.4	9.3	2.1	2.3	3.9	2.3	5.3	6.7	7.6	4.6
$slope^b$	-16.75	-17.96	-14.86	-15.23	-13.78	-15.82	-12.48	-12.92	-14.47	-15.47	-11.72	-12.53
σ^b_{slope}	11.29	12.20	12.25	8.01	11.62	12.56	13.98	9.15	11.8	12.43	13.93	9.12
H^b	44.2	41.9	51.4	49.3	53.7	47.5	61.2	58.2	51.1	48.6	65.2	60
σ^b_H	29.7	28.4	42.3	25.9	45.3	37.7	68.5	41.2	41.7	39.1	77.5	43

Table 3.15: continued.

	M11 models				**TMJ models**			
	1	**2**	**3**	**all**	**1**	**2**	**3**	**all**
$slope^a$	-4.61	-4.37	-3.90	-4.14	-24.34	-23.94	-24.51	-23.34
σ^a_{slope}	0.50	0.42	0.44	0.36	1.01	1.08	0.86	0.61
H^a	160.5	172.1	195.6	181.3	30.4	31.4	31.1	32.2
σ^a_H	17.7	16.7	22.0	15.9	1.0	1.0	0.8	0.8
$slope^b$	-5.83	-6.82	-7.50	-6.62				
σ^b_{slope}	10.89	12.56	13.65	9.05				
H^b	126.9	110.2	101.7	113.5				
σ^b_H	237.2	202.9	185.0	155.1				

3.10 Effect of systematic errors

There are different sources of error in the $H(z)$ estimate such as a statistical error and a systematic error. The statistical error is related to the age measurement itself. It is related to the weighted standard deviation for the individual fitting whereas to the covariance matrix for the stacked spectra. A full description about possible sources of the systematic errors is given below. There are many sources of systematic errors as discussed by various scientists who have worked on Cosmic Chronometers technique (Jimenez *et al.*, 2003; Moresco *et al.*, 2012a).

Firstly, the dependence of the stellar population models adopted is one factor. Each model has its own ingredients and settings to build the parameter grids (IMF, stellar library, wavelength range, sampling and coverage of stellar parameter space etc.). All four models are probably different among each other over the whole wavelength range. Therefore there are always some discrepancies in the parameter outputs of these models. In the case of the stacked spectra, the systematics errors between the different age-redshift relations (figure 3.26) seem to dominate the statistical ones (output errors from the fitting procedure). But they are less dominant for the age-redshift relation from the full spectral fitting. This model dependence obviously provides some changes on $H(z)$ estimates (figures 3.33, 3.34, 3.35, 3.36). The dispersion between these $H(z)$ measurements would then quantify the systematic errors $\sigma syst_H$ and will be assumed as the final errors. Each $H(z)$ measurement at each effective redshift is thus estimated as the weighted mean of the $H(z)$ values. M11 models provided a very different age-redshift relation among the others models due to the limited sampling and parameters coverage, we excluded these models for the analysis of systematic error effects on $H(z)$ measurements.

For the stacked spectra, the expected final values of $H(z)$ at $z \simeq 0.28$, $z \simeq 0.30$ and $z \simeq 0.32$ are 65.9 $\pm$ 19.2 km s^{-1} Mpc^{-1}, 51.3 $\pm$ 32.0 km s^{-1} Mpc^{-1} and 49.5 $\pm$ 54.3 km s^{-1} Mpc^{-1} respectively. For the individual spectra, the expected final values of $H(z)$ at $z \simeq 0.28$, $z \simeq 0.30$ and $z \simeq 0.32$ are 56 $\pm$ 8 km s^{-1} Mpc^{-1}, 45.1 $\pm$ 3.7 km s^{-1} Mpc^{-1} and 48.1 $\pm$ 5.2 km s^{-1} Mpc^{-1} respectively. Despite using different ingredients, the systematic errors among the three models were at $< 14\%$ level for the individual fitting, but could be reduced if models with similar ingredients are carefully chosen. We also notice that the $H(z)$ measurements are less independent of the spectra used whether they are stacked or single for the fits. Both fits usually gave consistent relative ages. The individual spectra should have at least at medium S/N and resolution to avoid surpassing or hitting the age of the universe. Most of the galaxies in our sample have S/N slightly higher than 10.

The relative ages of LRGs were obtained by assuming a single-burst and single metallicity stellar population model. We also tested whether there are some contributions from the possible younger stellar populations in the derived ages. We run the test on the stacked spectra by applying the full spectral fitting. We fitted two stellar components of one young

(from 0.1 Gyr to 2 Gyr) and one old (from 2 Gyr - age of the Universe) stellar populations and found that the fraction of the young population is negligible. These galaxies do show passively evolving populations and not experience any significant recent star formation activity even at low redshift. In case there are young populations, their ages do not surpass 1.2 Gyr. All of these tests suggest that our new selection/identification criteria along with the quiescent galaxy selection provide a very homogeneous passively evolving galaxy sample.

Many studies have proved that massive ellipticals are enhanced in α elements with respect to solar neighbourhood (e.g. Thomas *et al.*, 2003; Worthey *et al.*, 1992). The effect of the α-abundance inclusion is remained a subject of discussion. We have shown the effect of putting some priors on the [α/Fe] parameter while extracting SSP equivalent ages using Thomas *et al.* (2011) models. In order to study the detailed effect of α-abundance inclusion on measurements of $H(z)$, the use of SSP models with variable chemical composition is necessary, especially for the full spectral fitting method.

There are many systematic errors in the line-strength indices such as flux calibration effects; spectral resolution and velocity dispersion corrections; telluric effects; sky subtraction uncertainties; wavelength calibration and radial velocity errors; scattered light effects; seeing and focus corrections; deviation from linear response of the detectors and contamination by nebular emission lines (Cardiel *et al.*, 1998). The study of the effect of all systematics are beyond of the current study. However, we have taken into account the effect of the radial velocity errors, velocity corrections and the contamination by nebular emission lines. Errors on the radial velocity and velocity dispersion when co-adding a big number of spectra became negligible. The uncertainty in the calibration to the Lick/IDS system affects objects at all redshift. However, the telluric sky-line contamination affects different indices for objects at different redshifts. This is avoidable by determining the right redshift range that is not affected by telluric features, and the level of the contamination which is acceptable.

3.11 Comparison with other studies

The key novelty of this study is the use of an alternative LRG selection/identification criteria. Previous selection criteria are based on apparent magnitudes and well defined by Eisenstein *et al.* (2001), whereas absolute magnitudes were used in this study. These new selection criteria led to a more homogeneous sample of galaxies (Crawford *et al.*, 2010a). The similarity of this study to the work of Carson & Nichol (2010); Liu *et al.* (2012); Zhang *et al.* (2012) is the use of the archive data from SDSS DR7. Our selection criteria identified 50 425 galaxies in SDSS DR7 whereas 77 000 and 71 971 galaxies were selected by Carson & Nichol (2010) and Liu *et al.* (2012) respectively, by using the previous selection criteria. Zhang *et al.* (2012) used the same original sample as in Carson & Nichol (2010). In term of selecting quiescent galaxies, all of them used the same criteria as in Carson & Nichol (2010) which are based on zero Hα, Hβ and [OIII]λ5007 emission lines with the definition of the line-strengths of the

MPA-JHU catalogues (with small zero offsets) (Tremonti *et al.*, 2004). However, our emission line measurements were performed by GANDALF software, and they do not show any zero offsets. With our strict selection, we obtained a 10% of our original sample that we referred to as a sample of quiescent galaxies. However, the others studies obtained more than 30% of their original samples.

Another specification of this study is also the thorough comparison of different techniques of age-dating, from the use of the so-called Lick index method to the full spectral fitting. Carson & Nichol (2010) calibrated, for the first time, the SDSS spectra onto Lick/IDS system. They also co-added LRG spectra in each redshift bin in order to increase the S/N. They estimated ages of the combined spectra by using the Lick absorption line indices, compared with the SSP models of Korn *et al.* (2005) (older version of the TMJ models). They stopped at the age-redshift relation determination at redshift $z \sim 0.03 - 0.40$ of four different sub-samples according to their velocity dispersions. No further constrains on neither the Hubble parameter nor the cosmological parameters were carried out. However, Liu *et al.* (2012) followed the same steps as Carson & Nichol (2010), but instead of the Lick index method they used the full spectral fitting with ULySS software adopting the Galaxev or BC03 models. From the age-redshift relation fitting, they estimated four different Hubble parameters at the present time H_0 for the four sub-samples. They did compare different models other than BC03 models and found that there is some model dependence which we have concluded in this study as well. They also did not include the effect of systematics from this. They concentrated on the derivation of the parameter H_0 but did not pay to much attention on the expansion rate over cosmic time $H(z)$. Meanwhile, Zhang *et al.* (2012) used the same sample as in Carson & Nichol (2010), but did not combine spectra. They extracted fairly high S/N spectra instead. They fitted each galaxy with BC03 models, and established an age-redshift relation from which a four new $H(z)$ values were measured. They also constrained on cosmological parameters using their values combined with other available datasets.

Our method is not far from what these three studies have accomplished. By comparing our results with Carson & Nichol (2010), we confirmed that putting some priors on [Z/H] and [α/Fe] and using a combination of H$\gamma_{\rm F}$ with Fe lines provided a well defined age-redshift relation even though different sets of SSP models were used. Therefore no improvement was made in this regard.

The age-redshift relation, when the stacked spectra was used for the full spectral fitting with BC03 models, was in good agreement with what Liu *et al.* (2012) obtained in their second subsample with redshift step different from ours ($\delta z = 0.03$). The amount of less massive galaxies (i.e. in the same velocity dispersion range as their second subsample) in our sample is very high, hence similar ages. Our big improvement over Liu and collaborators work was the establishment of the expansion rate over cosmic time and the cosmological constraints. In addition, their H_0 values (without considering any systematics) obtained from the sub-sample with high velocity dispersions, by assuming a flat ΛCDM, were not as

good as what we obtained in this study (see Chapter 5 for our values). This means that the more datasets used the more accurate the results on cosmological parameters were.

The full spectral fitting with BC03 models was also applied to each of our galaxies as in Zhang *et al.* (2012). We measured $H(z)$ by using the mean relative ages of galaxies in each redshift bin. Our $H(z)$ value at $z \simeq 0.28$ was not as good as their value. They found a value of $H(z \simeq 0.28) = 88.8 \pm 36.6$ km s^{-1} Mpc^{-1} (no systematic error added) whereas we found a value of 55.1 ± 41.72 km s^{-1} Mpc^{-1} . This difference might be due to the different ways of dealing with galaxy ages in each bin and number of galaxies per bin. However, a big improvement was found when using the relative ages of galaxies extracted from the stacked spectra with a value of $H(z \simeq 0.28) = 76.8 \pm 5.3$ km s^{-1} Mpc^{-1}. Simon *et al.* (2005) found a value of $H(z) = 77 \pm 14$ km s^{-1} Mpc^{-1} at $z \simeq 0.27$ which is not far from our redshift. They used a combination of passively evolving galaxy samples from different surveys. We found a remarkable agreement between both measurements with an improvement in terms of the error bar without considering any systematics. It is also important to note that Simon and collaborators did not include any effect of the systematics on their measurements.

By applying the same technique of Cosmic Chronometers, there is no available $H(z)$ value in the literature at $z \simeq 0.30$ and $z \simeq 0.32$ to be compared with our measurements, making our two values new measurements to complete the observational Hubble parameter $H(z)$ data. The comparison plot between our dataset and the other $H(z)$ estimates is shown later in Chapter 5. Datasets from Moresco *et al.* (2012a); Simon *et al.* (2005); Stern *et al.* (2010a); Zhang *et al.* (2012) are included to check the $H(z)$ evolution up to $z \sim 1.8$.

3.12 Conclusion

In this chapter, we have used 4 428 passively evolving elliptical galaxies extracted from SDSS-DR7 by using different selection criteria which are based on the rest-frame magnitude and colour. The original sample is in the redshift range $0.10 < z < 0.40$. Further selection has been applied to the original sample to create a quiescent sample free from any emission lines and a sample which contains massive galaxies. We have divided the redshift range into 15 redshift bins with a step of δz=0.02. Two different fitting techniques have been used in order to obtain SSP equivalent ages of the galaxies: the use of Lick indices and full spectral fitting. In order to improve the fits, all galaxy spectra within redshift bin have been combined to obtain a high S/N spectrum. On the one hand, the SSP equivalent luminosity weighted ages, metallicities and α-elements of those galaxies were obtained, using the Lick absorption indices models of Thomas *et al.* (2011). One the other hand, the SSP equivalent ages, metallicities and velocity dispersions of the same galaxies have been extracted from the combined spectra, and their mean values by performing individual fitting in each spectrum for comparison. PEGASE-HR, VAZDEKIS, GALAXEV and Maraston (2011) models have been adopted during the full spectral fitting. Detailed comparisons between the models have

been carried out in this analysis.

We find that SSP models of Maraston (2011) do not give a perfect age-redshift relationship either using combined spectra or individual fitting. However, the other three models can give reasonable results and they are comparable to each other. The consistency between parameters results are due to the ingredients from which the modellers computed their SSP models. M11 models have a lack of sampling and parameter coverage. BC03 and VM models agree with ages at metallicities with an rms difference less than 0.5 Gyr in age and less than 0.05 dex in metallicity respectively. The little difference between BC03 and VM models with PE models might probably be due to the limitation on the parameters and the wavelength range applied to the fitting with PE models. Some scatter is found in the ages at low redshift $z < 0.20$ due to the lack of the number of galaxies to be combined to form the high S/N spectra, and to be fitted individually in order to calculate the mean parameters. From this, only ages at high redshift $z > 0.20$ were used to measure the Hubble parameters $H(z)$. We also find that the physical properties derived from the combined spectra fitting represent the mean properties of all galaxies in the redshift bin, since both derived parameters are very consistent.

Even though we are confident with our sample selection, particularly when considering the emission lines corrected spectra, the Lick indices fitting shows a significant difference in the derived SSP ages. We have applied a normal calibration correction onto the measured line-strength indices. The different type of correction has potentially introduced some errors into the measured line-strength, hence affecting the accuracy of the estimate results. We find that our SSP parameter results depend on the choice of the set of indices. We confirm that the use of the combination of Hγ_F, Mgb and <Fe> indices provides a well defined age-redshift relationship but still old ages.

The Hubble parameter $H(z)$ has been estimated using the differential technique on the age-redshift relation produced by SSP ages extracted from each model. The values of $H(z)$ at $z \simeq 0.28$, $z \simeq 0.30$ and $z \simeq 0.32$ were measured. Table 3.15 summarizes all values. We have demonstrated that the age-redshift relation of the quiescent passively evolving galaxies fitted with BC03 models can reliably be used to measure the Hubble parameters $H(z)$ at $z \simeq 0.28$, $z \simeq 0.30$ and $z \simeq 0.32$, and their values are 76.8 ± 5.3 km s^{-1} Mpc^{-1}, 78.5 ± 6.8 km s^{-1} Mpc^{-1} and 86.3 ± 7.6 km s^{-1} Mpc^{-1} respectively. These values were obtained by fitting high S/N spectra, and are within 9% precision, which show a good improvement when compared with the values found in the literature at these redshifts. Those estimated values of $H(z)$ will be combined with $H(z)$ available in literature to constrain the cosmological parameters.

Further investigation must be done on the systematic uncertainty between the different age-redshift relations given by the different models. A bayesian model averaging across the models would be the best solution and which is classified as a future work.

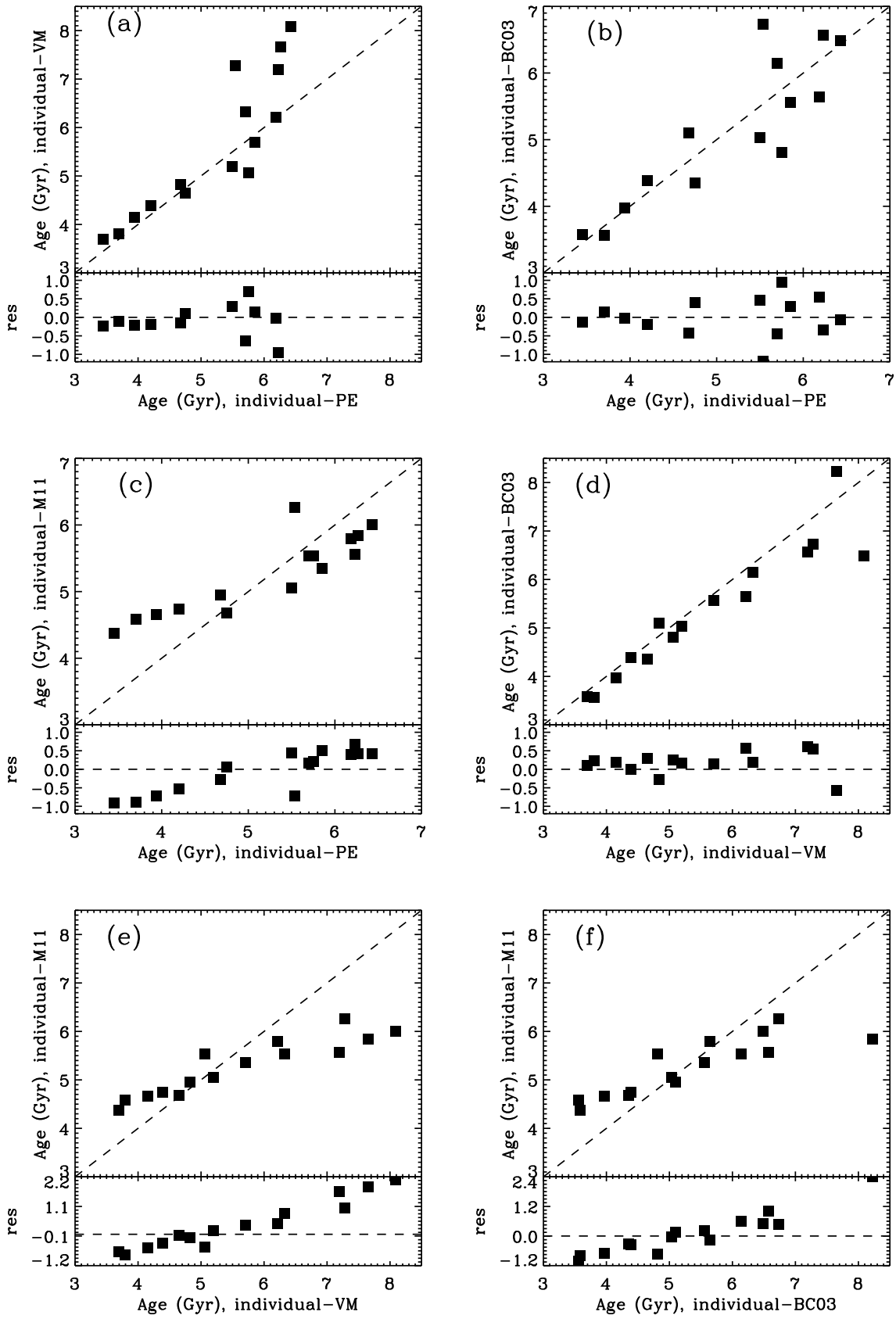

Figure 3.23: Comparison between the mean SSP-equivalent ages extracted from the individual fitting using PE, VM, BC03 and M11 models. The upper panels represent the age comparison between two models, whereas all residuals are plotted in lower panels. The dashed lines are the one-to-one relations.

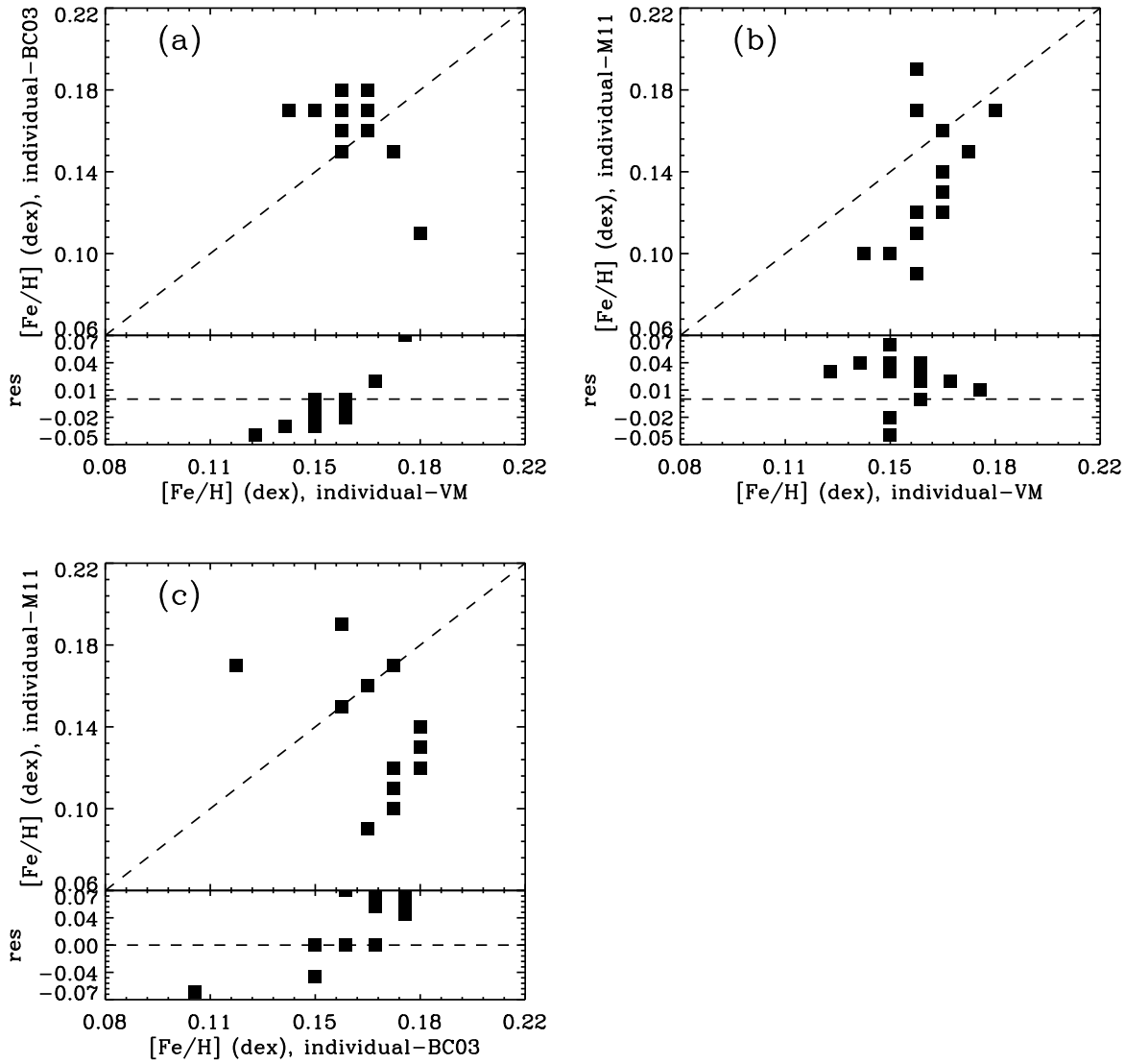

Figure 3.24: Comparison between the mean SSP-equivalent metallicities extracted from the individual fitting using PE, VM, BC03 and M11 models. The upper panels represent the metallicity comparison between two models, whereas all residuals are plotted in lower panels. The dashed lines are the one-one relations.

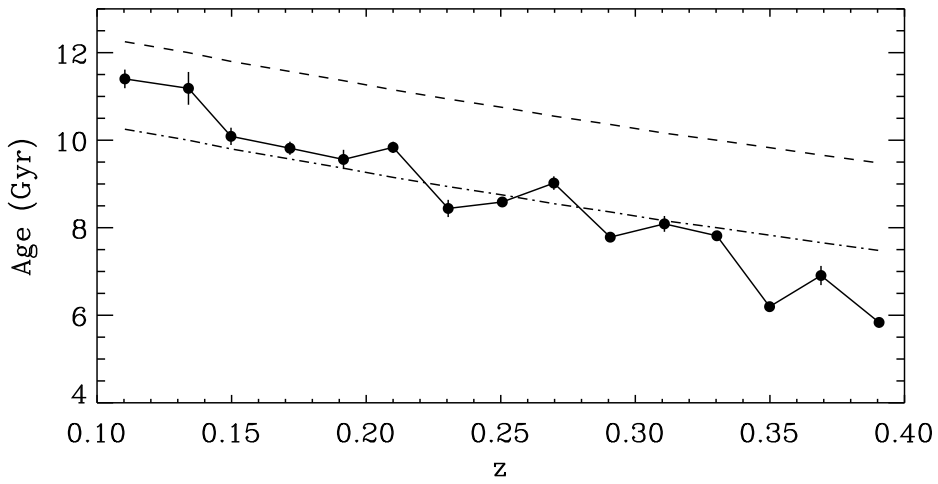

Figure 3.25: Age-redshift relation from the Lick index fitting of the stacked spectra using Hγ_F, Mg$_b$, and $< Fe >$ indices. The dashed line indicates the age of the Universe t$_U$(z) for a flat ΛCDM cosmology model assuming H_0 = 71 km s^{-1} Mpc^{-1} and Ω_m = 0.27. The doted-dashed line indicates t$_U$(z)−2 Gyr and it is only for reference. This plot is the same as panel (a) in 3.11 but applying a prior on [Z/H] and [α/Fe] parameters. The equivalent ages are the only one plotted here. The slope of the age-redshift relation do follow more or less the ΛCDM with exception at high redshift. [Z/H] are mostly constant unlike those in figure 3.11 , [α/Fe] stay approximately the same.

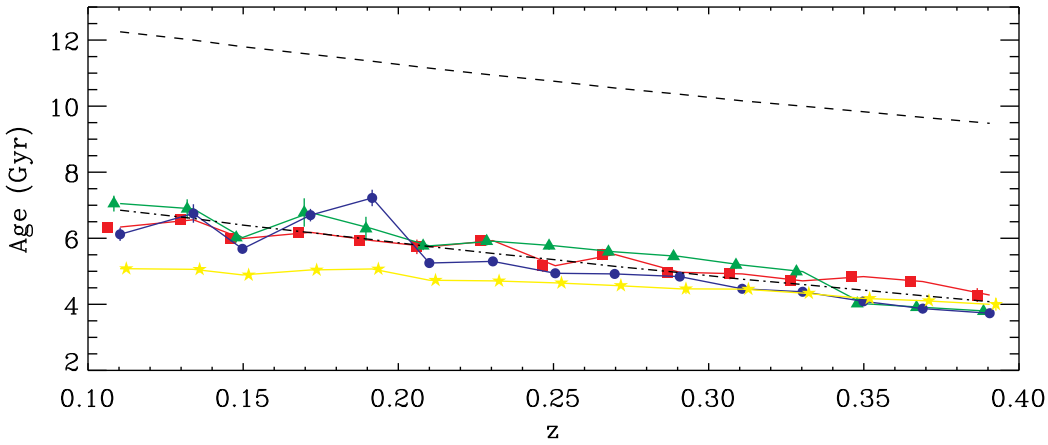

Figure 3.26: Age-redshift relation from the full spectral fitting of the stacked spectra using four different models: PE models (red squares), VM models (green triangles), BC03 models (blue circles) and M11 models (yellow stars). The dashed line indicates the age of the Universe t$_U$(z) for a flat ΛCDM cosmology models assuming H_0 = 71 km s^{-1} Mpc^{-1} and Ω_m = 0.27. The doted-dashed line indicates t$_U$(z)−5.4 Gyr and it is only for reference. For clarity, all symbols which represent the measured ages from the same redshift bin with different SSP models are plotted with small offsets δ z = -0.004, 0.002, 0, +0.002 along the horizontal axis from PE, VM, BC03 to M11 models respectively.

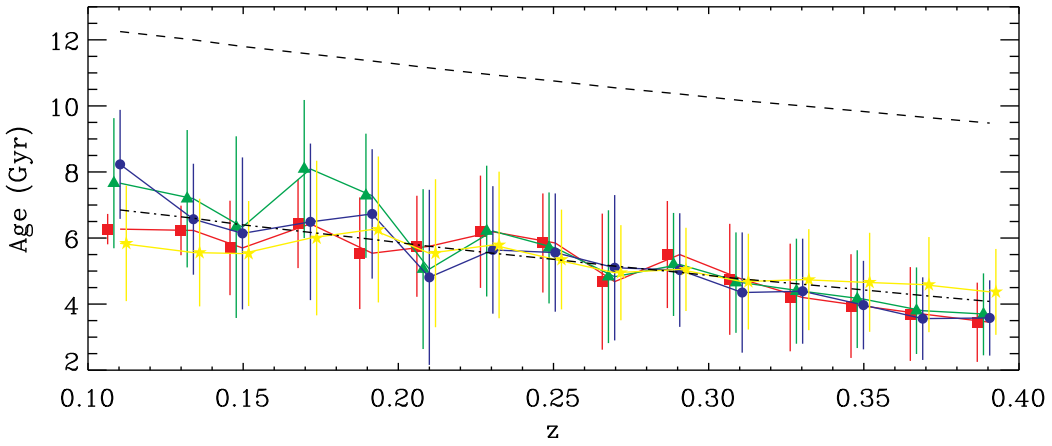

Figure 3.27: Age-redshift relation from the full spectral fitting of the individual spectra using four different models: PE models (red squares), VM models (green triangles), BC03 models (blue circles) and M11 models (yellow stars). The dashed line indicates the age of the Universe $t_U(z)$ for a flat ΛCDM cosmology model assuming H_0 = 71 km s^{-1} Mpc^{-1} and Ω_m = 0.27. The doted-dashed line indicates $t_U(z)-5.4$ Gyr and it is only for reference. For clarity, all symbols which represent the measured ages from the same redshift bin with different SSP models are plotted with small offsets δz = -0.004, 0.002, 0, +0.002 along the horizontal axis from PE, VM, BC03 to M11 models respectively.

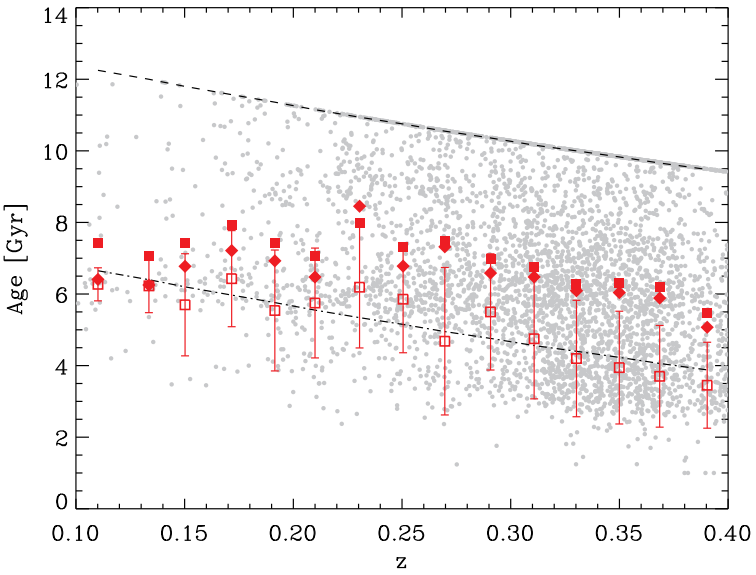

Figure 3.28: Individual fits using PE models (each grey symbols). Open square symbols are weighted mean ages with their associated errors (weighted standard deviation). Filled square symbols are mean ages, however filled diamond symbols are median ages.

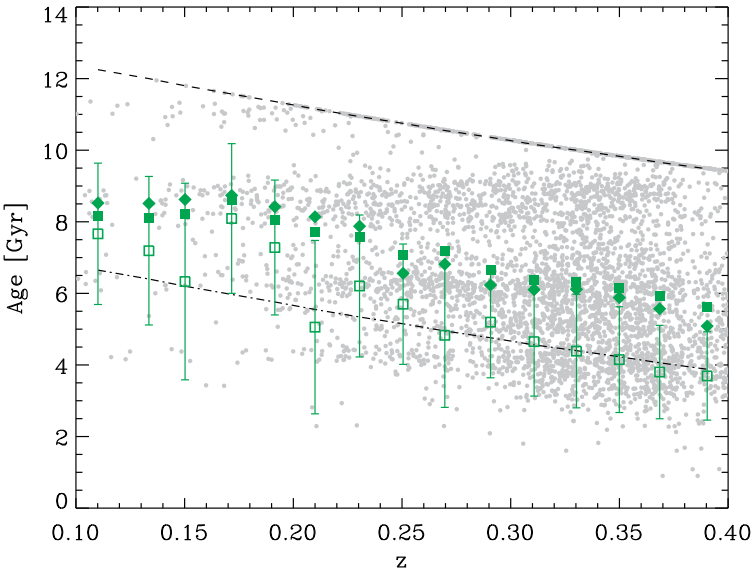

Figure 3.29: Individual fits using VM models (each grey symbols). Open square symbols are weighted mean ages with their associated errors (weighted standard deviation). Filled square symbols are mean ages, however filled diamond symbols are median ages.

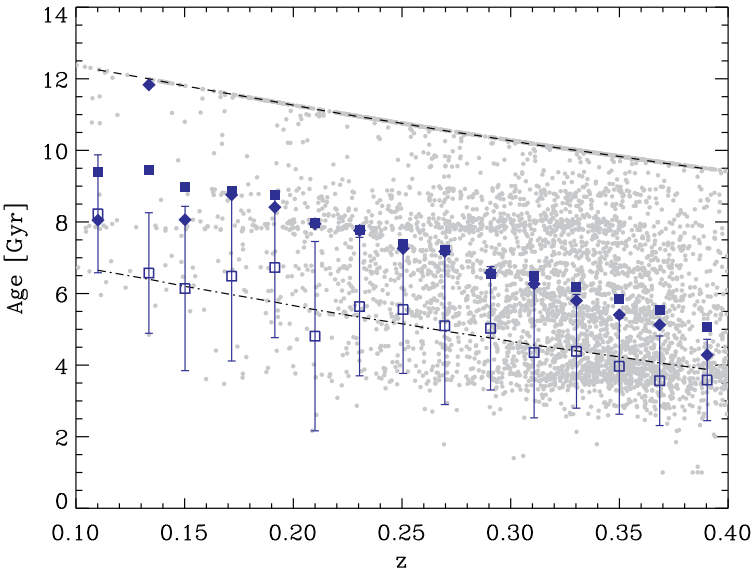

Figure 3.30: Individual fits using BC03 models (each grey symbols). Open square symbols are weighted mean ages with their associated errors (weighted standard deviation). Filled square symbols are mean ages, however filled diamond symbols are median ages.

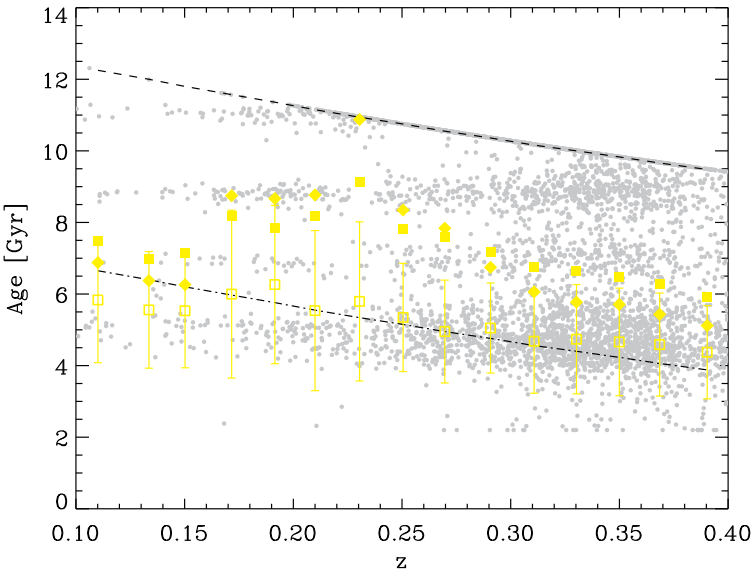

Figure 3.31: Individual fits using M11 models (each grey symbols). Open square symbols are weighted mean ages with their associated errors (weighted standard deviation). Filled square symbols are mean ages, however filled diamond symbols are median ages.

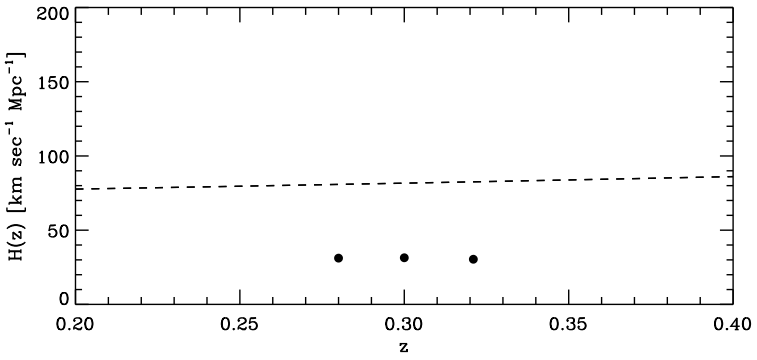

Figure 3.32: $H(z)$ measurements using SSP ages when fitting galaxies with TMJ models. The $H(z)$ estimates while using the SSP equivalent ages extracted from Lick indices fitting by assuming a prior on metallicity and α-element (black circles) and combining Hγ_F, Mgb, Fe5270 and Fe5335 indices. The dashed line is the theoretical $H(z)$ of a flat ΛCDM cosmology model assuming $H_0 = 71$ km s^{-1} Mpc^{-1} and $\Omega_m = 0.27$. $H(z \simeq 0.32)$, $H(z \simeq 0.30)$ and $H(z \simeq 0.28)$ were estimated when fitting a straight line on the ages over $0.24 < z < 0.40$, $0.22 < z < 0.38$, and $0.20 < z < 0.36$ respectively.

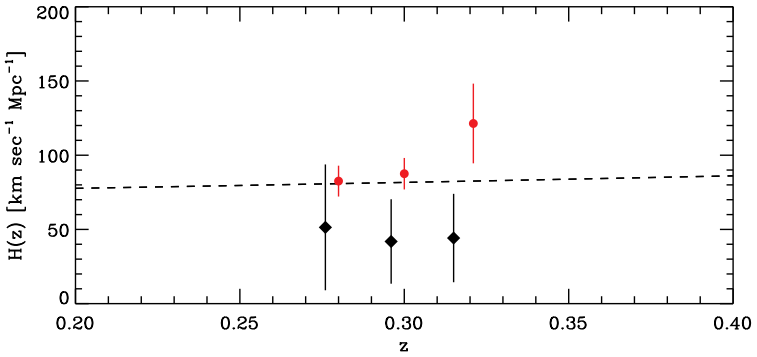

Figure 3.33: $H(z)$ measurements using SSP ages when fitting galaxies with PE models. The $H(z)$ estimates while using the mean ages (black diamonds), the ages extracted from the stacked spectra fitting (red circles). The dashed line is the theoretical $H(z)$ of a flat ΛCDM cosmology model assuming $H_0 = 71$ km s^{-1} Mpc^{-1} and $\Omega_m = 0.27$. $H(z \simeq 0.32)$, $H(z \simeq 0.30)$ and $H(z \simeq 0.28)$ were estimated when fitting a straight line on the ages over $0.24 < z < 0.40$, $0.22 < z < 0.38$, and $0.20 < z < 0.36$ respectively.

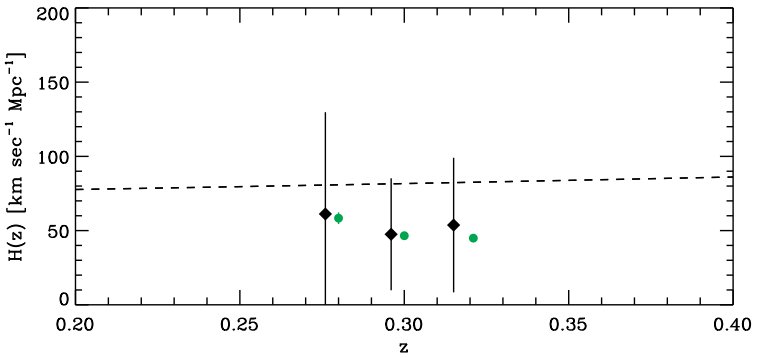

Figure 3.34: $H(z)$ measurements using SSP ages when fitting galaxies with VM models. The $H(z)$ estimates while using the mean ages (black diamonds), the ages extracted from the stacked spectra fitting (green circles). The dashed line is the theoretical $H(z)$ of a flat ΛCDM cosmology model assuming $H_0 = 71$ km s^{-1} Mpc^{-1} and $\Omega_m = 0.27$. $H(z \simeq 0.32)$, $H(z \simeq 0.30)$ and $H(z \simeq 0.28)$ were estimated when fitting a straight line on the ages over $0.24 < z < 0.40$, $0.22 < z < 0.38$, and $0.20 < z < 0.36$ respectively.

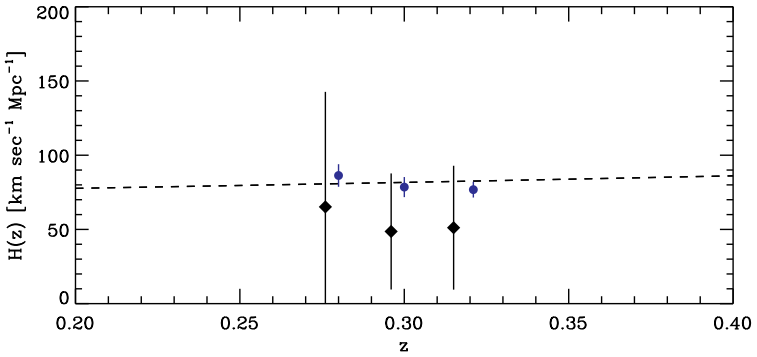

Figure 3.35: $H(z)$ measurements using SSP ages when fitting galaxies with BC03 models. The $H(z)$ estimates while using the mean ages (black diamonds), the ages extracted from the stacked spectra fitting (blue circles). The dashed line is the theoretical $H(z)$ of a flat ΛCDM cosmology model assuming $H_0 = 71$ km s^{-1} Mpc^{-1} and $\Omega_m = 0.27$. $H(z \simeq 0.32)$, $H(z \simeq 0.30)$ and $H(z \simeq 0.28)$ were estimated when fitting a straight line on the ages over $0.24 < z < 0.40$, $0.22 < z < 0.38$, and $0.20 < z < 0.36$ respectively.

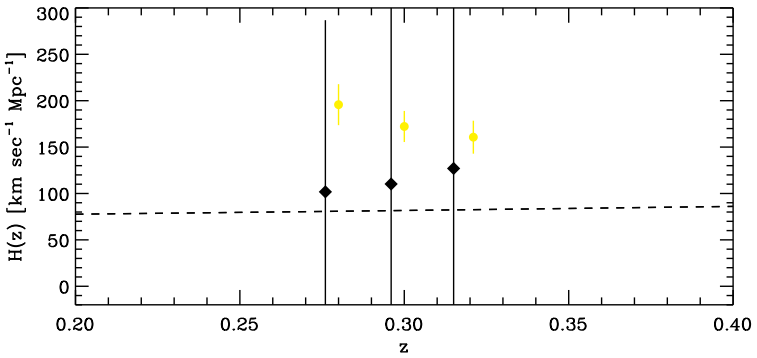

Figure 3.36: $H(z)$ measurements using SSP ages when fitting galaxies with M11 models. The $H(z)$ estimates while using the mean ages (black diamonds), the ages extracted from the stacked spectra fitting (yellow circles). The dashed line is the theoretical $H(z)$ of a flat ΛCDM cosmology model assuming $H_0 = 71$ km s^{-1} Mpc^{-1} and $\Omega_m = 0.27$. $H(z \simeq 0.32)$, $H(z \simeq 0.30)$ and $H(z \simeq 0.28)$ were estimated when fitting a straight line on the ages over $0.24 < z < 0.40$, $0.22 < z < 0.38$, and $0.20 < z < 0.36$ respectively.

Chapter 4

H(z) measurement with SALT-LRGs

4.1 Introduction

In this chapter, we discuss another CC experiment. It was carried out using LRGs observed with SALT. The availability of the SALT telescope for the South African Astronomical community allows us to focus on planning and conducting observations. This chapter highlights results of several observations with *SALT* telescope to obtain spectra of massive selected LRGs at $z \simeq 0.40$ and $z \simeq 0.55$ and demonstrates the $H(z \simeq 0.47)$ measurement.

Crawford *et al.* (2010a) found that a 3% measurement would be viable from a large redshift program, and have optimized an observation of using this experiment with SALT telescope. Therefore, observations with SALT in two narrow redshift ranges $z \simeq 0.40$ and $z \simeq 0.55$ were proposed in order to accurately measure $H(z)$ at $z \simeq 0.47$, providing constraints on the nature of the dark energy. In Crawford *et al.* (2010a), not only the total time required to complete this experiment using Robert Stobie Spectrograph (RSS) at SALT was estimated, but the estimation of the uncertainties in the mean age as function of galaxies that could possibly be observed was also studied. As underlined by several authors (Moresco *et al.*, 2012a; Simon *et al.*, 2005; Stern *et al.*, 2010b), this experiment requires the most massive early-type galaxies and it should be note that such galaxies have formed at highest redshifts. The possibility of having a wide optical wavelength coverage, and high resolution spectra from a 10-meter telescope like SALT helps us to explore the availability of the CC method. These data are obtained as a starting point of a future survey named SCALPEL (SALT Cosmic Ages of Luminous Passive ELlipticals survey).

4.2 SALT telescope

Located at the site of the South African Astronomical Observatory (SAAO) in Sutherland -South Africa, SALT is the largest single optical telescope in the southern hemisphere and among the largest in the world. This 10-meter class optical telescope consists of 91 individual 1.2 m hexagonal mirrors (see figure 4.1) resulting in a total of a hexagonal primary mirror array of 11.1 m by 9.8 m. The design was based upon the Hobby-Eberly Telescope (HET) in Texas. The optical system was redesigned, resulting in a larger field of view and effective collecting area. SALT has a fixed elevation angle (53°) and can rotate only about its azimuth axis (540°) to acquire objects, hence a significant cost saving compared to a complex telescope. The optical payload and the tracker are positioned above the primary mirror. The tracker moves across the mirror on a virtual spherical surface, allowing objects to be followed as the earth rotates, without adjusting the azimuth angle for a period of up to two hours. From this the observation area in the sky is more or less an annulus shaped area (between zenith distances from 48° to 59°), it can reach objects in the declination range from $\delta = -75°$ to $\delta = +10°$.

Figure 4.1: SALT primary mirror.

Similar to the HET, SALT specializes mainly in spectroscopic observations using different modes, although a facility CCD imaging camera (SALTICAM) is also available, and most recently a high-resolution spectrograph (SALTHRS) which is still being commissioned . The SALTICAM is used not only for imaging and photometry, but it also serves as the telescope acquisition camera. The Robert Stobie Spectrograph (RSS) operates in UV-Visible regime ($310 - 900nm$), and is available in three modes: long-slit and multi-object low to medium resolution spectroscopy, Fabry-Perot imaging spectroscopy and polarimetry.

SALT operates as a queue-scheduled telescope, where observations are planned in advance before the semester starts. The PIPT program was provided in order to propose (phase I) and plan (phase II) an observing time.

4.3 Sample selection

4.3.1 2dF-SDSS LRG survey

2dF-SDSS LRG and QSO (hereafter 2SLAQ) was a survey conducted by a collaboration between the UK, Australia and the US, and it was completed in August 2005. The 2SLAQ survey was a spectroscopy follow-up on LRG targets based on SDSS Data Release 4 photometric survey, focusing on targets beyond $z \geq 0.4$. The aim was to extend the SDSS-LRG survey which sampled LRGs in the redshift range $0.15 < z < 0.5$ (Eisenstein *et al.*, 2001) to higher redshifts $z \sim 0.8$. All LRGs and QSOs spectra were taken with the 2 degree Field (2dF) instrument on the 3.9 m Anglo-Australian Telescope (AAT). Over 10 000 high redshift QSOs and $\sim$ 14 000 LRGs were observed and their redshift was measured. The sky region of the survey is about 2° wide equatorial stripes. A wedge diagram of the sky is plotted in figure 4.3. The total area of the survey was approximately 180 degrees^2.

A brief technical review of the survey is given here. More details about the survey is given by Cannon *et al.* (2006). The SDSS survey used the selection criteria described by Eisenstein *et al.* (2001), which is based on their colours ($g - r$ and $r - i$) and apparent magnitudes, to select LRGs from the SDSS photometry for spectroscopy follow-up. Eisenstein *et al.* (2001) defined two different cuts: cut I helps to sample LRGs at redshifts $z < 0.40$ where the 4000 Å break features are noticeable in the g band, whereas cut II was used for higher redshifts where the 4000 Å break features are located in the r band. The 2SLAQ survey used the same colour criteria as cut II to extract LRG targets from the SDSS imaging. The colour selection (specially in $g - r$ colour) was refined in order to provide enough targets to fill the 2dF field. Thus the 2SLAQ selection allowed additional range of star forming LRGs over the SDSS selection which provided only LRGs close to the red and dead passively-evolving galaxies. In addition to the colour selection, a magnitude limit of $i_{devV} < 19.8$ (de-reddened) was imposed to acquire a reasonable S/N within 4 hours of observing time.

LRGs were observed using 2dF spectrograph 2 (Lewis & Simnett, 2002) with a 600 lines mm^{-1} V grating, yielding a dispersion of 2.2 Å pix^{-1} and an effective resolution of about 5Å (R $\sim$ 1000). The detector used was a Tek1024 CCD with 1024 $\times$ 1024 pixels. Almost all LRG spectra were taken with a central wavelength of 6150Å setting, covering a wavelength range of 5050 - 7250 Å. This coverage was chosen to assure the determination of redshifts of all target objects in the survey using the common lines Ca II H& K, and the detection of [OII]λ3727 emission line down to $z = 0.35$. All LRG redshifts were derived using ZCODE (a fortran code), a derivative of the code used to determine redshifts for 2dFGRS survey. There

was a quality flag "Qop" assigned to each derived redshift based on the visual inspection of the galaxy spectrum and the redshift cross-correlation function. A quality flag of "Qop" ≥ 3 indicates high level of confidence $(95 - 99\%)$ in the calculated redshift meaning that the redshift obtained from the spectrum is valid (Cannon *et al.*, 2006). Over 18,500 LRGs spectra were obtained, resulting in 13 121 spectroscopically confirmed LRGs and 663 foreground M type stars.

4.3.2 MegaZ-LRG catalogue

MegaZ-LRG catalogue (Collister *et al.*, 2007) was a photometric redshift catalogue of over a million LRGs in the redshift range $0.4 < z < 0.7$ with limiting magnitude $17.5 < i < 20$. The catalogue was based on SDSS DR4 five band (*u, g, r, i, z*; Fukugita *et al.* (1996); Smith *et al.* (2002)) imaging data using the same selection criteria for the 2SLAQ LRG survey. The photometric redshift of each one of the galaxies in this catalogue was obtained using a neural network ANNz photometric-redshift estimator code (Collister & Lahav, 2004; Firth *et al.*, 2003), tested in prior with the 2SLAQ catalogue (Cannon *et al.*, 2006), and based on the de-reddened *griz* model magnitudes. The rms photometric redshift error was about $\delta z \simeq 0.03(1 + z)$. LRGs in this catalogue cover almost 6000 degrees^2. The MegaZ-LRG catalogue could be obtained from **http://www.2slaq.info**.

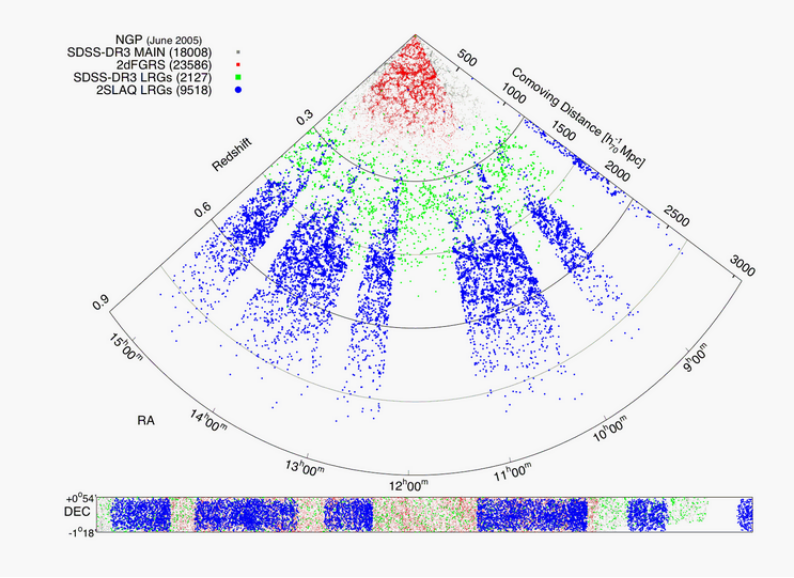

Figure 4.2: One patch of the sky in the Northern Galactic strip showing the distribution of the 2SLAQ LRGs (blue points). Redshifts of all galaxies are plotted in this diagram as function of RA. Grey and red points are all type of galaxies at $z < 0.3$ from SDSS-DR3 and 2dFGRS respectively. Green points are LRGs from SDSS-DR3 LRGs survey at the intermediate redshifts. Credit from the 2SLAQ website **http://www.2slaq.info**

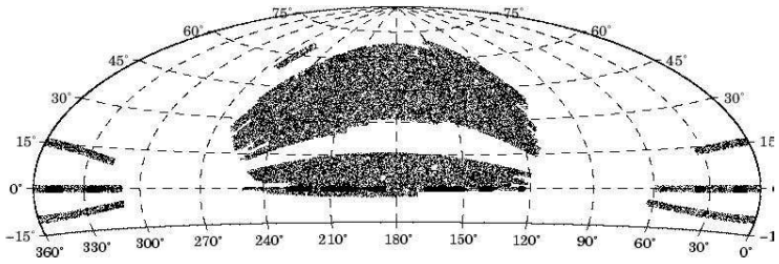

Figure 4.3: Map of 50 000 randomly selected galaxies from MegaZ-LRG catalogue which is represented by the grey points, and 2SLAQ fields are shown by the black points. This map covers the entire SDSS DR4 area. Taken from Collister *et al.* (2007)

Table 4.1: *WISE* conversion factors to the AB system.

Band	AB mag	zero mag Jy
W1	2.699	309.540
W2	3.339	171.787
W3	5.174	31.674
W4	6.620	8.363

4.3.3 Matching 2dF-SDSS with WISE catalogue

The Wide-field Infrared Survey Explorer *WISE* satellite was launched in 2009 December into a Sun-synchronous polar orbit, to survey the entire sky in four mid-infrared bands centred at 3.4, 4.6, 12 and 22 μm (hereafter W1, W2, W3, W4)(Wright *et al.*, 2010). It has detected hundreds of millions of objects, hence its data archive became an important tool to study the evolution of the stellar mass and star formation of local and distant Universe in its wavelength ranges. Optical and Infrared surveys have been already cross-matched in order to conduct multiwavelength studies of any extragalactic sources. For instance Donoso *et al.* (2012) and Yan *et al.* (2013) combined *WISE* and SDSS to investigate closely the properties of any type of galaxies in the mid-IR regime. A few authors (e.g. Jarrett *et al.*, 2011) have proved that *WISE* colours is an excellent AGN selection tool. Meanwhile, the BigBOSS (a continuation of the Baryon Oscillation Spectroscopic Survey) team is investigating a new technique to target LRGs at high redshift ($z > 0.6$) using *WISE* data. *WISE* is very sensitive at W1 (minimum 5σ sensitivity = 0.05 mJy) and least sensitive at W4 (minimum 5σ sensitivity = 6 mJy). *WISE* photometric data was calibrated relative to standard stars measurements using VEGA magnitude system. All *WISE* magnitudes were converted to the AB system as given by the formula $m_{AB} \equiv m_{Vega} + \Delta m$. The conversion factors to the AB system Δm were given in Jarrett *et al.* (2011) as shown in table 4.1.

The use of *WISE* data helped us to achieve our goal of selecting most massive early-type galaxies which have typically formed at highest redshifts. Prior to the selection of the observed LRGs, we calculated their masses by performing a SED fitting. In order to achieve

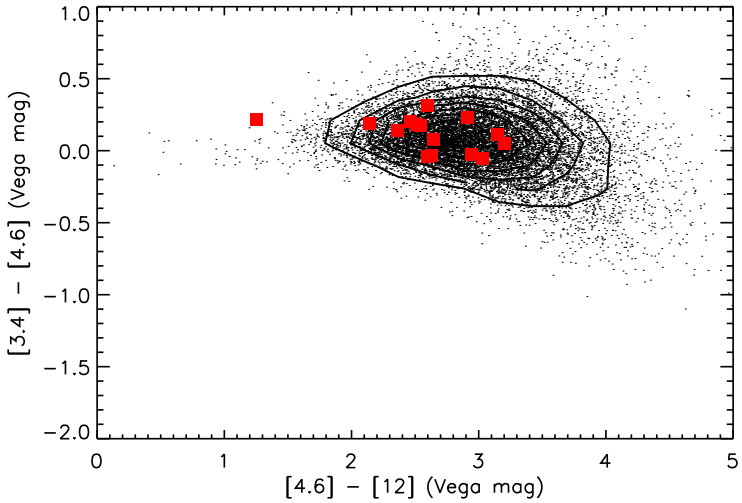

Figure 4.4: WISE colour-colour diagram of the matched sources with our sample (red points). This diagram is plotted using observed colours.

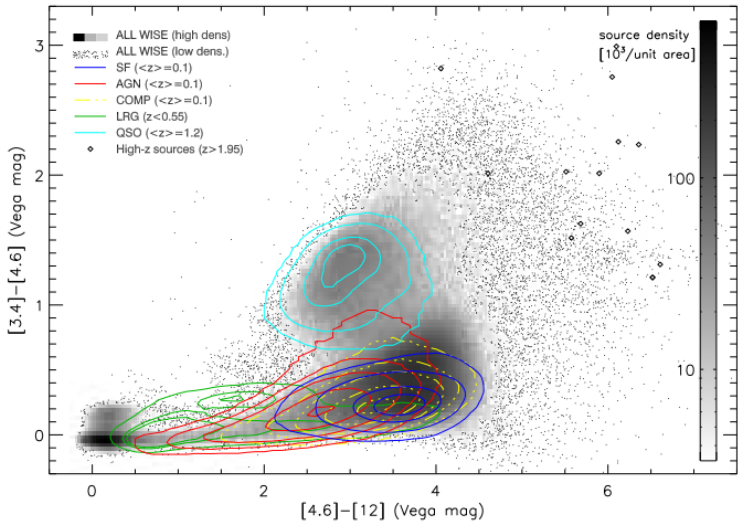

Figure 4.5: WISE colour-colour diagram with SDSS DR7 spectroscopy galaxy catalogue. LRGs at $z < 0.55$ are plotted in green contours, bright QSOs in cyan. The blue, red and yellow contours indicate sources classified as star forming (SF), seyfert AGNs and composite systems (COMP) respectively. Credit from Yan *et al.* (2013)

this fitting, more photometry datasets of each galaxy in 2SLAQ sample is needed to have a better fit. With the 2SLAQ catalogue, there are 5 different (u, g, r, i, z) magnitudes as in SDSS photometric survey. However only the model magnitudes were used during the SED fitting. The availability of the *WISE* catalogue helped us to add 4 photometric datasets in

the Infrared regime to our SED fitting. We cross-correlated the 2SLAQ LRGs catalogue with the *WISE* data and detected 13518 sources in four mid-infrared bands centred at 3.4, 4.6, 12 and 22μm. We then combined the optical photometry provided by 2SLAQ with mid-infrared flux densities to build a SED of these detected sources.

The combination of W1, W2 and W3 bands of *WISE* is used to produce the colour-colour diagram and to locate the various classes of astrophysical objects (Jarrett *et al.*, 2011). This diagram is then useful for separating galaxy population, in particular old stellar population, star forming and galaxies dominated by AGN activity. The W1 and W2 bands are very sensitive to the evolved stellar population and hot dust, meaning the more their colour increases, the more the object is very active, such as in AGN or starbust. However, W3 band is very sensitive to star formation activity and dominated by both the 11.3 μm polycyclic aromatic hydrocarbon (PAH) emission and the 10 μm amorphous silicate absorption. Yan *et al.* (2013) has reproduced the *WISE* colour diagram of SDSS-LRGs (DR7) and QSOs along with sources classified as star forming galaxies, seyfert AGNs and composite systems (See figure 4.5). In figure 4.4, the observed colours of all matched sample with our selected galaxies are shown. The location of our matched sample falls inside the location of LRGs plotted by Yan *et al.* (2013) in figure 4.5, but inclined towards the star forming sources. This is not surprising since a significant number of LRGs in the 2SLAQ catalogue have been found to undergo a recent star formation activity (Roseboom *et al.*, 2006).

4.3.4 Stellar masses

4.3.4.1 Spectral Energy Distribution fitting

In order to calculate the physical parameters such as galaxy mass, stellar mass and star formation history from the observations, SED fitting method is the most popular and efficient method. We performed a simple SED fitting using the 2dF-SDSS and *WISE* photometry data to obtain the stellar mass of the selected galaxies. The fitting procedure including the input and output parameters will be discussed.

CIGALE The SED fitting was performed with Code Investigating GALaxy Evolution (CIGALE[1], Burgarella *et al.* (2005), Noll *et al.* (2009)). This code calculates a grid of theoretical SEDs and fits observed photometric fluxes from ultraviolet to infrared. It consists of reproducing the dust-attenuated stellar population models, IR dust emission models and spectral lines templates. A Bayesian analysis is then used to derive the optimal physical parameters, the associated uncertainties of the observed galaxy as well as the best computed model. More details of the mechanism of CIGALE can be found in Noll *et al.* (2009) and Giovannoli *et al.* (2011). Figure 4.6 shows a summary on how CIGALE works. Green boxes represent the input parameters provided by the user such as: observed fluxes and redshift of

[1] http://cigale.oamp.fr/

each galaxy, star formation history (τ and ages t of old and young stellar populations, mass fraction of young populations f_{ySP}), dust attenuation (V-band attenuation A_V, reduction factor of A_V for old stellar populations given by f_{att}) and dust emission (IR power-law slope α, AGN related fraction of L_{dust}). Blue boxes correspond to the models and templates used such as: dust attenuation law of Calzetti *et al.* (2000), IR libraries of Dale & Helou (2002), SSP models of Maraston (2005) or PEGASE (Fioc & Rocca-Volmerange, 1997) etc. Pink boxes constitute the computational steps incorporated in CIGALE whereas yellow boxes are the outputs and final results.

Input and Output parameters The choice of the input parameter is critical depending on the aim of the study. Among the two stellar population synthesis models provided by CIGALE, Maraston (2005) were used to generate the models of the SED of galaxies. We assumed a solar metallicity and a Salpeter IMF. The star formation history implemented in CIGALE is a combination of two bursts representing an old more passively evolving and young populations. It has been proved that including the two populations improved results of the SED fitting rather than using a single star formation rate (Buat *et al.*, 2011; Giovannoli *et al.*, 2011). This was just a simple approximation as the real scenario is more complex, as in the case of LRGs. These galaxies are composed of old passively evolving stellar populations, nevertheless we chose a model of two stellar components, old and young stellar populations, to improve our results. The old stellar population is produced by an exponentially decreasing star formation rate over $t_1 = 6$ Gyr, adopting an e-folding time τ_1 ranging from 1 Gyr to 10 Gyr with 2 Gyr steps. However, the young stellar population is created not constantly but also exponentially over $t_2 = 0.2$ Gyr. Somehow the two star formation components in the code are linked by their mass fraction. The fraction of the young stellar population f_{ySP} corresponds to the fraction of the young stellar population mass over the total mass and we set this fraction as in the interval [0.001;0.999].

The attenuation curve based on the law of Calzetti *et al.* (2000) is a baseline of the CIGALE code. It also allows user to vary the attenuation law and to add a UV bump. The modification of the slope is controlled by the factor $(\lambda/\lambda_V)^\delta$ where $\lambda_V = 5500$ Å is the reference wavelength of the V filter, and δ is the slope of the attenuation curve. We decided not to modify the slope of the attenuation (i.e. no modification was added to the original Calzetti attenuation curve, $\delta = 0$) and not to add any UV bump. The UV bump is usually detected around 2175 Å. Our observed fluxes are in the optical and mid-IR wavelength regimes, therefore the UV bump may not affect our fits only in the NUV band. In addition its strength varies strongly from galaxy to galaxy and depends on the inclination of the galaxy. Its strength could be investigated with CIGALE by detecting the bump in the attenuation law (Buat *et al.*, 2011), but it requires a fine sampling of the SED in the rest-frame UV in order to accurately determine its amplitude. Such investigation is also beyond the objective of this study. We considered the effect of attenuation for old stellar population by adding the

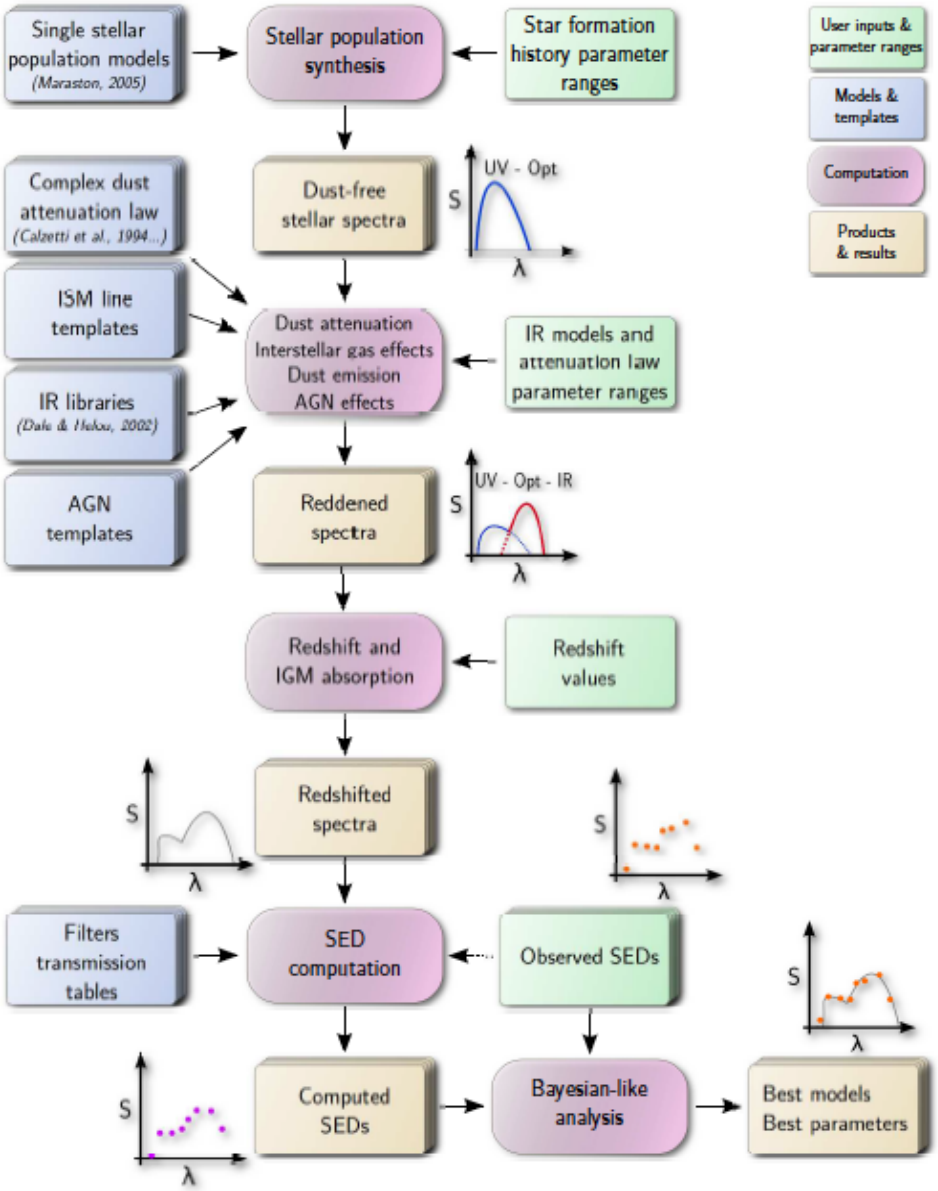

Figure 4.6: CIGALE operation workflow. This illustrates how CIGALE works. Credit from Roehlly *et al.* (2012).

reduction factor $f_{att} = 0.5$. The semi-empirical model templates of Dale & Helou (2002) was chosen to fit IR observations which are parametrized by the power law slope α in the interval [1; 2.5]. The normal galaxies are found to have this range of α where $\alpha \sim 2.5$ for quiescent (Dale & Helou, 2002). The input parameters values used for the SED fitting are listed in table 4.2. The *WISE* relative spectral response curves are from Wright *et al.* (2010) and are available as part of the Explanatory Supplement to the *WISE* preliminary data release products.

The output derived parameter - stellar mass - of each galaxy is given in table 4.5. The best fit models superposed on the observed fluxes are shown in figure 4.7. We can clearly see that few observed fluxes are not fitted well. For instance the observed u-band flux for most of the SED-fitting is not well reproduced by the code, which might be due to the fact that u-band flux for some galaxies is often swamped by the photon noise of the sky (Blanton *et al.*, 2003). This can be identified by the size of errors on the flux and the value of the flux itself (very faint) for some galaxies. Although the code is able to give a low value of minimal χ^2 for the fit, for example in the case of 2SLAQ J134058.83-003633.6 the minimal χ^2 is 1, it fails to reproduce the observed data as seen in figure 4.7. Note that the accuracy of the output relies on the input parameters. For our sample selection, we only require an estimate of the stellar mass, therefore we did not carry out exhaustive testing of input parameters.

Table 4.2: List of the input parameters of the code CIGALE and their selected range

Parameters	Symbol	Range
Star formation history		
metallicities (solar metallicity)	Z	0.02
τ of old stellar population models in Gyr	τ_1	1.0; 3.0; 5.0; 7.0; 10.0
ages of old stellar population models in Gyr	t_1	6.0
ages of young stellar population models in Gyr	t_2	0.025; 0.05; 0.1; 0.2
fraction of young stellar population	f_{ySP}	0.001; 0.01; 0.1; 0.999
IMF	S	Salpeter
Dust attenuation		
slope correction of the Calzetti law	δ	0.0
V-band attenuation for the young stellar population	$A_{V,ySP}$	0.15; 0.45; 0.60; 0.90; 1.20; 1.5; 1.8; 2.1
reduction of A_V basic for old stellar population	f_{att}	0.5
IR SED		
IR power-law slope	α	1.0; 1.5; 2.0; 2.5

4.3.5 Selection criteria

The selection was based on both the stellar mass and brightness of the galaxy. We further constrained the selection criteria by requiring objects without signature of any star formation or AGN-like activity. This is identified using the equivalent widths of Hδ absorption line and [OII]λ3727 emission line as in Roseboom *et al.* (2006). For the Hδ, they used the same definition of passband and sidebands as the standard Lick index Hδ_A (Worthey & Ottaviani, 1997), however for the [OII] emission line they used the definition from Balogh *et al.* (1999). The passbands and sidebands used are found in table 4.3. A negative equivalent width value is defined as emission line and a positive value as absorption line. We also calculated the equivalent widths of those two lines for those galaxies which are not included in the catalogue used by Roseboom *et al.* (2006). We followed their definitions of Hδ and [OII]. The publicly

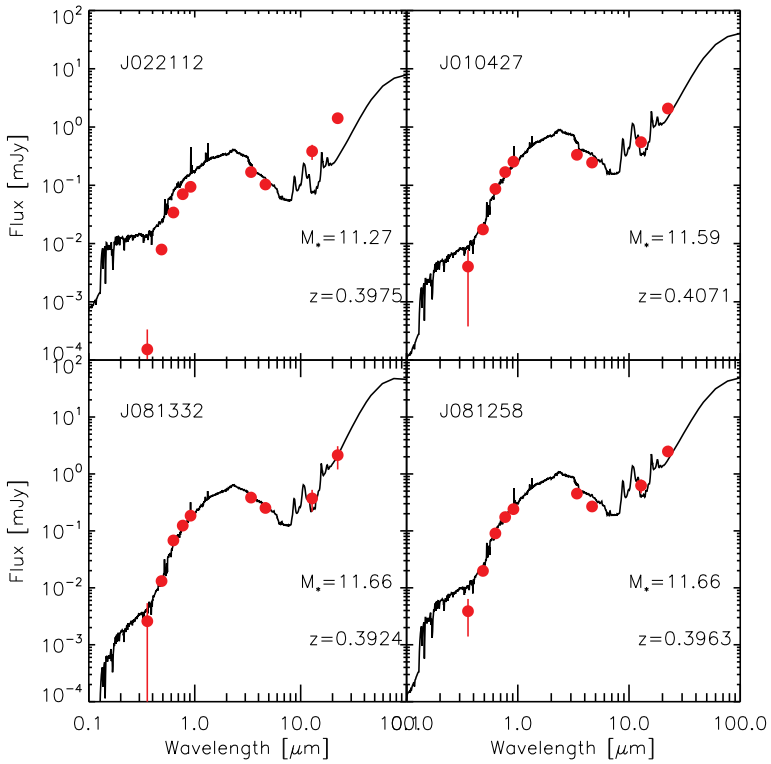

Figure 4.7: Examples of best fit models. The observed data are plotted with red points and the best fit model with a solid line. The stellar mass and redshift of each galaxy are also shown.

available code LECTOR[1] by Vazdekis was used to measure the equivalent widths of the two spectral features. This code also returns values of different line-strengths (e.g. Lick indices (Worthey & Ottaviani, 1997; Worthey *et al.*, 1994), indices of Rose (Rose, 1994), indices of Vazdekis (Vazdekis *et al.*, 2001), etc.) and allows users to define and measure additional indices as the case of [OII] used here. The errors on the equivalent widths were calculated on the basis of photon statistics following the formulae given in Cardiel *et al.* (1998); Cenarro *et al.* (2001); Vazdekis & Arimoto (1999). These errors are quite different from the ones calculated in Roseboom *et al.* (2006) where a formula defined by Bohlin *et al.* (1983) was used. Although both calculations did not take into account the contribution from the systematic errors in the spectra such as poor sky-subtraction or flat fielding. It should be noted that 2SLAQ spectra are not flux calibrated.

Table 4.4 shows the equivalent widths measured on Hδ and [OII] lines from both this study and the catalogue of Roseboom *et al.* (2006), and the spectral classification for each galaxy. Roseboom *et al.* (2006) classified LRGs according to their position in the EWHδ - EW[OII] space as the following:

[1]http://www.iac.es/galeria/vazdekis/vazdekis_software.html

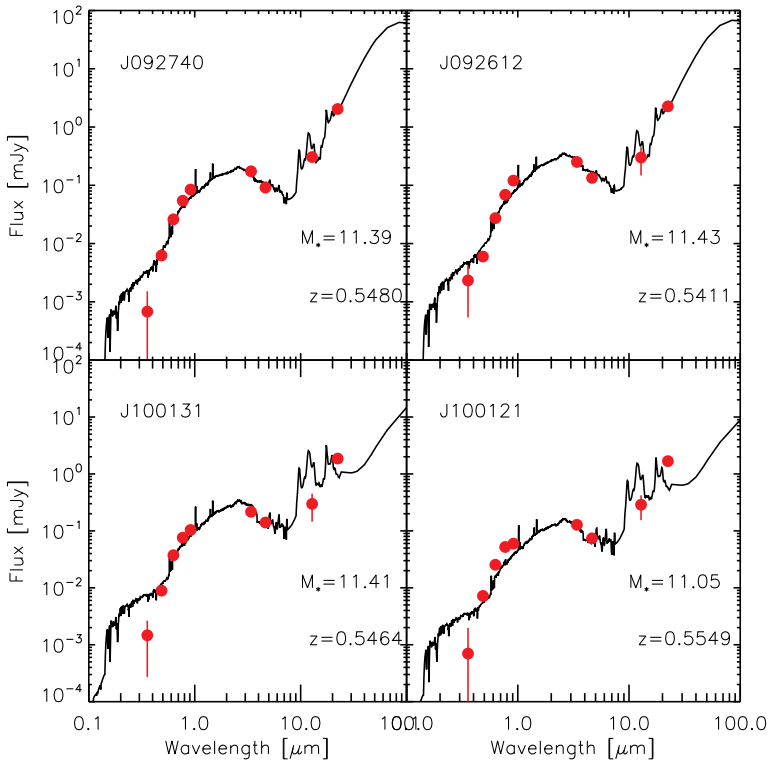

Figure 4.7: continued.

- Passive (old passively evolving stellar population): LRGs with no significant [OII] emission line or Hδ absorption line i.e. EW[OII] > -8Å and EWH$\delta < 2$Å.
- k+a : LRGs with significant Hδ absorption line but no [OII] emission line i.e. EW[OII] > -8Å and EWH$\delta > 2$Å.
- em: LRGs with significant [OII] emission line but no Hδ absorption line i.e. EW[OII] < -8Å and EWH$\delta < 2$Å.
- em+a: LRGs with significant $H\delta$ absorption line and significant [OII] emission line i.e. EW[OII] > 2Å and EWH$\delta > 2$Å.

Basically, we selected LRGs considered as passive, including five galaxies without [OII] detection that we still considered as passive for their insignificant Hδ absorption line (See table 4.4). We accidentally included two k+a LRGs in our sample that we thought would not affect our results. In addition, all the galaxies analysed in this chapter have redshift quality flags greater than or equal to 3, i.e. high level of confidence in the calculated redshift. This is very important for the accuracy of the full spectral fitting since this redshift will be used as the redshift guess. The stellar mass of these galaxies must be higher than $10^{11} M_{\odot}$ and their magnitude $V > 21$. We also included an extra object SDSS J013403.82+004358.8 in

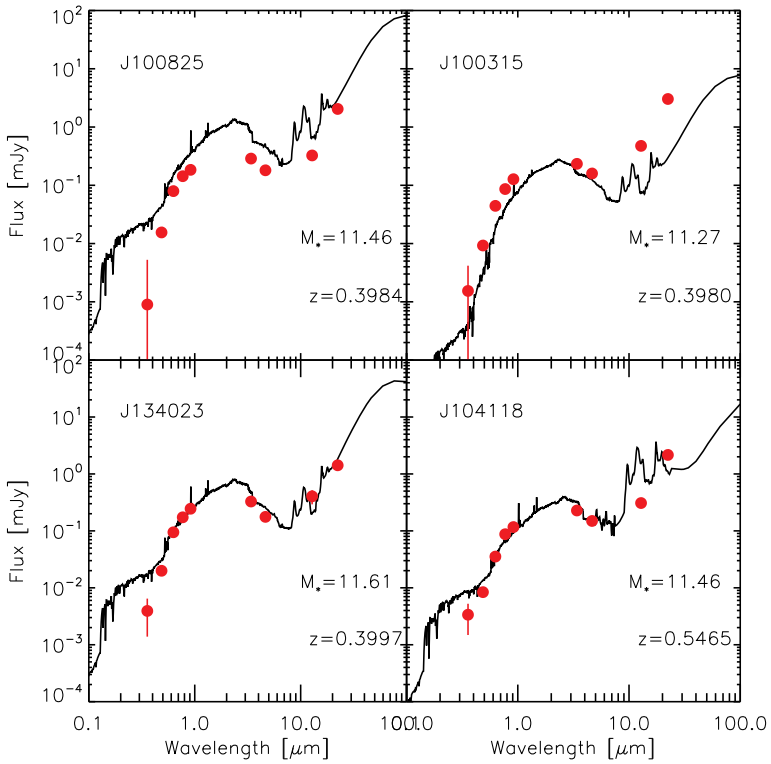

Figure 4.7: continued.

our sample. This target was selected from the MegaZ-LRG photometric redshift catalogue (Collister *et al.*, 2007). This galaxy has been confirmed as a central cluster galaxy of a very rich cluster in Szabo *et al.* (2011) and Wen *et al.* (2012) cluster catalogues where we obtained the spectroscopic redshift. The mass of this object was derived by fitting only its model u, g, r, i, z fluxes. Since LRGs are often found sitting in groups or clusters, we have verified the other galaxies whether any of them is a member of any cluster. 2SLAQ J134023.93-003126.8 has also been classified as a central cluster galaxy by Wen *et al.* (2012). The names, coordinates and the characteristics of the LRGs candidates being studied are summarized in table 4.5.

Table 4.3: Passbands and side continuum bands used to measure H_δ and [OII] equivalent widths.

Index	Line passband (Å)	Blue continuum sideband (Å)	Red continuum sideband (Å)
H_δ	4083.5 - 4122.25	4041.6 - 4079.75	4128.5 - 4161.0
[OII]	3713 - 3741	3653 - 3713	3741 -3801

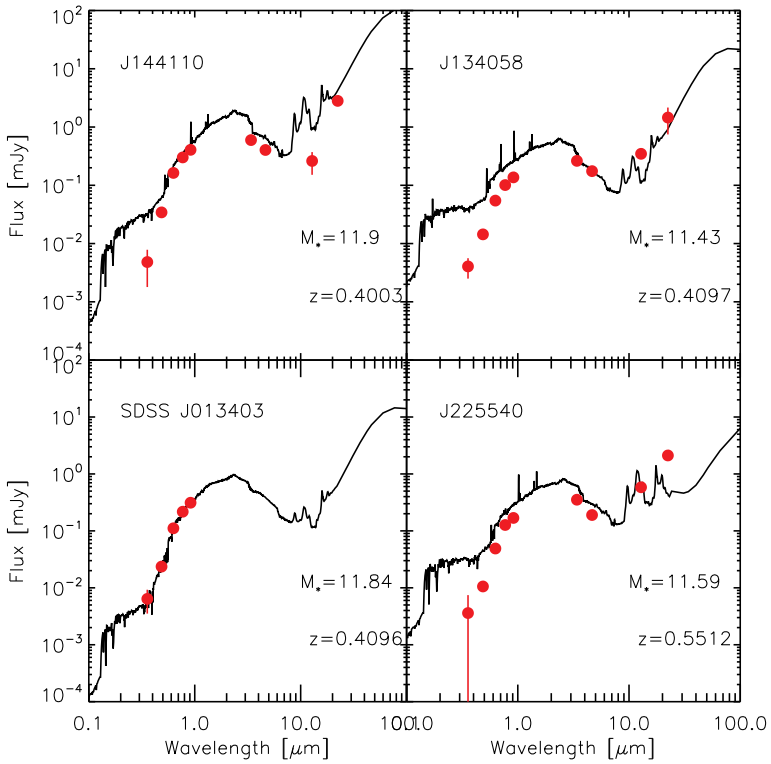

Figure 4.7: continued.

Table 4.4: The equivalent widths measured on H_δ and [OII] lines from Roseboom *et al.* (2006) and from this study.

Name	EW[OII] (Å)	EWH_δ (Å)	classification	comments
2SLAQ J081258.12−000213.8	NAN	-0.38±0.44	Passive?	this study
2SLAQ J081332.20−004255.1	NAN	-3.15±0.47	Passive?	this study
2SLAQ J100315.23−001519.2	-2.57±0.53	-1.09±0.46	Passive	this study
2SLAQ J100825.72−002443.3	NAN	-0.24±0.42	Passive?	this study
2SLAQ J134023.93−003126.8	NAN	0.57± 0.32	Passive?	this study
2SLAQ J134058.83−003633.6	NAN	1.29± 0.36	Passive?	this study
2SLAQ J092612.79+000455.8	2.77±0.65	-1.69±0.70	Passive	this study
2SLAQ J092740.75+003634.1	1.28±0.21	-5.38±0.15	Passive	Roseboom *et al.* (2006)
2SLAQ J100121.88+002636.4	1.35±0.36	1.37±0.46	Passive	this study
2SLAQ J100131.77−000548.0	0.63±0.30	2.77±0.15	k+a	Roseboom *et al.* (2006)
2SLAQ J104118.06+001922.3	-1.61±0.55	-6.42±0.31	Passive	Roseboom *et al.* (2006)
2SLAQ J144110.62−002754.5	-2.06±0.85	-3.73±0.76	Passive	this study
2SLAQ J010427.15+001921.5	-1.90±0.51	0.71±0.477	Passive	this study
2SLAQ J022112.71+001240.3	-4.85	4.29±0.74	k+a	this study
2SLAQ J225540.39−001810.7	-3.23±0.50	0.68±0.29	Passive	Roseboom *et al.* (2006)
SDSS J013403.82+004358.8	-1.14	-0.47	Passive	this study

Table 4.5: Characteristics of the galaxies observed with SALT telescope. All galaxies were selected from the 2dF-SDSS LRG catalogue (Cannon *et al.*, 2006), except for SDSS J013403.82+004358.8 which was extracted from the photo-z catalogue known as MegaZ-LRG (Collister *et al.*, 2007). Its spectroscopic redshift was taken by matching it with the cluster catalogue of Wen *et al.* (2012); and its magnitude in $g-$band was from NED database **(http://ned.ipac.caltech.edu/**, however all remained magnitudes i.e. in $V-band$ are from SIMBAD database **(http://simbad.u-strasbg.fr/simbad/)**.

Name	RA (2000.0)	DEC (2000.0)	V mag	Redshift	$logM_{star}$ $M_{\odot}$	$E(B-V)_{galactic}$ mag
2SLAQ J081258.12−000213.8	08 12 58.1	−00 02 14	19.65	0.4063	11.66±0.03	0.039
2SLAQ J081332.20−004255.1	08 13 32.2	−00 42 55	19.62	0.3924	11.66±0.02	0.031
2SLAQ J100315.23−001519.2	10 03 15.2	−00 15 19	19.62	0.3980	11.27±0.01	0.039
2SLAQ J100825.72−002443.3	10 08 25.7	−00 24 43	19.44	0.3984	11.46±0.02	0.033
2SLAQ J134023.93−003126.8	13 40 23.9	−00 31 27	18.89	0.3997	11.54±0.01	0.032
2SLAQ J134058.83−003633.6	13 40 58.8	−00 36 34	19.29	0.4097	11.43±0.05	0.026
2SLAQ J092612.79+000455.8	09 26 12.8	+00 04 56	20.52	0.5411	11.43±0.02	0.032
2SLAQ J092740.75+003634.1	09 27 40.7	+00 36 34	20.25	0.5480	11.39±0.01	0.038
2SLAQ J100121.88+002636.4	10 01 21.9	+00 26 36	19.48	0.5549	11.05±0.04	0.025
2SLAQ J100131.77−000548.0	10 01 31.8	−00 05 48	20.03	0.5464	11.41±0.01	0.035
2SLAQ J104118.06+001922.3	10 41 18.0	+00 19 22	20.02	0.5465	11.46±0.01	0.055
2SLAQ J144110.62−002754.5	14 41 10.6	−00 27 54	20.55	0.4003	11.90±0.01	0.038
2SLAQ J010427.15+001921.5	01 04 27.1	+00 19 21	19.71	0.4071	11.59±0.02	0.035
2SLAQ J022112.71+001240.3	02 21 12.7	+00 12 40	20.80	0.3975	11.27±0.04	0.036
2SLAQ J225540.39−001810.7	22 55 40.4	−00 18 11	20.10	0.5512	11.59±0.01	0.086
SDSS J013403.82+004358.8	01 34 03.8	+00 43 59	20.3g	0.4092	11.84±0.01	0.024

4.4 Data reduction

4.4.1 Spectroscopic Observations

The spectroscopic observations of this sample was carried out with the Robert Stobie Spectrograph (RSS, Burgh *et al.*, 2003; Kobulnicky *et al.*, 2003) at SALT. The observations were done in long-slit mode. Originally, this project was proposed to use the Multi-Object spectroscopy (MOS) mode in order to target more LRGs in each observation time. But due to the unavailability of the MOS during our proposals, we adjusted this project to use the long-slit mode. Long-slit optical spectra of the sample were obtained during the special semester of 2011 and the first semester of 2012 under proposal codes 2011-3-RSA_OTH-026 (PI: A. Ratsimbazafy) and 2012-1-RSA_OTH-013 (PI: A. Ratsimbazafy) respectively. We have used two different settings of PG0900 grating to cover the wavelength range $\sim 4000-6000$Å (rest-frame wavelength) at both redshift. For the 2011 observations, we used a slit width of 1" giving a spectral resolution of about $\sim$ 4-6 Å (R $\sim$ 1900). However, the 2012 observations were obtained with a slit width of 1.5" yielding a spectral resolution of R $\sim$ 1300. The log of observations is given in table 4.6.

For all of our observation we used the setting `FAINT` and `SLOW` for gain setting and readout speed respectively.

In order to perform a standard reduction of two-dimensional long-slit spectra, spectra

of a Neon arc lamp were taken after each observation to correct for wavelength calibration. Five flat-field images were also obtained in order to correct for pixel to pixel variations. The spectrophotometric standard stars were observed either during evening or morning twilight for flux calibration.

Table 4.6: The observing log. The first 11 galaxies were observed during the semester 2011-3 run, and the last 5 during the first semester of 2012-1 observations.

Name	Date YYYY-MM-DD	Exposure time (sec)	slit (arcsec)	Grism (grooves/mm)	Resolution (Å/pix)	P.A. (deg)	Comments moon,seeing
2SLAQ J081258.12−000213.8	2012-01-25	2883	1	900	0.95	0.0	dark-grey, 1.5”
2SLAQ J081332.20−004255.1	2011-12-20	2883	1	900	0.95	0.0	dark-grey, 1”
2SLAQ J100315.23−001519.2	2012-01-29	2883	1	900	0.95	0.0	dark-grey, 1”
2SLAQ J100825.72−002443.3	2012-01-22	2883	1	900	0.95	0.0	dark-grey, 1.4”
2SLAQ J134023.93−003126.8	2012-02-21	2697	1	900	0.95	0.0	dark, 1.95”
2SLAQ J134058.83−003633.6	2012-02-20	2697	1	900	0.95	0.0	dark, 1.3”
2SLAQ J092612.79+000455.8	2012-01-26	2883	1	900	0.95	0.0	dark-grey, 1.4”
2SLAQ J092740.75+003634.1	2012-01-26	2883	1	900	0.95	0.0	dark-grey, 1.4”
2SLAQ J100121.88+002636.4	2012-02-28	3183	1	900	0.95	0.0	grey, 1.6”, no flats
2SLAQ J100131.77−000548.0	2012-02-20	3483	1	900	0.95	0.0	grey, 1.3”
2SLAQ J104118.06+001922.3	2012-02-23	3183	1	900	0.95	0.0	grey, 1.7”
2SLAQ J144110.62−002754.5	2012-07-19	3915	1.5	900	0.95	0.0	dark, 2.0”
2SLAQ J010427.15+001921.5	2012-09-17	3714	1.5	900	0.95	69.5	dark, 1.5”
2SLAQ J022112.71+001240.3	2012-09-19	3714	1.5	900	0.96	115.0	dark, 1.46”
2SLAQ J225540.39−001810.7	2012-09-20	3714	1.5	900	0.95	-161.0	dark, 1.5”
SDSS J013403.82+004358.8	2012-09-20	3714	1.5	900	0.95	-132.0	dark, 1.9”

4.4.2 Spectroscopic Data Reduction

4.4.2.1 Longslit data reduction

For each observation, a tar file containing the raw data, the semi-reduced products and the documentation describing the observation log was provided to the principal investigator. The product subdirectory contains the semi-reduced data processed with the semi-automated code SALT PyRAF pipeline called PySALT [1] Crawford *et al.* (2010b). This includes fidelity checking, overscan subtraction, gain and cross-talk correction, and mosaicking the 6 amplifiers of the 3 CCDs. It is important to read through the observation log to identify each type of file (science, flat, arc, standard star). Additional information is also available in the document such as the seeing or the exposure time.

The standard long-slit reduction procedures such as wavelength calibration, background subtraction, extracting one-dimensional spectra and flux calibration were then carried out on the pre-processed data. All of these were performed with the IRAF [2] `TWODSPEC` package. A detailed description of each of these steps are given below.

A - CCD reduction

Fidelity checking The first step was performed by the task `saltprepare`. This task prepared the raw FITS files for the reduction pipeline processing. It verified and added the missing but required keywords in the headers such as `NSCIEXT`, `EXTNAME`, `EXTVER` in order to be consistent with the IRAF-based tools. It could also create variance frames for the data based on the pixel variance and the read noise.

Gains This step was performed by the task `saltgain`. It corrected for the gain of the different CCDs by multiplying images by a constant factor appropriate for the gain correction. Each amplifier had its own specific gain factor which is assumed constant across the amplifiers. The program reads the values of the gain and readout noise from an ASCII file provided by users through the "*gaindb*" argument and updates the values of the keywords `GAIN` and `RDNOISE`. If no ASCII file was provided, the program will extract the default values form the data header `GAIN`. The gain correction is based on the following equation:

$$\text{electrons} = (\text{gain} + \text{GAIN1} \times 10^{-6} \times \text{data}) \times \text{data} \tag{4.1}$$

where data is in ADU and gain is in electrons/ADU. The parameter `GAIN1` is a keyword in the header. `GAIN1` is equal to 0 unless the user set this keyword to a non zero value meaning non-linear gain. The SALT CCDs have shown evidence of non-linearity[3] and this correction

[1] pysalt.salt.ac.za

[2] Image Reduction and Analysis Facility, a software system distributed by the National Optical Astronomy Observatories (NOAO). http://iraf.noao.edu/

[3] https://sciencewiki.salt.ac.za/index.php/Gain_measurements_made_on_20110622

takes account of that.

Table 4.7 represents the values of the gain that we have used.

Table 4.7: Gain database of CCD amplifiers used during 2011 and 2012 observation runs. Rdn means read-out-noise.

	Amplifier 1		**Amplifier 2**		**Amplifier 3**		**Amplifier 4**		**Amplifier 5**		**Amplifier 6**	
	Gain	**Rdn**	**Gain**	**Rdn**	**Gain**	**Rdn**	**Gain**	**Rdn**	**Gain**	**Rdn**	**Gain**	**Rdn**
2011	1.48	2.56	1.55	2.55	1.58	2.38	1.50	2.36	1.49	2.53	1.42	2.48
2012	2.14	2.47	2.27	2.51	1.68	2.40	1.59	2.44	1.52	2.45	1.47	2.39

Cross talk The cross talk process was performed by the task `saltxtalk`. Each SALTICAM and RSS CCD has two readout amplifiers. The task corrected images for the cross talk between these amplifiers occurring during the readout of the chips and creating faint ghost sources across them. The ghost sources are in the form of faint mirror images across amplifier boundaries of bright sources. The cross talk could be corrected by subtracting a scaled image of one amplifier from its neighbour, assuming that images are not saturated or non-linear. The scaling factors were provided as an ASCII file through the `XTALKFILE` argument or extracted from the header keyword `XTALK`.

Bias subtraction The task `saltbias` was performed to correct for the CCD overscan and bias. This task extracts the CCD overscan region from the headers and will then fit and subtract it. After that it will trim the image and update its headers. Finally it will subtract the master bias if required. At the moment, the master bias subtraction is not recommended for SALT data, therefore only the overscan and trimming option are used.

A master bias frame can be created by stacking several bias images with the same gain setting and readout noise as the science data.

Mosaicking The amplifier images obtained during the same exposure time could be mosaicked into a single frame and stored in a single extension of the output FITS file. Mosaicking the 6 amplifiers of the 3 CCD was performed by the task `saltmosaic`. The program will read the CCD geometry definition file (ASCII format) provided by the users through the "*geomfile*" argument. Then, it will combine each of the individual amplifiers into a single frame and apply the geometric CCD transformation to the image.

B - long-slit reduction

Trimming and Cosmic ray removal The first step was to change the extension format of the output data from the CCD primary reduction. The goal was to prepare FITS files for the standard IRAF reduction tasks. The two dimensional science spectrum, the flat field images and the arc spectrum were trimmed to exclude non useful areas before performing the rest of the reduction. Cosmic ray hits were then removed from the two dimensional spectra using the LAplacian COSMIC (LACOSMIC) ray identification software (van Dokkum, 2001). This is an algorithm for robust cosmic ray identification and rejection using Laplacian edge detection. The procedure works robustly by detecting cosmic rays of arbitrary shapes and sizes by the sharpness of their edges and distinguishes between poorly sampled point sources and comic rays with high confidence. The effectiveness of the cosmic ray removal depended on the maximum number of iterations chosen. Any remaining signature was removed by hand using `splot`. The two ccd gaps were filled with interpolated pixel values.

Flat fielding The five flat-field images were combined into a master flat by the IRAF task `scombine`. The median combine was used to remove any existing cosmic rays. This had to be normalized by its mean to preserve the mean level of the input image and was then applied to the science data. We used the task `mkillumflat` to create the illumination corrected master flat. This process helped to correct for the differences in sensitivity across the field and between detector pixels.

Wavelength Calibration The `twodspec.longslit` package from IRAF was used for the purposes of the wavelength calibration, more precisely the following tasks `identify`, `reidentify`, `fitcoords` and `transform` were performed. Firstly, the task `identify` identified arc lines in a spectra and calculated the wavelength solution. For the redshift of the objects studied here, Neon arc lamp was always observed. The `Ne.salt` table was added to the default linelist of IRAF. The task first plotted the center of the arc image and few features were identified manually. The remaining lines were then identified automatically and fitted by the function Chebyshev with 5^{th} order for the wavelength solution. The poorly fitted points were removed until a reliable RMS was obtained.

The wavelength solution was then used to reidentify the identified lines in all the other rows of the 2D spectra, which could be done using the task `reidentify`. This task also traced the curvature of the lines in the spatial direction. The task `fitcoords` created the transformation function that would be applied to the image in order to estimate the wavelength solution and rectify. To transform a spectroscopic image based on the wavelength solution from the arc lamp, the task `transform` was needed, and it used the transformation function previously calculated by `fitcoords`.

Background subtraction The night sky background and emission lines were then subtracted from the data. The task used was `background`. It estimated background emission

from each wavelength by fitting a 5^{th} order Chebyshev polynomial to each wavelength column and subtracts it from the science spectra.

Extraction standard star spectra All of the above tasks were also applied to the standard star spectra. The spectra of the spectrophotometric standard stars were taken at the same instrumental configuration as the corresponding science target. The 1D spectra was extracted from the 2D image using the `apall` task from the `APEXTRACT` package.

Flux calibration Due to the nature of the SALT telescope, the unfilled entrance pupil of the telescope moves during the observation, therefore an absolute flux calibration is not possible. However, a relative flux correction can be feasible to recover the spectral shape using the observed spectrophotometric standard stars. We used the spectra of the spectrophotometric standard stars extracted above to create the sensitivity curve of the CCD. They were used to flux calibrate the science frames. The effective airmass for each individual target had already been calculated by the SALT pipeline PySALT and was mostly stored in the header. However, if it is missing or has a negative value, it could be calculated using the following formula:

$$\frac{1}{\cos(0.017453292 \times (90 - \mathrm{TELALT}))} \tag{4.2}$$

where `TELALT` is the telescope elevation at readout which is available in the header. The task `standard` was used to integrate the spectrophotometric standard star spectra over the bandpasses in the associated calibration fluxes. To derive the sensitivity curve, the task `sensfunc` was run, fitting observed spectral energy distribution of the standard star with a 20th order polynomial. The sensitivity curve was then applied to the science spectra using task `calibrate`. All spectra were corrected for the atmospheric extension using the table of atmospheric extinction of Sutherland versus airmass, provided as a complementary document on SALT webpage.

Extraction science spectra As for the spectrophotometric standard, we used the task `apall` to extract the one dimensional spectrum. The extracted 1D spectra were then median combined by using the task `scombine`. The extraction aperture and background windows were defined interactively. The sky background was fitted by a low order polynomial.

The red ends of the spectra suffer from significant fringing effects. Due to these effects, there are numerous remaining sky emission lines. Removing fringes was a little bit of a challenge, but we tried our best to remove them using flat fielding method. Recently it seems that taking some dithering could help to remove the fringe patterns. Unfortunately, this option was not fully operated during our observation runs. In addition to the sky emission lines contamination, the red regions of the spectra were also contaminated by the absorption features that originate in the Earth's atmosphere, referred to as telluric features. The strongest telluric features occur in A band $\lambda\lambda 7600 - 7630$Å, in B band $\lambda\lambda 6860 - 6890$Å

and in the following wavelength range $\lambda\lambda 7170 - 7350$Å. The 1D spectra were not corrected for the effects of the telluric contamination.

4.4.3 Estimate signal-to-noise ratio

To verify how good the reduced spectra are we measured the S/N ratio per pixel. The task `splot` was run to review the 1D spectra. With this program we were able to measure the S/N for different regions in the spectrum. Each region has about 100 pixels wide. The final S/N ratio was the mean of all measured S/N within each region. The `splot` does not know about the gain and readnoise of the detector. It only assumes that the bumps and wiggles in the spectrum represent the noise, and compares the size of the "noise" to the level of signal in the continuum. The value of S/N per pixel was then converted to a S/N per resolution element by multiplying by the square root of the number of pixels per resolution element. Since multiple exposures were used to make up the total exposure time, then the single exposure S/N was multiplied by the square root of the number of exposures.

4.4.4 Galactic extinction

Even though there was a small effect on the correction in our observed wavelength ranges, all spectra were corrected for foreground Galactic extinction using the reddening maps of Schlegel *et al.* (1998) and the extinction curve of the Fitzpatrick (1999) with R=3.1. The E(B − V) parameter at galactic for each galaxy is given in table 4.5. The description of the process is as follows: RA & DEC coordinates of the observed galaxy were converted to the required galactic coordinates, l, b. via `EULER` an IDL code. The `DUST_GETVAL` routine was then run to get the reddening value E(B − V) for a given position on the sky. It returned an extinction correction in magnitudes. Values of E(B − V) calculated here are quite similar to the values found in the NED database. The derived values were then used to deredden a flux vector using the Fitzpatrick (1999) parametrization.

4.5 Fitting LRG spectra

Modern techniques of full spectral fitting allow comparison of observations and models on a pixel by pixel basis, for example: GANDALF, Sarzi *et al.* (2006)), pPXF, Cappellari & Emsellem (2004)), ULySS (Koleva *et al.*, 2009) etc. ULySS is the package we used to fit our observed spectra. As mentioned before in chapter 3 section 3.7.7, ULySS is not strictly for an absolute flux calibrated spectra, as it is not sensitive to galactic extinction or any other cause affecting the shape of the spectrum. Besides, it gives options to visualize the degeneracies and validate the errors on the parameters. We fitted each LRG spectrum to single-age, single-metallicity population synthesis models. LRGs are believed to form most of their stars very early in the Universe, and as such, SSP models are generally found to be good

descriptions for their spectra (Jimenez *et al.*, 2003; Liu *et al.*, 2012; Moresco *et al.*, 2012a; Simon *et al.*, 2005; Stern *et al.*, 2010a; Zhang *et al.*, 2012, , etc.). Although in our previous work (Crawford *et al.*, 2010a) we did find that LRGs may better be described by slightly extended star formation histories, we have only fit the LRGs to SSPs in order to compare this work to previous studies.

4.5.1 LSF study

Prior to fitting our science spectra, we needed to match the resolution between the observed spectra and models. The spectral resolution matching is described by the LSF (more details about LSF in chapter 3 section 3.7.7.3). In this study, we used the spectrum of a standard star HD 14802 observed with SALT during the night of 2012/10/11 along with the target SDSS J013403.82+004358.8. The atmospheric parameters (T_{eff}, log (g) and [Fe/H]) of this star are already known in SIMBAD database. They have been measured by several scientists but we chose the recent ones by Ramírez *et al.* (2013). If those parameters are unknown, they also can be determined by fitting the star spectrum with ULySS and used to calculate the relative LSF. Measuring the LSF means determining the broadening function (cz, σ and possibly h3, h4) in a sequence of small wavelength ranges. Here we used an overlapping windows of 200 Å separated with 100 Å steps. After comparing different relative LSF using different spectral object, the decrease instrumental velocity dispersion, σ_{instr} is typically from 150 km s^{-1} (blue) to 110 $km\ s^{-1}$ (red) which is the characteristic of the spectrograph and grating. While the radial velocity, v_{rad} changes from 0 to 31 km s^{-1}, due to the uncertainty in the wavelength calibration. The LSF relative to the Elodie.3.1 library obtained with ULySS is shown in figure 4.8. This relative LSF was then injected to the models to generate the resolution-matched models by the convolution function in ULySS. The injection of the LSF to the models is necessary in order to take into consideration the variation of the resolution with wavelength and to remove possible small uncertainties in the wavelength calibration. We used the resolution-matched models to perform the fitting process of the observed spectra.

4.5.2 SSP fitting

The SSP models that we used are based on the Pegase-HR (PE) models (Le Borgne *et al.*, 2004). These models were introduced in chapter 3 section 3.7.7.2. The PE models were chosen among the other models because their empirical libraries have a wide range and number of age and metallicity with high spectral resolution. After testing different fits using four models described in chapter 3, these models provided the most stable SSP results. Since LRG are supposed to be old, sometimes the oldest ages of these galaxies hit the upper limits of the models. To avoid this problem during the fitting, we used an age limit, which is the age of the Universe at each redshift. We take this into account especially during the Monte-Carlo simulation runs.

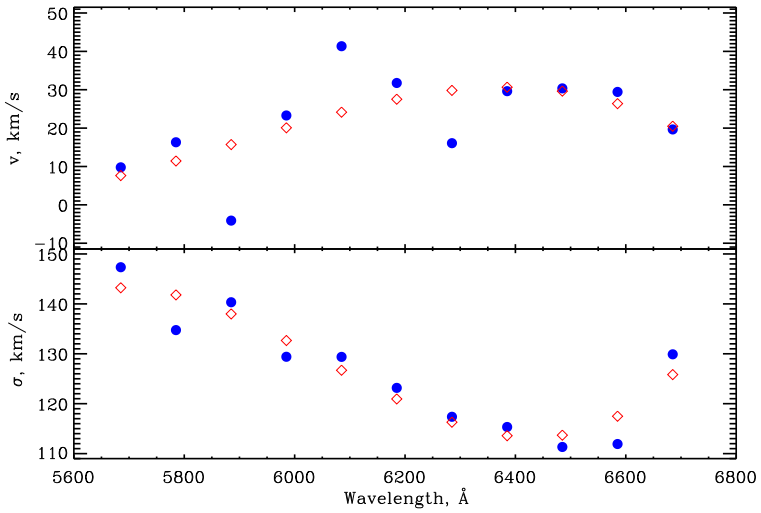

Figure 4.8: Relative LSF between the observed spectrum and the models as a function of wavelength. Radial velocity is at the top panel, the instrumental velocity dispersion is at the bottom panel. Blue points are the measured LSF, and red points are the smoothed version which are used to inject to the model spectra.

We derived ages and metallicities as well as the kinametics of the LRGs by fitting our observations to the SSP models. The full wavelength range of each galaxy spectrum was mostly used during the fitting process. The red end of some of the spectra was significantly affected by the fringing. Due to the presence of the fringes, removal of the sky emission lines became very difficult. Thus the residuals from the bright sky emission lines are very significant. For those spectra where the residuals of the sky emission lines removal are very significant, we set the maximum wavelength range to be 5500Å.

The errors on the parameters are the 1 sigma errors. These errors are computed from the covariance matrix by the ULySS calling function MPFIT (a fitting function) algorithm. MPFIT provides the optimal parameters from the best fit and the 1 sigma errors on each one of them. In addition, ULySS provides the possibility of exploring and visualising the parameter space with χ^2 maps, convergence maps and Monte-Carlo simulations to validate the errors on the parameters. We performed Monte-Carlo simulations and χ^2 maps experiments to carefully test the reliability of the fitting. A series of 500 Monte-Carlo simulations was performed. At each step of the simulation, a random noise equivalent to the observed noise was added. The outputs from this simulation are the mean values of the resulting distributions of all parameters: age, metallicity, velocity dispersion and their corresponding standard deviations. To help assess the quality of the fits, χ^2 maps and convergence maps were examined. We could also improve the fit by changing initial guesses according to their outputs.

4.6 SSP paramaters

We report results of the SSP fits using PE model in table 4.8, including ages, metallicities and kinematics. Individual fit is shown in figure 4.9. The wavelength range used for the fit is also given in the plots. The results of the SSP best fits and the Monte-Carlo simulations are also shown in figure 4.9. The Monte-Carlo simulations help us to verify our SSP results by visualizing the degeneracies. The mean values of the simulations are consistent with the best fit results which are valid in most cases. Nonetheless there is some discrepancy between the two results (Koleva *et al.*, 2009) which is mostly due to the degeneracy between parameters and the level of noise in the the spectra. The estimated noises obviously influence the results of the Monte-Carlo simulations in term of the errors in the parameters. High S/N spectra show well defined point distributions as in figure 4.9, and hence lead to more precise measurements of the age and metallicity of the galaxies. However, there are a few galaxies as exceptions, for instance SDSS J013403.82+004358.8 and 2SLAQ J134023.93-003126.8 (both of them at $z \simeq 0.40$). Only these two behave differently during the MC fitting. Note that both of them are defined as central cluster galaxies by Wen *et al.* (2012). These two galaxies might have some complex star formation history as in those central galaxies at the focus of a cooling flow (Crawford *et al.*, 1999; Loubser, 2014; Loubser *et al.*, 2009). They also have higher velocity dispersion in the sample of galaxies at $z \simeq 0.40$. Note that it is clear that older galaxies have higher velocity dispersions than those younger galaxies. Results of velocity dispersions are shown in the table 4.8 and plotted in figure 4.12.

Examples of χ^2 and convergence maps of 2SLAQ J092740.75+003634.1 are presented in figure 4.10. We present both of them in the age-metallicity plane with the results of the Monte-Carlo simulations. Either the χ^2 or the convergence maps gives similar output results compared to the best fits (Age is about 2.85±0.31 Gyr and metallicity around 0.38±0.08 dex).

Figure 4.11 shows ages and metallicities obtained during the fits of galaxies at $z \simeq 0.40$ and $z \simeq 0.55$. 2SLAQ J092612.79+000455.8 seems to have an older age, and higher velocity dispersion than the other galaxies at $z \simeq 0.55$. This galaxy has the lowest S/N spectrum in that redshift. Its S/N is high enough (a minimum S/N = 10 per resolution element) to be used in our analysis (see table 4.8). Despite the number of galaxies at $z \simeq 0.55$, it is clear that there is an age-redshift relation, that is, the mean age at $z \simeq 0.40$ is older than that at $z \simeq 0.55$. The galaxies at $z \simeq 0.40$ have an average age of 3.64 ± 0.23 Gyr, 2.72 ± 0.25 Gyr for galaxies at $z \simeq 0.55$. However the overall metallicity spreads from [Fe/H] ≈ 0.0 dex to [Fe/H] ≈ 0.4 dex and has an average of [Fe/H] ≈ 0.2 dex which is consistent with the metallicity of a typical LRG found in the literature. It is important to note that these galaxies are assumed to have similar metallicities (Jimenez *et al.*, 2003; Liu *et al.*, 2012; Zhang *et al.*, 2012) i.e. no evolution, and the value should be scattered between about 0.1 dex and 0.2 dex. The errors on the mean age and metallicity were obtained by applying the standard propagation of error

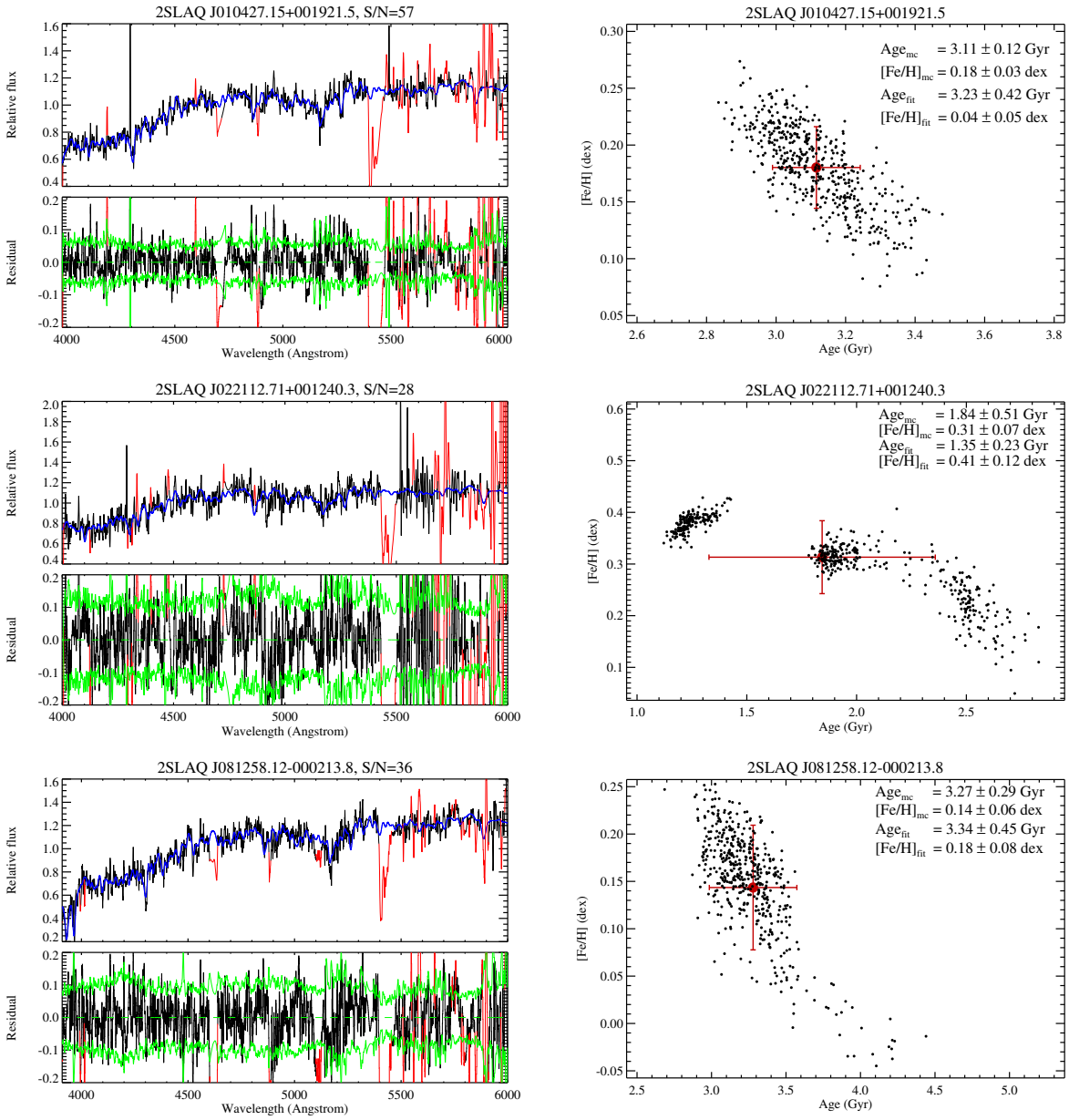

Figure 4.9: All the fits performed with ULyss. The left-hand panel shows individual spectral fitting, galaxy spectra are in black and best fit in blue line. The red regions were excluded and masked in the fit: outliers. The green lines in the residuals from the fit are the estimated $1-\sigma$ deviation. Each spectrum is plotted in the wavelength range adopted during the fits. Fluxes are expressed in erg cm^{-2} s^{-1} Å^{-1}. S/N ratios per resolution element of the observed spectra are also given. The right-hand panel illustrates the results from the 500 Monte-Carlo simulations. Ages and metallicities values from the simulations indicated by the red points are compared with the those provided by single fits (written in the legend).

technique.

In this work, we find higher metallicity values, and younger ages than the total sample of red galaxies in Stern *et al.* (2010a) at both redshifts but we note that we have a small

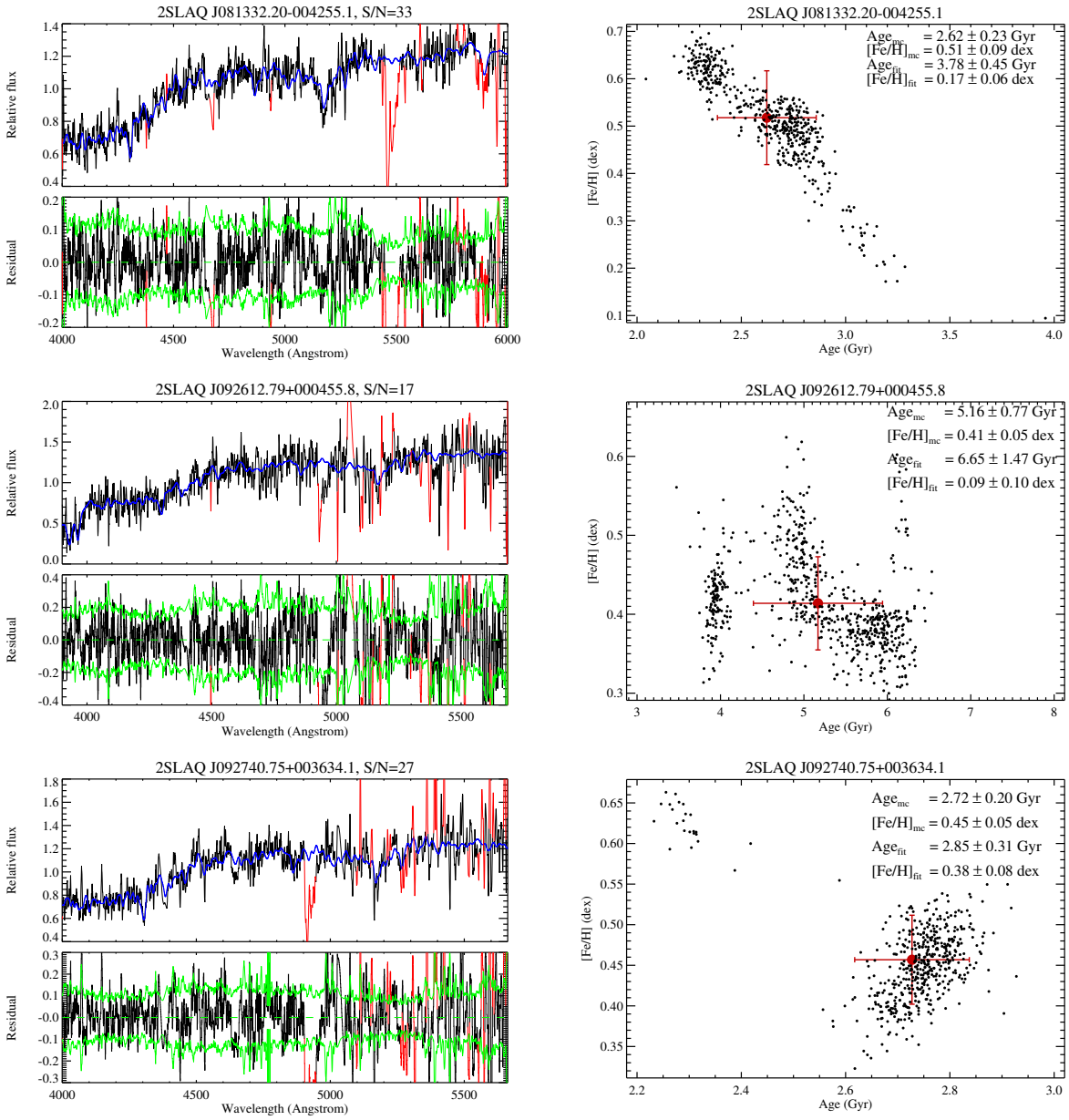

Figure 4.9: continued.

number of galaxies in our sample. In their results using the SPICES and VVDS samples, they found mostly younger ages. Basically, the number of galaxies in our sample is very few to be compared with the whole sample of Stern *et al.* (2010a).

4.7 H(z) estimates

If the ages of the SSP represent the ages of the galaxies, we can use the estimated ages to calculate the Hubble parameter $H(z)$ via the difference in ages associated with the corresponded

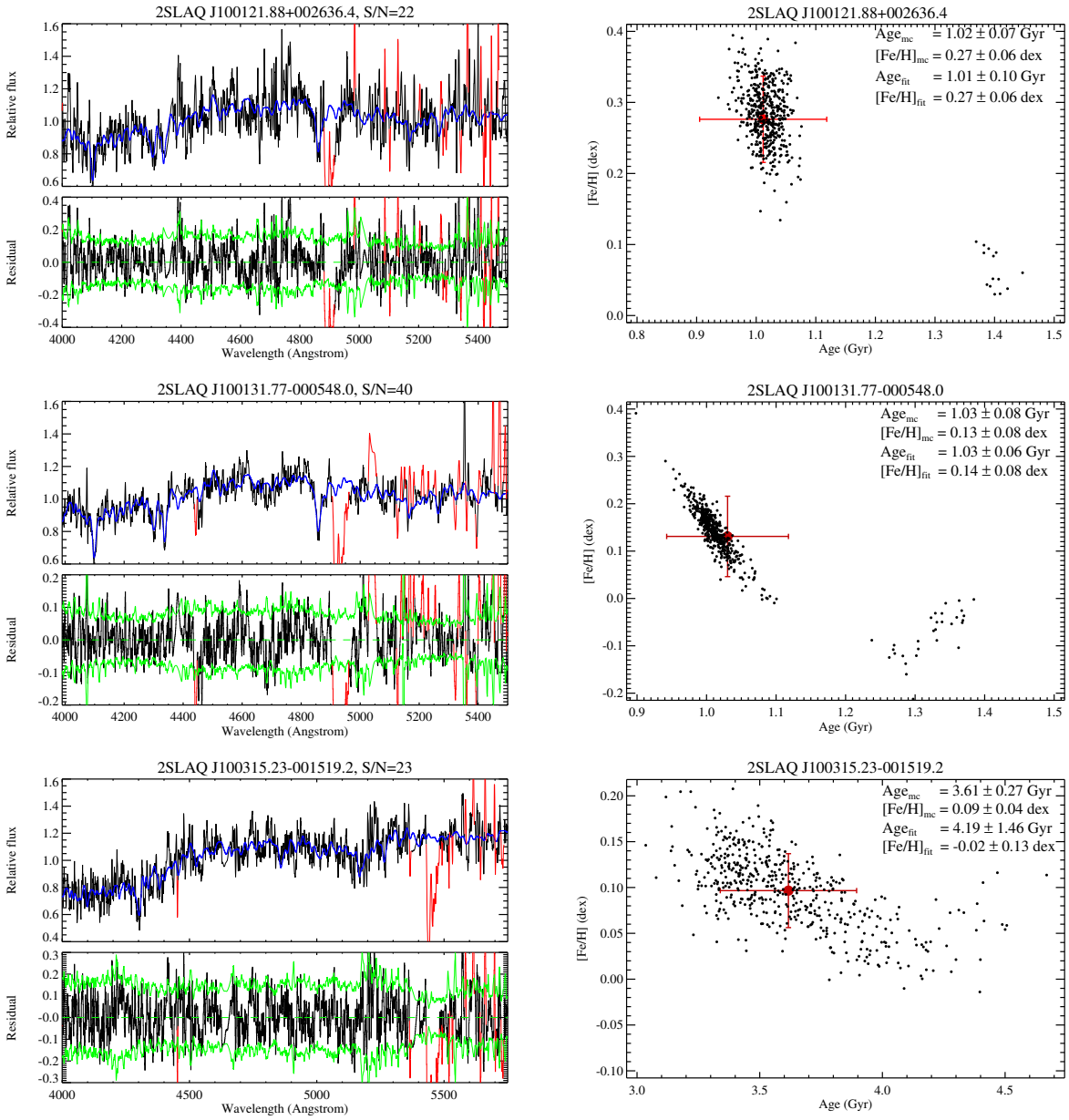

Figure 4.9: continued.

difference in redshifts ($\Delta z/\Delta t$). The mean of the age distribution in each redshift was used to measure the differential ages. We considered galaxies with sufficient S/N which are all shown here. The two k+a LRGs were also included in the average results. For the statistic purpose, a number of galaxies is needed. Unfortunately, we could not reach the number of galaxies in order to obtain a $H(z)$ measurement within 20% precision. Therefore we used all the spectra that we could obtain from the observations which all presented here.

Applying the equation 1.17 for the intermediate redshift between $z \simeq 0.40$ and $z \simeq 0.55$, we obtained a new observational Hubble parameter $H(z \simeq 0.47) = 105\pm$ 39 km s^{-1} Mpc^{-1}

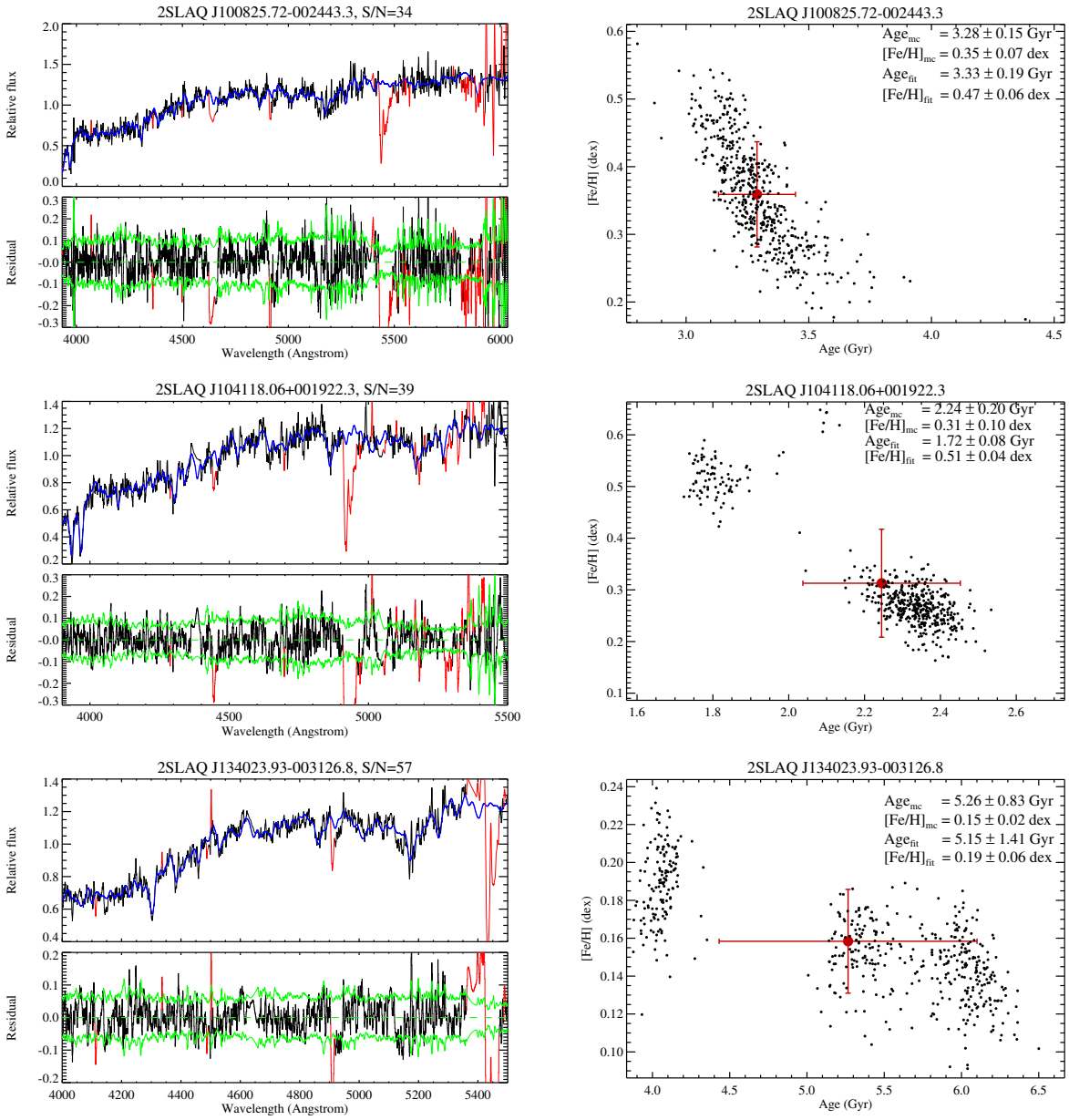

Figure 4.9: continued.

using SSP equivalent ages. The error in $H(z)$ depends only on the age at each redshift since the error on the redshift is negligible, and was calculated from:

$$\frac{\sigma_{\mathrm{H}}^2}{\mathrm{H(z)}^2} = \frac{(\sigma_{\mathrm{t_1}}^2 + \sigma_{\mathrm{t_2}}^2)}{(\mathrm{t_1} - \mathrm{t_2})^2} \tag{4.3}$$

details are demonstrated in Crawford *et al.* (2010a).

We plot our result with all available observational $H(z)$ values up to in figure $z \sim 1$ derived using the cosmic chronometer methodology in figure 4.13. The most comparable measurement

Table 4.8: Results of SSP fit with PE model including the SSP equivalent ages, metallicities and central velocity dispersions. Errors of each parameter are from the covariance matrix.

Name	Redshift	Age (Gyr)	[Fe/H] (dex)	σ (km s^{-1})	χ^2	S/N (Å^{-1})	MD
2SLAQ J081258.12−000213.8	0.4063	3.34±0.45	0.18±0.08	242±18	0.43	36	7
2SLAQ J081332.20−004255.1	0.3924	3.78±0.70	0.17±0.06	336±26	0.41	33	7
2SLAQ J100315.23−001519.2	0.3980	4.19±1.46	-0.02±0.13	234±32	0.38	23	9
2SLAQ J100825.72−002443.3	0.3984	3.33±0.19	0.47±0.06	266±17	0.50	34	2 or 6
2SLAQ J134023.93−003126.8	0.3997	5.15±1.41	0.19±0.06	342±17	0.46	57	9
2SLAQ J134058.83−003633.6	0.4097	2.08±0.16	0.26±0.04	172±11	0.51	21	7
2SLAQ J144110.62−002754.5	0.4003	5.19±0.50	-0.06±0.03	327±11	0.81	86	9 or 5
2SLAQ J010427.15+001921.5	0.4071	3.42±0.25	0.18±0.04	255±9.6	1.46	57	7
2SLAQ J022112.71+001240.3	0.3975	1.35±0.23	0.41±0.12	314±32	0.44	28	10 or 13
SDSS J013403.82+004358.8	0.4092	4.75±0.38	0.45±0.04	442±16	0.50	60	5
2SLAQ J092612.79+000455.8	0.5411	6.65±1.47	0.09±0.10	357±35	0.59	17	6
2SLAQ J092740.75+003634.1	0.5480	2.85±0.31	0.38±0.08	287±19	0.75	27	7
2SLAQ J100121.88+002636.4	0.5549	1.01±0.10	0.27±0.06	223±32	0.53	22	10
2SLAQ J100131.77−000548.0	0.5464	1.03±0.06	0.14±0.08	191±17	0.53	40	10
2SLAQ J104118.06+001922.3	0.5465	1.72±0.08	0.51±0.04	259±13	0.48	39	9
2SLAQ J225540.39−001810.7	0.5512	3.07±0.12	0.43±0.04	227±11	0.51	39	8

at the same redshift is by Stern *et al.* (2010a) who measured a value of $H(z) = 97 \pm 60$ km s^{-1} Mpc^{-1} at $z = 0.48$. Nonetheless, our value is consistent with the standard cosmology model with parametrization of $\Omega_m = 0.27$, $\Omega_\Lambda = 0.73$ and $H_0 = 71$ km s^{-1} Mpc^{-1}.

As described by Crawford *et al.* (2010a) and also evident in works at lower redshift, further improvements in the value of $H(z)$ can be made by increasing the sample size. The relatively small sample presented here was part of an initial pilot study and further observations will be required to improve on the measurement presented here.

We have addressed the estimated number of galaxies required to obtain the desired precision in Crawford *et al.* (2010a). In reality, we could not reach the estimated accuracy because of the observation constraints such as the quality of the observed spectra in terms of S/N, or the fact that the number of observed objects could not complete our original estimation. A larger and better quality sample would help us to reach our main goal for the future. The relatively small sample presented here was part of an initial pilot study and further observations will be required to improve on the measurement.

4.8 Conclusion

We have obtained, reduced and analysed 16 long-slit spectra of LRGs recently observed with the SALT telescope. These galaxies are selected from the 2SLAQ and MegaZ-LRGs catalogues at redshift $z \simeq 0.40$ and $z \simeq 0.55$. Our selection is based on stellar mass, brightness and emission lines of the galaxy in order to have a sample of old and massive passively-evolving galaxies. In this chapter, we derive their ages, metallicities and velocity dispersions by applying the full spectral fitting method. The Pegase-HR model with the ELODIE stellar

library is used to extract those SSP parameters. We have also verified any possible emission lines in our galaxy sample, focusing in particular on the signature of $H\beta$ and [OIII]λ5007 lines. Any emission lines could not been detected in our wavelength range meaning that we have used mostly a sample of passively-evolving galaxies.

The mean age at each redshift bin is used to measure the Hubble parameter $H(z)$ at $z \simeq 0.47$ by adopting the method of Cosmic Chronometers. We find an improved $H(z)$ measurement over the Stern *et al.* (2010a).

This sample constitutes a test of this method using observed LRGs with SALT and will contribute to completing the long term goal of our future survey. We aim to observe more galaxies in order to improve our $H(z)$ measurement and to build the evolution of the Hubble parameter as a function of redshift over $0.1 < z < 1$. Furthermore, the current estimate $H(z)$ at $z \simeq 0.47$ is comparable to the existed value in literature which is reassuring for the future survey. This value will be combined with the available $H(z)$ in the literature in order to constrain cosmological parameters. The datasets used here will also be useful for studying in detail the stellar population and properties of the central cluster galaxies since two of them are included in our sample.

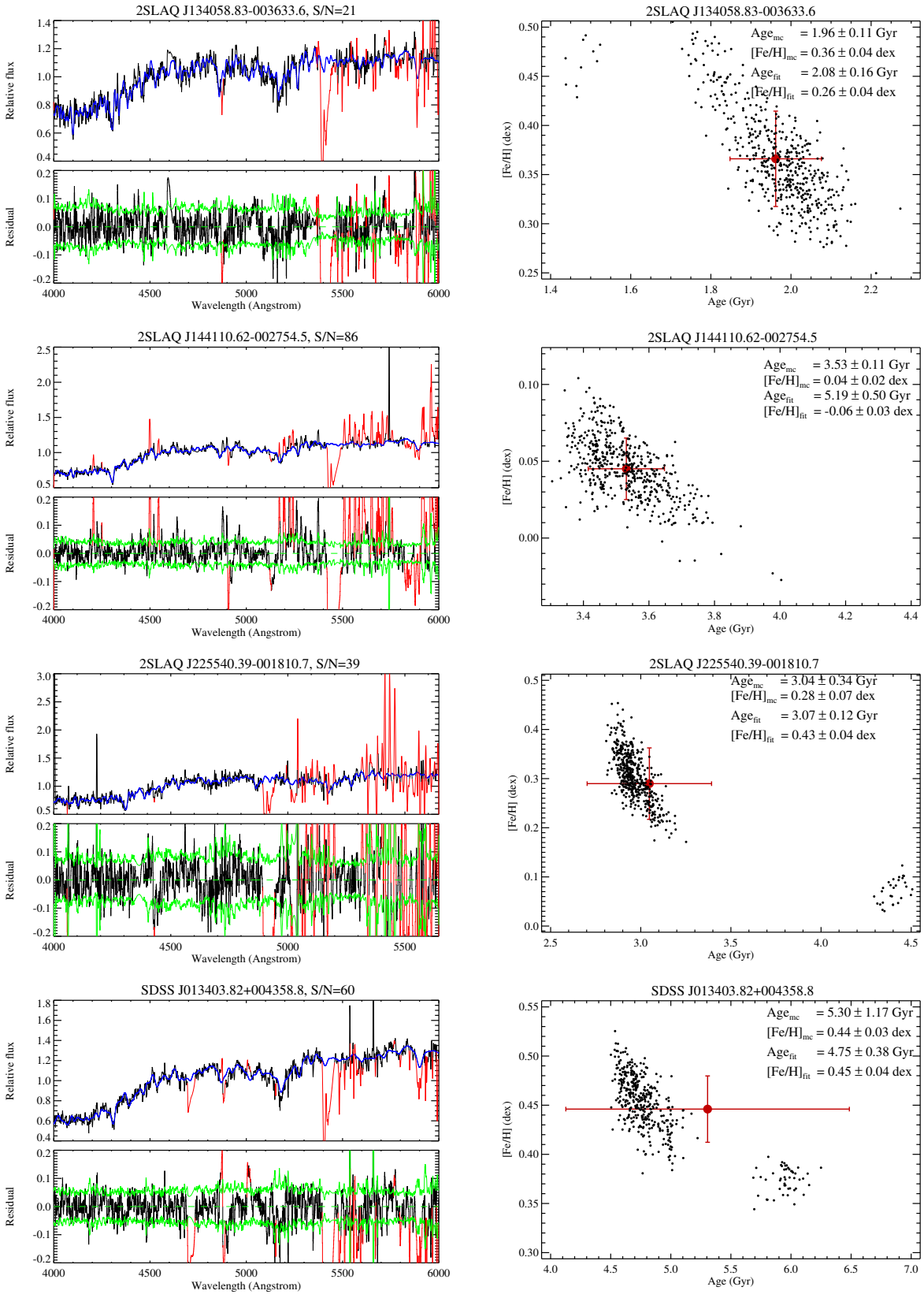

Figure 4.9: continued.

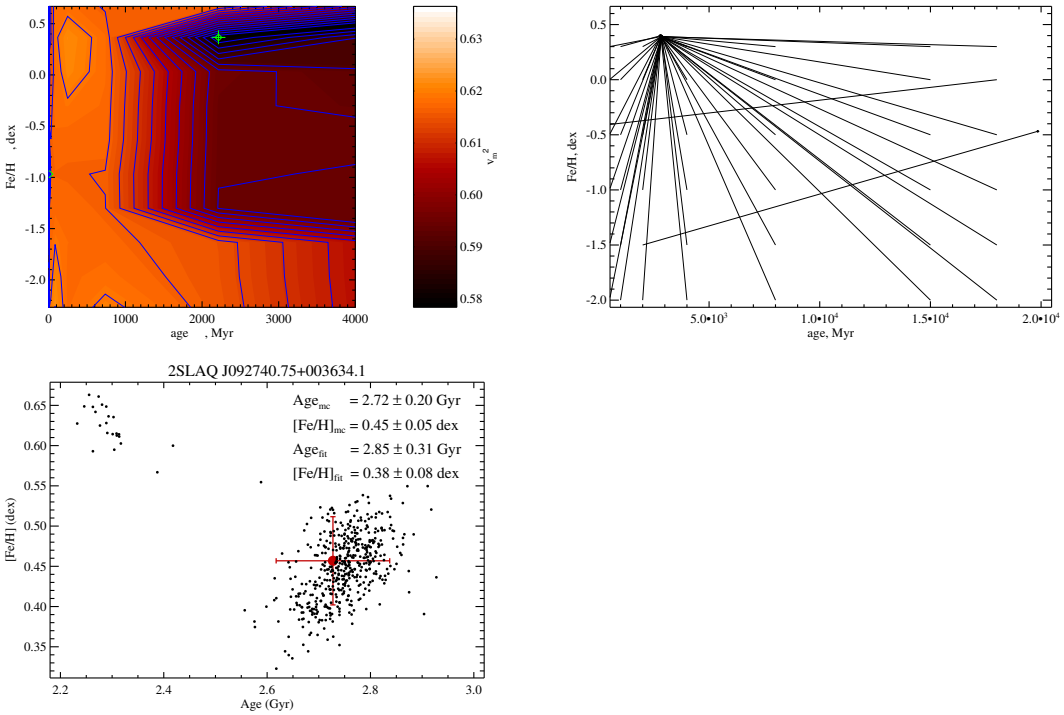

Figure 4.10: Examples of the χ^2 and convergence maps of 2SLAQ J092740.75+003634.1. The results of the 500 Monte-Carlo simulations are also plotted with the best fit results in the legend (bottom panel). The global minimum is indicated with a green symbol in the χ^2 maps (top panel in the left). The top panel in the right displays the corresponding convergence maps. All results converge to the best fit results ($\mathrm{Age_{fit}}$ and $\mathrm{[Fe/H]_{fit}}$).

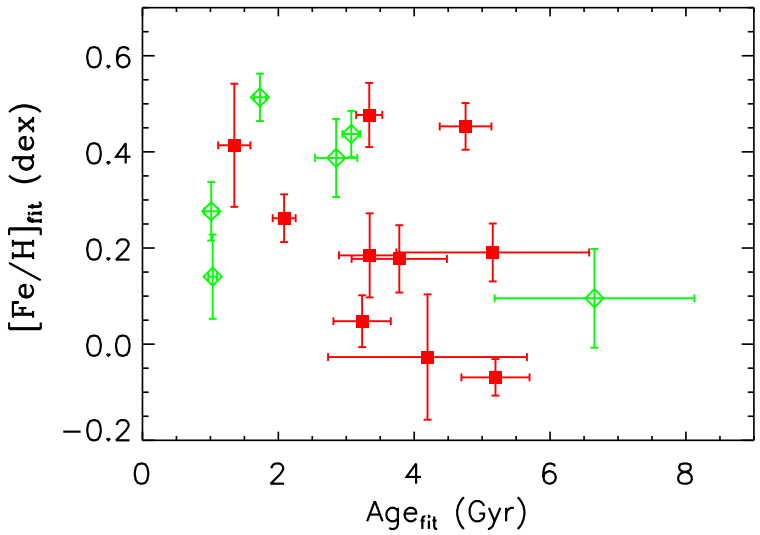

Figure 4.11: This shows different ages and $[Fe/H]$ obtained from the full spectral fitting using PE model. Red filled squares are galaxies at $z \simeq 0.40$, green open diamonds are galaxies at $z \simeq 0.55$. The mean age and metallicity at $z \simeq 0.40$ is 3.64 ± 0.23 Gyr, 0.21 ± 0.02 dex respectively. The mean age and metallicity at $z \simeq 0.55$ is 2.72 ± 0.25 Gyr, 0.30 ± 0.03 dex respectively.

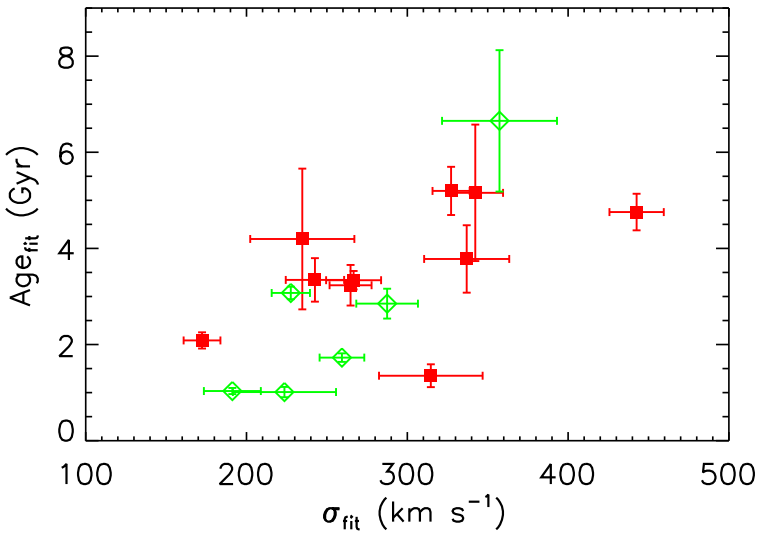

Figure 4.12: SSP ages from best fits plotted with velocity dispersion. Red filled squares are galaxies at z =0.40, green open diamonds are galaxies at z =0.55.

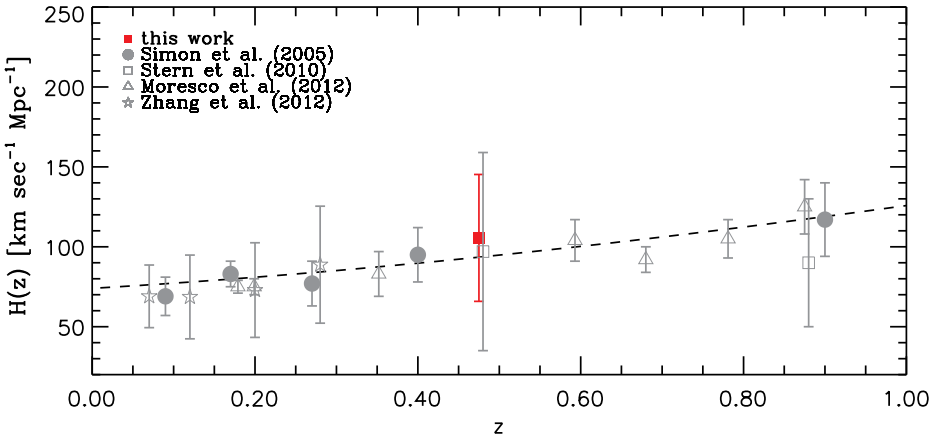

Figure 4.13: Our estimate $H(z \simeq 0.47)$ measured using SALT LRG spectra is represented by the red filled rectangle. It has a value of $H(z) = 105 \pm 39$ km s^{-1} Mpc^{-1}. Our result is plotted with all available $H(z)$ in the literature. The dashed line is the theoretical H(z) of a flat ΛCDM model with $\Omega_m = 0.27$, $\Omega_\Lambda = 0.73$ and $H_0 = 71$ km s^{-1} Mpc^{-1}.

Chapter 5

Cosmological constraints

5.1 Introduction

As mentioned earlier in the general introduction, cosmological measurements such as the CMB, SNIa, BAO as well as the large scale structure (LSS) all play major roles in understanding the Universe as well as in constraining the cosmological parameters. There are many factors that prevent us obtaining very good constraints on some important cosmological parameters. One example of those factors is degeneracies among the cosmological parameters. In this chapter, we make use of our $H(z)$ measurements combined with the recent and available $H(z)$ in the literature to investigate their constraining power on the determination of cosmological parameters. We also explore the availability of combining those $H(z)$ data with other cosmological measurements: BAO, WMAP and HST to better determine the constrain on the parameter calculations. The first calculation was done with our own code, the second one was performed by using the publicly available code `cosmoMC`. Both calculations were based on the Markov Chain Monte Carlo (MCMC) techniques to determine the cosmological parameters in the standard ΛCDM models, such as the density of matter parameter today Ω_m, the cosmological constant Ω_Λ, the spatial curvature parameter today Ω_k and the Hubble constant today H_0.

5.2 Methodology

5.2.1 Markov Chain Monte Carlo

The MCMC is a commonly used statistical technique for constraining parameters from observed data. This technique is adapted for high dimensional parameter space, often called "a chain", which is well suited for cosmology with a large number of parameters. A most basic MCMC algorithm is to construct a sequence of points or "samples" in that parameter space from an arbitrary distribution, with a relaxing requirement that the samples should be independent.

A Markov Chain is defined as a sequence of random variables $\mathrm{X}_1, \mathrm{X}_2, ..., \mathrm{X}_\mathrm{n}$ of some set where the probability of the $(n+1)^{th}$ element in the chain only depends on the n^{th} element but not on $(\mathrm{n}-1)^{\mathrm{th}}$, i.e $\mathrm{p}(\mathrm{X}_{\mathrm{n}+1}|\mathrm{X}_1, \mathrm{X}_2, ..., \mathrm{X}_\mathrm{n}) = \mathrm{p}(\mathrm{X}_{\mathrm{n}+1}|\mathrm{X}_\mathrm{n})$. The set in which the X_i take place is called the "state space" of the Markov Chain.

The important property of the Markov Chains is that they can be shown to converge to a stationary state where successive elements of the chain are samples from the target distribution, in our case the posterior probability density $p(\Theta|D)$. The goal of the MCMC implementation is then to ensure that the sequence of random variables is drawn from the stationary distribution.

The generation of the elements of the chain is probabilistic in nature, and is described by a transition probability, often called the "transition kernel" $\mathrm{T}(\Theta_\mathrm{n}, \Theta_{\mathrm{n}+1})$, giving the probability of going from the point Θ_n to the point Θ_{n+1} in parameter space. A sufficient condition to obtain a Markov Chain is that the transition probability satisfies the detailed balance condition

$$\mathrm{p}(\Theta_\mathrm{n}|\mathrm{D})\mathrm{T}(\Theta_\mathrm{n}, \Theta_{\mathrm{n}+1}) = \mathrm{p}(\Theta_{\mathrm{n}+1}|\mathrm{D})\mathrm{T}(\Theta_{\mathrm{n}+1}, \Theta_\mathrm{n}) \tag{5.1}$$

It can be explained as the ratio of the probabilities for jumping from Θ_n to $\Theta_{\mathrm{n}+1}$, and is inversely proportional to the ratio of the posterior probabilities at the two points. The above equation also means that the chain would look the same whether you run it forwards in time or backwards (reversible). This kind of chain behaviour is the desirable property for any MCMC transition kernel to have, since any transition kernel in such equation will have stationary distribution (here, $\mathrm{p}(\Theta|\mathrm{D})$). It is then important to find the appropriate transition kernels which are associated with the different algorithms to construct a Markov chain which performs well.

There are some issues while working with MCMC methods. For instance, MCMC is a local algorithm, and it can be trapped at the vicinity of the local maxima of the posterior density, instead of exploring the regions of higher posterior. It is therefore necessary to find an implementation of the MCMC algorithm that is able to explore the parameter space of interest well (One of MCMC algorithms: Metropolis-Hastings algorithm is discussed below). Despite these problems, MCMC can also offer a significant advantage. Compared to other approaches like the grid based approach, this approach is very cheap in term of the length of computer time required to complete the task, especially with high dimensional parameter space.

5.2.1.1 Bayesian Inference

The goal of the Bayesian Inference is to maximise the un-normalized joint posterior distribution and collect samples of the target distributions, which are marginal posterior distributions. The MCMC process produces a random sequence of dependent variables that are

drawn directly from the posterior distribution. This is achieved using Bayes' Theorem:

$$\mathrm{p}(\Theta|\mathrm{D}) = \frac{\mathrm{p}(\mathrm{D}|\Theta)\mathrm{p}(\Theta)}{\int \mathrm{p}(\mathrm{D}|\Theta)\mathrm{p}(\Theta)\mathrm{d}\Theta} \tag{5.2}$$

where $\mathrm{p}(\Theta|\mathrm{D})$ is the posterior probability density for Θ or often called "posterior" for short. It assigns a probability to the model given the data D and any prior knowledge concerning the model. $\mathrm{p}(\mathrm{D}|\Theta)$ is the probability density associated with obtaining the data, D, given a certain value of the model parameters, Θ, and is well known as the "likelihood " ($\mathrm{p}(\mathrm{D}|\Theta) = \mathcal{L}(\Theta)$). The quantity $\mathrm{p}(\Theta)$ is the prior probability distribution, often called "prior" for short (or the marginal probability density). It describes the degree of the belief in the value of Θ before seeing the data, and allows to put constraints on the model parameters. This represents the essential ingredient of Bayesian statistics. The denominator in the equation 5.2 is a normalization factor, often called the "evidence", and ensures that the posterior is normalized to unity. This term is often ignored as it is not essential to evaluate the integral in order to determine the posterior probability density. In our case, it is ignored. We also adopted "flat prior" (also called "uniform " prior).

MCMC is a technique that can offer an easy computation of the marginalised distribution of the parameters from the posterior distribution by determining the appropriate density function (histogram) of the desired parameters, even in the high dimensional parameter space.

5.2.1.2 Metropolis-Hastings Algorithm

There are different types of the MCMC algorithms, such as the Metropolis algorithm (Metropolis et al., 1953), Metropolis-Hastings algorithm (Hastings, 1970), the Gibbs sampling (Geman and Geman, 1984), the Metropolis-Hastings-Green algorithm (Green, 1995) etc. The simplest of all algorithms is the Metropolis Algorithm. The Metropolis-Hastings algorithm is the most popularly used variety of MCMC as it is simple, intuitive, and very effective to solving a wide variety of problems. The principle of this algorithm is to produce a "random walk" in likelihood space that preferentially samples from the high probability regions while exploring the wide range of possibilities. This algorithm utilizes some prior information in order to put constraints on model parameters; more precisely it employs a likelihood ratio test in order to accept or not a candidate position in parameter space.

To define the algorithm, let $\pi(.)$ denote the starting point of the MCMC which is often chosen randomly. The goal of the MCMC is to draw random samples from this starting point, the stationary or posterior distribution, and then to allow inference of model parameters. Any MCMC algorithm is designed to explore a target distribution, therefore any results calculated from a sufficiently large set of samples should be independent of this staring point. As stated before, a transition probability $\mathrm{T}(\Theta_\mathrm{n}, \Theta_{\mathrm{n}+1})$ is required to generate the Markov chain from $\pi(.)$, such that after the n^{th} iteration of the chain, π is the stationary distribution, i.e $\pi = \pi T$.

The aim of any MCMC implementation is to employ a proper transition probability.

The key roles of the Metropolis-Hastings algorithm are to ensure that π is the only stationary distribution of T and that the chain generates samples from the posterior distribution $\mathrm{p}(\Theta|\mathrm{D})$ (in other term $\pi(.) \rightarrow \mathrm{p}(\Theta|\mathrm{D})$ as $n \rightarrow \infty$). The transition kernel in the Metropolis-Hastings algorithm is defined as the following:

$$\mathrm{T}(\Theta_{\mathrm{n+1}}, \Theta_{\mathrm{n}}) = \alpha(\Theta_{\mathrm{n+1}}, \Theta_{\mathrm{n}})\mathrm{q}(\Theta_{\mathrm{n+1}}, \Theta_{\mathrm{n}}) \tag{5.3}$$

where $\alpha(\Theta_{\mathrm{n+1}}, \Theta_{\mathrm{n}})$ describes the probability of accepting a transition from Θ_n to $\Theta n + 1$, referring to the "probability of move" and it is given by:

$$\alpha(\Theta_{\mathrm{n+1}}, \Theta_{\mathrm{n}}) = \begin{cases} \min\left\{\dfrac{\pi(\Theta_{\mathrm{n+1}})\mathrm{q}(\Theta_{\mathrm{n+1}}, \Theta_{\mathrm{n}})}{\pi(\Theta_{\mathrm{n}})\mathrm{q}(\Theta_{\mathrm{n}}, \Theta \mathrm{n}+1)}, \quad 1\right\} & \text{if } \pi(\Theta_n)q(\Theta_n, \Theta_{n+1}) > 0 \\ 1 & \text{if } \pi(\Theta_n)q(\Theta_n, \Theta_{n+1}) = 0 \end{cases} \tag{5.4}$$

and $\mathrm{q}(\Theta_{\mathrm{n+1}}, \Theta_{\mathrm{n}})$ is the candidate-generating distribution (also known as the "proposal distribution"), which generates or proposes a new candidate location in the parameter space $\Theta_{\mathrm{n+1}}$ given the current location Θ_{n}.

In Short, the Metropolis-Hastings algorithm is defined by two steps:

- the first step is where a proposal value is drawn from the candidate-generating distribution $\mathrm{q}(\Theta_{\mathrm{n+1}}, \Theta_{\mathrm{n}})$, and
- the second step is where the proposal value is accepted as the next iterate in the Markov chain according to the probability $\alpha(\Theta_{\mathrm{n+1}}, \Theta_{\mathrm{n}})$.

If the proposal value is rejected, then the next sampled value is taken to be the current value.

It appears that equation 5.4 is a ratio in the probability $\alpha(\Theta_{\mathrm{n+1}}, \Theta_{\mathrm{n}})$ and therefore the algorithm can be implemented without knowledge of the normalizing constant of $\pi(.)$ since it appears both in the numerator and denominator. In addition, if the candidate distribution is symmetric, i.e. $\mathrm{q}(\Theta_{\mathrm{n}}, \Theta_{\mathrm{n+1}}) = \mathrm{q}(\Theta_{\mathrm{n+1}}, \Theta_{\mathrm{n}})$, the acceptance probability $\alpha(\Theta_{\mathrm{n+1}}, \Theta_{\mathrm{n}})$ of moving from Θ_{n} to $\Theta_{\mathrm{n+1}}$ only contains the ratio $\pi(\Theta_{\mathrm{n+1}})/\pi(\Theta_{\mathrm{n}})$. When considering flat priors in equation 5.2, the expression of the probability of the move is reduced as follows:

$$\alpha(\Theta_{\mathrm{n+1}}, \Theta_{\mathrm{n}}) = \begin{cases} \min\left\{\dfrac{\mathcal{L}(\Theta_{\mathrm{n+1}})}{\mathcal{L}(\Theta_{\mathrm{n}})}, \quad 1\right\} & \text{if } \mathcal{L}(\Theta_n)q(\Theta_n, \Theta_{n+1}) > 0 \\ 1 & \text{if } \mathcal{L}(\Theta_n)q(\Theta_n, \Theta_{n+1}) = 0 \end{cases} \tag{5.5}$$

All of these mean that if $\mathcal{L}(\Theta_{\mathrm{n+1}}) \geq \mathcal{L}(\Theta_{\mathrm{n}})$, the chain will always take the step. If $\mathcal{L}(\Theta_{\mathrm{n+1}}) < \mathcal{L}(\Theta_{\mathrm{n}})$ the chain will move to $\Theta_{\mathrm{n+1}}$ with probability $\mathcal{L}(\Theta_{\mathrm{n+1}})/\mathcal{L}(\Theta_{\mathrm{n}})$. In this case a number u is drawn from a uniform distribution $\mathcal{U}(0, 1)$ and if $u \leq \mathcal{L}(\Theta_{\mathrm{n+1}})/\mathcal{L}(\Theta_{\mathrm{n}})$ then the step is taken as above. In another way, the next step is rejected then the current step is re-saved as part of the chain.

Here is the summary of the Metropolis-Hastings algorithm in algorithmic way:
Specify an initial value $\Theta_{(0)}$ with associated posterior probability $\mathrm{p}(\Theta_{(0)}|\mathrm{D})$

- Repeat for $j = 1, 2, 3...N$
- Propose a candidate point $\Theta_{\mathrm{n+1}} \sim \mathrm{q}(\Theta_{(\mathrm{j})}, .)$ and u from $\mathcal{U}(0, 1)$.
- if $u \leq \alpha(\Theta_{(\mathrm{j})}, \Theta_{\mathrm{n+1}})$

  -set $\Theta_{(\mathrm{j+1})} = \Theta_{\mathrm{n+1}}$
- Else

  -set $\Theta_{(\mathrm{j+1})} = \Theta_{(\mathrm{j})}$
- Return values $\Theta_{(1)}, \Theta_{(2)}, ..., \Theta_{(\mathrm{N})}$

5.2.2 MCMC code description

Recalling the theoretical equation of the non-flat ΛCDM model:

$$\mathrm{H_{th}(z)} = \mathrm{H_0}\sqrt{\Omega_\mathrm{m}(1+\mathrm{z})^3 + \Omega_\Lambda + \Omega_\mathrm{k}(1+\mathrm{z})^2} \tag{5.6}$$

where $\Omega_m + \Omega_\Lambda + \Omega_k = 1$;
and the theoretical equation of the flat ΛCDM model ($\Omega_k = 0$):

$$\mathrm{H_{th}(z)} = \mathrm{H_0}\sqrt{\Omega_\mathrm{m}(1+\mathrm{z})^3 + \Omega_\Lambda} \tag{5.7}$$

the general aim is to fit a model with N adjustable parameters, a vector $\Theta = (\Theta_1, \Theta_2, \Theta_3, ...\Theta_n)$, to a set of M observational data points $\mathrm{D} = (\mathrm{H_i}, \mathrm{z_i}, \sigma_\mathrm{i})$, $i = 1, 2..., M$ where H_i is the measured Hubble parameter at a given redshift z_i.

In our case, $H_{th}(z)$ for a non-flat model is represented by three parameters (N = 3) $\Theta_{non-flat} = (H_0, \Omega_m, \Omega_\Lambda)$. However, $H_{th}(z)$ for a flat model is described by two parameters (N = 2) $\Theta_{flat} = (H_0, \Omega_m)$.

From the Bayes' Theorem, the likelihood $\mathcal{L} \equiv \mathcal{L}(\mathrm{D}|\Theta)$ was introduced into MCMC method. It can be obtained by assuming that the observed data $\mathrm{D_i}$ is a set of M independent normally distributed random variables (Gaussian) (Cowan, 1998). Each $\mathrm{D_i}$ has a different unknown mean, μ_i, but known variance, σ_i^2. The likelihood of the data is then the product of the probability of each data point:

$$\mathcal{L} = \prod_{\mathrm{i=1}}^{\mathrm{M}} \exp\left(-\frac{1}{2}\chi^2\right) \tag{5.8}$$

Maximizing the equation 5.8 is equivalent to maximizing its logarithm, or minimizing the negative of its logarithm. Thus, the maximum likelihood estimate of the parameters is

minimizing χ^2 function:

$$\chi^2(\Theta) = \sum_{\mathrm{i}=1}^{\mathrm{M}} \frac{(\mathrm{H_i}(\mathrm{z_i}) - \mathrm{H_{th}}(\mathrm{z_i}))^2}{\sigma_{\mathrm{i}}^2} \tag{5.9}$$

The general algorithm presented here is following the Donar & Muller (2004) definition. After choosing a starting point Θ_0, the likelihood $\mathcal{L}(\mathrm{D}|\Theta_0)$ of observing the experimental data D given parameter vector Θ_0 was computed. We obtained a new parameter vector $\Delta\Theta$ by sampling the jump from a Gaussian distribution with mean 0 and standard deviation vector σ, i.e. the jump of each parameter is controlled by this new parameter vector. A vector equation, parameter dependent $\mathcal{U}_i = \Theta_{i-1} + \Delta\Theta_{i-1}$, was constructed. The maximisation of the likelihood was then used iteratively as in general MCMC approach, meaning at each jump on the evolution of the chain, the likelihood, $\mathcal{L}_\mathrm{i} = \mathcal{L}(\mathrm{D}|\mathcal{U}_\mathrm{i})$ was calculated at the new candidate position in parameter space, Θ_i and compared with the likelihood, $\mathcal{L}_{\mathrm{i}-1} = \mathcal{L}(\mathrm{D}|\mathcal{U}_{\mathrm{i}-1})$ at the previous location, Θ_{i-1}. The Metropolis-Hastings algorithm was then used in order to accept or reject the new candidate position. If it gets accepted, then $\mathcal{U}_i$ was saved as a new position Θ_i in the chain. Contrarily, if it gets rejected, a random variable $\mathcal{U}$ from [0,1] was generated and retested again. If it gets rejected again, the previous position was saved as a new point in the chain.

The chain then performed a random walk in the parameter space and generated the sequence of parameter samples. It will approach regions of higher likelihood after a certain amount of time, and converge to a stationary position as well. Normally, the value of each parameter from the fit would be the mean of the distribution of parameter samples and the associated error is obtained by the variance of that distribution. However, since the chain file is already produced by our own MCMC code, the `getdist` program implemented in `cosmoMC` can be used for statistical analyses and plotting. This is very independent of the main `cosmoMC` program.

We implemented some prior distributions on each parameter. Table 5.1 lists the prior of model parameters, They are set to be uniform distributions

Table 5.1: List of prior distributions on each parameter

Parameter	Prior distribution
Ω_m	[0.0 , 1.5]
Ω_Λ	[0.0 , 2.5]
H_0	[50 , 100]

5.2.3 The Observational Datasets

Since 2002, after Jimenez & Loeb established the method of the direct measurement of $H(z)$, many scientists have explored the availability of this method to constrain the cosmological parameters. All available direct measurements on the Hubble parameter up to $z \sim 1.8$ were used widely as in Moresco *et al.* (2012b) and in Zhang *et al.* (2012); Zheng *et al.* (2014) including their new measurements. They also used the datapoints obtained by Gaztañaga *et al.* (2009b). Note that these data points are from the BAO measurements, not from a direct $H(z)$ measurement. These data points are included in our analysis in order to compare our results with the literature Zhang *et al.* (2012); Zheng *et al.* (2014). Table 5.1 summarizes all the available observational $H(z)$ data points including our four measurements, and displayed in figure 5.2. We built a sample of 29 observational $H(z)$ measurements including our new 4 data points in the range of $0.1 < z < 1.8$, which is equivalent to 10 Gyr of cosmic time. The 25 observational $H(z)$ measurements represent the the widest up-to-date sample. To set constraints on cosmological parameters, the $H(z)$ estimates using the SDSS passively evolving galaxies and the LRGs observed with SALT were combined.

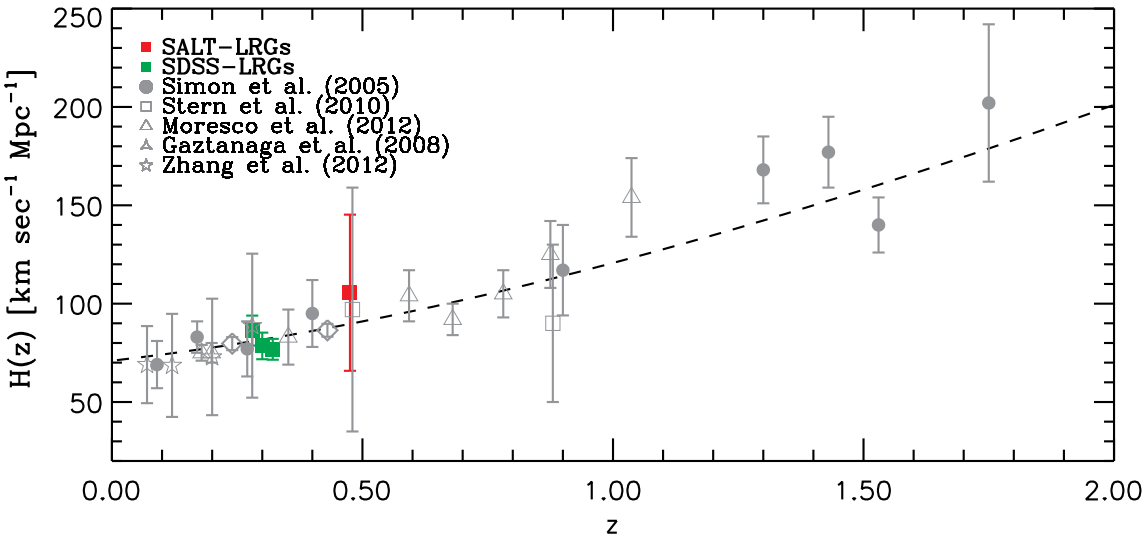

Figure 5.1: All available observational $H(z)$ data points. The green points are our measurements using SDSS-LRGs and red point while using SALT-LRGs

Table 5.2: All available observational $H(z)$ data points with their errors, including our measurements using SDSS-LRGs and SALT-LRGs. $H(z)$ measurements are in units of km $s^{-1}Mpc^{-1}$. Some of these data points are available at **http://www.physics-astronomy.unibo.it/en/research/areas/astrophysics/cosmology-with-cosmic-chronometers**

z	$H(z)$	$\sigma_{H(z)}$	Reference
0.07	69.0	19.6	Zhang *et al.* (2012)
0.090	69	12	Simon *et al.* (2005)
0.12	68.6	26.2	Zhang *et al.* (2012)
0.170	83	8	Simon *et al.* (2005)
0.179	75	4	Moresco *et al.* (2012a)
0.199	75	5	Moresco *et al.* (2012a)
0.20	72.9	29.6	Zhang *et al.* (2012)
0.24	79.69	3.32	Gaztañaga *et al.* (2009b)
0.27	77	14	Simon *et al.* (2005)
0.28	88.8	36.6	Zhang *et al.* (2012)
0.352	83	14	Moresco *et al.* (2012a)
0.40	95	17	Simon *et al.* (2005)
0.43	86.45	3.27	Gaztañaga *et al.* (2009b)
0.48	97	62	Stern *et al.* (2010a)
0.593	104	13	Moresco *et al.* (2012a)
0.680	92	8	Moresco *et al.* (2012a)
0.781	105	12	Moresco *et al.* (2012a)
0.875	125	17	Moresco *et al.* (2012a)
0.88	90	40	Stern *et al.* (2010a)
0.90	117	23	Simon *et al.* (2005)
1.037	154	20	Moresco *et al.* (2012a)
1.30	168	17	Simon *et al.* (2005)
1.43	177	18	Simon *et al.* (2005)
1.53	140	14	Simon *et al.* (2005)
1.75	202	40	Simon *et al.* (2005)
0.475	105	39	SALT-LRGs
0.28	76.8	5.3	SDSS-LRGs
0.30	78.5	6.8	SDSS-LRGs
0.32	86.3	7.6	SDSS-LRGs

5.3 Constraints on cosmological parameters from LRG measurements of $H(z)$

Figures 5.2, 5.3 show the one-dimensional (1D) marginalised probability distribution of each parameter and the two dimensional (2D) marginalised confidence regions of the non-flat and flat ΛCDM models respectively when using all 29 data points and the previous dataset used by Zhang *et al.* (2012) (25 data points). The inner and outer contours show the 1σ error (68%) and 2σ (95%) error respectively. The best fit parameters are also pointed in the plots

as long cross lines, and given in table 5.3 for non-flat ΛCDM model and in table 5.4 for flat ΛCDM model. The H_0, Ω_m and Ω_Λ parameter values from the WMAP9 alone are also plotted as a black cross symbol in the flat ΛCDM model for comparison. The CMB data alone are found to tightly constrain the parameters in that model, however they show consistency with the observational $H(z)$ data Moresco *et al.* (2012b).

The two plots illustrate the comparison of the constraint results of the old dataset (25 data points) shown in red and the new dataset (29 data points) shown in green, in both ΛCDM models. The missing parts on the 2D marginalised confidence regions with a non-flat ΛCDM model are due to the priors applied to the parameters. Our new measurements have an impact on the constraints results in H_0, Ω_m and Ω_Λ parameters even though only 4 data points were added on top of the old ones. The 1D marginalised probability distribution of using 29 data points show a more reduced distribution than using the old dataset, while they tighten each parameter contour of the confidence level in the 2D marginalization plots.

Table 5.3: Marginalised constraints on H_0, Ω_m, and Ω_Λ at 1-σ for a non-flat ΛCDM model

Model Parameter	25 data points	29 data points
H_0	$69.2^{+3.9}_{-5.2}$	$68.8^{+4.0}_{-4.7}$
Ω_m	$0.335^{+0.180}_{-0.187}$	$0.336^{+0.171}_{-0.181}$
Ω_Λ	$0.696^{+0.367}_{-0.380}$	$0.690^{+0.350}_{-0.361}$
Ω_k	$-0.032^{+0.555}_{-0.536}$	$-0.027^{+0.541}_{-0.505}$

Table 5.4: Marginalised constraints on H_0, Ω_m, and Ω_Λ at 1-σ for a flat ΛCDM model

Model Parameter	25 data points	29 data points
H_0	$68.7^{+2.8}_{-2.5}$	68.5 ± 2.4
Ω_m	$0.323^{+0.050}_{-0.066}$	$0.324^{+0.050}_{-0.065}$
Ω_Λ	$0.676^{+0.066}_{-0.050}$	$0.675^{+0.065}_{-0.050}$

5.4 Combining LRG results from $H(z)$ with other measurements

We further combined the above observational H(z) measurements datasets with the other major datasets such as WMAP9, BAO and HST to investigate their constraints on the determination of the cosmological parameters. The latest results of the CMB temperature and polarization power spectra from WMAP9 (Hinshaw *et al.*, 2013) were used. In this analysis, we also used the BAO measurement from:

- 6dF Galaxy Redshift Survey (6dFGRS) at z =0.106 (Beutler *et al.*, 2011)

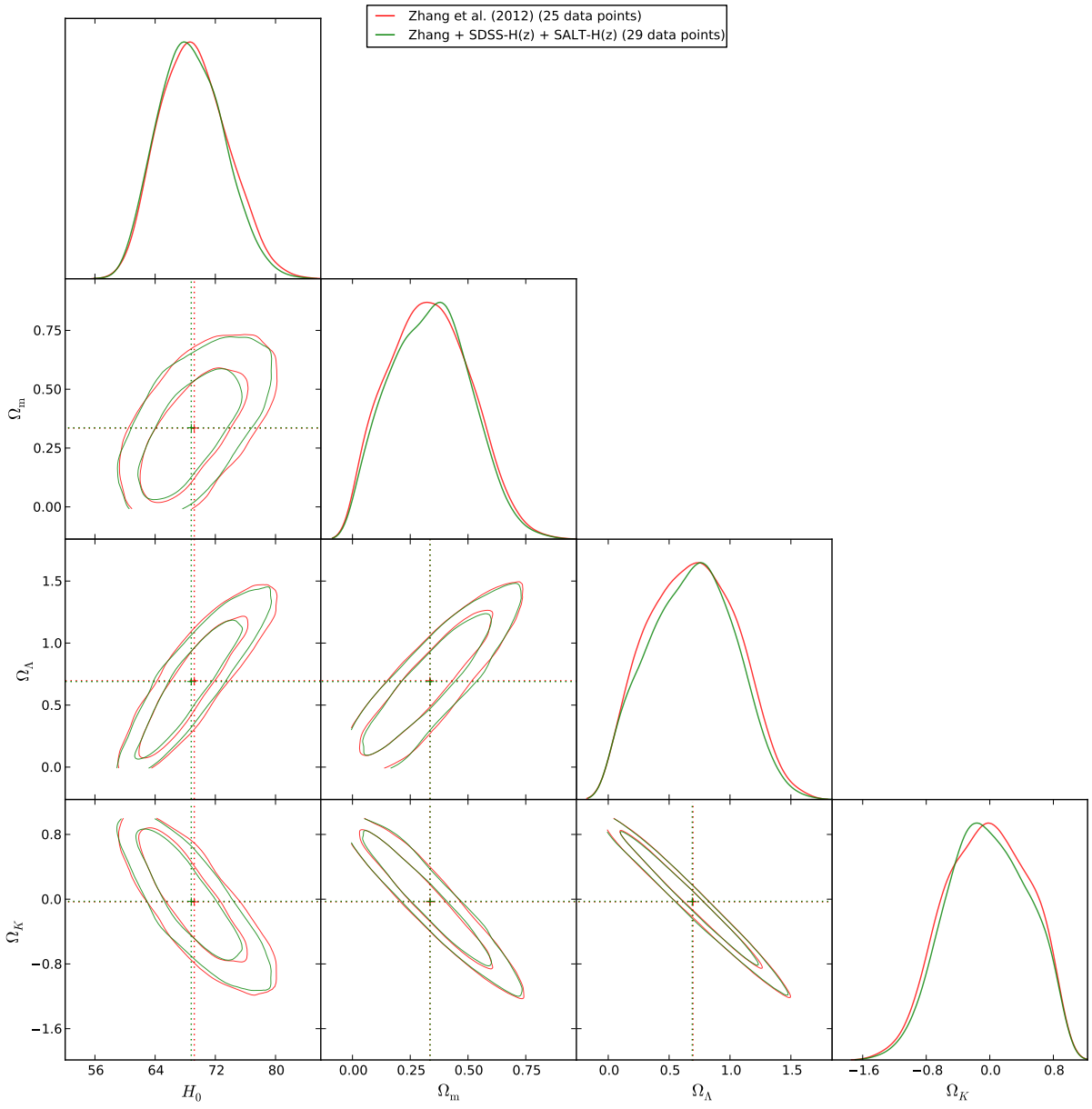

Figure 5.2: Observational $H(z)$ data points constraining results of the non-flat ΛCDM model. This plot shows the 1D and the 2D marginalised posterior probability distributions. The inner and outer contours show the 1σ error and 2σ error respectively. The red lines show the old version of Zhang *et al.* (2012), the green lines show the new version which includes the datasets used by Zhang *et al.* (2012) in addition to the $H(z)$ measured using LRGs with SALT and LRGs with SDSS. The dotted lines show the best fit parameter values.

- SDSS-LRGs DR7 sample at $z = 0.35$ (Padmanabhan *et al.*, 2012)
- SDSS-LRGs DR9 sample at $z = 0.57$ (Anderson *et al.*, 2014)
- WiggleZ survey at $z = 0.44$, $z = 0.60$ and $z = 0.73$ (Busca *et al.*, 2013)

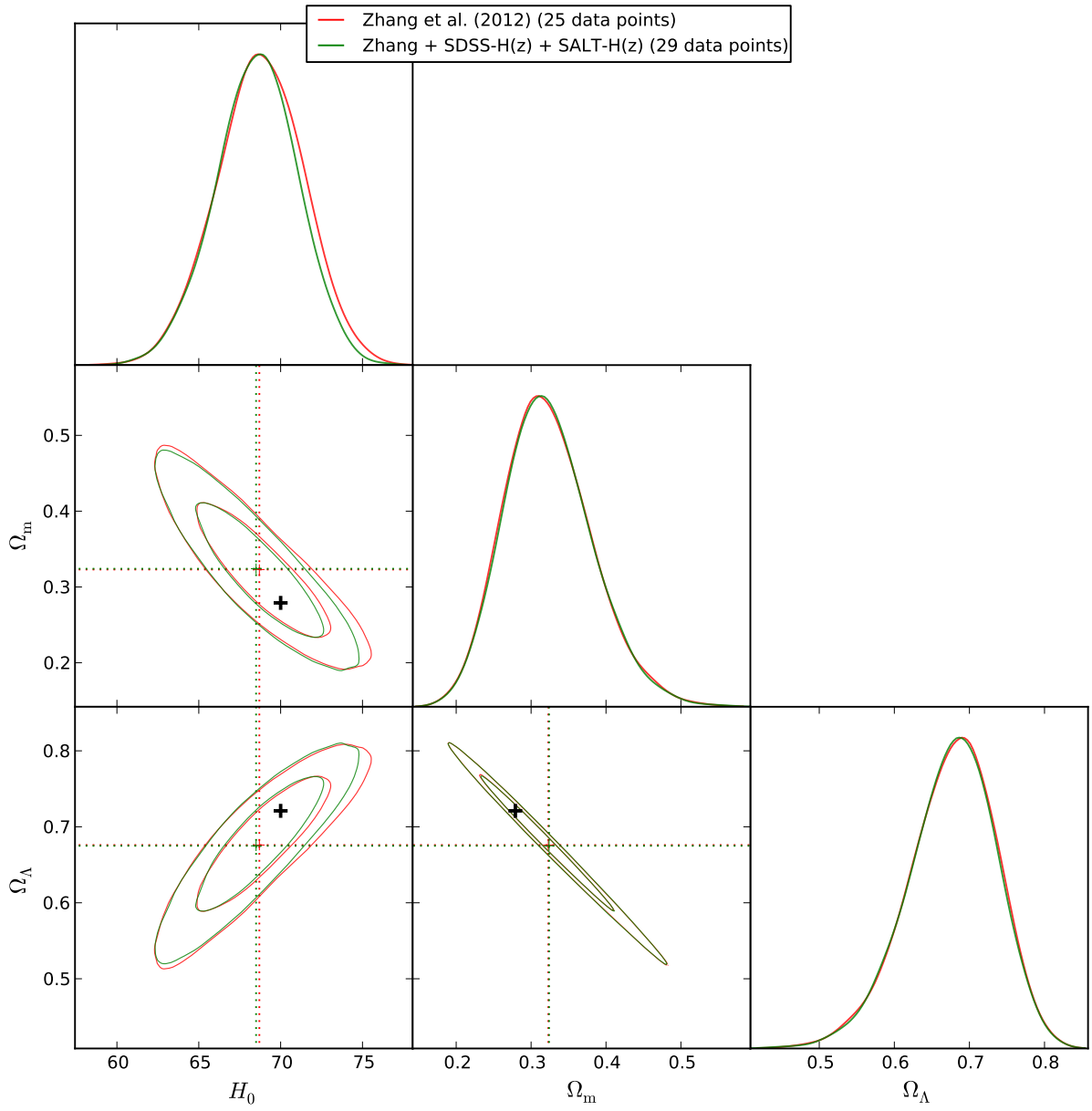

Figure 5.3: Observational $H(z)$ data points constraining results of the flat ΛCDM model. This plot shows the 1D and the 2D marginalised posterior probability distributions. The inner and outer contours show the 1σ error and 2σ error respectively. The red lines show the old version of Zhang *et al.* (2012), the green lines show the new version which includes the datasets used by Zhang *et al.* (2012) in addition to the $H(z)$ measured using LRGs with SALT and LRGs with SDSS. The dotted lines show the best fit parameter values. The black symbols represent the parameter values from the WMAP9 for a comparison.

The last dataset used is the Hubble Space Telescope (HST) measurement of the Hubble parameter today $H_0 = 73.8 \pm 2.3$ km s^{-1}Mpc^{-1}. This value was obtained from the magnitude-redshift relation of 235 SN Ia observed with HST. The best fit parameter from the $H(z)$

dataset was obtained in the same manner as using $H(z)$ alone by the χ^2 minimization.

We made use of the publicly available MCMC package named `cosmoMC`[1]. This package is written with Fortran code in order to explore the cosmological parameter space, plus some codes for analysing the Monte-Carlo samples and importance sampling.

By assuming different sets of initial conditions, and with the current cosmological observations, we constrain the different cosmological parameters of the ΛCDM model which are listed in table 5.5 . The first block of the table represents the choice of the primary parameters and parameters in the second block are the derived parameters. The choice of the primary parameters in `cosmoMC` depends on the derived parameters. All the primary parameters here represent the cosmology for Θ parametrization (the default parameters). The use of this parametrization is found to be more efficient than the H_0 parametrization as it is less correlated with other parameters. We derived the Hubble constant H_0, the ratio of the critical density in the form of the dark energy Ω_Λ and the total matter density, Ω_m (from the constraint $\Omega_m + \Omega_\Lambda + \Omega_k = 1$). The numerical calculations were performed with an equation of state ω = -1 and a flat curvature $\Omega_k = 0$.

Table 5.5: List of the cosmological parameters in the ΛCDM model.

Parameter	Description
Primary parameters	
$\Omega_b h^2$	Physical baryon density today
$\Omega_c h^2$	Physical cold dark matter density today
Θ	100 times angular size of sound horizon
τ	Re-ionisation optical depth
Ω_k	Spatial curvature parameter today
Σm_ν	The sum of the neutrino mass (eV)
N_{eff}	The effective density parameter for neutrinos
ω	The equation of state of the dark energy
n_s	Scalar spectral index of the initial power spectrum
n_t	The tensor spectral index
n_{run}	The running of the scalar spectral index
$ln(10^{10} A_s)$	Amplitude of the primordial curvature perturbations
r	The tensor to scalar ratio of the primordial spectrum
Secondary parameters	
H_0	The Hubble constant
Ω_m	The density of the matter
Ω_Λ	Cosmological constant

[1] http://cosmologist.info/cosmomc/

5.5 Results - joint analysis

For a flat ΛCDM, we obtained the constraints shown in table 5.6. It shows the constraints when using WMAP9 combined with the $H(z)$ measurements (WMAP9+Hz), WMAP9+Hz combined with BAO, WMAP9+Hz combined with BAO and H_0 measurement from HST. The last three dataset combinations were used to study the constraints due to the contribution of $H(z)$ and H_0 measurements. Through this analysis, we can see that the overall joint constraints are consistent with the standard cosmological model. We find that adding the $H(z)$ datasets and H_0 shows a noticeable constraints on H_0, Ω_m parameters. This is also due to the better constraint on the measured Hubble constant. WMAP9+Hz joint analysis does not provide any improvement over the WMAP9 alone since the WMAP9 constraint is much more precise than $H(z)$ constraint.

A combination of WMAP9+BAO with the $H(z)$ data significantly improves the 1-σ error. Figure 5.4 illustrates the 1 and 2$-\sigma$ of these joints constraints in H_0, Ω_m and Ω_Λ planes and their marginalised probability distribution. The parameter values of $H_0 = 69.6^{+1.4}_{-1.5}$ and $\Omega_m = 0.295\pm0.011$ are consistent with results of Zheng *et al.* (2014).

Table 5.6: Marginalised constraints at 1-σ on H_0, Ω_m parameters obtained for a flat ΛCDM model. Hz means including $H(z)$ datasets.

	H_0	Ω_m
WMAP9+Hz	68.8 ± 2.4	$0.320^{+0.047}_{-0.059}$
WMAP9+HST+Hz	$71.4^{+1.9}_{-1.7}$	$0.274^{+0.035}_{-0.045}$
WMAP9+BAO	$68.1^{+3.8}_{-4.7}$	$0.299^{+0.016}_{-0.022}$
WMAP9+BAO+Hz	$69.6^{+1.4}_{-1.5}$	0.295 ± 0.011
WMAP9+BAO+HST	$72.5^{+0.7}_{-0.6}$	0.284 ± 0.003
WMAP9+BAO+HST+Hz	70.7 ± 1.2	$0.289^{+0.010}_{-0.011}$

5.6 Conclusion

In this chapter, we have used our four $H(z)$ measurements combined with other $H(z)$ in literature plus other cosmological measurements to better constrain the cosmological parameters. In this study, we have only focused on H_0, Ω_m, Ω_Λ and Ω_k parameters. We have our own MCMC code to fit the observational $H(z)$ data. The new set of data which includes our $H(z)$ estimates shows tighter constraints than the old set of data in both flat and non-flat ΛCDM models. The degree of the constraint on the cosmological parameters is fairly weak because the number of the added data points is small.

We have also added some external datasets from WMAP9, BAO and HST to further

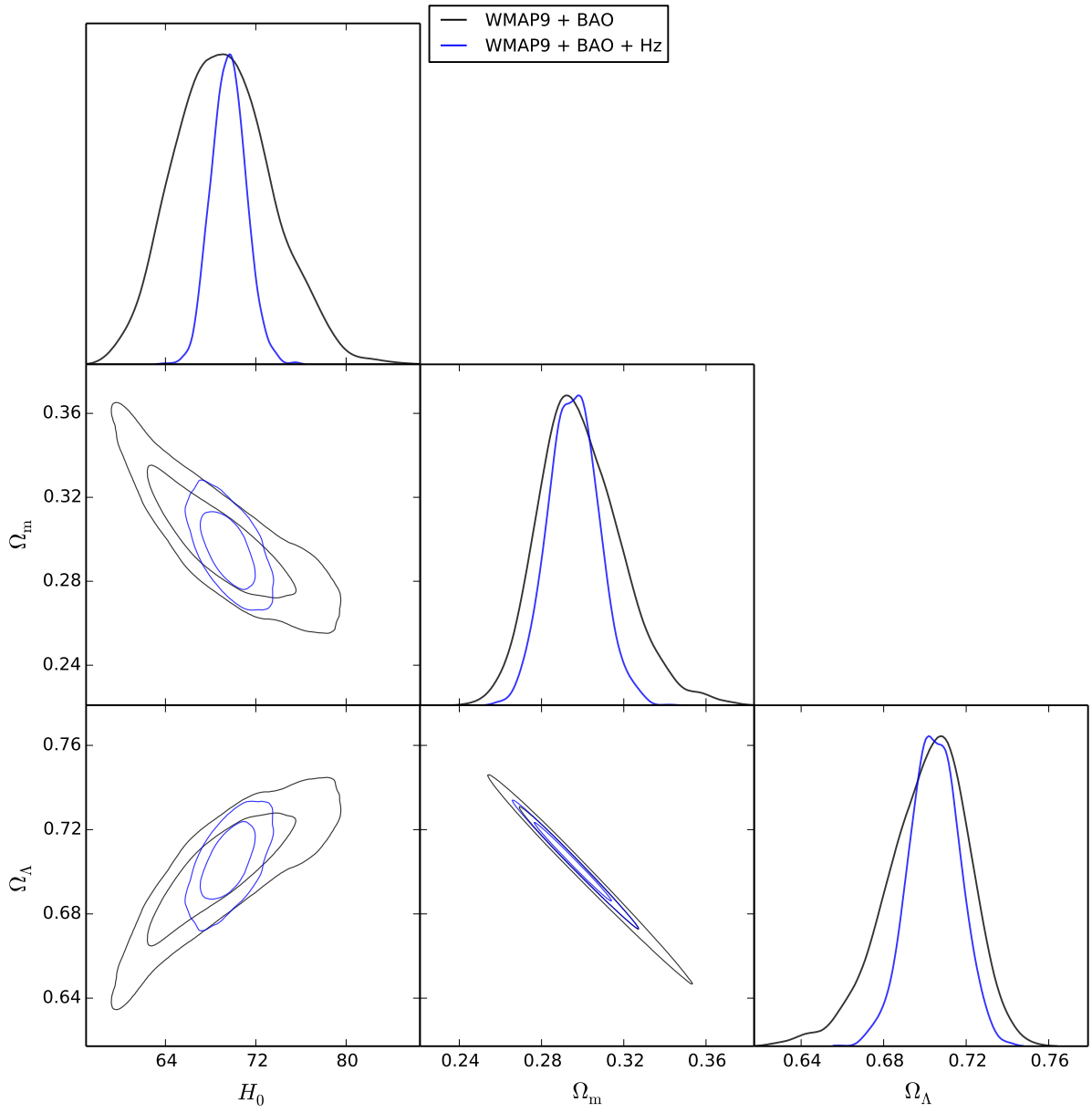

Figure 5.4: Observational $H(z)$ data points constraining results of the flat ΛCDM model. This plot show the 1D and the 2D marginalised posterior probability distributions. The inner and outer contours show the 1σ error and 2σ error respectively. The black lines show the combination of WMAP9+BAO datasets, the blue lines show the combination of WMAP9+BAO+Hz datasets.

constrain the power of measurements of $H(z)$. We find a significant improvement on the 1-σ constraint when combining observational $H(z)$ data with WMAP9+BAO. The inclusion of the $H(z)$ measurement tends to break the degeneracies among the other parameters, since the $H(z)$ data can provide information about the expansion rate at the late time. Therefore, the $H(z)$ and H_0 datasets are necessary for other observations for cosmological study.

Chapter 6

Conclusions and Future Work

6.1 Summary

The differential age or cosmic chronometers technique is an interesting way to measure the expansion rate of the Universe, since it gives a direct measurement between two distinct redshifts. This approach uses passively evolving quiescent galaxies in order to accurately reconstruct the expansion rate of the Universe over cosmic time. The work presented in this thesis highlights the exploration of this technique by using two different samples of passively evolving galaxies.

A better selection criteria has been used to form a very homogeneous sample of passively evolving galaxies from the SDSS-DR7 over the redshift range $0.10 < z < 0.40$. A further selection based on their emission lines has been applied to establish a sample free from any star formation or AGN activity. All galaxies have been corrected from any possible remaining nebular emission lines which can be found to affect the stellar absorption line-strengths, causing inaccurate age determination. Furthermore, all spectra within redshift bins of $\delta z = 0.02$ have been combined to form a high signal-to-noise spectrum to estimate reliable SSP equivalent parameters.

Two different age-dating techniques have been used to determine the stellar parameters of those galaxies. On the one hand, we have used the Lick indices analysis where the SSP models with variable element abundance ratios of TMJ have been used. On the other hand, four different SSP spectral models including models from M11, BC03, VM and PE have been adopted to extract the SSP equivalent parameters. For the full spectral fitting, the package ULySS has been employed, whereas simple Monte Carlo simulations has been used to fit the calibrated Lick indices measured from the stacked spectra. The Lick indices fitting shows a significant difference in the derived SSP ages. Moreover, the derived SSP parameters are found to be dependent on the set of Lick indices used.

We have extensively compared the parameter results derived from each model, in particular from the full spectral fitting. With the exception of the models by Maraston (2011), all models do not show a very significant inconsistency. We have provided different age-redshift

relations depending on 5 different SSP models: including one Lick indices model and four SED models. The general trends are consistent with expectations from the ΛCDM, and can be used for cosmology constraints. A few models could not reproduce the age-redshift relationship properly, such as the TMJ model of Lick indices and the M11 models. It has been proved in this analysis that the full spectral fitting provides more accurate SSP parameters than using Lick indices. With the latter, a necessary calibration to the Lick/IDS system has to be applied to the measured line-strengths, leading to the inclusion of different errors into the calibrated indices. For each model, the expansion rate of the Universe $H(z)$ has been measured at $z \simeq 0.28$, $z \simeq 0.30$ and $z \simeq 0.32$ using ages over the redshift range of $0.20 < z < 0.40$. Galaxies at <0.20 have not been used because the number of galaxies is fewer. We have obtained <9% accuracy measurements of $H(z)$ when using BC03. These $H(z)$ values have been employed to constrain the cosmological parameters.

We have carried out another cosmic chronometers study using 16 long-slit spectra of LRGs observed with SALT telescope. A massive and passively evolving sample of LRGs at redshift $\simeq 0.40$ and $\simeq 0.55$ has been selected. We have reduced and analysed those spectra. The PE models have been used to extracted the SSP equivalent parameters of these LRGs. The mean age of galaxies in each redshift has been used to estimate the Hubble parameter $H(z)$ value at $\simeq 0.47$.

In constraining the cosmological parameters, we have combined our $H(z)$ estimates from using SDSS passively evolving galaxies and LRGs observed with SALT with the external datasets. We have implemented an MCMC approach that provides the best fit parameters of H_0, Ω_m and Ω_Λ for a flat ΛCDM model and H_0, Ω_m, Ω_Λ and Ω_k for a non-flat ΛCDM. We have obtained parameter values which are consistent with the standard cosmological model. We have also combined all observational $H(z)$ data with data from WMAP9, BAO and HST to further constrain the cosmological parameters. For a flat ΛCDM model, significant improvements on the 1-σ constraints for Ω_m and H_0 are found when combining observational $H(z)$ data with WMAP9+BAO which are very consistent with previous results.

6.2 Future work

With the recent release of the BOSS spectra and α-enhanced spectral models, the full spectral fitting of the LRGs will improve and will provide more accurate SSP parameters than models which used solar-scaled parameters. Therefore, the use of the Lick indices or the Lick system will not be very essential for age-dating galaxies over a high redshift range. We will apply the cosmic chronometers technique to the BOSS spectra and other surveys like the Sandage-Loeb test (Corasaniti *et al.*, 2007) which can allow us to go deeper in redshift. Our measurement will then contribute to the extension of the number of the observational $H(z)$ data. Currently, this number is still tiny compared with the SN Ia data sets, but in the next few decades with the availability of high redshift surveys, it will be extended.

The systematic errors between SSP models used remain a subject of discussion. Further analysis on this must be done by performing a Bayesian model averaging across the models. Therefore average values of the age-redshift relation will be used to measure $H(z)$ and constrain cosmological parameters. With the release of the new *PLANCK* data, a joint analysis with the measurements of the $H(z)$ datasets will help to further investigate on cosmological parameters.

Some multi-object spectra (MOS) of LRGs at $z \simeq 0.40$ and $z \simeq 0.55$ were available during the 2012 and 2013 observation runs. After reducing these data, SSP parameters of these galaxies will be determined by performing a full spectral fitting. This sample will be added into the current one (long-slit spectra) in order to improve the measurement of the Hubble parameter $H(z)$ at $z \simeq 0.47$ as well as the cosmological constraints. We are also planning more SALT observations to study the evolution and the environment of the most massive galaxies at intermediate redshift.

References

Abate, A. & Erdoğdu, P. (2009). Peculiar velocities into the next generation: cosmological parameters from the SFI++ survey. *MNRAS*, **400**, 1541–1547. 6

Abazajian, K., Adelman-McCarthy, J.K., Agüeros, M.A., Allam, S.S., Anderson, S.F. & collaborators (2003). The First Data Release of the Sloan Digital Sky Survey. *AJ*, **126**, 2081–2086. 30

Abazajian, K., Adelman-McCarthy, J.K., Agüeros, M.A., Allam, S.S., Anderson, K. & collaborators (2004). The Second Data Release of the Sloan Digital Sky Survey. *AJ*, **128**, 502–512. 30, 34

Abazajian, K., Adelman-McCarthy, J.K., Agüeros, M.A., Allam, S.S., Anderson, K.S.J. & collaborators (2005). The Third Data Release of the Sloan Digital Sky Survey. *AJ*, **129**, 1755–1759. 30

Abazajian, K.N., Adelman-McCarthy, J.K., Agüeros, M.A., Allam, S.S., Allende Prieto, C. & collaborators (2009). The Seventh Data Release of the Sloan Digital Sky Survey. *ApJS*, **182**, 543–558. 30, 31, 38

Adelman-McCarthy, J.K., Agüeros, M.A., Allam, S.S., Anderson, K.S.J., Anderson, S.F. & collaborators (2006). The Fourth Data Release of the Sloan Digital Sky Survey. *ApJS*, **162**, 38–48. 30

Adelman-McCarthy, J.K., Agüeros, M.A., Allam, S.S., Anderson, K.S.J., Anderson, S.F. & collaborators (2007). The Fifth Data Release of the Sloan Digital Sky Survey. *ApJS*, **172**, 634–644. 30

Adelman-McCarthy, J.K., Agüeros, M.A., Allam, S.S., Allende Prieto, C., Anderson, K.S.J. & collaborators (2008). The Sixth Data Release of the Sloan Digital Sky Survey. *ApJS*, **175**, 297–313. 30, 33

Afshordi, N., Loh, Y.S. & Strauss, M.A. (2004). Cross-correlation of the cosmic microwave background with the 2MASS galaxy survey: Signatures of dark energy, hot gas, and point sources. *Phys. Rev. D*, **69**, 083524. 7

Ahn, C.P., Alexandroff, R. & collaborators (2012). The Ninth Data Release of the Sloan Digital Sky Survey: First Spectroscopic Data from the SDSS-III Baryon Oscillation Spectroscopic Survey. *ApJS*, **203**, 21. 30

Ahn, C.P., Alexandroff, R. & collaborators (2014). The Tenth Data Release of the Sloan Digital Sky Survey: First Spectroscopic Data from the SDSS-III Apache Point Observatory Galactic Evolution Experiment. *ApJS*, **211**, 17. 30

Aihara, H., Allende Prieto, C., An, D., Anderson, S.F., Aubourg, É., Balbinot, E. & collaborators (2011). The Eighth Data Release of the Sloan Digital Sky Survey: First Data from SDSS-III. *ApJS*, **193**, 29. 30

Almeida, C., Baugh, C.M., Wake, D.A., Lacey, C.G., Benson, A.J., Bower, R.G. & Pimbblet, K. (2008). Luminous red galaxies in hierarchical cosmologies. *MNRAS*, **386**, 2145–2160. 14

Anders, E. & Grevesse, N. (1989). Abundances of the elements - Meteoritic and solar. *Geochim. Cosmochim. Acta*, **53**, 197–214. 18

Anderson, L., Aubourg, É., Bailey, S., Beutler, F., Bhardwaj, V., Blanton, M. & collaborators (2014). The clustering of galaxies in the SDSS-III Baryon Oscillation Spectroscopic Survey: baryon acoustic oscillations in the Data Releases 10 and 11 Galaxy samples. *MNRAS*, **441**, 24–62. 143

Bagnulo, S., Jehin, E., Ledoux, C., Cabanac, R., Melo, C., Gilmozzi, R. & ESO Paranal Science Operations Team (2003). The UVES Paranal Observatory Project: A Library of High- Resolution Spectra of Stars across the Hertzsprung-Russell Diagram. *The Messenger*, **114**, 10–14. 24

Baldwin, J.A., Phillips, M.M. & Terlevich, R. (1981). Classification parameters for the emission-line spectra of extragalactic objects. *PASP*, **93**, 5–19. 40

Balogh, M.L., Morris, S.L., Yee, H.K.C., Carlberg, R.G. & Ellingson, E. (1999). Differential Galaxy Evolution in Cluster and Field Galaxies at z˜0.3. *ApJ*, **527**, 54–79. 108

Baraffe, I., Chabrier, G., Allard, F. & Hauschildt, P.H. (1998). Evolutionary models for solar metallicity low-mass stars: mass-magnitude relationships and color-magnitude diagrams. *A&A*, **337**, 403–412. 22

Barber, T., Meiksin, A. & Murphy, T. (2007). Properties of luminous red galaxies in the Sloan Digital Sky Survey. *MNRAS*, **377**, 787–805. 12, 13

Bastian, N., Covey, K.R. & Meyer, M.R. (2010). A Universal Stellar Initial Mass Function? A Critical Look at Variations. *ARA&A*, **48**, 339–389. 20

Bauer, A.E., Drory, N., Hill, G.J. & Feulner, G. (2005). Specific Star Formation Rates to Redshift 1.5. *ApJ*, **621**, L89–L92. 12

Baugh, C.M. (2006). Cosmic cookery: growing galaxies in a computer. *Astronomy and Geophysics*, **47**, 10–2. 14

Baum, W.A. (1959). Population Inferences from Star Counts, Surface Brightness and Colors. *PASP*, **71**, 106–117. 27

Beifiori, A., Maraston, C., Thomas, D. & Johansson, J. (2011). On the spectral resolution of the MILES stellar library. *A&A*, **531**, A109. 52

Bernardi, M. (2007). The σ-L Correlation in Nearby Early-Type Galaxies. *AJ*, **133**, 1954–1961. 35

Bernardi, M., Sheth, R.K. & collaborators (2003). Early-Type Galaxies in the Sloan Digital Sky Survey. I. The Sample. *AJ*, **125**, 1817–1848. 35

Bernardi, M., Nichol, R.C., Sheth, R.K., Miller, C.J. & Brinkmann, J. (2006). Evolution and Environment of Early-Type Galaxies. *AJ*, **131**, 1288–1317. 12

Bertelli, G., Bressan, A., Chiosi, C., Fagotto, F. & Nasi, E. (1994). Theoretical isochrones from models with new radiative opacities. *A&AS*, **106**, 275–302. 22, 61

Beutler, F., Blake, C., Colless, M., Jones, D.H., Staveley-Smith, L., Campbell, L., Parker, Q., Saunders, W. & Watson, F. (2011). The 6dF Galaxy Survey: baryon acoustic oscillations and the local Hubble constant. *MNRAS*, **416**, 3017–3032. 142

Blake, C. & Wall, J. (2002). A velocity dipole in the distribution of radio galaxies. *Nature*, **416**, 150–152. 5

Blake, C., Brough, S., Colless, M., Contreras, C., Couch, W., Croom, S., Davis, T., Drinkwater, M.J., Forster, K., Gilbank, D., Gladders, M., Glazebrook, K., Jelliffe, B., Jurek, R.J., Li, I.H., Madore, B., Martin, D.C., Pimbblet, K., Poole, G.B., Pracy, M., Sharp, R., Wisnioski, E., Woods, D., Wyder, T.K. & Yee, H.K.C. (2011a). The WiggleZ Dark Energy Survey: the growth rate of cosmic structure since redshift z=0.9. *MNRAS*, **415**, 2876–2891. 8

Blake, C., Davis, T., Poole, G.B., Parkinson, D., Brough, S., Colless, M., Contreras, C., Couch, W., Croom, S., Drinkwater, M.J., Forster, K., Gilbank, D., Gladders, M., Glazebrook, K., Jelliffe, B., Jurek, R.J., Li, I.H., Madore, B., Martin, D.C., Pimbblet, K., Pracy, M., Sharp, R., Wisnioski, E., Woods, D., Wyder, T.K. & Yee, H.K.C. (2011b). The WiggleZ Dark Energy Survey: testing the cosmological model with baryon acoustic oscillations at z= 0.6. *MNRAS*, **415**, 2892–2909. 8

Blanton, M.R., Lin, H., Lupton, R.H., Maley, F.M., Young, N., Zehavi, I. & Loveday, J. (2003). An Efficient Targeting Strategy for Multiobject Spectrograph Surveys: the Sloan Digital Sky Survey "Tiling" Algorithm. *AJ*, **125**, 2276–2286. 26, 31, 108

Bohlin, R.C., Jenkins, E.B., Spitzer, L., Jr., York, D.G., Hill, J.K., Savage, B.D. & Snow, T.P., Jr. (1983). A survey of ultraviolet interstellar absorption lines. *ApJS*, **51**, 277–308. 109

Bono, G., Caputo, F., Cassisi, S., Castellani, V. & Marconi, M. (1997). Evolutionary and Pulsational Constraints for Super-Metal-rich Stars with Z = 0.04. *ApJ*, **489**, 822–847. 52

Boughn, S.P. & Crittenden, R.G. (2005). A detection of the integrated Sachs Wolfe effect. *New A Rev.*, **49**, 75–78. 7

Bower, R.G., Ellis, R.S., Rose, J.A. & Sharples, R.M. (1990). The stellar populations of early-type galaxies as a function of their environment. *AJ*, **99**, 530–539. 13

Bower, R.G., Lucey, J.R. & Ellis, R.S. (1992). Precision photometry of early-type galaxies in the Coma and Virgo clusters: A test of the universality of the colour-magnitude relation. I - The data. II. Analysis. *MNRAS*, **254**, 589–613. 26, 27

Bower, R.G., Benson, A.J., Malbon, R., Helly, J.C., Frenk, C.S., Baugh, C.M., Cole, S. & Lacey, C.G. (2006). Breaking the hierarchy of galaxy formation. *MNRAS*, **370**, 645–655. 14

Bruzual, G. & Charlot, S. (2003). Stellar population synthesis at the resolution of 2003. *MNRAS*, **344**, 1000–1028. 19, 28, 29, 36, 61

Buat, V., Giovannoli, E., Takeuchi, T.T., Heinis, S., Yuan, F.T., Burgarella, D., Noll, S. & Iglesias-Páramo, J. (2011). Spectral energy distributions of an AKARI-SDSS-GALEX sample of galaxies. *A&A*, **529**, A22. 106

Burgarella, D., Buat, V. & Iglesias-Páramo, J. (2005). Star formation and dust attenuation properties in galaxies from a statistical ultraviolet-to-far-infrared analysis. *MNRAS*, **360**, 1413–1425. 105

Burgh, E.B., Nordsieck, K.H., Kobulnicky, H.A., Williams, T.B., O'Donoghue, D., Smith, M.P. & Percival, J.W. (2003). Prime Focus Imaging Spectrograph for the Southern African Large Telescope: optical design. In M. Iye & A.F.M. Moorwood, eds., *Instrument Design and Performance for Optical/Infrared Ground-based Telescopes*, vol. 4841 of *Society of Photo-Optical Instrumentation Engineers (SPIE) Conference Series*, 1463–1471. 113

Busca, N.G., Delubac, T., Rich, J., Bailey, S., Font-Ribera, A., Kirkby, D. & collaborators (2013). Baryon acoustic oscillations in the Lyα forest of BOSS quasars. *A&A*, **552**, A96. 143

Cabré, A. & Gaztañaga, E. (2009). Clustering of luminous red galaxies - II. Small-scale redshift-space distortions. *MNRAS*, **396**, 1119–1131. 13

Caldwell, N., Rose, J.A. & Concannon, K.D. (2003). Star Formation Histories of Early-Type Galaxies. I. Higher Order Balmer Lines as Age Indicators. *AJ*, **125**, 2891–2926. 27, 73

Caldwell, N., Harding, P., Morrison, H., Rose, J.A., Schiavon, R. & Kriessler, J. (2009). Star Clusters in M31. I. A Catalog and a Study of the Young Clusters. *AJ*, **137**, 94–110. 52

Calzetti, D., Armus, L., Bohlin, R.C., Kinney, A.L., Koornneef, J. & Storchi-Bergmann, T. (2000). The Dust Content and Opacity of Actively Star-forming Galaxies. *ApJ*, **533**, 682–695. 64, 106

Cannon, R., Drinkwater, M., Edge, A., Eisenstein, D., Nichol, R., Outram & collaborators (2006). The 2dF-SDSS LRG and QSO (2SLAQ) Luminous Red Galaxy Survey. *MNRAS*, **372**, 425–442. xxi, 101, 102, 113

Cao, S., Pan, Y., Biesiada, M., Godlowski, W. & Zhu, Z.H. (2012). Constraints on cosmological models from strong gravitational lensing systems. *J. Cosmology Astropart. Phys.*, **3**, 16. 9

Capozziello, S., Cardone, V.F., Funaro, M. & Andreon, S. (2004). Constraining dark energy models using the lookback time to galaxy clusters and the age of the universe. *Phys. Rev. D*, **70**, 123501. 11

Cappellari, M. & Emsellem, E. (2004). Parametric Recovery of Line-of-Sight Velocity Distributions from Absorption-Line Spectra of Galaxies via Penalized Likelihood. *PASP*, **116**, 138–147. 36, 120

Cardiel, N. (2010). indexf: Line-strength Indices in Fully Calibrated FITS Spectra. Astrophysics Source Code Library. 49

Cardiel, N., Gorgas, J., Cenarro, J. & Gonzalez, J.J. (1998). Reliable random error estimation in the measurement of line-strength indices. *A&AS*, **127**, 597–605. 45, 49, 87, 109

Carretta, E., Gratton, R.G., Clementini, G. & Fusi Pecci, F. (2000). Distances, Ages, and Epoch of Formation of Globular Clusters. *ApJ*, **533**, 215–235. 11

Carroll, S.M., Press, W.H. & Turner, E.L. (1992). The cosmological constant. *ARA&A*, **30**, 499–542. 6

Carson, D.P. & Nichol, R.C. (2010). The age-redshift relation for luminous red galaxies in the Sloan Digital Sky Survey. *MNRAS*, **408**, 213–233. 11, 25, 30, 40, 41, 42, 49, 50, 53, 54, 66, 82, 87, 88

Cassisi, S., Castellani, M. & Castellani, V. (1997). Intermediate-age metal deficient stellar populations: the case of metallicity Z=0.00001. *A&A*, **317**, 108–113. 52, 62

Cenarro, A.J., Gorgas, J., Cardiel, N., Pedraz, S., Peletier, R.F. & Vazdekis, A. (2001). Empirical calibration of the near-infrared Ca ii triplet - II. The stellar atmospheric parameters. *MNRAS*, **326**, 981–994. 109

Cenarro, A.J., Peletier, R.F., Sánchez-Blázquez, P., Selam, S.O., Toloba, E. & collaborators (2007). Medium-resolution Isaac Newton Telescope library of empirical spectra - II. The stellar atmospheric parameters. *MNRAS*, **374**, 664–690. 23, 24

Chaboyer, B., Demarque, P., Kernan, P.J., Krauss, L.M. & Sarajedini, A. (1996). An accurate relative age estimator for globular clusters. *MNRAS*, **283**, 683–689. 11

Chabrier, G. (2003). Galactic Stellar and Substellar Initial Mass Function. *PASP*, **115**, 763–795. 21, 62

Chabrier, G. & Baraffe, I. (1997). Structure and evolution of low-mass stars. *A&A*, **327**, 1039–1053. 22

Charbonnel, C., Meynet, G., Maeder, A. & Schaerer, D. (1996). Grids of stellar models. VI. Horizontal branch and early asymptotic giant branch for low mass stars (Z=0.020, 0.001). *A&AS*, **115**, 339. 61

Charbonnel, C., Däppen, W., Schaerer, D., Bernasconi, P.A., Maeder, A., Meynet, G. & Mowlavi, N. (1999). Grids of stellar models. VIII. From 0.4 to 1.0 $\{M_{sun}\}$ at Z=0.020 and Z=0.001, with the MHD equation of state. *A&AS*, **135**, 405–413. 61

Charlot, S., Worthey, G. & Bressan, A. (1996). Uncertainties in the Modeling of Old Stellar Populations. *ApJ*, **457**, 625. 22

Chen, Y., Trager, S., Peletier, R. & Lançon, A. (2011). XSL: The X-Shooter Spectral Library. *Journal of Physics Conference Series*, **328**, 012023. 24

Chilingarian, I., Prugniel, P., Sil'Chenko, O. & Koleva, M. (2007). NBursts: Simultaneous Extraction of Internal Kinematics and Parametrized SFH from Integrated Light Spectra. **241**, 175–176. 56

Cid Fernandes, R. & González Delgado, R.M. (2010). Testing spectral models for stellar populations with star clusters - I. Methodology. *MNRAS*, **403**, 780–796. 22

Cid Fernandes, R., Mateus, A., Sodré, L., Stasińska, G. & Gomes, J.M. (2005). Semi-empirical analysis of Sloan Digital Sky Survey galaxies - I. Spectral synthesis method. *MNRAS*, **358**, 363–378. 56, 60

Coelho, P., Barbuy, B., Meléndez, J., Schiavon, R.P. & Castilho, B.V. (2005). A library of high resolution synthetic stellar spectra from 300 nm to 1.8 μm with solar and α-enhanced composition. *A&A*, **443**, 735–746. 25

Collister, A., Lahav, O., Blake, C., Cannon, R., Croom, S., Drinkwater & collaborators (2007). MegaZ-LRG: a photometric redshift catalogue of one million SDSS luminous red galaxies. *MNRAS*, **375**, 68–76. xvi, xxi, 102, 103, 111, 113

Collister, A.A. & Lahav, O. (2004). ANNz: Estimating Photometric Redshifts Using Artificial Neural Networks. *PASP*, **116**, 345–351. 102

Conroy, C. (2013). Modeling the Panchromatic Spectral Energy Distributions of Galaxies. *ARA&A*, **51**, 393–455. 21

Conroy, C., Ho, S. & White, M. (2007). Constraints on the merging time-scale of luminous red galaxies, or, where do all the haloes go? *MNRAS*, **379**, 1491–1497. 13

Conroy, C., Gunn, J.E. & White, M. (2009). The Propagation of Uncertainties in Stellar Population Synthesis Modeling. I. The Relevance of Uncertain Aspects of Stellar Evolution and the Initial Mass Function to the Derived Physical Properties of Galaxies. *ApJ*, **699**, 486–506. 21, 22, 29

Corasaniti, P.S., Huterer, D. & Melchiorri, A. (2007). Exploring the dark energy redshift desert with the Sandage-Loeb test. *Phys. Rev. D*, **75**, 062001. 149

Cordier, D., Pietrinferni, A., Cassisi, S. & Salaris, M. (2007). A Large Stellar Evolution Database for Population Synthesis Studies. III. Inclusion of the Full Asymptotic Giant Branch Phase and Web Tools for Stellar Population Analyses. *AJ*, **133**, 468–478. 22

Cowan, G. (1998). *Statistical Data Analysis*. 138

Crawford, C.S., Allen, S.W., Ebeling, H., Edge, A.C. & Fabian, A.C. (1999). The ROSAT Brightest Cluster Sample - III. Optical spectra of the central cluster galaxies. *MNRAS*, **306**, 857–896. 123

Crawford, S.M., Ratsimbazafy, A.L., Cress, C.M., Olivier, E.A., Blyth, S.L. & van der Heyden, K.J. (2010a). Luminous red galaxies in simulations: cosmic chronometers? *MNRAS*, **406**, 2569–2577. 10, 11, 87, 99, 121, 127, 128

Crawford, S.M., Still, M., Schellart, P., Balona, L., Buckley, D.A.H., Dugmore, G. & collaborators (2010b). PySALT: the SALT science pipeline. In *Society of Photo-Optical Instrumentation Engineers (SPIE) Conference Series*, vol. 7737 of *Society of Photo-Optical Instrumentation Engineers (SPIE) Conference Series*. 38, 116

Dale, D.A. & Helou, G. (2002). The Infrared Spectral Energy Distribution of Normal Star-forming Galaxies: Calibration at Far-Infrared and Submillimeter Wavelengths. *ApJ*, **576**, 159–168. 106, 107

Dantas, M.A., Alcaniz, J.S., Jain, D. & Dev, A. (2007). Age constraints on the cosmic equation of state. *A&A*, **467**, 421–426. 11

Dauphas, N. (2005). The U/Th production ratio and the age of the Milky Way from meteorites and Galactic halo stars. *Nature*, **435**, 1203–1205. 11

De Lucia, G. & Blaizot, J. (2007). The hierarchical formation of the brightest cluster galaxies. *MNRAS*, **375**, 2–14. 12

De Lucia, G., Springel, V., White, S.D.M., Croton, D. & Kauffmann, G. (2006). The formation history of elliptical galaxies. *MNRAS*, **366**, 499–509. 12, 14

Dias, B., Coelho, P., Barbuy, B., Kerber, L. & Idiart, T. (2010). Age and metallicity of star clusters in the Small Magellanic Cloud from integrated spectroscopy. *A&A*, **520**, A85. 57, 77

Djorgovski, S. & Davis, M. (1987). Fundamental properties of elliptical galaxies. *ApJ*, **313**, 59–68. 27

Donoso, E., Yan, L., Tsai, C., Eisenhardt, P., Stern, D., Assef, R.J. & collaborators (2012). Origin of 12 μm Emission across Galaxy Populations from WISE and SDSS Surveys. *ApJ*, **748**, 80. 103

Dotter, A., Chaboyer, B., Jevremović, D., Kostov, V., Baron, E. & Ferguson, J.W. (2008). The Dartmouth Stellar Evolution Database. *ApJS*, **178**, 89–101. 22

Dressler, A., Lynden-Bell, D., Burstein, D., Davies, R.L., Faber, S.M., Terlevich, R. & Wegner, G. (1987). Spectroscopy and photometry of elliptical galaxies. I - A new distance estimator. *ApJ*, **313**, 42–58. 27

Dvali, G., Gabadadze, G. & Porrati, M. (2000). 4D gravity on a brane in 5D Minkowski space. *Physics Letters B*, **485**, 208–214. 6

Eisenstein, D.J., Annis, J., Gunn, J.E., Szalay, A.S., Connolly, A.J., Nichol, R.C. & collaborators (2001). Spectroscopic Target Selection for the Sloan Digital Sky Survey: The Luminous Red Galaxy Sample. *AJ*, **122**, 2267–2280. 12, 30, 38, 41, 87, 101

Eisenstein, D.J., Hogg, D.W., Fukugita, M., Nakamura, O. & collaborators (2003). Average Spectra of Massive Galaxies in the Sloan Digital Sky Survey. *ApJ*, **585**, 694–713. 12

Eisenstein, D.J., Zehavi, I., Hogg, D.W., Scoccimarro, R., Blanton, M.R., Nichol, R.C. & collaborators (2005). Detection of the Baryon Acoustic Peak in the Large-Scale Correlation Function of SDSS Luminous Red Galaxies. *ApJ*, **633**, 560–574. 9, 12, 13

Faber, S.M. (1973). Variations in Spectral-Energy Distributions and Absorption-Line Strengths among Elliptical Galaxies. *ApJ*, **179**, 731–754. 12

Faber, S.M. & Jackson, R.E. (1976). Velocity dispersions and mass-to-light ratios for elliptical galaxies. *ApJ*, **204**, 668–683. 27

Faber, S.M., Friel, E.D., Burstein, D. & Gaskell, C.M. (1985). Old stellar populations. II - an analysis of K-giant spectra. *ApJS*, **57**, 711–741. 44, 45

Faber, S.M., Willmer, C.N.A., Wolf, C., Koo, D.C., Weiner, B.J., Newman, J.A. & collaborators (2007). Galaxy Luminosity Functions to z˜1 from DEEP2 and COMBO-17: Implications for Red Galaxy Formation. *ApJ*, **665**, 265–294. 26

Fabian, A.C. & Barcons, X. (1992). The origin of the X-ray background. *ARA&A*, **30**, 429–456. 5

Ferreras, I., Melchiorri, A. & Silk, J. (2001). Setting new constraints on the age of the Universe. *MNRAS*, **327**, L47–L51. 11

Ferreras, I., Melchiorri, A. & Tocchini-Valentini, D. (2003). Using bright ellipticals as dark energy cosmic clocks. *MNRAS*, **344**, 257–261. 11

Fioc, M. & Rocca-Volmerange, B. (1997). PEGASE: a UV to NIR spectral evolution model of galaxies. Application to the calibration of bright galaxy counts. *A&A*, **326**, 950–962. 106

Firth, A.E., Lahav, O. & Somerville, R.S. (2003). Estimating photometric redshifts with artificial neural networks. *MNRAS*, **339**, 1195–1202. 102

Fitzpatrick, E.L. (1999). Correcting for the Effects of Interstellar Extinction. *PASP*, **111**, 63–75. 120

Fosalba, P., Gaztañaga, E. & Castander, F.J. (2003). Detection of the Integrated Sachs-Wolfe and Sunyaev-Zeldovich Effects from the Cosmic Microwave Background-Galaxy Correlation. *ApJ*, **597**, L89–L92. 7

Fowler, W.A. (1987). The age of the observable universe (The Tenth Edward Arthur Milne Lecture). *QJRAS*, **28**, 87–108. 11

Fukugita, M., Ichikawa, T., Gunn, J.E., Doi, M., Shimasaku, K. & Schneider, D.P. (1996). The Sloan Digital Sky Survey Photometric System. *AJ*, **111**, 1748. 12, 30, 102

Gallazzi, A., Charlot, S., Brinchmann, J., White, S.D.M. & Tremonti, C.A. (2005). The ages and metallicities of galaxies in the local universe. *MNRAS*, **362**, 41–58. 12

Gallazzi, A., Charlot, S., Brinchmann, J. & White, S.D.M. (2006). Ages and metallicities of early-type galaxies in the Sloan Digital Sky Survey: new insight into the physical origin of the colour-magnitude and the Mg_2-σ_V relations. *MNRAS*, **370**, 1106–1124. 26

Gaztañaga, E., Cabré, A., Castander, F., Crocce, M. & Fosalba, P. (2009a). Clustering of luminous red galaxies - III. Baryon acoustic peak in the three-point correlation. *MNRAS*, **399**, 801–811. 13

Gaztañaga, E., Cabré, A. & Hui, L. (2009b). Clustering of luminous red galaxies - IV. Baryon acoustic peak in the line-of-sight direction and a direct measurement of H(z). *MNRAS*, **399**, 1663–1680. 140, 141

Giovannoli, E., Buat, V., Noll, S., Burgarella, D. & Magnelli, B. (2011). Population synthesis modelling of luminous infrared galaxies at intermediate redshift. *A&A*, **525**, A150. 105, 106

Girardi, L., Bressan, A., Bertelli, G. & Chiosi, C. (2000). Evolutionary tracks and isochrones for low- and intermediate-mass stars: From 0.15 to 7 M_{sun}, and from Z=0.0004 to 0.03. *A&AS*, **141**, 371–383. 22, 52, 61

Glazebrook, K., Blake, C., Couch, W., Forbes, D., Drinkwater, M., Jurek, R., Pimbblet, K., Madore, B., Martin, C., Small, T., Forster, K., Colless, M., Sharp, R., Croom, S., Woods, D., Pracy, M., Gilbank, D., Yee, H. & Gladders, M. (2007). The WiggleZ project: AAOmega and Dark Energy. *ArXiv Astrophysics e-prints*. 7

González, J.J. (1993). *Line strength gradients and kinematic profiles in elliptical galaxies*. Ph.D. thesis, Thesis (PH.D.)–UNIVERSITY OF CALIFORNIA, SANTA CRUZ, 1993.Source: Dissertation Abstracts International, Volume: 54-05, Section: B, page: 2551. 45, 56

González-Díaz, P.F. (2000). Cosmological models from quintessence. *Phys. Rev. D*, **62**, 023513. 6

Gunn, J.E., Siegmund, W.A., Mannery, E.J., Owen, R.E., Hull, C.L. & collaborators (2006). The 2.5 m Telescope of the Sloan Digital Sky Survey. *AJ*, **131**, 2332–2359. 30

Gustafsson, B., Edvardsson, B., Eriksson, K., Jørgensen, U.G., Nordlund, Å. & Plez, B. (2008). A grid of MARCS model atmospheres for late-type stars. I. Methods and general properties. *A&A*, **486**, 951–970. 62

Guth, A.H. (1981). Inflationary universe: A possible solution to the horizon and flatness problems. *Phys. Rev. D*, **23**, 347–356. 6

Haiman, Z., Mohr, J.J. & Holder, G.P. (2001). Constraints on Cosmological Parameters from Future Galaxy Cluster Surveys. *ApJ*, **553**, 545–561. 9

Hansen, B.M.S., Richer, H.B., Fahlman, G.G., Stetson, P.B., Brewer, J., Currie, T., Gibson, B.K., Ibata, R., Rich, R.M. & Shara, M.M. (2004). Hubble Space Telescope Observations of the White Dwarf Cooling Sequence of M4. *ApJS*, **155**, 551–576. 11

Heap, S.R. & Lindler, D. (2011). Atmospheric Parameters of Stars in Hubble's Next Generation Spectral Library. In C. Johns-Krull, M.K. Browning & A.A. West, eds., *16th Cambridge Workshop on Cool Stars, Stellar Systems, and the Sun*, vol. 448 of *Astronomical Society of the Pacific Conference Series*, 887. 24

Heavens, A.F., Jimenez, R. & Lahav, O. (2000). Massive lossless data compression and multiple parameter estimation from galaxy spectra. *MNRAS*, **317**, 965–972. 56

Hinshaw, G., Larson, D., Komatsu, E., Spergel, D.N. & Bennett, C.L.a.a. (2013). Nine-year Wilkinson Microwave Anisotropy Probe (WMAP) Observations: Cosmological Parameter Results. *ApJS*, **208**, 19. 9, 142

Hodge, J.A., Zeimann, G.R., Becker, R.H. & White, R.L. (2009). Faint, Evolving Radio Active Galactic Nuclei in SDSS Luminous Red Galaxies. *AJ*, **138**, 900–910. 13

Hogg, D.W., Finkbeiner, D.P., Schlegel, D.J. & Gunn, J.E. (2001). A Photometricity and Extinction Monitor at the Apache Point Observatory. *AJ*, **122**, 2129–2138. 30

Hogg, D.W., Blanton, M., Strateva, I., Bahcall, N.A., Brinkmann, J., Csabai, I. & collaborators (2002). The Luminosity Density of Red Galaxies. *AJ*, **124**, 646–651. 12

Hogg, D.W., Eisenstein, D.J., Blanton, M.R., Bahcall, N.A., Brinkmann, J., Gunn, J.E. & Schneider, D.P. (2005). Cosmic Homogeneity Demonstrated with Luminous Red Galaxies. *ApJ*, **624**, 54–58. 5

Hoversten, E.A. & Glazebrook, K. (2008). Evidence for a Nonuniversal Stellar Initial Mass Function from the Integrated Properties of SDSS Galaxies. *ApJ*, **675**, 163–187. 21

Jarrett, T.H., Cohen, M., Masci, F., Wright, E., Stern, D., Benford, D. & collaborators (2011). The Spitzer-WISE Survey of the Ecliptic Poles. *ApJ*, **735**, 112. 103, 105

Jimenez, R. & Loeb, A. (2002). Constraining Cosmological Parameters Based on Relative Galaxy Ages. *ApJ*, **573**, 37–42. 10, 11

Jimenez, R., Verde, L., Treu, T. & Stern, D. (2003). Constraints on the Equation of State of Dark Energy and the Hubble Constant from Stellar Ages and the Cosmic Microwave Background. *ApJ*, **593**, 622–629. 10, 11, 66, 71, 85, 86, 121, 123

Johansson, J., Thomas, D. & Maraston, C. (2012). Chemical element ratios of Sloan Digital Sky Survey early-type galaxies. *MNRAS*, **421**, 1908–1926. 53

Jorgensen, I., Franx, M. & Kjaergaard, P. (1995). Spectroscopy for E and S0 galaxies in nine clusters. *MNRAS*, **276**, 1341–1364. 51

Kauffmann, G., Heckman, T.M., Tremonti, C., Brinchmann, J., Charlot, S. & collaborators (2003). The host galaxies of active galactic nuclei. *MNRAS*, **346**, 1055–1077. 40

Kobulnicky, H.A., Nordsieck, K.H., Burgh, E.B., Smith, M.P., Percival, J.W., Williams, T.B. & O'Donoghue, D. (2003). Prime focus imaging spectrograph for the Southern African large telescope: operational modes. In M. Iye & A.F.M. Moorwood, eds., *Instrument Design and Performance for Optical/Infrared Ground-based Telescopes*, vol. 4841 of *Society of Photo-Optical Instrumentation Engineers (SPIE) Conference Series*, 1634–1644. 113

Koleva, M., Prugniel, P., Ocvirk, P., Le Borgne, D. & Soubiran, C. (2008). Spectroscopic ages and metallicities of stellar populations: validation of full spectrum fitting. *MNRAS*, **385**, 1998–2010. 29, 56, 57, 60, 65, 68, 75, 76

Koleva, M., Prugniel, P., Bouchard, A. & Wu, Y. (2009). ULySS: a full spectrum fitting package. *A&A*, **501**, 1269–1279. 25, 56, 59, 64, 65, 120, 123

Komatsu, E., Smith, K.M., Dunkley, J., Bennett, C.L., Gold, B., Hinshaw, G. & collaborators (2011). Seven-year Wilkinson Microwave Anisotropy Probe (WMAP) Observations: Cosmological Interpretation. *ApJS*, **192**, 18.

Kormendy, J. (1977). Brightness distributions in compact and normal galaxies. II - Structure parameters of the spheroidal component. *ApJ*, **218**, 333–346. 27

Korn, A.J., Maraston, C. & Thomas, D. (2005). The sensitivity of Lick indices to abundance variations. *A&A*, **438**, 685–704. 88

Kowalski, M., Rubin, D., Aldering, G., Agostinho, R.J., Amadon, A., Amanullah, R. & Supernova Cosmology Project (2008). Improved Cosmological Constraints from New, Old, and Combined Supernova Data Sets. *ApJ*, **686**, 749–778. 6

Kroupa, P. (2001). On the variation of the initial mass function. *MNRAS*, **322**, 231–246. 21

Kroupa, P. (2002). The Initial Mass Function of Stars: Evidence for Uniformity in Variable Systems. *Science*, **295**, 82–91. 20

Kuntschner, H. (2000). The stellar populations of early-type galaxies in the Fornax cluster. *MNRAS*, **315**, 184–208. 25

Lançon, A. & Wood, P.R. (2000). A library of 0.5 to 2.5 mu m spectra of luminous cool stars. *A&AS*, **146**, 217–249. 24

Lançon, A., Hauschildt, P.H., Ladjal, D. & Mouhcine, M. (2007). Near-IR spectra of red supergiants and giants. I. Models with solar and with mixing-induced surface abundance ratios. *A&A*, **468**, 205–220. 17

Le Borgne, D., Rocca-Volmerange, B., Prugniel, P., Lançon, A., Fioc, M. & Soubiran, C. (2004). Evolutionary synthesis of galaxies at high spectral resolution with the code PEGASE-HR. Metallicity and age tracers. *A&A*, **425**, 881–897. 19, 28, 61, 121

Le Borgne, J.F., Bruzual, G., Pelló, R., Lançon, A., Rocca-Volmerange, B., Sanahuja, B., Schaerer, D., Soubiran, C. & Vílchez-Gómez, R. (2003). STELIB: A library of stellar spectra at R ˜ 2000. *A&A*, **402**, 433–442. 24, 61

Leaman, R. (2012). Insights into Pre-enrichment of Star Clusters and Self-enrichment of Dwarf Galaxies from Their Intrinsic Metallicity Dispersions. *AJ*, **144**, 183. 63

Lee, H.c., Worthey, G., Trager, S.C. & Faber, S.M. (2007). On the Age and Metallicity Estimation of Spiral Galaxies Using Optical and Near-Infrared Photometry. *ApJ*, **664**, 215–225. 22

Lewis, D.J. & Simnett, G.M. (2002). Bulk flow velocities in the solar corona at solar maximum. *MNRAS*, **333**, 969–976. 101

Liu, G., Lu, Y., Chen, X., Zhao, Y., Du, W. & Meng, X. (2012). The Age-redshift Relation for Luminous Red Galaxies Obtained from Full Spectrum Fitting and its Cosmological Implications. *ApJ*, **758**, 107. 10, 11, 30, 41, 66, 71, 73, 75, 82, 85, 87, 88, 121, 123

Liu, G.C., Lu, Y.J., Chen, X.L., Du, W. & Zhao, Y.H. (2013). On fitting the full spectrum of luminous red galaxies by using ULySS and STARLIGHT. *Research in Astronomy and Astrophysics*, **13**, 1025–1040. 57, 60, 66

Loubser, S.I. (2014). Stellar populations in central cluster galaxies: the influence of cooling flows. *MNRAS*. 123

Loubser, S.I., Sánchez-Blázquez, P., Sansom, A.E. & Soechting, I.K. (2009). Stellar populations in the centres of brightest cluster galaxies. *MNRAS*, **398**, 133–156. 53, 123

Lupton, R., Gunn, J.E., Ivezić, Z., Knapp, G.R. & Kent, S. (2001). The SDSS Imaging Pipelines. In F.R. Harnden Jr., F.A. Primini & H.E. Payne, eds., *Astronomical Data Analysis Software and Systems X*, vol. 238 of *Astronomical Society of the Pacific Conference Series*, 269. 30

Maraston, C. (1998). Evolutionary synthesis of stellar populations: a modular tool. *MNRAS*, **300**, 872–892. 28, 52

Maraston, C. (2005). Evolutionary population synthesis: models, analysis of the ingredients and application to high-z galaxies. *MNRAS*, **362**, 799–825. 19, 28, 29, 52, 61, 62, 106

Maraston, C. & Strömbäck, G. (2011). Stellar population models at high spectral resolution. *MNRAS*, **418**, 2785–2811. 24, 28, 62, 63, 67

Markevitch, M., Gonzalez, A.H., Clowe, D., Vikhlinin, A., Forman, W., Jones, C., Murray, S. & Tucker, W. (2004). Direct Constraints on the Dark Matter Self-Interaction Cross Section from the Merging Galaxy Cluster 1E 0657-56. *ApJ*, **606**, 819–824. 9

Martins, L.P. & Coelho, P. (2007). Testing the accuracy of synthetic stellar libraries. *MNRAS*, **381**, 1329–1346. 24

Martins, L.P., González Delgado, R.M., Leitherer, C., Cerviño, M. & Hauschildt, P. (2005). A high-resolution stellar library for evolutionary population synthesis. *MNRAS*, **358**, 49–65. 25

Masjedi, M., Hogg, D.W., Cool, R.J., Eisenstein, D.J., Blanton, M.R., Zehavi, I. & collaborators (2006). Very Small Scale Clustering and Merger Rate of Luminous Red Galaxies. *ApJ*, **644**, 54–60. 13

Mehlert, D., Thomas, D., Saglia, R.P., Bender, R. & Wegner, G. (2003). Spatially resolved spectroscopy of Coma cluster early-type galaxies. III. The stellar population gradients. *A&A*, **407**, 423–435. 51, 52

Melia, F. & Maier, R.S. (2013). Cosmic chronometers in the $R_h = ct$ Universe. *MNRAS*, **432**, 2669–2675. 12

Melia, F. & Shevchuk, A.S.H. (2012). The R_h=ct universe. *MNRAS*, **419**, 2579–2586. 12

Meurer, G.R., Wong, O.I., Kim, J.H., Hanish, D.J., Heckman, T.M., Werk, J., Bland-Hawthorn, J., Dopita, M.A., Zwaan, M.A., Koribalski, B., Seibert, M., Thilker, D.A., Ferguson, H.C., Webster, R.L., Putman, M.E., Knezek, P.M., Doyle, M.T., Drinkwater, M.J., Hoopes, C.G., Kilborn, V.A., Meyer, M., Ryan-Weber, E.V., Smith, R.C. & Staveley-Smith, L. (2009). Evidence for a Nonuniform Initial Mass Function in the Local Universe. *ApJ*, **695**, 765–780. 21

Meynet, G. & Maeder, A. (2000). Stellar evolution with rotation. V. Changes in all the outputs of massive star models. *A&A*, **361**, 101–120. 22

Michielsen, D., Koleva, M., Prugniel, P., Zeilinger, W.W., De Rijcke, S., Dejonghe, H. & collaborators (2007). Toward a Solution for the Ca II Triplet Puzzle: Results from Dwarf Elliptical Galaxies. *ApJ*, **670**, L101–L104. 60

Milone, A.D.C., Sansom, A.E. & Sánchez-Blázquez, P. (2011). Element abundances in the stars of the MILES spectral library: the Mg/Fe ratio. *MNRAS*, **414**, 1227–1252. 23

Moore, S.A. (2001). *Stellar populations in early-type coma cluster galaxies*. Ph.D. thesis, Thesis (PH.D.)–DURHAM UNIVERSITY, 2001.Source: Dissertation Abstracts International, Volume: 54-05, Section: B, page: 2551. xx, 18

Moresco, M., Jimenez, R., Cimatti, A. & Pozzetti, L. (2011). Constraining the expansion rate of the Universe using low-redshift ellipticals as cosmic chronometers. *J. Cosmology Astropart. Phys.*, **3**, 45. 10, 11

Moresco, M., Cimatti, A., Jimenez, R., Pozzetti, L., Zamorani, G., Bolzonella, M. & collaborators (2012a). Improved constraints on the expansion rate of the Universe up to z ˜ 1.1 from the spectroscopic evolution of cosmic chronometers. *J. Cosmology Astropart. Phys.*, **8**, 6. 10, 11, 12, 86, 89, 99, 121, 141

Moresco, M., Verde, L., Pozzetti, L., Jimenez, R. & Cimatti, A. (2012b). New constraints on cosmological parameters and neutrino properties using the expansion rate of the Universe to z ˜ 1.75. *J. Cosmology Astropart. Phys.*, **7**, 53. 12, 140, 142

Munari, U., Sordo, R., Castelli, F. & Zwitter, T. (2005). An extensive library of 2500 10 500 Å synthetic spectra. *A&A*, **442**, 1127–1134. 25

Nelan, J.E., Smith, R.J., Hudson, M.J., Wegner, G.A., Lucey, J.R. & collaborators (2005). NOAO Fundamental Plane Survey. II. Age and Metallicity along the Red Sequence from Line-Strength Data. *ApJ*, **632**, 137–156. 27, 73

Noll, S., Burgarella, D., Giovannoli, E., Buat, V., Marcillac, D. & Muñoz-Mateos, J.C. (2009). Analysis of galaxy spectral energy distributions from far-UV to far-IR with CIGALE: studying a SINGS test sample. *A&A*, **507**, 1793–1813. 105

Ocvirk, P., Pichon, C., Lançon, A. & Thiébaut, E. (2006a). STECKMAP: STEllar Content and Kinematics from high resolution galactic spectra via Maximum A Posteriori. *MNRAS*, **365**, 74–84. 56, 60

Ocvirk, P., Pichon, C., Lançon, A. & Thiébaut, E. (2006b). STECMAP: STEllar Content from high-resolution galactic spectra via Maximum A Posteriori. *MNRAS*, **365**, 46–73. 56, 60

Oh, K., Sarzi, M., Schawinski, K. & Yi, S.K. (2011). Improved and Quality-assessed Emission and Absorption Line Measurements in Sloan Digital Sky Survey Galaxies. *ApJS*, **195**, 13. 36, 47, 50, 175

Padmanabhan, N., Schlegel, D.J., Seljak, U., Makarov, A. & collaborators. (2007). The clustering of luminous red galaxies in the Sloan Digital Sky Survey imaging data. *MNRAS*, **378**, 852–872. 13

Padmanabhan, N., Xu, X., Eisenstein, D.J., Scalzo, R., Cuesta, A.J., Mehta, K.T. & Kazin, E. (2012). A 2 per cent distance to z = 0.35 by reconstructing baryon acoustic oscillations - I. Methods and application to the Sloan Digital Sky Survey. *MNRAS*, **427**, 2132–2145. 143

Paudel, S.A. (2011). *Early-type dwarf galaxies: Insight from stellar population studies*. Ph.D. thesis, Thesis (PH.D.)–UNIVERSITY OF HEIDELBERG, 2011.Source: Dissertation Abstracts International, Volume: 54-05, Section: B, page: 2551. ix, 20

Peebles, P.J.E. (1980). *The large-scale structure of the universe*. 8

Peebles, P.J.E. (2007). Galaxies as a cosmological test. *Nuovo Cimento B Serie*, **122**, 1035–1042. 6

Penzias, A.A. & Wilson, R.W. (1965). A Measurement of Excess Antenna Temperature at 4080 Mc/s. *ApJ*, **142**, 419–421. 5

Percival, W.J., Reid, B.A., Eisenstein, D.J., Bahcall, N.A., Budavari, T. & collaborators (2010). Baryon acoustic oscillations in the Sloan Digital Sky Survey Data Release 7 galaxy sample. *MNRAS*, **401**, 2148–2168. 9

Perlmutter, S., Aldering, G., Goldhaber, G., Knop, R.A., Nugent, P. & collaborators (1999). Measurements of Ω and Λ from 42 High-Redshift Supernovae. *ApJ*, **517**, 565–586. 4, 7

Pforr, J., Maraston, C. & Tonini, C. (2012). Recovering galaxy stellar population properties from broad-band spectral energy distribution fitting. *MNRAS*, **422**, 3285–3326. 21

Pickles, A.J. (1998). A Stellar Spectral Flux Library: 1150-25000 Å. *PASP*, **110**, 863–878. 24

Pietrinferni, A., Cassisi, S., Salaris, M. & Castelli, F. (2004). A Large Stellar Evolution Database for Population Synthesis Studies. I. Scaled Solar Models and Isochrones. *ApJ*, **612**, 168–190. 22

Planck Collaboration, Ade, P.A.R., Aghanim, N., Armitage-Caplan, C. & collaborators (2013). Planck 2013 results. XVI. Cosmological parameters. *ArXiv e-prints*. 9

Prugniel, P. & Soubiran, C. (2001). A database of high and medium-resolution stellar spectra. *A&A*, **369**, 1048–1057. 23, 24

Prugniel, P., Soubiran, C., Koleva, M. & Le Borgne, D. (2007). New release of the ELODIE library: Version 3.1. *ArXiv Astrophysics e-prints*. 23, 24, 61, 67

Prugniel, P., Vauglin, I. & Koleva, M. (2011). The atmospheric parameters and spectral interpolator for the MILES stars. *A&A*, **531**, A165. 23

Ramírez, I., Allende Prieto, C. & Lambert, D.L. (2013). Oxygen Abundances in Nearby FGK Stars and the Galactic Chemical Evolution of the Local Disk and Halo. *ApJ*, **764**, 78. 121

Rayner, J.T., Cushing, M.C. & Vacca, W.D. (2009). The Infrared Telescope Facility (IRTF) Spectral Library: Cool Stars. *ApJS*, **185**, 289–432. 24

Refregier, A. (2003). Weak Gravitational Lensing by Large-Scale Structure. *ARA&A*, **41**, 645–668. 9

Renzini, A. (2006). Stellar Population Diagnostics of Elliptical Galaxy Formation. *ARA&A*, **44**, 141–192. 26

Richards, G.T., Fan, X. & collaborators (2002). Spectroscopic Target Selection in the Sloan Digital Sky Survey: The Quasar Sample. *AJ*, **123**, 2945–2975. 30

Riess, A.G., Filippenko, A.V., Challis, P., Clocchiatti, A., Diercks, A. & collaborators (1998). Observational Evidence from Supernovae for an Accelerating Universe and a Cosmological Constant. *AJ*, **116**, 1009–1038. 4, 7, 9

Rodríguez-Merino, L.H., Chavez, M., Bertone, E. & Buzzoni, A. (2005). UVBLUE: A New High-Resolution Theoretical Library of Ultraviolet Stellar Spectra. *ApJ*, **626**, 411–424. 25

Roehlly, Y., Burgarella, D., Buat, V., Giovannoli, É., Noll, S. & Serra, P. (2012). CIGALE: Code Investigating GALaxy Emission. In P. Ballester, D. Egret & N.P.F. Lorente, eds., *Astronomical Data Analysis Software and Systems XXI*, vol. 461 of *Astronomical Society of the Pacific Conference Series*, 569. xvi, 107

Rose, J.A. (1994). The integrated spectra of M32 and of 47 Tuc: A comparative study at high spectral resolution. *AJ*, **107**, 206–229. 109

Roseboom, I.G., Pimbblet, K.A., Drinkwater, M.J., Cannon, R.D., de Propris, R. & collaborators (2006). The 2dF-SDSS LRG and QSO Survey: the star formation histories of luminous red galaxies. *MNRAS*, **373**, 349–360. xxi, 12, 39, 40, 105, 108, 109, 112

Ross, N.P., Shanks, T. & Cruz da Ângela, J. (2007). The 2dF-SDSS LRG and QSO (2SLAQ) Survey: LRG Clustering and Redshift-Space Distortions. In N. Metcalfe & T. Shanks, eds., *Cosmic Frontiers*, vol. 379 of *Astronomical Society of the Pacific Conference Series*, 68. 13

Ross, N.P., Shanks, T., Cannon, R.D., Wake, D.A., Sharp, R.G., Croom, S.M. & Peacock, J.A. (2008). Luminous red galaxy clustering at z ˜= 0.7 - first results using AAOmega. *MNRAS*, **387**, 1323–1334. 13

Rubin, V.C., Burstein, D., Ford, W.K., Jr. & Thonnard, N. (1985). Rotation velocities of 16 SA galaxies and a comparison of Sa, Sb, and SC rotation properties. *ApJ*, **289**, 81–98. 8

Salpeter, E.E. (1955). The Luminosity Function and Stellar Evolution. *ApJ*, **121**, 161. 20, 21, 61

Samushia, L., Dev, A., Jain, D. & Ratra, B. (2010). Constraints on dark energy from the lookback time versus redshift test. *Physics Letters B*, **693**, 509–514. 11

Sánchez-Blázquez, P., Peletier, R.F., Jiménez-Vicente, J., Cardiel, N., Cenarro, A.J., Falcón-Barroso, J., Gorgas, J., Selam, S. & Vazdekis, A. (2006). Medium-resolution Isaac Newton Telescope library of empirical spectra. *MNRAS*, **371**, 703–718. 23, 24, 52, 53, 61

Sánchez-Blázquez, P., Jablonka, P., Noll, S., Poggianti, B.M., Moustakas, J. & collaborators (2009). Evolution of red-sequence cluster galaxies from redshift 0.8 to 0.4: ages, metallicities, and morphologies. *A&A*, **499**, 47–68. 13

Sánchez-Blázquez, P., Ocvirk, P., Gibson, B.K., Pérez, I. & Peletier, R.F. (2011). Star formation history of barred disc galaxies. *MNRAS*, **415**, 709–731. 25

Sarzi, M., Falcón-Barroso, J., Davies, R.L., Bacon, R., Bureau, M. & collaborators (2006). The SAURON project - V. Integral-field emission-line kinematics of 48 elliptical and lenticular galaxies. *MNRAS*, **366**, 1151–1200. 36, 37, 38, 120

Schaller, G., Schaerer, D., Meynet, G. & Maeder, A. (1992). New grids of stellar models from 0.8 to 120 solar masses at Z = 0.020 and Z = 0.001. *A&AS*, **96**, 269–331. 22, 61

Schiavon, R.P., Caldwell, N. & Rose, J.A. (2004). The Integrated Spectrum of M67 and the Spectroscopic Age of M32. *AJ*, **127**, 1513–1530. 63

Schlegel, D.J., Finkbeiner, D.P. & Davis, M. (1998). Maps of Dust Infrared Emission for Use in Estimation of Reddening and Cosmic Microwave Background Radiation Foregrounds. *ApJ*, **500**, 525. 64, 120

Schmidt, B.P., Suntzeff, N.B., Phillips, M.M. & Schommer, R.A.a.a. (1998). The High-Z Supernova Search: Measuring Cosmic Deceleration and Global Curvature of the Universe Using Type IA Supernovae. *ApJ*, **507**, 46–63. 4

Schoenberner, D. (1983). Late stages of stellar evolution. II - Mass loss and the transition of asymptotic giant branch stars into hot remnants. *ApJ*, **272**, 708–714. 22

Simon, J., Verde, L. & Jimenez, R. (2005). Constraints on the redshift dependence of the dark energy potential. *Phys. Rev. D*, **71**, 123001. 10, 11, 85, 89, 99, 121, 141

Smith, J.A., Tucker, D.L., Kent, S., Richmond, M.W., Fukugita, M., Ichikawa, T. & collaborators (2002). The u'g'r'i'z' Standard-Star System. *AJ*, **123**, 2121–2144. 102

Smith, R.J., Lucey, J.R. & Hudson, M.J. (2009). Ages and metallicities for quiescent galaxies in the Shapley supercluster: driving parameters of the stellar populations. *MNRAS*, **400**, 1690–1705. 73

Spergel, D.N., Verde, L., Peiris, H.V., Komatsu, E., Nolta, M.R., Bennett, C.L. & collaborators (2003). First-Year Wilkinson Microwave Anisotropy Probe (WMAP) Observations: Determination of Cosmological Parameters. *ApJS*, **148**, 175–194. 7

Spergel, D.N., Bean, R., Doré, O., Nolta, M.R., Bennett, C.L., Dunkley, J. & collaborators (2007). Three-Year Wilkinson Microwave Anisotropy Probe (WMAP) Observations: Implications for Cosmology. *ApJS*, **170**, 377–408.

Spiniello, C., Koopmans, L.V.E., Trager, S.C., Czoske, O. & Treu, T. (2011). The X-Shooter Lens Survey - I. Dark matter domination and a Salpeter-type initial mass function in a massive early-type galaxy. *MNRAS*, **417**, 3000–3009. 21

Spolaor, M., Kobayashi, C., Forbes, D.A., Couch, W.J. & Hau, G.K.T. (2010). Early-type galaxies at large galactocentric radii - II. Metallicity gradients and the [Z/H]-mass, [α/Fe]-mass relations. *MNRAS*, **408**, 272–292. 28

Stern, D., Jimenez, R., Verde, L., Kamionkowski, M. & Stanford, S.A. (2010a). Cosmic chronometers: constraining the equation of state of dark energy. I: H(z) measurements. *J. Cosmology Astropart. Phys.*, **2**, 8. 10, 11, 85, 89, 121, 124, 125, 128, 129, 141

Stern, D., Jimenez, R., Verde, L., Stanford, S.A. & Kamionkowski, M. (2010b). Cosmic Chronometers: Constraining the Equation of State of Dark Energy. II. A Spectroscopic Catalog of Red Galaxies in Galaxy Clusters. *ApJS*, **188**, 280–289. 99

Stoughton, C., Lupton, R.H., Bernardi, M., Blanton, M.R., Burles, S., Castander, F.J., Connolly, A.J., Eisenstein, D.J., Frieman, J.A., Hennessy, G.S., Hindsley, R.B., Ivezić, Ž., Kent, S., Kunszt, P.Z., Lee, B.C., Meiksin, A., Munn, J.A., Newberg, H.J., Nichol, R.C., Nicinski, T., Pier, J.R., Richards, G.T., Richmond, M.W., Schlegel, D.J., Smith, J.A. & collaborators (2002). Sloan Digital Sky Survey: Early Data Release. *AJ*, **123**, 485–548. 30, 32, 34

Strateva, I., Ivezić, Ž., Knapp, G.R., Narayanan, V.K., Strauss, M.A. & collaborators (2001). Color Separation of Galaxy Types in the Sloan Digital Sky Survey Imaging Data. *AJ*, **122**, 1861–1874. 26

Strauss, M.A., Weinberg, D.H., Lupton, R.H., Narayanan, V.K., Annis, J. & collaborators (2002). Spectroscopic Target Selection in the Sloan Digital Sky Survey: The Main Galaxy Sample. *AJ*, **124**, 1810–1824. 30

SubbaRao, M., Frieman, J. & collaborators (2002). The Sloan Digital Sky Survey 1-Dimensional Spectroscopic Pipeline. In J.L. Starck & F.D. Murtagh, eds., *Astronomical Data Analysis II*, vol. 4847 of *Society of Photo-Optical Instrumentation Engineers (SPIE) Conference Series*, 452–460. 32

Szabo, T., Pierpaoli, E., Dong, F., Pipino, A. & Gunn, J. (2011). An Optical Catalog of Galaxy Clusters Obtained from an Adaptive Matched Filter Finder Applied to Sloan Digital Sky Survey Data Release 6. *ApJ*, **736**, 21. 111

Tantalo, R., Chiosi, C. & Bressan, A. (1998). Ages and metallicities in elliptical galaxies from the H_beta, <Fe>, and Mg_2 diagnostics. *A&A*, **333**, 419–432. 18

The Dark Energy Survey Collaboration (2005). The Dark Energy Survey. *ArXiv Astrophysics e-prints*. 6

Thomas, D., Maraston, C. & Bender, R. (2003). Stellar population models of Lick indices with variable element abundance ratios. *MNRAS*, **339**, 897–911. xi, 18, 45, 50, 52, 53, 55, 59, 87

Thomas, D., Maraston, C. & Korn, A. (2004). Higher-order Balmer line indices in α/Fe-enhanced stellar population models. *MNRAS*, **351**, L19–L23. 52

Thomas, D., Maraston, C. & Bender, R. (2005). Stellar Population Models with Variable Element Abundance Ratios. *Highlights of Astronomy*, **13**, 189–3. 18, 27, 29, 73

Thomas, D., Maraston, C. & Johansson, J. (2011). Flux-calibrated stellar population models of Lick absorption-line indices with variable element abundance ratios. *MNRAS*, **412**, 2183–2198. 28, 29, 50, 52, 53, 62, 87, 89

Thomas, D., Steele, O., Maraston, C., Johansson, J., Beifiori, A., Pforr, J., Strömbäck, G., Tremonti, C.A., Wake, D., Bizyaev, D., Bolton, A., Brewington, H., Brownstein, J.R., Comparat, J., Kneib, J.P., Malanushenko, E., Malanushenko, V., Oravetz, D., Pan, K., Parejko, J.K., Schneider, D.P., Shelden, A., Simmons, A., Snedden, S., Tanaka, M., Weaver, B.A. & Yan, R. (2013). Stellar velocity dispersions and emission line properties of SDSS-III/BOSS galaxies. *MNRAS*, **431**, 1383–1397. 36

Tinsley, B.M. (1980). Evolution of the Stars and Gas in Galaxies. *Fund. Cosmic Phys.*, **5**, 287–388. 21

Tojeiro, R., Heavens, A.F., Jimenez, R. & Panter, B. (2007). Recovering galaxy star formation and metallicity histories from spectra using VESPA. *MNRAS*, **381**, 1252–1266. 56

Tolstoy, E., Hill, V. & Tosi, M. (2009). Star-Formation Histories, Abundances, and Kinematics of Dwarf Galaxies in the Local Group. *ARA&A*, **47**, 371–425. 18

Tonry, J. & Davis, M. (1979). A survey of galaxy redshifts. I - Data reduction techniques. *AJ*, **84**, 1511–1525. 34

Trager, S.C., Faber, S.M., Worthey, G. & González, J.J. (2000). The Stellar Population Histories of Local Early-Type Galaxies. I. Population Parameters. *AJ*, **119**, 1645–1676. 18, 25

Trager, S.C., Faber, S.M. & Dressler, A. (2008). The stellar population histories of early-type galaxies - III. The Coma cluster. *MNRAS*, **386**, 715–747. 13

Tremonti, C.A., Heckman, T.M., Kauffmann, G., Brinchmann, J., Charlot, S. & collaborators (2004). The Origin of the Mass-Metallicity Relation: Insights from 53,000 Star-forming Galaxies in the Sloan Digital Sky Survey. *ApJ*, **613**, 898–913. 36, 37, 38, 47, 75, 88, 175

Valdes, F., Gupta, R., Rose, J.A., Singh, H.P. & Bell, D.J. (2004). The Indo-US Library of Coudé Feed Stellar Spectra. *ApJS*, **152**, 251–259. 24

van Dokkum, P.G. (2001). Cosmic-Ray Rejection by Laplacian Edge Detection. *PASP*, **113**, 1420–1427. 118

van Dokkum, P.G. (2008). Evidence of Cosmic Evolution of the Stellar Initial Mass Function. *ApJ*, **674**, 29–50. 21

van Dokkum, P.G. & Conroy, C. (2010). A substantial population of low-mass stars in luminous elliptical galaxies. *Nature*, **468**, 940–942. 21

van Dokkum, P.G. & Conroy, C. (2011). Confirmation of Enhanced Dwarf-sensitive Absorption Features in the Spectra of Massive Elliptical Galaxies: Further Evidence for a Non-universal Initial Mass Function. *ApJ*, **735**, L13. 21

Vandenberg, D.A. (1985). Evolution of 0.7-3.0 solar masses stars having Fe/H between -1.0 and 0.0. *ApJS*, **58**, 711–769. 18, 22

VandenBerg, D.A., Bergbusch, P.A. & Dowler, P.D. (2006). The Victoria-Regina Stellar Models: Evolutionary Tracks and Isochrones for a Wide Range in Mass and Metallicity that Allow for Empirically Constrained Amounts of Convective Core Overshooting. *ApJS*, **162**, 375–387. 22

Vassiliadis, E. & Wood, P.R. (1994). Post-asymptotic giant branch evolution of low- to intermediate-mass stars. *ApJS*, **92**, 125–144. 22, 62

Vazdekis, A. (1999). Evolutionary Stellar Population Synthesis at 2 Å Spectral Resolution. *ApJ*, **513**, 224–241. 61

Vazdekis, A. & Arimoto, N. (1999). A Robust Age Indicator for Old Stellar Populations. *ApJ*, **525**, 144–152. 109

Vazdekis, A., Salaris, M., Arimoto, N. & Rose, J.A. (2001). 47 Tucanae: The Spectroscopic versus Color-Magnitude Diagram Age Discrepancy. *ApJ*, **549**, 274–280. 109

Vazdekis, A., Cenarro, A.J., Gorgas, J., Cardiel, N. & Peletier, R.F. (2003). Empirical calibration of the near-infrared CaII triplet - IV. The stellar population synthesis models. *MNRAS*, **340**, 1317–1345. 61

Vazdekis, A., Sánchez-Blázquez, P., Falcón-Barroso, J., Cenarro, A.J. & collaborators (2010). Evolutionary stellar population synthesis with MILES - I. The base models and a new line index system. *MNRAS*, **404**, 1639–1671. 28, 29, 61

Verkhodanov, O.V., Parijskij, Y.N. & Starobinsky, A.A. (2005). Determination of Ω and H_0 from photometric data of radio galaxies. *Bulletin of the Special Astrophysics Observatory*, **58**, 5–15. 11

Visvanathan, N. & Sandage, A. (1977). The color-absolute magnitude relation for E and S0 galaxies. I - Calibration and tests for universality using Virgo and eight other nearby clusters. *ApJ*, **216**, 214–226. 12, 27

Wake, D.A., Nichol, R.C., Eisenstein, D.J., Loveday, J., Edge, A.C. & collaborators (2006). The 2df SDSS LRG and QSO survey: evolution of the luminosity function of luminous red galaxies to z = 0.6. *MNRAS*, **372**, 537–550. 12

Watkins, R., Feldman, H.A. & Hudson, M.J. (2009). Consistently large cosmic flows on scales of $100h^{-1}$Mpc: a challenge for the standard ΛCDM cosmology. *MNRAS*, **392**, 743–756. 6

Wen, Z.L., Han, J.L. & Liu, F.S. (2012). A Catalog of 132,684 Clusters of Galaxies Identified from Sloan Digital Sky Survey III. *ApJS*, **199**, 34. xxi, 111, 113, 123

Wilkins, S.M., Hopkins, A.M., Trentham, N. & Tojeiro, R. (2008). Extragalactic constraints on the initial mass function. *MNRAS*, **391**, 363–368. 21

Worthey, G. (1999). The Age-Metallicity Degeneracy. In I. Hubeny, S. Heap & R. Cornett, eds., *Spectrophotometric Dating of Stars and Galaxies*, vol. 192 of *Astronomical Society of the Pacific Conference Series*, 283. ix, 25, 26

Worthey, G. & Ottaviani, D.L. (1997). H gamma and H delta Absorption Features in Stars and Stellar Populations. *ApJS*, **111**, 377. 44, 45, 48, 50, 108, 109

Worthey, G., Faber, S.M. & Gonzalez, J.J. (1992). MG and Fe absorption features in elliptical galaxies. *ApJ*, **398**, 69–73. 23, 87

Worthey, G., Faber, S.M., Gonzalez, J.J. & Burstein, D. (1994). Old stellar populations. 5: Absorption feature indices for the complete LICK/IDS sample of stars. *ApJS*, **94**, 687–722. 16, 18, 44, 45, 109

Wright, E.L., Eisenhardt, P.R.M., Mainzer, A.K., Ressler, M.E., Cutri, R.M. & collaborators (2010). The Wide-field Infrared Survey Explorer (WISE): Mission Description and Initial On-orbit Performance. *AJ*, **140**, 1868–1881. 103, 107

Yan, L., Donoso, E., Tsai, C.W., Stern, D., Assef, R.J., Eisenhardt, P., Blain, A.W., Cutri, R., Jarrett, T., Stanford, S.A., Wright, E., Bridge, C. & Riechers, D.A. (2013). Characterizing the Mid-infrared Extragalactic Sky with WISE and SDSS. *AJ*, **145**, 55. xvi, 103, 104, 105

Yanny, B., Newberg, H.J. & collaborators (2004). Erratum: "A Low-Latitude Halo Stream around the Milky Way" (¡A href="/abs/2003ApJ...588..824Y"¿ApJ, 588, 824 [2003]¡/A¿). *ApJ*, **605**, 575–577. 34

Yi, S., Demarque, P., Kim, Y.C., Lee, Y.W., Ree, C.H., Lejeune, T. & Barnes, S. (2001). Toward Better Age Estimates for Stellar Populations: The Y^2 Isochrones for Solar Mixture. *ApJS*, **136**, 417–437. 22

Yi, S.K. (2003). Uncertainties of Synthetic Integrated Colors as Age Indicators. *ApJ*, **582**, 202–214. 22

York, D.G., Adelman, J., Anderson, J.E., Jr., Anderson, S.F., Annis, J. & SDSS Collaboration (2000). The Sloan Digital Sky Survey: Technical Summary. *AJ*, **120**, 1579–1587. 30

Zehavi, I., Eisenstein, D.J., Nichol, R.C., Blanton, M.R., Hogg, D.W. & collaborators (2005). The Intermediate-Scale Clustering of Luminous Red Galaxies. *ApJ*, **621**, 22–31. 13

Zhang, C., Zhang, H., Yuan, S., Zhang, T.J. & Sun, Y.C. (2012). Four New Observational $H(z)$ Data From Luminous Red Galaxies Sloan Digital Sky Survey Data Release Seven. *ArXiv e-prints*. xvii, 11, 66, 71, 85, 87, 88, 89, 121, 123, 140, 141, 143, 144

Zheng, W., Li, H., Xia, J.Q., Wan, Y.P., Li, S.Y. & Li, M. (2014). Constraints on cosmological models from Hubble parameters measurements. *International Journal of Modern Physics D*, **23**, 50051. 140, 146

Zwicky, F. (1933). Die Rotverschiebung von extragalaktischen Nebeln. *Helvetica Physica Acta*, **6**, 110–127. 8

Appendix A

Comparisons of σ_v and emission lines with MPA-JHU catalogue

As we did not used either the measured velocity dispersion or the emission lines values from the SDSS or the MPA-JHU catalogues, it is necessary to compare the results from the pPXF and GANDALF routines in order to see its performance. We used the sample of galaxies within redshift bin $0.24 < z < 0.26$ without any selection have been applied to it. Figure A.1 shows the agreement between both velocity dispersion measurements. This is not surprising since the MPA-JHU group have used the same stellar templates by Tremonti *et al.* (2004) to determine the stellar kinematics. We found that pPXF can recover the velocity dispersion values of the MPA-JHU.

We also used the same sample to select the corresponded equivalent widths (EWs) of Hβ, [OIII]λ5007 and Hα emission lines from the MPA-JHU catalogue. Without considering any exception about the strength of the emission lines (strong or weak), figure A.2 represents the comparison between our emission lines values (EWs) and those from the catalogue. The Hα line widths agree fairly with the MPA-JHU measurements as proved by other studies (Oh *et al.*, 2011). However, [OIII]λ5007 and Hβ EWs show little biases, our values are lower than the MPA-JHU estimates. The cause of these small deviations are very difficult to understand, it might become negligible when comparing a larger sample. The straight lines found at zero on our measurements would be our quiescent galaxies sample, which fall into the definition of the passively evolving galaxies introduced by Tremonti *et al.* (2004). The outliers values on that zero lines are probably those objects with higher velocity dispersion and which were excluded in our final sample.

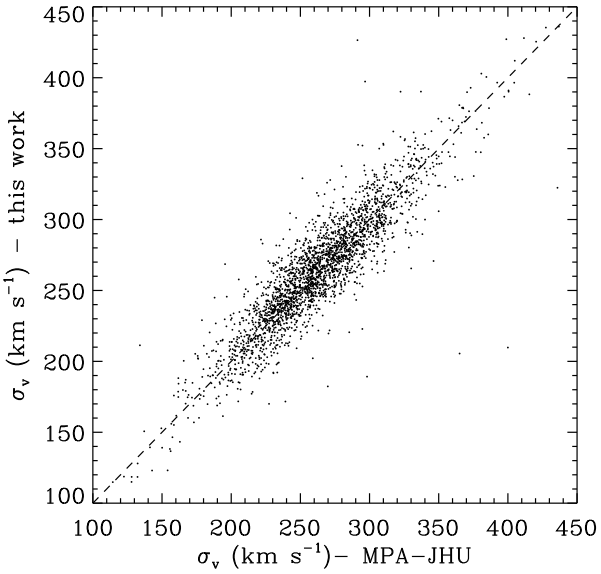

Figure A.1: Comparison of our values of the central velocity dispersion and those listed from the MPA-JHU catalogue for objects at $0.24 < z < 0.26$. The dashed line shows the one-to-one line.

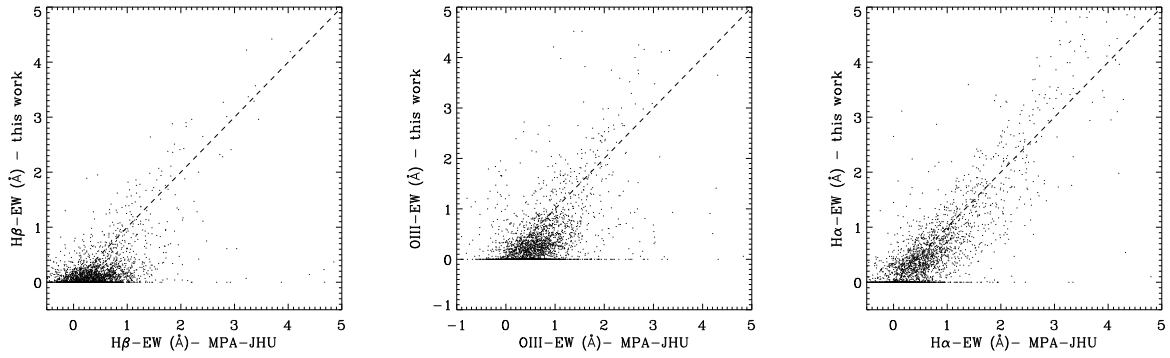

Figure A.2: Comparison of our values of emission line EWs and those from the MPA-JHU catalogue for objects at $0.24 < z < 0.26$. The dashed lines show the one-to-one lines.The straight lines found at zero represent our quiescent galaxies sample. The outliers values from that lines were excluded in our final sample since they might be the objects with higher velocity dispersion.

Appendix B

Fits of all stacked spectra

In this appendix, we present all fits of the other 14 stacked spectra with PE, VM, BC03 and M11 models. The fits were done in the whole wavelength ranges when using the last three models, whereas set as 4000 - 5500 Å for PE model. After applying the LSF injection in order to match the resolution of both model and observed spectra, and a degree of multiplicative polynomial of ∼12, plots of the SSP fitting of all stacked spectra are given in figure B.1 to B.14. The fitting plots of the stacked spectra at $0.24 < z < 0.26$ have already shown in chapter 3. The corresponded SSP parameter results are found in tables 3.10, 3.11, 3.22, and 3.13 of chapter 3. The telluric lines and all possible undesirable spikes were masked.

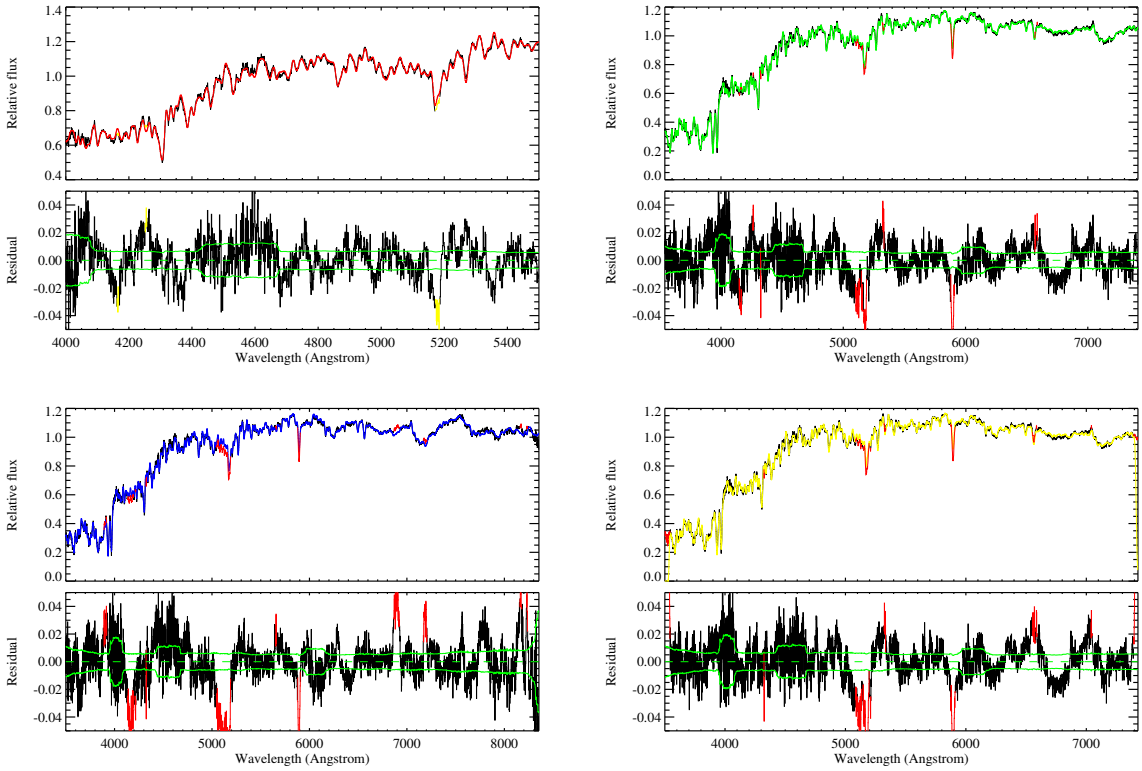

Figure B.1: Fitting stacked spectra with PE (red), VM (green), BC03 (blue) and M11 (yellow) models. All upper panels of each subfigure display the stacked spectra at $0.10 < z < 0.12$ (black lines) and the best fit models (coloured spectra). All bottom panels show the residual from the fits, the solid green lines are the 1σ deviation and the dashed green lines represent zero residuals. Red and yellow (in the first plot) regions were rejected from the fits. They were masked due to the telluric lines, the interstellar absorption line (NaD), and automatic rejection of outliers.

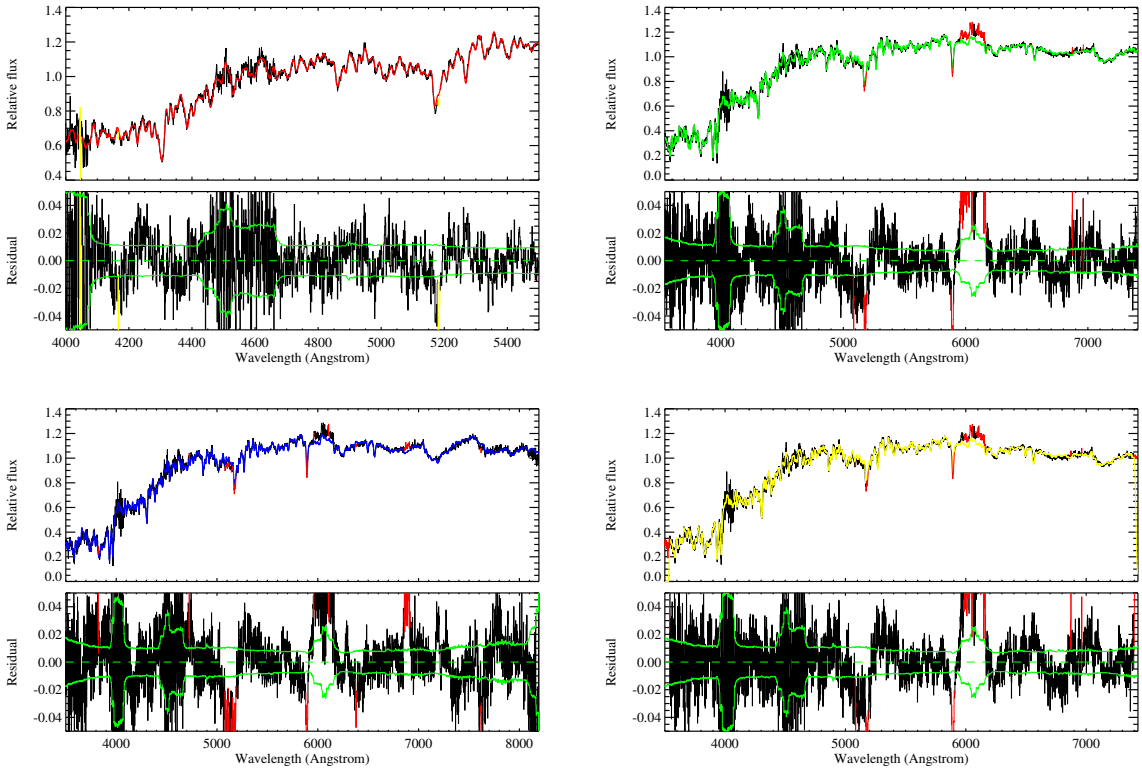

Figure B.2: Fitting stacked spectra at $0.12 < z < 0.14$ with PE (red), VM (green), BC03 (blue) and M11 (yellow) models.

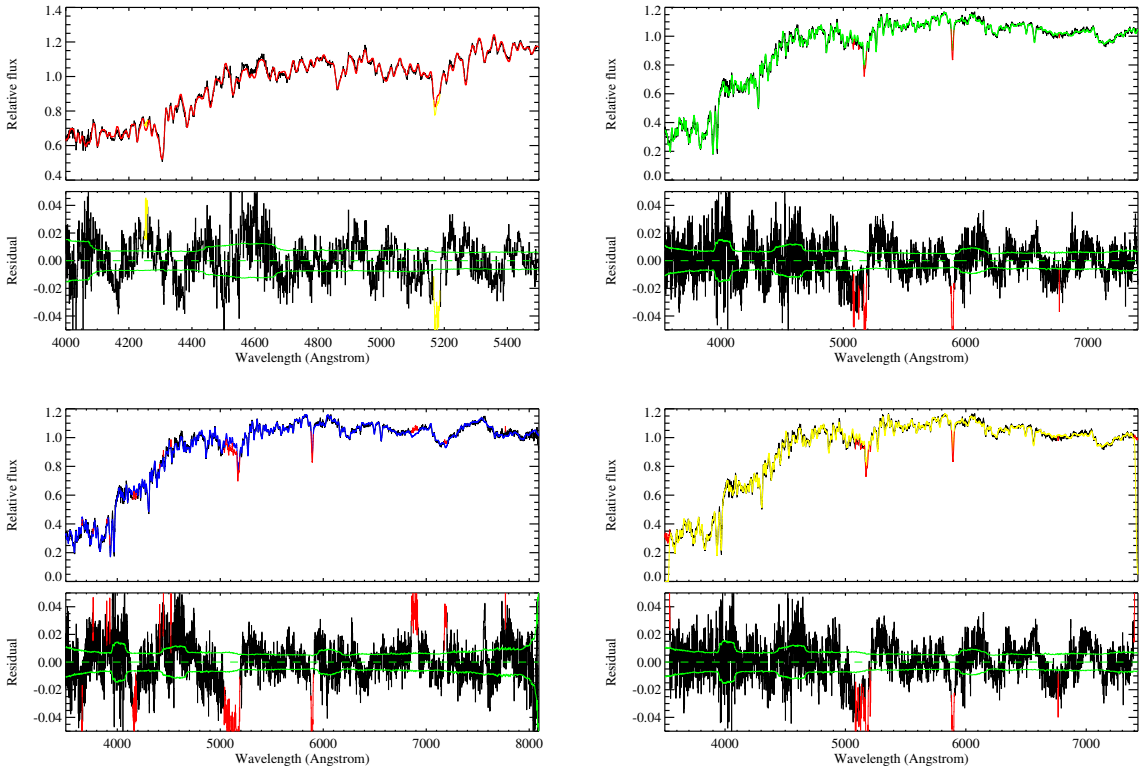

Figure B.3: Fitting stacked spectra at $0.14 < z < 0.16$ with PE (red), VM (green), BC03 (blue) and M11 (yellow) models.

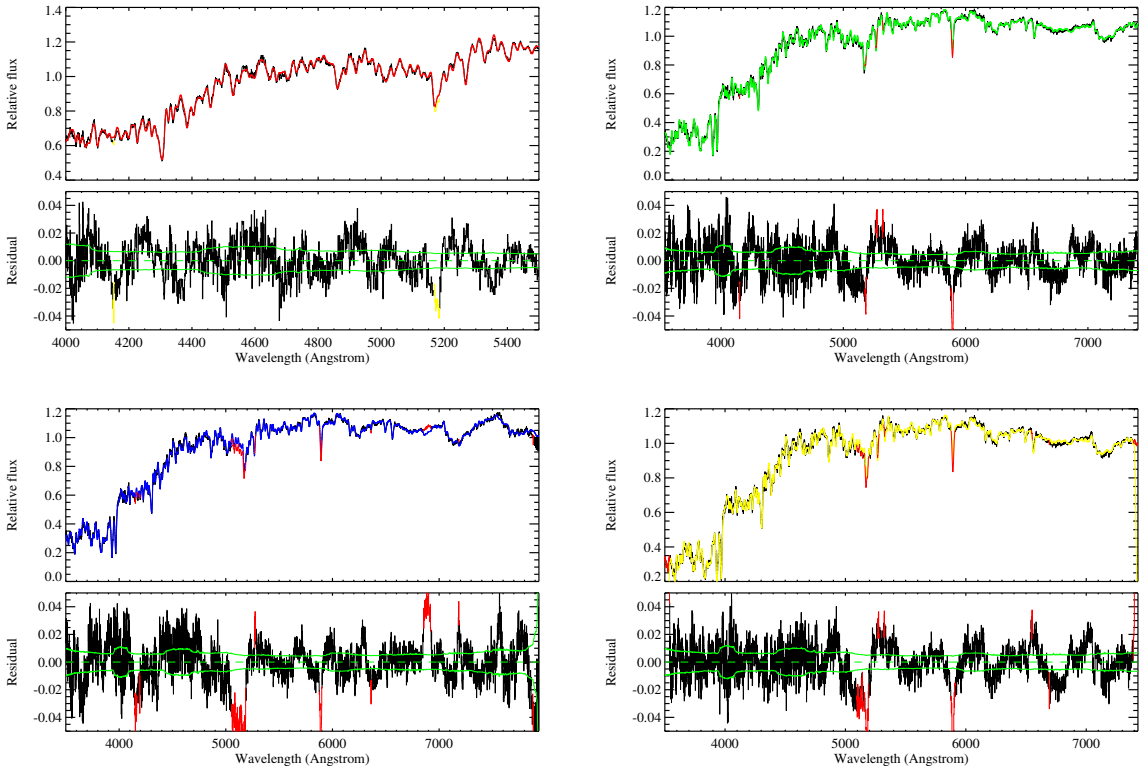

Figure B.4: Fitting stacked spectra at $0.16 < z < 0.18$ with PE (red), VM (green), BC03 (blue) and M11 (yellow) models.

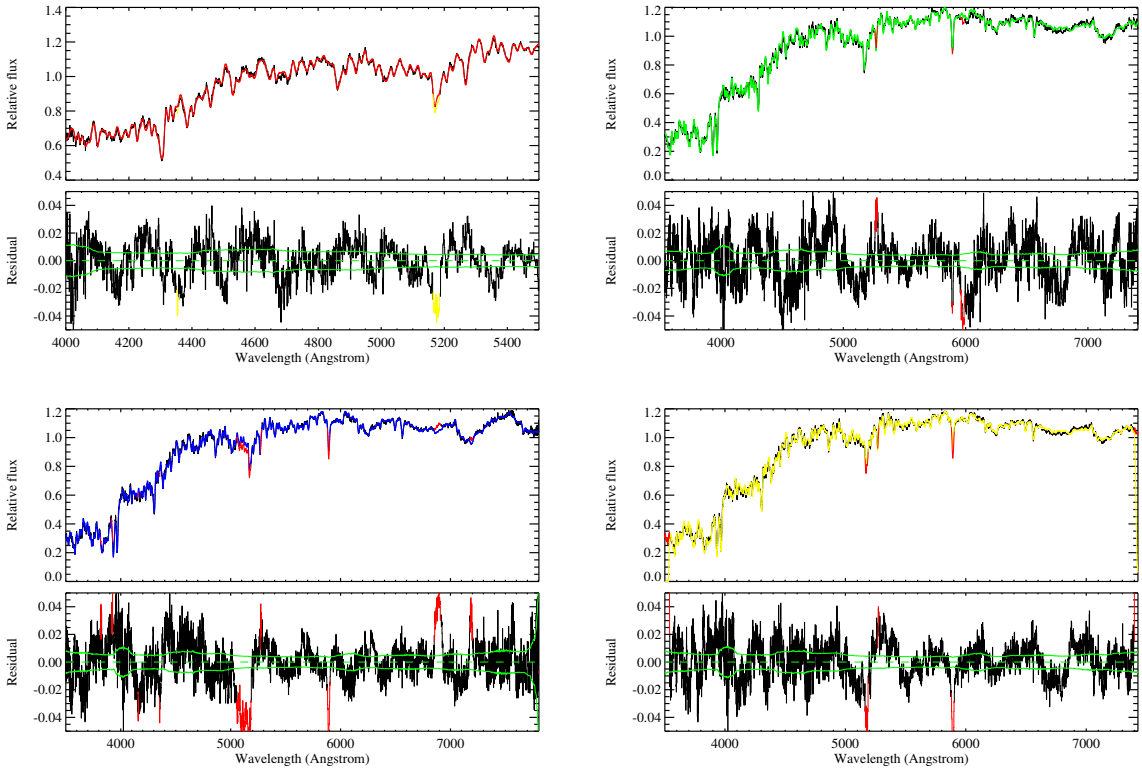

Figure B.5: Fitting stacked spectra at $0.18 < z < 0.20$ with PE (red), VM (green), BC03 (blue) and M11 (yellow) models.

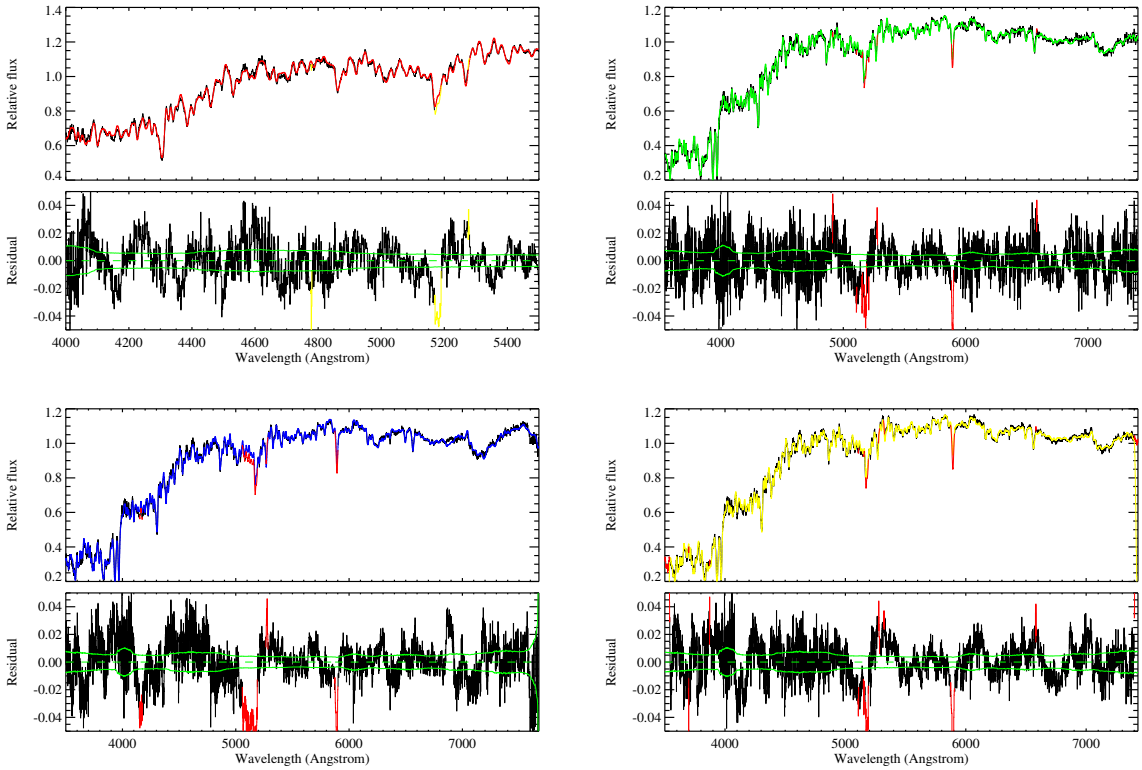

Figure B.6: Fitting stacked spectra at $0.20 < z < 0.22$ with PE (red), VM (green), BC03 (blue) and M11 (yellow) models.

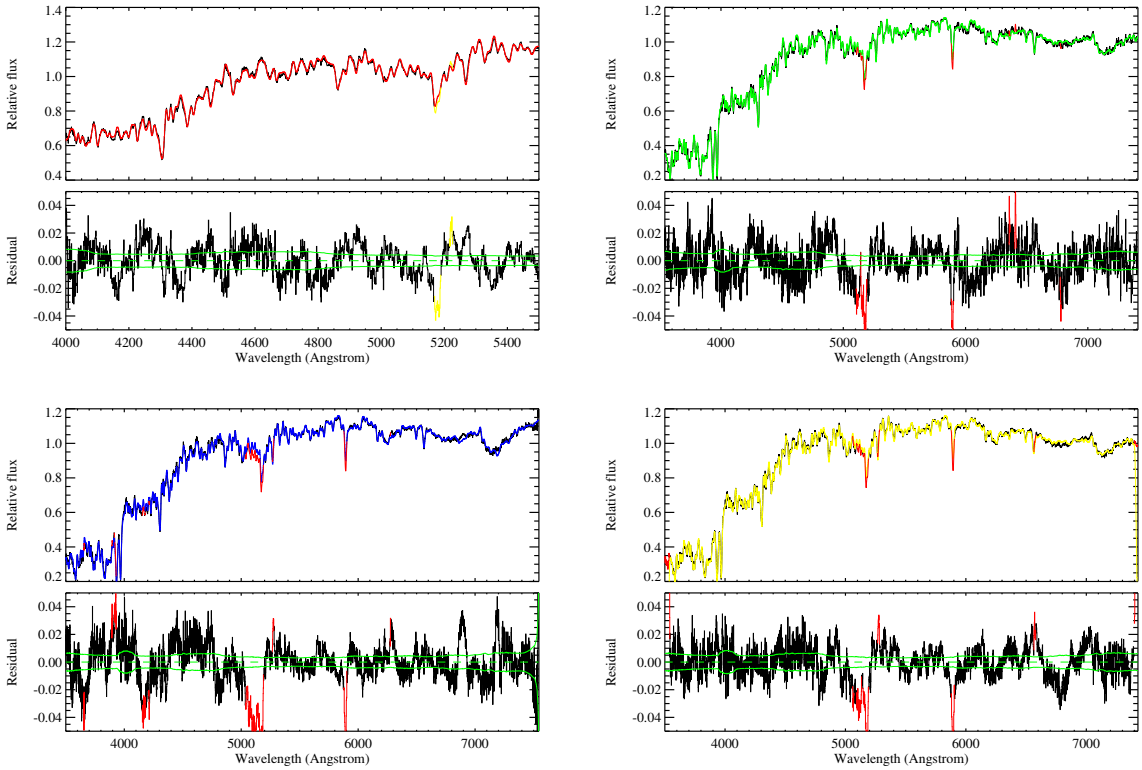

Figure B.7: Fitting stacked spectra at $0.22 < z < 0.24$ with PE (red), VM (green), BC03 (blue) and M11 (yellow) models.

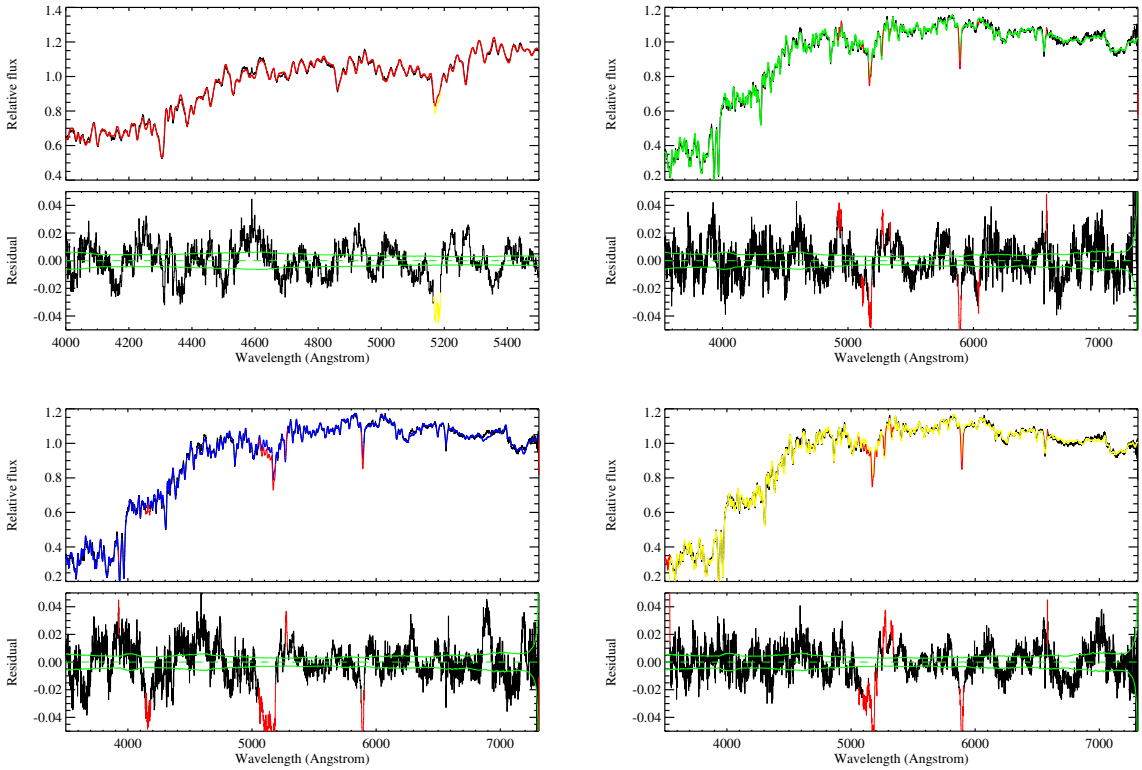

Figure B.8: Fitting stacked spectra at $0.26 < z < 0.28$ with PE (red), VM (green), BC03 (blue) and M11 (yellow) models.

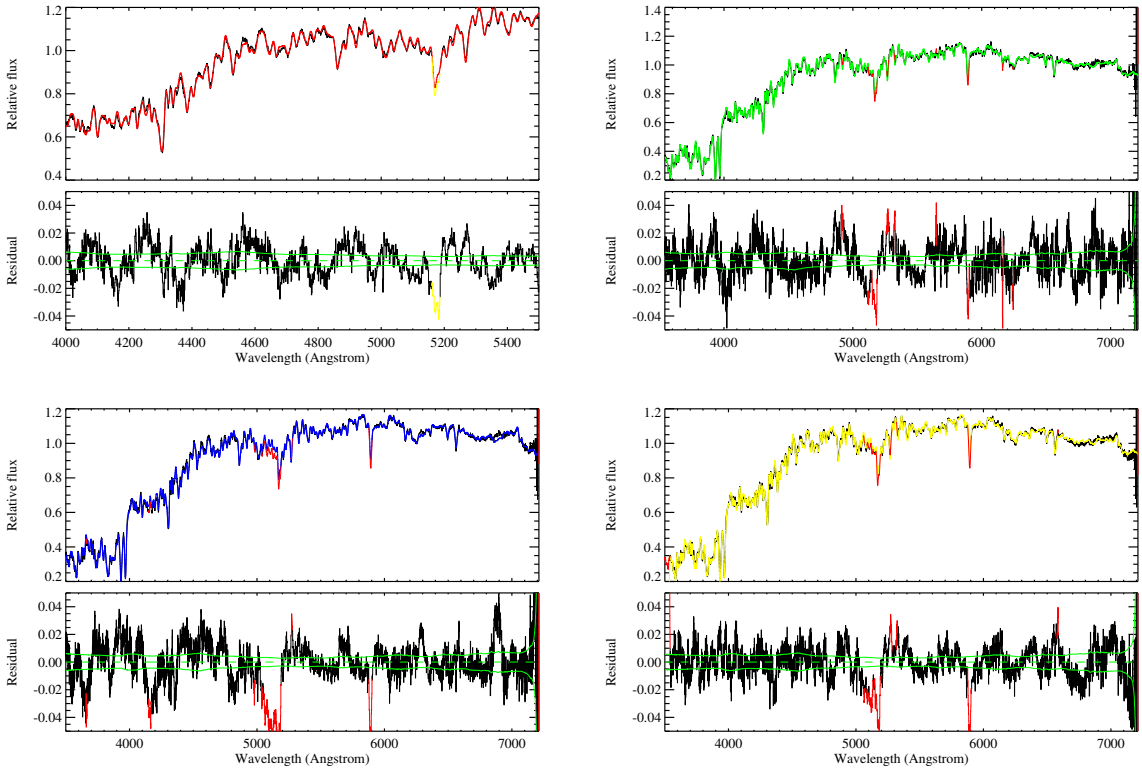

Figure B.9: Fitting stacked spectra at $0.28 < z < 0.30$ with PE (red), VM (green), BC03 (blue) and M11 (yellow) models.

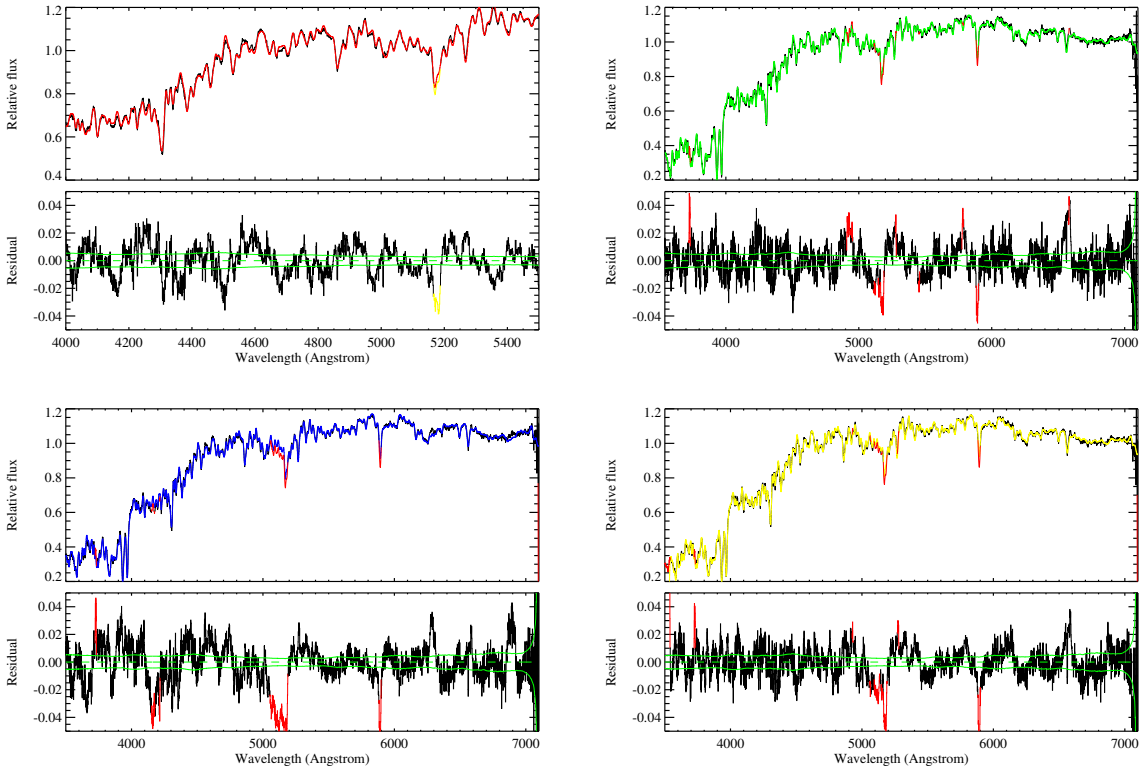

Figure B.10: Fitting stacked spectra at $0.30 < z < 0.32$ with PE (red), VM (green), BC03 (blue) and M11 (yellow) models.

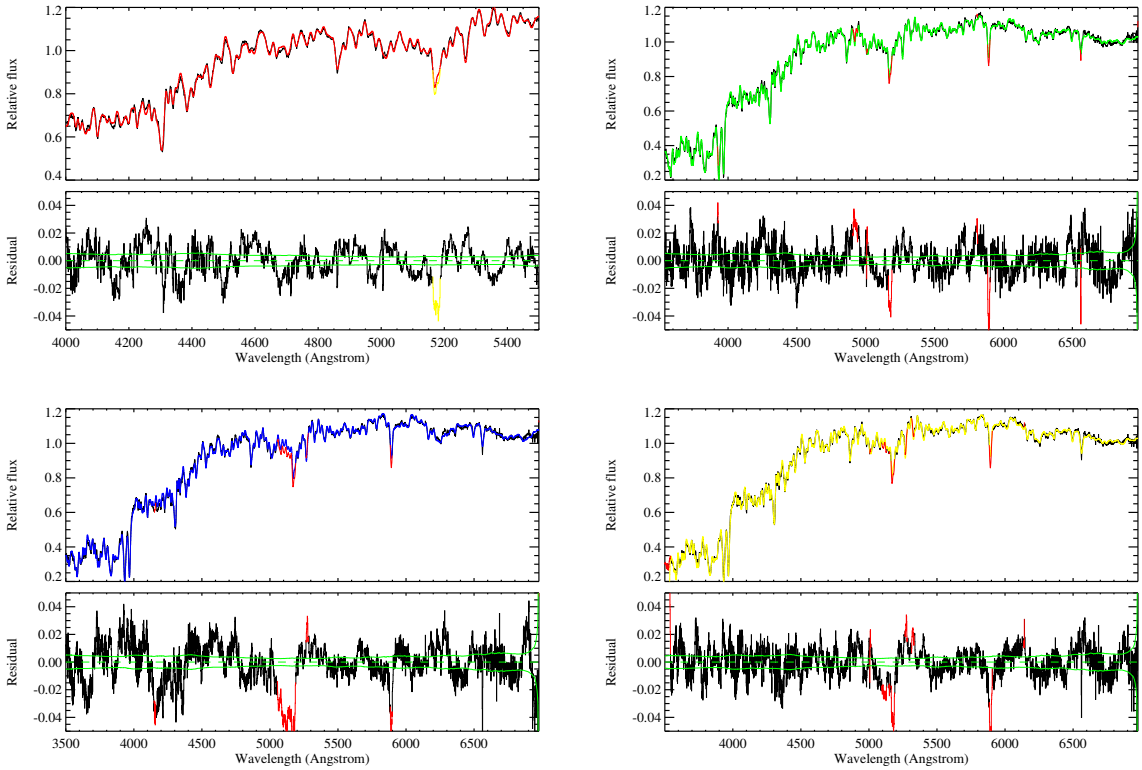

Figure B.11: Fitting stacked spectra at $0.32 < z < 0.34$ with PE (red), VM (green), BC03 (blue) and M11 (yellow) models.

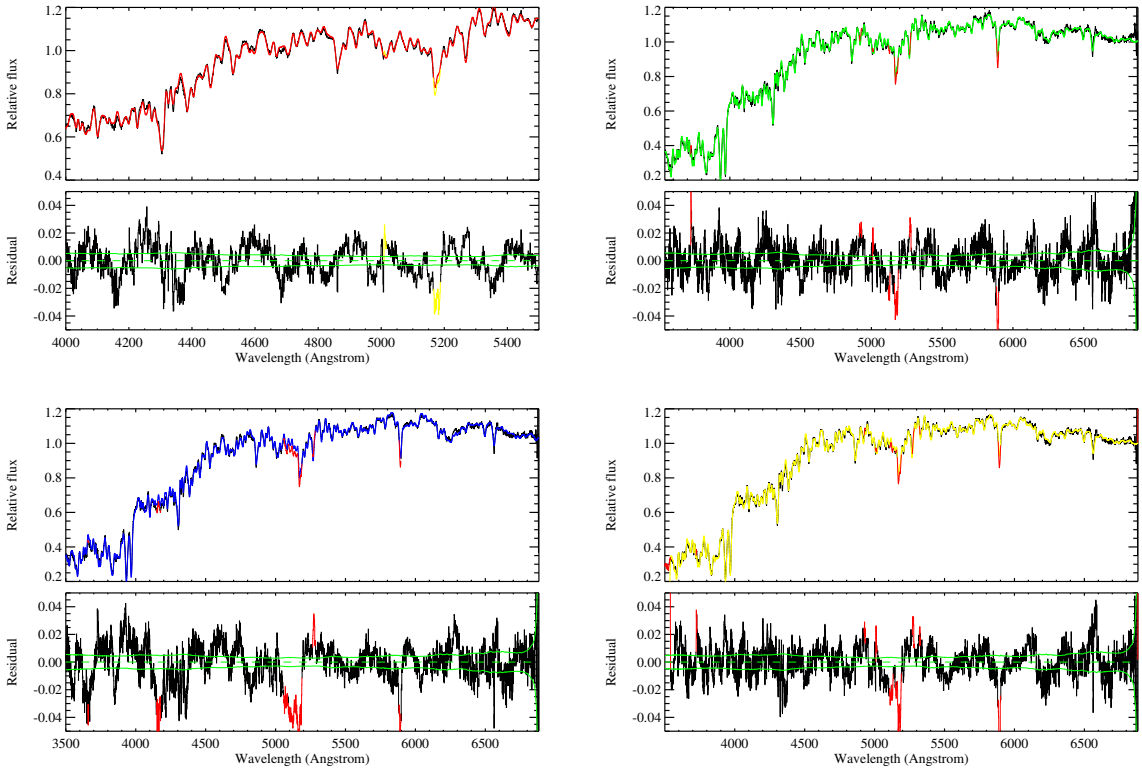

Figure B.12: Fitting stacked spectra at $0.34 < z < 0.36$ with PE (red), VM (green), BC03 (blue) and M11 (yellow) models.

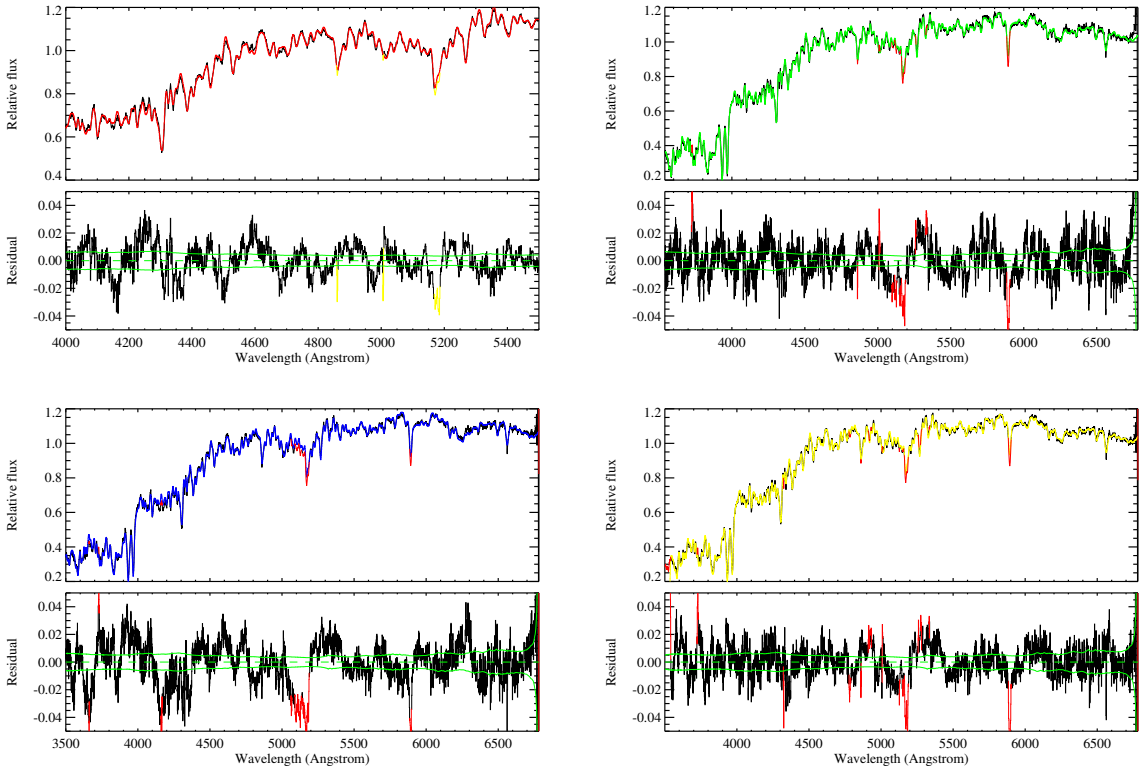

Figure B.13: Fitting stacked spectra at $0.36 < z < 0.38$ with PE (red), VM (green), BC03 (blue) and M11 (yellow) models.

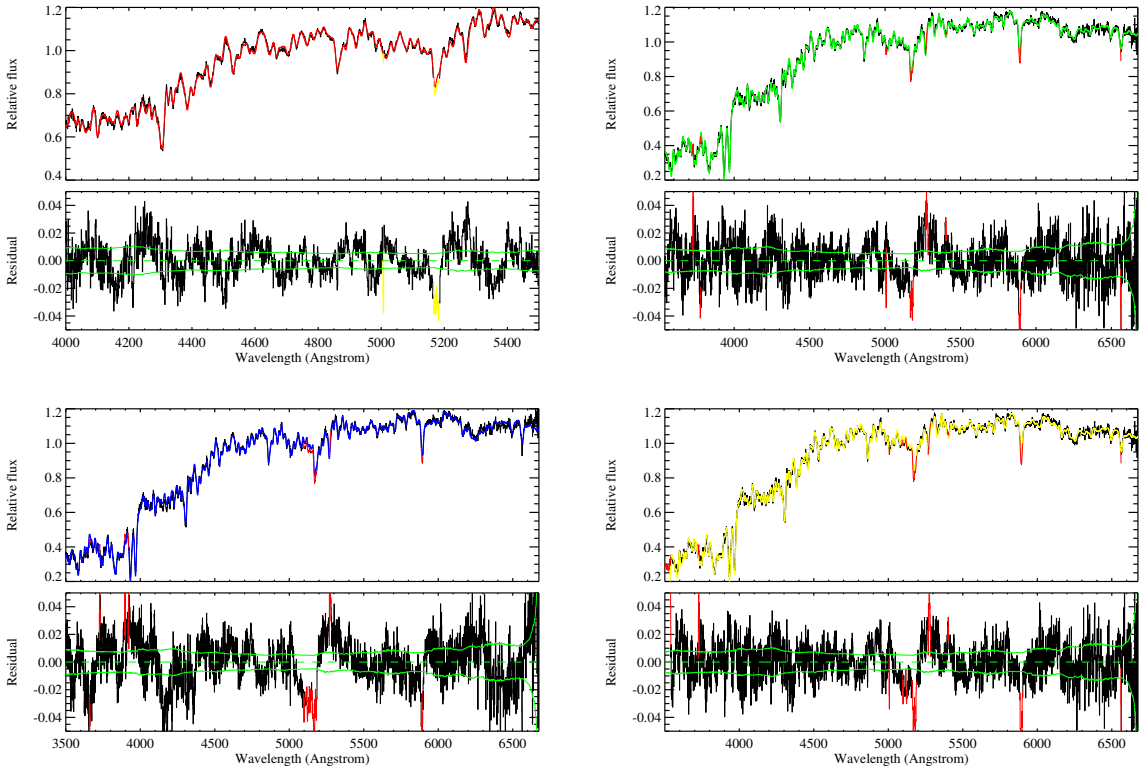

Figure B.14: Fitting stacked spectra at $0.38 < z < 0.40$ with PE (red), VM (green), BC03 (blue) and M11 (yellow) models.